Dissertations and Theses (Open Access)   MD Anderson UTHealth Houston Graduate School

5-2022

Integration Of Biomedical Imaging And Translational Approaches For Management Of Head And Neck Cancer

Abdallah Mohamed

Abdallah Mohamed

INTEGRATION OF BIOMEDICAL IMAGING AND TRANSLATIONAL APPROACHES FOR

MANAGEMENT OF HEAD AND NECK CANCER
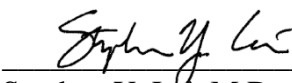
by

Abdallah Sherif Radwan Mohamed, M.D., M.Sc.
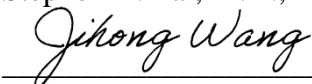
APPROVED:

_____
Clifton D. Fuller, M.D., Ph.D.
Advisory Professor
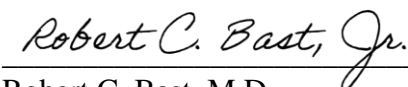
_____
Stephen Y. Lai, M.D., Ph.D.

_____
Jihong Wang, Ph.D.

_____
R. Jason Stafford, Ph.D.

_____
Robert C. Bast, M.D.

_____
Panayiotis Mavroidis, Ph.D.

APPROVED:

_____
Dean, The University of Texas
MD Anderson Cancer Center UTHealth Graduate School of Biomedical Science

INTEGRATION OF BIOMEDICAL IMAGING AND TRANSLATIONAL APPROACHES FOR

MANAGEMENT OF HEAD AND NECK CANCER

A

Dissertation

Presented to the Faculty of

The University of Texas

MD Anderson Cancer Center UTHealth

Graduate School of Biomedical Sciences

in Partial Fulfillment

of the Requirements

for the Degree of

Doctor of Philosophy

by

Abdallah Sherif Radwan Mohamed, M.D., M.Sc.

Houston, Texas

May, 2022

Dedication

Dedicated to my family. You always support and motivate me to be a better person. I owe all my success to you. I also dedicate it to the brave Egyptian souls who were part of the 2011 revolution that changed my life forever.

Acknowledgment

I wholeheartedly express my thanks and gratitude to my advisor, Dr. Clifton D. Fuller for his continuous and unlimited support during and well before I joined the PhD program. He provided me with the guidance, friendship, and wisdom of research and life in general. I owe him all the success I had through my research journey. Honestly, I would not be the researcher or person I am today without him. Thank you to every member of the Fuller Lab, past and present, who have all contributed to my success. They were all exemplar of the true meaning of team science and are integral part of this work.

I also would like to express my extreme gratitude and thanks to Dr. Stephen Y. Lai for all the help and support he provided to me before and during the PhD work. He offered me all the resources I need to fulfill the translational component of this dissertation. I owe him and his lab members Ying Henderson, Yunyun Chen, and Nikhil Chari all the basic and translational science skills I have.

Thank you to my committee members and MRI gurus, Dr. Jihong Wang and Dr. Jason Stafford who guided me and offered all the help and support to execute the MRI component of this dissertation.

Thank you to my committee member and translational cancer research role model, Dr. Robert Bast who was the first GSBS faculty member to interview me before expressing my interest to join the Clinical and Translational Oncology Track of the Cancer Biology Program and since then he always provides me with precious career and life related advises.

Thank you to my external committee member, Dr. Panayiotis Mavroidis who has been very supportive of my work and provided me with extremely valuable tips and advises.

Thank you to my parents, siblings, wife, and children who all showed non-stop encouragement and emotional support during this long journey. I love you all.

INTEGRATION OF BIOMEDICAL IMAGING AND TRANSLATIONAL APPROACHES FOR
MANAGEMENT OF HEAD AND NECK CANCER

Abdallah Sherif Radwan Mohamed, M.D., M.Sc.

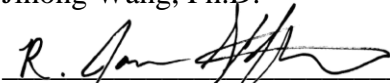Advisory Professor: Clifton D. Fuller, M.D., Ph.D.

Abstract

The aim of the clinical component of this work was to determine whether the currently available clinical imaging tools can be integrated with radiotherapy (RT) platforms for monitoring and adaptation of radiation dose, prediction of tumor response and disease outcomes, and characterization of patterns of failure and normal tissue toxicity in head and neck cancer (HNC) patients with potentially curable tumors. In Aim 1, we showed that the currently available clinical imaging modalities can be successfully used to adapt RT dose based-on dynamic tumor response, predict oncologic disease outcomes, characterize RT-induced toxicity, and identify the patterns of disease failure. We used anatomical MRIs for the RT dose adaptation purpose. Our findings showed that after proper standardization of the immobilization and image acquisition techniques, we can achieve high geometric accuracy. These images can then be used to monitor the shrinkage of tumors during RT and optimize the clinical target volumes accordingly. Our results also showed that this MR-guided dose adaptation technique has a dosimetric advantage over the standard of care and was associated with a reduction in normal tissue doses that translated into a reduction of the odds of long-term RT-induced toxicity.

In the second aim, we used quantitative MRIs to determine its benefit for prediction of oncologic outcomes and characterization of RT-induced normal tissue toxicity. Our findings showed that delta changes of apparent diffusion coefficient parameters derived from diffusion-

weighted images at mid-RT can be used to predict local recurrence and recurrence free-survival. We also showed that K^{trans} and V_e vascular parameters derived from dynamic contrast-enhanced MRIs can characterize the mandibular areas of osteoradionecrosis.

In the final clinical aim, we used CT images of recurrence and baseline CT planning images to develop a methodology and workflow that involves the application of deformable image registration software as a tool to standardize image co-registration in addition to granular combined geometric- and dosimetric-based failure characterization to correctly attribute sites and causes of locoregional failure. We then successfully applied this methodology to identify the patterns of failure following postoperative and definitive IMRT in HNC patients. Using this methodology, we showed that most recurrences occurred in the central high dose regions for patients treated with definitive IMRT compared with mainly non-central high dose recurrences after postoperative IMRT. We also correlated recurrences with pretreatment FDG-PET and identified that most of the central high dose recurrences originated in an area that would be covered by a 10-mm margin on the volume of 50% of the maximum FDG uptake.

In the translational component of this work, we integrated radiomic features derived from pre-RT CT images with whole-genome measurements using TCGA and TCIA data. Our results demonstrated a statistically significant associations between radiomic features characterizing different tumor phenotypes and different genomic features. These findings represent a promising potential towards non-invasively tract genomic changes in the tumor during treatment and use this information to adapt treatment accordingly. In the final project of this dissertation, we developed a high-throughput approach to identify effective systemic agents against aggressive head and neck tumors with poor prognosis like anaplastic thyroid cancer. We successfully identified three candidate drugs and performed extensive *in vitro* and *in vivo* validation using orthotopic and PDX models. Among these drugs, HDAC inhibitor and LBH-589 showed the most effective tumor growth inhibition that can be used in future clinical trials.

Table of Contents

List of Figures

List of Tables

Chapter 1: Introduction

1.1 Background and significance

Head and neck cancers (HNCs) encompass a diverse group of tumors that arise at different locations in the upper aerodigestive track and affect around 65,000 individuals per year in the United States, with approximately 14,000 deaths from the disease.(1) The prognosis of HNCs is considerably variable in different tumor types ranging from excellent prognosis, as in early stage Human papillomavirus (HPV) positive squamous cell carcinoma (2, 3), to very deadly disease as in advanced HPV-negative tumors and anaplastic thyroid carcinoma.(4-7) Radiation treatment (RT) is a cornerstone of HNCs treatment both in the definitive (i.e. organ preserving) and the adjuvant post-operative setting. The goal of RT is to maximize the tumoricidal dose to abnormal cancer cells while minimizing the toxic dose to adjacent normal tissues.(8, 9)

Tumors with good prognosis such as early-stage HPV positive oropharyngeal carcinomas (OPC) in non-smokers are relatively sensitive to RT and have good survival outcomes compared to advanced-stage disease in heavy smoker and HPV negative tumors.(10-16) In this subset of patients local control and survival probabilities exceed 80-85% in most of the reported studies. However, many patients continue to exhibit dose-dependent normal tissue injury. This can leave these comparatively young patients with potentially quality-of-life altering permanent radiation sequelae that can persist for decades of survivorship.(17-20) This is because, fundamentally, RT dose to normal tissue organs-at-risk (OARs) such as the swallowing muscles, mandible, parotid glands, and submandibular glands are the cause of

subsequent long-term RT side effects. Ideally, we would prefer to restrict dose to OARs, while maintaining tumoricidal doses to active tumor volumes. However, it remains to be seen whether RT dose reduction to the entire tumor volume will compromise disease control in a tumor site where prolonged survival is achievable with current standard multimodality treatment despite its long-term toxicity implications.(21-27) Consequently, as oncologic control becomes a realizable goal for most of these patients, reduction of treatment-induced toxicity for the increasing fraction of long-term survivors becomes an unmet priority.(28)

On the contrary, other head and neck cancer types such as HPV negative or advanced stage tumors in heavy smokers remain to have grim outcome rates despite maximal multimodality therapy. The local-regional control (LRC) for these patients can go as low as 30-40%. In addition, these tumors have variable sensitivity to RT leading to different disease response rates.(29, 30) Current RT dose and fractionation are largely driven by empirical data rather than tumor specific information regarding potential radiosensitivity or radioresistance.(4-7, 30) Therefore, the ability to predict RT response in these higher-risk patients before and/or during the treatment course can allow for the timely adaptation of RT doses and potentially achieve better treatment outcomes.

Recent RT delivery techniques like intensity-modulated radiation therapy (IMRT), volumetric modulated arc therapy (VMAT), and intensity-modulated radiation therapy (IMPT) are important innovations in modern RT and represent a paradigm shift in the treatment of HNCs. However, there are certain hazards that may increase the risk of loco-regional failure including inadequate definition of the tumor extension and clinically important target volumes

(TVs), uncertainties related to daily positioning, weight loss or deformation of tumor and normal tissues during the course of treatment, and uncertainties in plan optimization, dose calculation and treatment delivery.(25, 31-34) The accurate and specific definition of the exact site of failure, in addition to the radiation dose given to this site is, therefore, mandatory to identify the possible cause(s) of failure. The classic definition of failures as "local", or "regional", was appropriate in previous eras of conventional RT using large homogeneous dose-volumes, but is no longer helpful nor descriptive of distinct types of failure in patients treated with advanced conformal RT techniques.(35-37) The ability to accurately describe the relation of the origin of disease failure to original TVs or RT dose mandates a fairly precise analysis methodology and represent another important priority in these patients.

Non-invasive imaging such as magnetic resonance imaging (MRI) can provide important information related to tumor characteristics and response to RT. The development of MRI correlates of RT response and normal tissue toxicity could be critical for implementing adaptive RT strategies that maximize therapeutic ratio where patients with aggressive non-responsive tumors may require RT dose escalation (5, 7) while patients with radiosensitive tumors may benefit from dose de-escalation to spare normal tissues with equivalent tumor control.(6) This represents a significant unmet clinical need since patients with radiosensitive tumors are being over-treated and patients with radio-resistant tumors are being under-treated. The leading-edge solution to the anatomic adaptive therapy problem has been to integrate MRI into radiation delivery devices (e.g. MR-Linear accelerator).(38, 39) The richer data of MRI enables computer-driven identification of tumors and normal tissues and allows radiation plans

to be adapted on a daily basis with limited human intervention.(39, 40) Yet, gross anatomic changes represent only one dimension of patient response to RT. Having incorporated high-field MRI into the delivery device, there is now the potential to monitor, on a daily basis, the biologic changes within the patient using functional MRI sequences without excess radiation, contrast exposure, or excess burden on patients' time or institutional resources.

Moreover, the integration of granular quantitative imaging data acquired during the 6-7 weeks course of RT can increase our ability to individualize and optimize the RT dose according to the response of target volumes and therefore, the development of effective treatment adaptation at an actionable time point. Pilot data from our group and other investigators has recently demonstrated that diffusion-weighted imaging (DWI) has a promising predictive utility in HNC applications. Specifically, DWI has been shown to predict response to induction chemotherapy(41, 42) RT(42-50), and tumor recurrence.(51) Preliminary data from a prospective trial at our institution(52), supported by other group's data(42, 44-46, 49, 53, 54), has demonstrated that DWI was able to discriminate patients who will have a complete response at mid-RT. That is, patients with lower pre-treatment diffusion measurement (ADC) values were associated with early radiologic complete response, whereby there was no residual disease by mid-therapy. In addition, lesions that showed a mid-treatment complete response had significantly higher change in diffusion measurements (ΔADC) values than lesions that did not show an early complete response.(52) Additionally, recent data from our group demonstrated that early tumor regression rate ≥25% at fraction 15 (i.e. mid-RT) in HNC patients is associated with better local control and overall survival.(55) This favorable risk group

represent suitable candidates for RT dose de-escalation if dose could be coupled to a quantitative marker of tumor response probability (i.e. ADC). As adaptive dose painting techniques could serially track and identify early responders to therapy, modify their radiation plans by shrinking the target volume coverage, and thus allow increased treatment efficacy with minimal normal tissue toxicity.

Another promising quantitative MR technique is dynamic contrast-enhanced MRI (DCE-MRI). DCE-MRI can be used to monitor changes in tissue vascularity and can play a role in the assessment of both treatment response and normal tissue toxicity. Our group has recently demonstrated the DCE-MRI can be used to measure the changes in mandibular bone vascularity induced by RT. Vascular parameters derived from DC-MRI such as K^{trans} and V_e have been also suggested to be associated with tumor response and normal tissue injury in other cancer sites.

Another avenue for integration of advanced biomedical imaging for tumor response and normal tissue injury assessment is radiomic feature analysis. Radiomics is a method of medical image analysis that extracts a large number of quantitative tissue characteristics from a 2- or 3-dimensional images. Radiomic features describe the texture, shape, and size of an ROI defined on an image, and can be mined to predict RT outcomes. These features may allow to detect characteristics of tissues that cannot be appreciated by the naked eye.(56-58) Early results from radiomic studies also showed that these features can used to discriminate distinct tumor phenotypes (e.g. HPV status, lymphovascular invasion, and extracapsular extension). However, the relationship between tumor imaging phenotypes and underlying tumor genomic

mechanisms remains to be interrogated. Imaging-genomics translational research combines radiographic image analysis with genomic research to improve disease diagnosis and prognosis, discover novel biomarkers, and identify genomic mechanisms associated with phenotype formation.(59-63) Such imaging-genomics studies have been performed for multiple cancer sites(59-65) and remains to be investigated in HNC.

 All the approaches described above including functional MRI, radiomic, and patterns of failure analysis can allow for better stratification of patients to accurate risk group, tailoring of RT dose with potential dose escalation/de-escalation, and prediction of side effects. However, certain tumor types still fail treatment despite maximal RT dose delivery combined with multimodality treatment that may include surgery, chemotherapy, and/or targeted therapy. Anaplastic thyroid carcinoma (ATC) is a clear example of such tumor with a median survival of less than 12 months despite maximal therapy. At the present time, there are not widely accepted and effective systemic drugs against aggressive thyroid cancers. Although combination therapy of targeted agents such as BRAF and MEK inhibition has been recently FDA approved for treatment of ATC, it remains effective mainly in patients with *BRAF* V600E mutations that ultimately develop drug resistance.(66, 67) This creates the necessity to identify effective novel systemic agents against this aggressive disease. Therefore, it is necessary to reorient translational efforts for such tumor types. One approach is to evaluate the broad array of currently available agents with anti-solid tumor activity, which may demonstrate substantial efficacy in ATC with already established safety profiles.

Most previous drug identification and preclinical testing efforts in the context of ATC have been restricted by several deficiencies including: 1) limited availability of validated human cell lines with a known genomic and epigenetic background, 2) limited utilization of orthotopic models, and 3) limited availability of relevant patient derived xenograft (PDX) models.(68) All three of these factors can severely impact the ability to identify promising systemic agents, both due to false positive and false negative results. The increasing availability of well-characterized ATC human cell lines as well as increasing stocks of PDX models will allow for better identification of more effective drugs against such deadly tumors. A high-throughput drug screening (HTS) as an initial filter can represent a proper initial step for subsequent preclinical testing and drug validation in these tumors.(69) This is an attractive approach since our group has already generated and authenticated a large panel of thyroid cancer cell lines as well as PDX models for further validation.(70-72)

1.2 Hypothesis and specific aims

The current dissertation has two main research components: clinical and translational. The central hypothesis of the clinical component is that the currently available clinical imaging tools can be integrated with radiotherapy platforms for prediction of tumor response and outcomes, monitoring and adaptation of radiation dose, as well as characterization of patterns of failure and normal tissue toxicity in head and neck cancer patients with potentially curable tumors. The central hypothesis of the translational component is that a high-throughput drug screening with subsequent preclinical testing and drug validation in authenticated *in vitro* and *in vivo* tumor models will identify effective agents against aggressive head and neck tumors with poor prognosis.

To test these hypotheses, we propose the following specific aims:

Specific Aim 1: Determine the feasibility and dosimetric benefits of MR-guided dose-adaption strategy for HPV positive oropharyngeal cancer patients using serial in-treatment MRIs acquired in radiation treatment positioning and immobilization setup.

The working hypothesis is that T2 weighted MRI can be used for MR-guided RT dose adaptation to achieve same tumor control as standard therapy but with additional sparing of surrounding normal tissue. To achieve this aim two projects were done.

Project 1.1: Standardization of MRI integration in radiotherapy application for head and neck cancer.

Project 1.2: MR-guided dose adaptation.

Specific Aim 2: Determine quantitative MRI parameters associated with tumor response, oncologic outcomes, and normal tissue toxicity in head and neck cancer patients treated with definitive radiation therapy.

The working hypothesis is that quantitative MRI parameters can be used for prediction of tumor response to radiation therapy as well as for the prediction of long-term oncologic outcomes. The quantitative MRI parameters can be also used for the characterization of radiation-induced normal tissue toxicity.

To achieve this aim two projects were done.

Project 2.1: Diffusion-weighted MRI as a biomarker for tumor response and disease control.

Project 2.2: Dynamic Contrast-Enhanced MRI for assessment of normal tissue toxicity.

Specific Aim 3: Develop and apply a methodology to standardize the analysis and reporting of the patterns of failure after radiation for head and neck cancer patients.

The working hypothesis is that using novel deformable image registration analyses of combined spatial and dosimetric patterns of failure parameters will allow for the accurate identification of the radiation-technique related causes that led to radiation treatment failure and the possible interventions to reduce these failures in radiation therapy practice. Using a standardized typology for reporting patterns of failure can be adopted by multiple institutions in a manner that allows improved detection of possible modes of preventable causes of disease recurrence. This could allow for pooling of data to infer differences in treatment approaches and subsequent outcomes amongst different institutions.

To achieve this aim three projects were done.

Project 3.1: Methodology for analysis and reporting patterns of failure after radiation therapy.

Project 3.2: Patterns of locoregional failure following post-operative intensity-modulated radiotherapy.

Project 3.3: Patterns-of-failure guided biological target volume definition: FDG-PET and dosimetric analysis of dose escalation candidate subregions.

Specific Aim 4: Determine the associations between imaging phenotypes and genomic mechanisms in head and neck tumors and identify effective systemic agents against aggressive tumors with a reasonable toxicity profile to allow for rapid translational development.

The working hypothesis is that imaging-genomics translational research can improve disease diagnosis and prognosis, discover novel biomarkers, and identify genomic mechanisms associated with phenotype formation. In addition, the utilization of high-throughput drug screening with subsequent preclinical testing and drug validation in authenticated *in vitro* and *in vivo* tumor models will identify effective agents against aggressive head and neck tumors with poor prognosis.

To achieve this aim two projects were done.

Project 4.1: Associations between imaging phenotypes and genomic mechanisms.

Project 4.2: A high-throughput approach to identify effective systemic agents for the treatment of anaplastic thyroid cancer.

Chapters 2: Standardization of MRI integration in radiotherapy application for head and neck cancer.

This chapter is based upon:

Joint Head and Neck Radiotherapy-MRI Development Cooperative. **Mohamed AS**, Hansen C, Weygand J, Ding Y, Frank SJ, Hwang K, Hazle J, Fuller CD, Wang J. Prospective analysis of in vivo landmark point-based MRI geometric distortion in head and neck cancer patients scanned in immobilized radiation treatment position: Results of a prospective quality assurance protocol. Clin Transl Radiat Oncol. 2017 Oct 10;7:13-19. doi: 10.1016/j.ctro.2017.09.003. PMID: 29594224; PMCID: PMC5862642.

2.1 Introduction

There has been a steady increase in the utilization of magnetic resonance imaging (MRI) in radiation therapy (RT) for treatment planning because of its superior soft tissue contrast, including tumor conspicuity. Recent advancements in integrated MRI guided radiation therapy systems further enable the tracking of patient's gross tumor volume (GTV) and other critical organs in real-time during treatment (73-75). This significant technical improvement promises increasing accuracy and fidelity of the actual dose delivered. However, MRI can have larger geometric distortions than x-ray computed tomography (CT), resulting from the scanner's magnetic field imperfections (B_0 inhomogeneity and gradient non-linearity) (76-80), and patient-related effects such as susceptibility variations between different tissues (81, 82). To be used

as a primary RT planning modality, MRI's geometric distortion must be compensated by increasing margins after target delineation, resulting in limited capacity for dose reduction to the surrounding normal tissues.

At present, CT remains the imaging modality of choice for treatment planning and the gold standard for GTV delineation and adaptive RT applications. Compared with MRI, CT has minimal geometric distortion and its intrinsic information on electron density for dose calculation of various tissues, making it a natural imaging choice for treatment planning (83). In head and neck cancer (HNC), CT provides better visualization of cortical bone invasion and tumor-fat boundaries than MRIs. However, poor soft tissue contrast, which is extremely critical in determining tumor edges, organs at risk, and bone marrow, remains a major limitation for CT utilization as a single image modality in RT applications(79). Additionally, CT is susceptible to metal artifacts caused by dental fillings and other prosthesis. These limitations require the additional use of other imaging modalities, like MRI or positron emission tomography (PET), which complement each other to allow for precise target definition and organ at risk sparing.

As a part of an on-going research effort aiming to develop MR-guided RT platforms, we have been acquiring MR images of HNC patients in their customized radiation immobilization devices, to match their radiation therapy treatment position, as well as their CT treatment scanning position(84). In this study, we aim to quantify the geometric distortion in patient images by comparing their in-treatment position MRIs with the corresponding planning CTs, using CT as the non-distorted gold standard.

Our specific aims are to 1) determine the intra- and inter-observer variation that exists when measuring specific distances between landmarks on both CT and MR images after rigid co-registration, and 2) verify that MRI geometric distortion is within practical limits to support increased clinical utility of MRI guided radiotherapy, particularly for future MRI-only treatment planning and the combined MR-CT systems.

2.2 Materials and Methods

2.2.1 Patient selection

As part of a programmatic effort to develop quality assurance and performance tolerance for MRI-guided radiotherapy, twenty-one HNC patients were selected in this prospective study, after obtaining institutional review board approval and written informed consents from all participants. Criteria of patient's inclusion were; age≥ 18 years, histologically documented stage III or IV human papillomavirus positive (HPV+) squamous cell carcinoma of the oropharynx, definitive chemoradiotherapy, Eastern Cooperative Oncology Group (ECOG) performance status of 0 to 2, and no contraindications to MRI. All patients had their treatment planning CT done within one week of the MRI to avoid any significant anatomical changes between both images (e.g. tumor progression or weight loss). Both images were collected prior to the initiation of treatment.

2.2.2 Imaging acquisition

2.2.2.1 MRI

MR images were acquired with a 3.0-T Discovery 750 MRI scanner (GE Healthcare, Waukesha, WI, USA) with laterally placed 6-channel phased array flex coils (GE Healthcare)

centered on tumor covering from palatine process down to the lower edge of cricoid cartilage. T2-weighted fast spin echo (FSE) sequence were acquired in the same immobilization position as in the treatment planning CT scans as described in details in a previous report(84). By doing so, we minimized patient positioning differences in the acquisition of CT and MR images resulting in a minimized registration error between the two sets of images. Specific imaging acquisition parameters of the T2-weighted FSE sequence are as follows: FOV=256 mm, Slice thickness=2.5 mm and Matrix=512 x 512, giving pixel size of 0.5x0.5x2.5mm; Repetition Time (TR) =3.7s; Echo Time (TE) = 97ms; Echo Train Length (ETL) =16. The distance from the skin surface to the center of FOV was less than 10 cm for all patients included in this study.

2.2.2.2 CT

CT was acquired using the standard institutional protocol for simulation non-contrast enhanced CT; slice thickness= 2.5 mm, tube current=350 mA at 120 kVp, display field of view=500 mm, matrix of 512 x 512 pixels, pixel size of 0.98 x 0.98 mm, isocenter at arytenoid cartilage, and coverage from vertex to carina.

2.2.3 Image selection and evaluation of geometric distortion

CT and T2-weighted MRI were transferred to commercial image registration and segmentation software VelocityAI (Velocity Medical Solutions, Atlanta, GA). The navigator module was selected, and the T2 MRI was rigidly registered to the CT. The module consists of selection of primary (CT) and secondary (T2 MRI) images, manual alignment, selection of region of interest, and rigid registration. Deformable registration was not used in order to assess the inherent distortion in MRI.

14

Utilizing the measurement tool within the VelocityAI software, several skin to skin (STS, total of 9 landmarks), bone to bone (BTB, 9 landmarks), and soft tissue to soft tissue (TTT, 3 landmarks) measurements were done at specific levels in horizontal and vertical direction of both CT and MRI images. Landmarks were anatomical features that can be reliably identified and reproduced by observers on both CT and MRI. Table 2.1 illustrates the details of the anatomical boundaries of the selected landmarks. The difference between measurements of corresponding anatomical landmark on both MR and CT images was considered to be overall geometric distortion. Figure 2.1 summarizes the workflow process utilized to obtain these measurements.

Planning CT

Rigid Co-Registration

Planning MRI

Bone-to-Bone measurement

- Planning CT and MR images import to Velocity AI
- Rigid co-registration of MRI to CT
- Measure the distance between 21 different landmarks
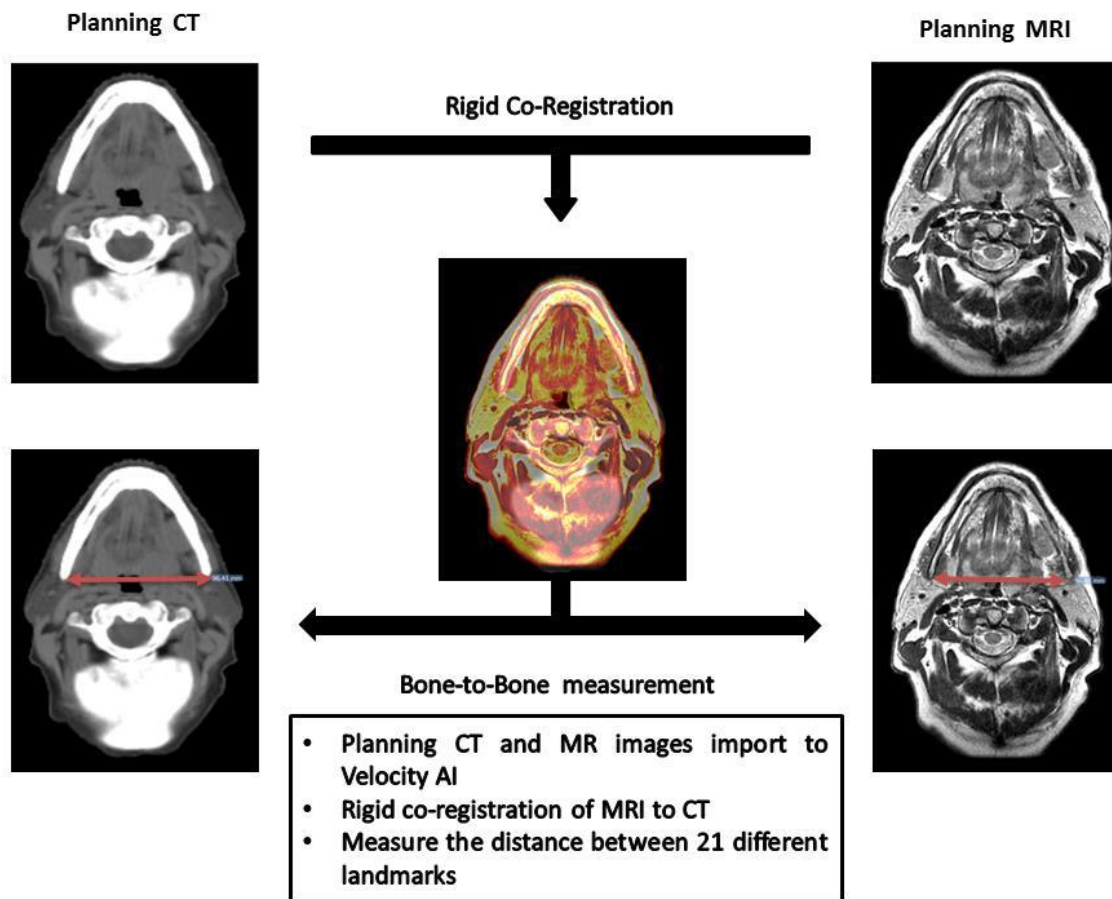
Figure 2. 1: Study workflow

This figure depicts the workflow of anatomical landmark measurements and comparison.

The landmarks were mainly selected in three levels (i.e. upper, middle, and lower). Criteria for selecting each of the three specific imaging levels were as follows: the top slice was the cranial-most co-registered image depicting clear maxillary sinuses and homogenous intensity. Clear lower edge of the mandible, anterior vertebral body, and complete vertebral encasing of the vertebral canal distinguished the middle slice. Similarly, the caudal-most image

was selected based on clear superior border of the body of hyoid bone, anterior vertebral body, and complete vertebral encasing of the vertebral canal. Nearly 43% of the anatomical landmarks are peripheral (skin to skin) while the rest are more central landmarks such as two points on a bony structure or muscle structures as illustrated in Table 2.1. For each patient, ten (48%) of the measurements were distances in the horizontal direction while the rest were in the anteroposterior direction. Also, the landmarks were chosen to be distributed in the upper, middle and lower sections of the head and neck (Figure 2.2). Geometric error was subsequently compared for all different axes, levels, and nature.

Table 2. 1: List of the selected landmarks

Skin to skin landmarks

1- Horizontal line at the level of pterygomaxillary fissure

2- Horizontal line at level of tip of lateral pterygoid plate

3- Horizontal line at level of the pterygoid notch

4- Oblique line passing through the left zygomatic process and pharyngeal tubercle at midline

5- Vertical line passing through the left zygomatic process and the lateral edge of left cerebellar tonsil.

6- Vertical midline at the level of superior border of body of hyoid bone

7- Horizontal line at the level of anterior vertebral body of the inferior border of C2

8- Horizontal line at the level of anterior vertebral body of the inferior border of C4

9- Vertical midline at the level of inferior border of C4

Bone to bone landmarks

1- Horizontal line between the medial edge of bilateral mandibular condyles

2- Horizontal line between the tip of bilateral mastoid processes

3- Vertical line between the mentum and the midpoint of the anterior surface of the vertebral body

4- Vertical midline of the spinal canal of C2

5- Horizontal line of the spinal canal of C2

6- Horizontal line between the angles of the mandible

7- Vertical midline of the spinal canal of C4

8- Horizontal line of the spinal canal of C4

9- Vertical line between the midpoint of the posterior border of the superior surface of body of hyoid bone to the midpoint of anterior vertebral body

Soft tissue to soft tissue landmarks

1- Right lateral pterygoid muscle vertical length

2- Vertical midline cerebellar length

3- Left sternocleidomastoid muscle vertical width
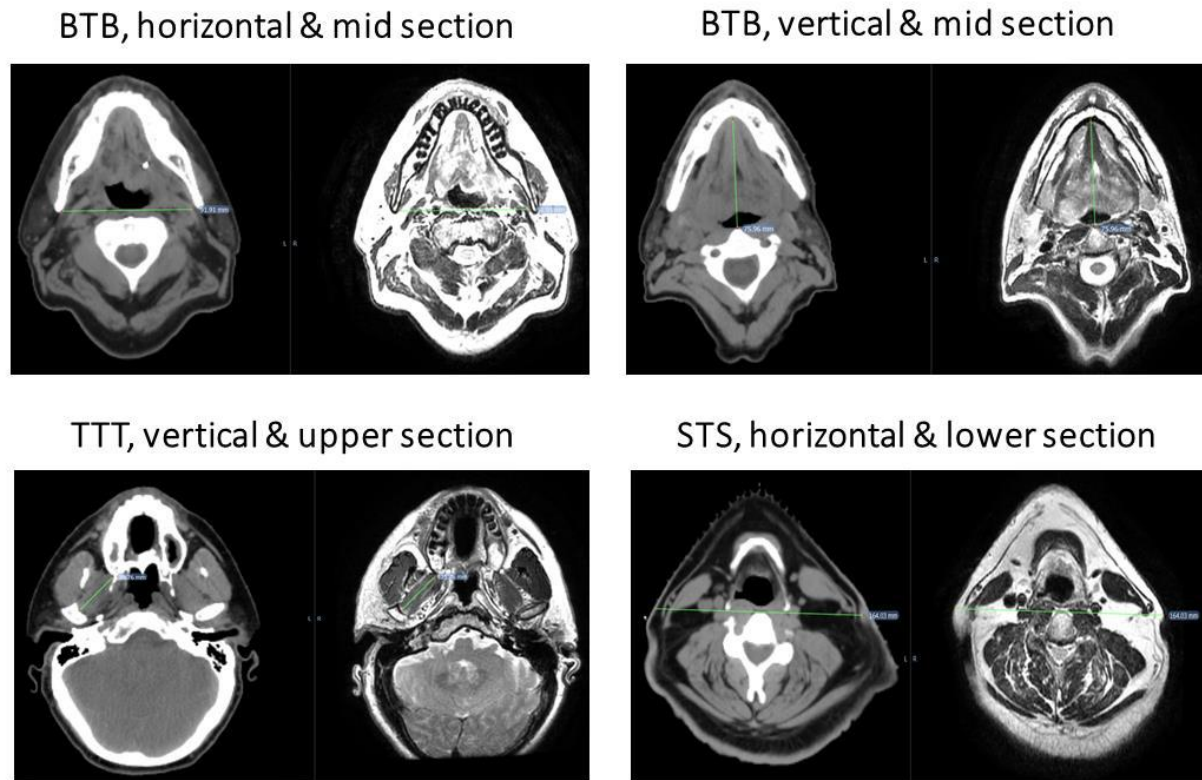
Figure 2. 2: Examples of anatomical landmarks included in the study.

This figure shows the landmarks that were strategically selected to encompass a broad

coverage of the anatomical areas and varieties of anatomical structures (bone, soft tissue) and

direction (vertical vs. horizontal).

2.2.4 Inter- and intra-observer variation

For assessment of intra-observer variation, a single observer repeated a total of 100

landmark measurements (i.e. 10 landmark measurements per patient for 10 patients) to

determine the intra-observer variation. For assessment of inter-observer variation in landmark measurement, four observers collectively repeated the assigned 100 measurements independently to assess the inter-observer variation.

2.2.5 Statistical analysis

Numeric variables are expressed in mean and SD. Comparison of mean errors by different stratification was done using non parametric statistics, $p < 0.05$ was considered statistically significant. Intraclass correlation (ICC) was calculated for intra- and inter-observer variation. All analyses were done with JMP v 11Pro (SAS institute, Cary, NC), and Microsoft Excel (Redman, Washington).

2.3 Results

2.3.1 Geometric distortion

Eleven landmark points were not attainable due to variation in the range of MR coverage in four patients' scans, leaving a total of 430 landmark measurements for final analysis. The mean distortion for all landmark measurements in all scans was 1.6±1.7 mm. There was no statistically significant difference of distortion magnitude for measurements at the horizontal vs. vertical direction (1.5±1.6 vs. 1.6±1.7 mm, respectively, p=0.4) as shown in figure 2.3. Likewise, there were no significant differences in error measurements in the upper, middle, and lower section of the head and neck (1.5±1.6 vs 1.4±1.2 vs 1.7±1.9 mm, respectively, p=0.3) as shown in figure 2.4. However, we observed a statistically significant difference in peripheral (STS) vs. more central landmarks (2.0±1.9 vs. 1.2±1.3 mm, respectively, p<0.0001) as shown in figure 2.5.

21
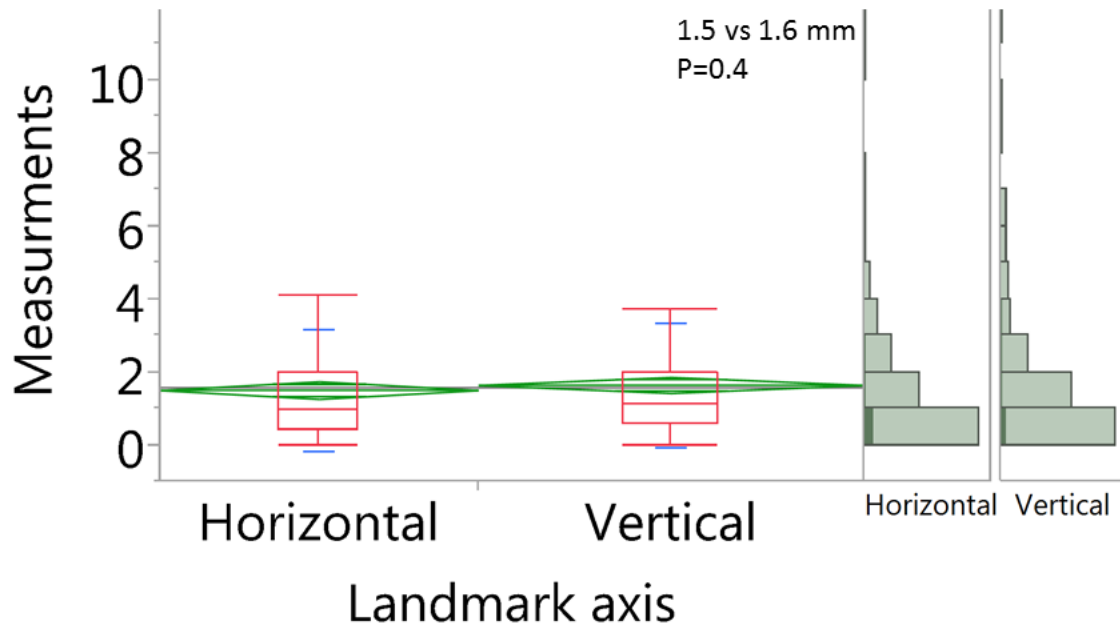
Figure 2. 3: Box plots for the landmark measurements in horizontal vs. vertical axis.

By landmark level

1.7 vs 1.4 vs 1.5 mm
P=0.3
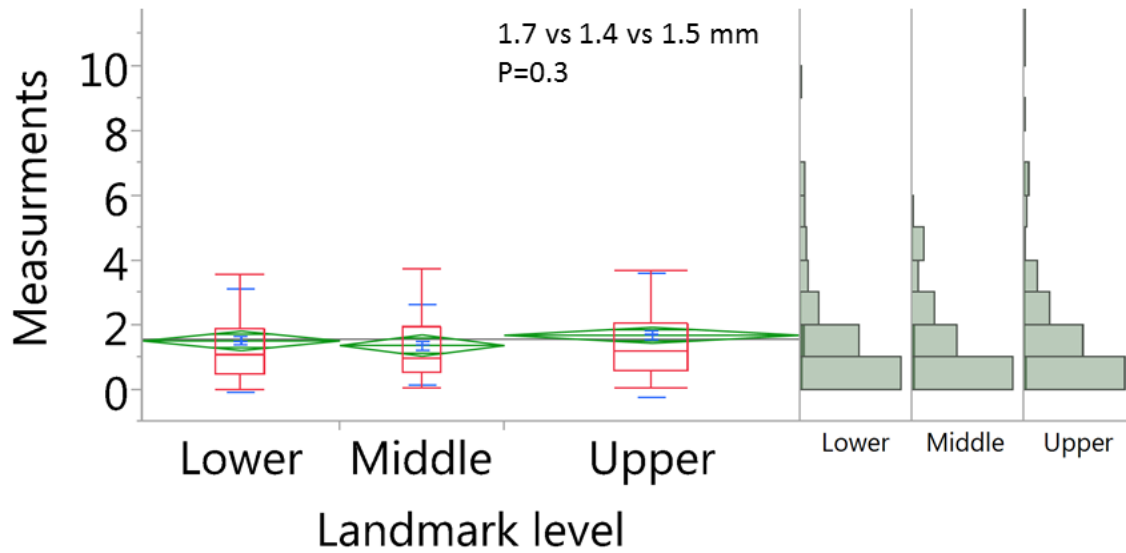
Figure 2. 4: Box plots for the landmark measurements in the upper, middle, and lower section of the head and neck.

Full vs. partial thickness (i.e. central vs. peripheral)
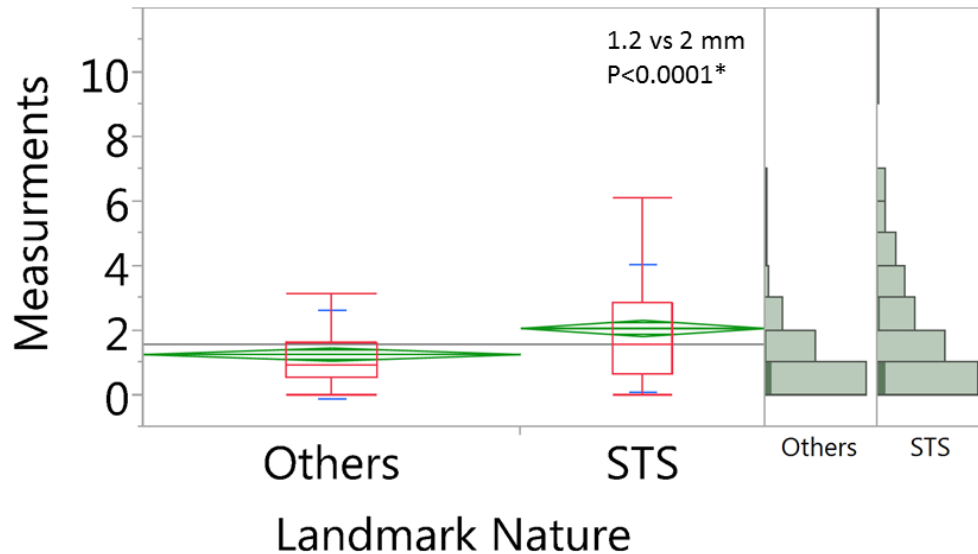
Figure 2. 5: Box plots for the landmark measurements in the peripheral vs. central landmarks.

2.3.2 Inter- and intra-observer variations

The average error measurements between the MRI and respective CT for the selected 100 landmarks were 1.05±0.87, 1.23±0.82, 1.06±0.99 and 1.05±0.79 mm for observer 1, 2, 3, and 4, respectively as shown in figure 2.6. The ICC for inter-observer variation was 0.84 (95% CI, 0.78-0.88). Likewise, the average error for repeated measurements of observer 1 were 0.97 mm for the initial measurement and 0.99 mm for the repeats (p=0.9) and the ICC for intra-observer variation was 0.76 (95% CI, 0.64-0.84).
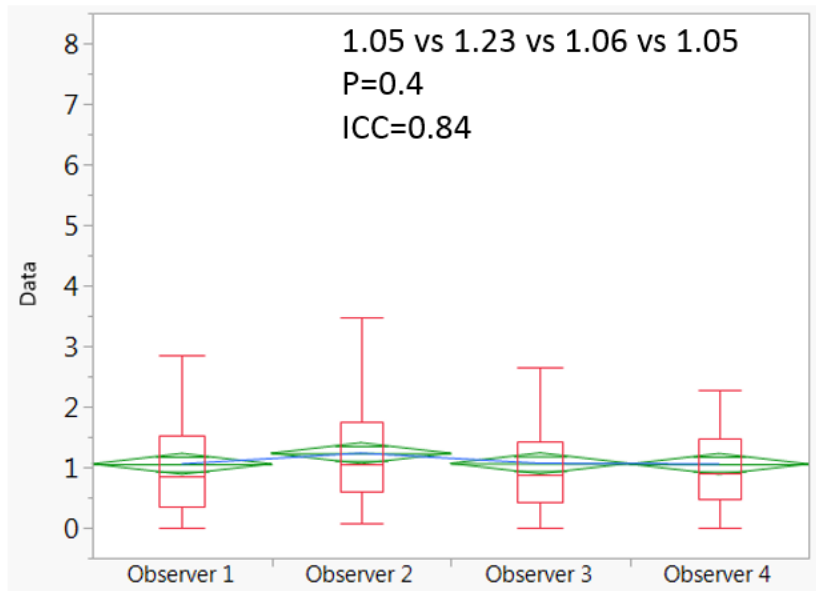
Figure 2. 6 Box plots of the inter-observer variability for the landmark measurements between observers.

2.4 Discussion

Our results showed that the overall average discrepancies of geometric fidelity of MRI were within 2 mm from that of the CT. We also demonstrated that there were no significant differences in the degree of geometric distortion in different axes and levels of the studied MR images. However, distortions were significantly higher peripherally for skin to skin landmarks than for more central bone to bone of soft tissue to soft tissue landmarks. These results were consistent among different observer and with repeated measurements for the same single observer with excellent ICC for both inter- and intra-observer observations.

25

One of the main goals of radiotherapy is to accurately define the tumor target with high certainty. MRI has superior soft tissue contrast enabling better delineation of tumor from those of surrounding healthy tissues, where the relatively poor contrast of CT resulted in uncertainties in target delineation. Therefore, in spite of the fact that MRI has a certain degree of distortion, MRI may still provide higher confidence in target delineation and consistency compared with CT. Our data support that additional margins around target volumes to account for geometric uncertainty may not be needed for radiotherapy planning using anatomical MR sequences particularly if tumors are close to the image isocenter. This is partly because the relatively small error introduced by geometric distortion compared with higher inter-observer delineation error observed in radiotherapy planning using CT, as widely published in the literature (34, 85, 86). We are also running a separate investigation of the inter-observer delineation error using anatomical MR sequences acquired using the radiotherapy immobilization platform used in the current study. However, for functional MR sequences (e.g. diffusion weighted imaging) the magnitude of distortion is much higher and requires dedicated study to investigate its optimal use in radiotherapy planning context.(87, 88)

Geometric distortion due to MRI scanner system imperfection is also spatially dependent. The magnitude of distortion is typically small at isocenter (the center of the magnet and gradient system) and larger in areas away from isocenter (i.e. near the skin) due to the falloff in gradient linearity at the periphery. Therefore, the actual geometric distortion in practice can be smaller than the average distortion reported in this study, depending on the tumor and other structure location. For head and neck cancer patients, the region of MR imaging volume

26

is relatively small and can be completely contained by the "sweet zone" (i.e. area of relatively linear gradients and homogeneous B0 field). For other anatomical areas such as the GI and GU, and when the tumor is off to the peripheral of the body, the geometric distortion may be larger than that of the central location. Thus, the geometric distortion for those specific anatomical areas may still need to be assessed for radiation therapy applications. Additionally, each MRI scanner system's geometric distortion is different and, thus, must be assessed individually.

Susceptibility-induced geometric inaccuracies occur at boundaries between tissues with large differences in susceptibility (e.g. bone-tissue, air cavity-tissues). Those geometric inaccuracies are difficult to assess but usually occur in the frequency encoding direction and can be somewhat minimized by increasing the bandwidth in the MRI acquisition. From the results of our measurements, the overall discrepancies (which include the susceptibility induced inaccuracies, system-specific inaccuracies, and the registration error between CT and MR) are within 2 mm, which is an encouraging finding.

Additionally, MRI is more complicated than CT in which many acquisition parameters may affect the geometric distortion. Therefore, for each clinical practice, the commonly used MRI acquisition sequences and parameters need to be optimized based on the recommendations of physicists or vendors. The actual distortion must be assessed by phantoms, and quality control program needs to be in place to ensure such consistency and quality.

At the present, there is no specific, commonly agreed upon guidelines for the quality control and quality assessment for MRI geometric distortion. Professional organization such as the AAPM has established several task groups (e.g. AAPM TG117) looking into these very issues. There is lack of commonly agreeable phantom to use in the assessment of geometric fidelity. For radiotherapy applications, minimizing geometric distortion is a fundamental element before clinical implementation. Several prior attempts were implemented to optimize the MR sequences, including using 3D spin echo sequences with vendor-supplied distortion correction and widening the bandwidth to reduce susceptibility related distortion(89, 90). Placement of the region of interest at or near the isocenter of the magnet, where gradient field nonlinearities are minimum is another solution. Additionally, increasing the sampling bandwidth at the cost of SNR, because the bandwidth is inversely proportional to susceptibility-induced errors is another alternative for radiotherapy applications where very high SNR may not be as critical as in diagnostic applications.

Our study is limited by the relatively small number of patients in the study. However, this is our attempt to measure the actual discrepancies in geometric fidelity as compared with CT, which is considered to have little or no distortion. This study is still valid because the large number of landmark measurements included. Furthermore, the MRI sequence (T2w) we used in this study was a multiple 2D acquisition with a slice thickness of 2.5 mm (superior-inferior direction) which, thereby, has lower resolution compared with the in-plane (anterior-posterior and right-left) that was 0.5 mm. Therefore, reliable and reproducible landmarks in the superior-inferior direction were not attainable. While for slice locations away from the isocenter, the axial

planes tend to "warp", introducing out-of-plane distortion. This introduces additional uncertainties in geometric fidelity in MRI. Therefore, it is critical to apply 3D geometric distortion correction in the acquisition to minimize the out-of-plane distortion. Also, our study did not explore the possibilities of further optimizing the pulse sequences in the image acquisition such that distortion due to MRI can be further minimized, and the scanner used in our study is a regular MRI scanner used for diagnostic purpose, rather than optimized for radiation therapy treatment planning purposes. It is expected that with MRI scanners that are designed for such purpose, the geometric distortion and optimization of MRI sequences, the distortion due to MRI can be reduced further.

Our future works include the assessment of geometric discrepancies between CT simulation scans and that of MRI in other anatomical areas such as GI and GU. These other studies present other challenges including patient and internal organ motion and the needs of developing patient immobilization devices and procedures for MRI scans. Despite the challenges, these kinds of validation studies are important and much needed for using MRI in radiotherapy applications. This current study has given us the confidence that the geometric distortion in MRI is manageable and is within a reasonable range. With proper immobilization devices, optimization of MRI sequences, and QA/QC procedure in the future, implementing MRI for radiation therapy treatment planning in most if not all anatomical areas are possible.

Chapter 3: MRI-guided dose adaptation

This chapter is based upon:

3.1 Introduction

Human-papilloma virus positive (HPV+) oropharyngeal cancer (OPC) is epidemic in the United States, with an estimated 20,000 new cases annually, and rising incidence projected in the coming decades.(91) HPV+ cancers are sensitive to radiotherapy but despite excellent survival outcomes and the introduction of intensity modulated radiotherapy, current regimens continue to be associated with toxicity to adjacent normal tissue.(10-16) This leaves comparatively young survivors with potentially quality-of-life altering, permanent radiation sequelae that can persist for decades of survivorship, and limit future compensatory functionality in the face of new challenges.(17-20) To address this issue, it is necessary to find

the optimal therapeutic window of HPV+ OPC, where dose to organs at risk (OARs) can be reduced while tumoricidal doses to active tumor volumes can be achieved. However, safely achieving this target by anatomically adapting the dose to follow serially shrinking tumor volumes during the 6-7-week radiation therapy course is currently impossible using CT without repeated use of exogenous contrast. In addition, existing functional imaging biomarkers, such as radiolabeled positron emission tomography (PET) tracers cannot be safely repeated iteratively during treatment. Therefore, the ability to image tumors during therapy to adapt radiation fields for responding tumors, reducing OAR dose and subsequent toxicity, is currently an unmet need.

Adaptive radiotherapy strategies have been previously implemented at our facility.(92, 93) Schwartz et al. performed adaptive replanning mid-therapy for head and neck cancer patients, using daily computed tomography (CT)-on-rails image-guidance. The lack of contrast delivery for the CT-on-rails impeded the accurate visualization of tumor changes during treatment, and thus did not allow for reduction of clinical target volumes as tumor shrank, but instead accounted for weight-loss and normal tissue deformation.(92, 93) Magnetic resonance imaging (MRI) provides superior tumor/soft tissue contrast(94). In a recent study by our group(52), 31 patients with locally advanced HPV+ OPC were examined for mid-treatment response as assessed by MRI. The study showed that approximately 50% of patients had complete resolution of clinical and radiographically primary disease at mid-therapy. Using serial MRI-guided dose adaptation in this cohort of patients would allow selective, patient-specific precise dose-reduction, such that patients with brisk radiation response would have

commensurate dose reduction, while comparatively radiation resistant tumor subvolumes would be ensured a tumoricidal dose. Using serial in-treatment MRI without exogenous/IV contrast, we can potentially track tumor shrinkage during treatment, conceivably de-escalating OARs doses to reduce side effects without sacrificing locoregional control and survival.

In this dosimetric study, we propose a novel MRI-guided IMRT dose-adaption strategy for HPV+ OPC, whereby dose to gross disease is reduced on an "as needed" basis, such that responders could achieve substantive dose reduction to adjacent normal tissue at levels not observed with standard radiotherapy, while non-responsive disease would not be *a priori* de-escalated. This represents a truly "personalized" therapy, as, rather than assigning dose *a priori*, the cumulative dose received by each patient would be predicated on imaging response. To this end, we aim to determine the feasibility and dosimetric benefits of this MRI-based dose-adaption strategy for HPV+ OPC patients using serial in-treatment MRIs acquired in radiation treatment positioning and immobilization setup.

3.2 Materials and Methods

3.2.1 Patients

Patients in the current study were prospectively enrolled under an Institutional Review Board (IRB)-approved imaging protocol (PA14-0582) after signing a study-specific informed consent form. Patients were scanned between July 2015 and June 2016. Inclusion criteria were age older than 18 years; histologically proven P16+ oropharyngeal squamous cell carcinoma; eligibility for definitive IMRT; intact primary tumor; Stage III, IVa, or IVb disease as defined by

American Joint Committee on Cancer (AJCC) 7th edition cancer staging criteria; ECOG performance status of 0-2; no administration of induction chemotherapy before radiotherapy; and no contraindications to MR imaging.

3.2.2 MRI Protocol

Serial MRI simulation images were acquired at baseline (within one week prior to first radiation fraction), and every two weeks during the IMRT course (i.e. at weeks 2, 4, and 6). Patients were dispositioned to receive a custom-fitted oral stent and an immobilization mask same to that used for radiotherapy treatment planning prior to receiving their study MRIs. The stent was made by the dental oncology team to hold the tongue and the remainder of the oral cavity in place. The thermoplastic mesh mask, for the head and neck region, was made during the simulation phase to immobilize the head, neck, and shoulders of the patient in a reproducible way. We previously detailed the positioning and immobilization setup for our MRI-simulation process in a separate publication.[84]

Patients' images were acquired using a 3.0T MR scanner (Ingenia, Philips Healthcare, Best, The Netherlands) with two SENSE Flex-M coils laterally and SENSE spine coil posteriorly. MRI sequences included axial T2 weighted image (repetition time/echo time = 8755/100 ms, echo train length = 15, field of view = 25.6 cm, spatial resolution = 0.5x0.5x2.5 mm^3, number of signal averages = 2, pixel bandwidth = 184 Hz, number of slices = 90). Geometrical scan parameters were prescribed for a standardized spatial region encompassing the vertex cranially to the cricoid cartilage caudally for all scans.

3.2.3 CT Simulation

Standard simulation CTs were acquired for each patient at baseline prior to treatment, followed by serial simulation CT imaging for adaptive replanning at the same time points of MR-simulation (i.e. at weeks 2, 4, and 6) using identical positioning and immobilization setup (see schema of protocol, Figure 3.1).
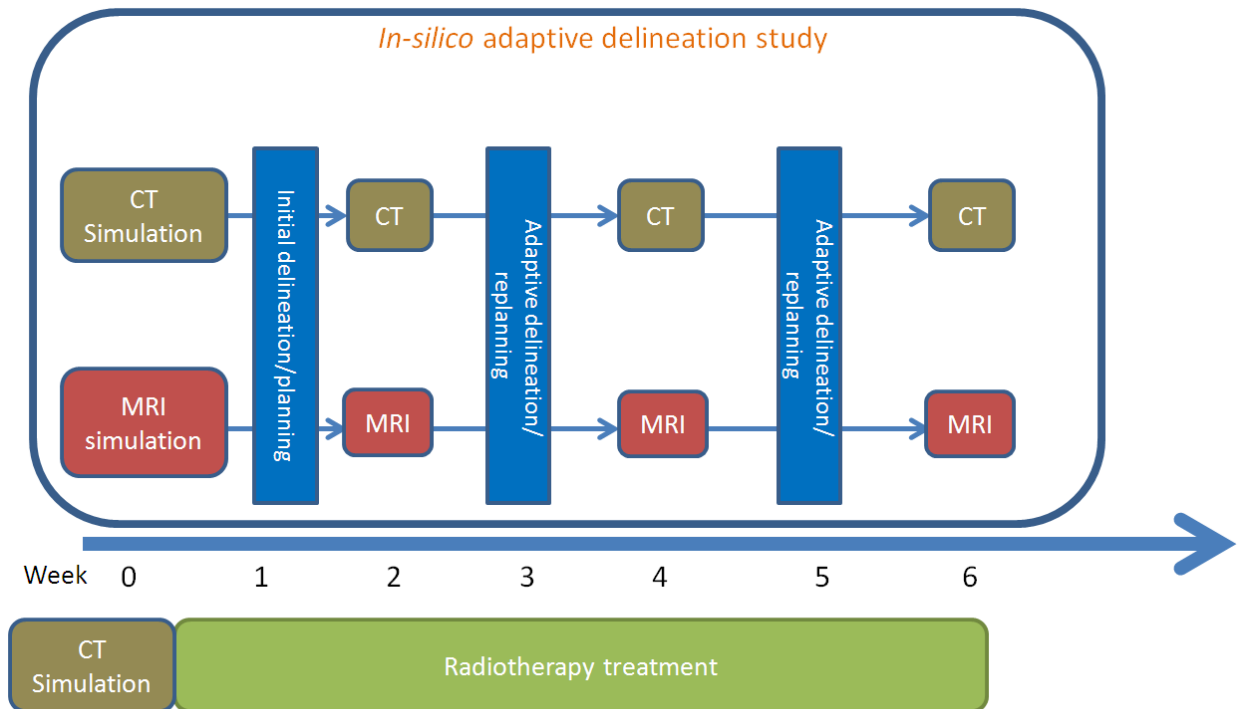
Figure 3. 1: Schema of *in silico* adaptive planning protocol.

3.2.4 Target Volumes and dose specification

Target volumes were delineated, and peer reviewed by MD Anderson's Radiation Oncology Head-and-Neck Planning and Development Clinic. The process of peer-review of segmented contours was explained in details in a prior report by our group.(95) In brief, the process entails comprehensive review of a patient's history, pathology, diagnostic imaging, and discussion of the planned treatment. All patients undergo physical examination (PE) including video-camera nasopharyngolaryngoscopy and bimanual palpation performed by a team of head-and-neck radiation oncology sub-specialists. The proposed segmentations were reviewed slice-by-slice for gross tumor volume (GTV), clinical target volume (CTV) and OAR segmentation, as well as dose-volume specifications. By this manner, intra- and inter-observer variability in segmentation are minimized because of the utilization of multi-observer's agreement contours rather than single-observer contours.

The initial gross tumor volume (e.g. $GTV\_p_{initial}$ for primary disease and $GTV\_n_{initial}$ for nodal disease) was manually segmented using T2-weighted MR images at baseline then propagated to the co-registered simulation CT acquired at the same day. The initial clinical target volume ($CTV_{initial}$) was defined as the $GTV_{initial}$ plus 5mm expansion, trimmed from uninvolved bone, muscle, skin or mucosal surfaces; to incorporate high-risk subclinical disease.

For each patient, two IMRT plans were created: a standard and an adaptive treatment plan. The prescription dose for the standard plans was 2.12 Gy/fx for 33 fractions to the $PTV_{initial}$ ($CTV_{initial}$ +3mm). For adaptive plans, a new $GTV_{adaptive}$ was segmented on serial MRIs using T2-weighted MR images at time points showing a detectable shrinkage of

35

the $GTV_{initial}$. Subsequently, a new $CTV_{adaptive}$ was generated to cover the $GTV_{adaptive}$ propagated from MRI to the corresponding same day CT with additional 5mm margin. Detectable shrinkage was defined as any $GTV_{initial}$ reduction of more than 2mm in the reference plane (largest cross-sectional distance axially on the pretherapy imaging).

The prescription dose to $PTV_{adaptive}$ ($CTV_{adaptive}$+3mm) was 2.12 Gy/fx to allow delivery of maximum dose to the residual disease, resulting in a cumulative dose, should disease persist through therapy, of up to 70 Gy. Prescription dose for any previously involved volumes was 1.52 Gy/fx to ensure a minimum "floor" dose of 50.16 Gy to any region ever deemed to have been directly involved with tumor. All uninvolved upper-neck elective nodal volumes outside the $CTV_{initial}$/$CTV_{adaptive}$ were encompassed in the $CTV_{elective}$, and prescribed 1.52 Gy/fx for a total prescription of 50.16 Gy/33 fractions. Figure 3.2 illustrates the workflow for adaptive vs. standard plans.
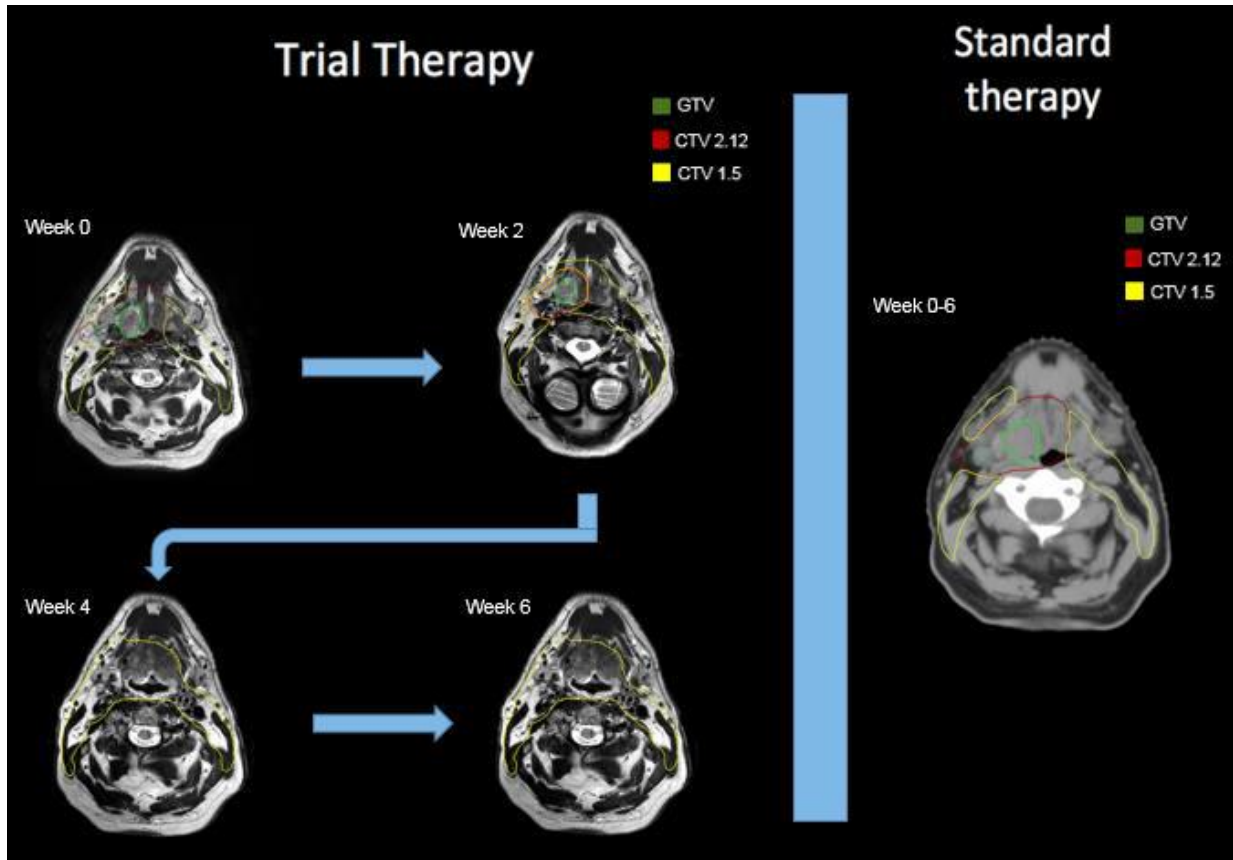
Figure 3. 2: Adaptive dose reduction workflow.

Adaptive dose reduction workflow shown on the left; as GTV (green) shrinks, so does the high

dose (CTV 2.12 Gy/day region) which become included in the low dose target (CTV 1.52

Gy/day region). Standard radiotherapy doses are shown on the right.

3.2.5 OAR Segmentation

Organs at risk (OARs) were auto-segmented on simulation CTs at baseline and at

weeks 2, 4, and 6 using a previously validated atlas-based auto-segmentation software

program ADMIRE v1.13 (Elekta AB, Stockholm, Sweden). This was followed by review and

correction of the contours when needed by an experienced radiation oncologist (ASRM). The following OARs were included: spinal cord; brain stem; bilateral parotid and submandibular glands; thyroid gland; larynx; oral cavity; brachial plexus; superior, middle, and inferior pharyngeal constrictors; medial and lateral pterygoid muscles; masseter; sternocleidomastoid; intrinsic and extrinsic tongue muscles; hard palate; and soft palate.

3.2.6 Radiation planning

All plans were optimized to full dose (70Gy or 50.16 Gy if no residual disease was present) to keep the total dose to each OAR below the tolerance limit for every adaptive plan while maintaining at least 99% coverage to the PTV with a hot spot less than 110% to ensure that no normal tissue limit would be reached for a specific organ before the end of treatment. Once the plan was finalized, the number of fractions was adjusted to the number that would be delivered for the next adaptive phase. Dose accumulation was performed at the end of each adaptive phase to ensure target volumes met prescription dose and OARs met dose constraints.

Planning was performed with Pinnacle3 v.9.10 (Philips Medical Systems, Fitchburg, WI). All patients were planned with volumetric modulated arc therapy. For bilateral neck irradiation, two 360-degree arcs were utilized, while for cases of unilateral neck irradiation, two half arcs were used. The duration of the MRI-simulation was one hour and the duration of segmentation and replanning was four hours per patient.

3.2.7 Statistical analysis

38

Three dimensional volumetric changes of GTV_p and GTV_n were recorded at all time points. Dosimetric parameters of target volumes and OARs were recorded for standard vs. adaptive plans for each patient. Subsequently, normal tissue complication probability (NTCP) for toxicity endpoints was calculated using literature-derived multivariate logistic regression models (96-99). The toxicity endpoints examined were: 1) persistence of feeding tube 6 months after treatment (96), 2) grade ≥2 dysphagia 6 months after treatment (97), 3) hypothyroidism 12 months after treatment (98), and 4) xerostomia 6 months after treatment (99). The rationale for NTCP model selection was detailed in a previous publication by our group(100). All statistical analyses were performed using statistical software (JMP Pro version 11, SAS Institute, Cary, NC).

3.3 Results

Five patients were included in this pilot study; 3 men and 2 women. Median age was 58 years (range 45-69). Three tumors originated at the tonsillar fossa and two at the base of tongue. Patient demographic, disease, and treatment characteristics are summarized in Table 3.1.

Table 3. 1: Patient demographic, disease, and treatment characteristics.

Patient	Origin	Gender	Age (years)	Smoking history	T stage	N stage	AJCC stage	Concurrent chemotherapy
1	Tonsil	Female	45	Never	T2	N2c	IVA	weekly Cisplatin

2	Base of Tongue	Male	60	Never	T2	N1	III	No chemotherapy
3	Tonsil	Female	69	Former	T2	N2b	IVA	weekly Cetuximab
4	Tonsil	Male	51	Never	T2	N2c	IVA	weekly Cisplatin
5	Base of Tongue	Male	58	Never	T2	N2b	IVA	weekly Cetuximab

The average decrease in GTV_p volume at weeks 2, 4, and 6 was 44%, 90%, and 100%, respectively. The GTV_n volume shrinkage, however, had a relatively slower pace with average decrease in GTV_n volume at weeks 2, 4, and 6 of 25%, 60%, and 80%, respectively. These significant shrinkages qualified all patients for adaptive plans at weeks 2, 4, and 6. The course of target volume response is presented graphically in figure 3.3 for all patients included in the analysis.
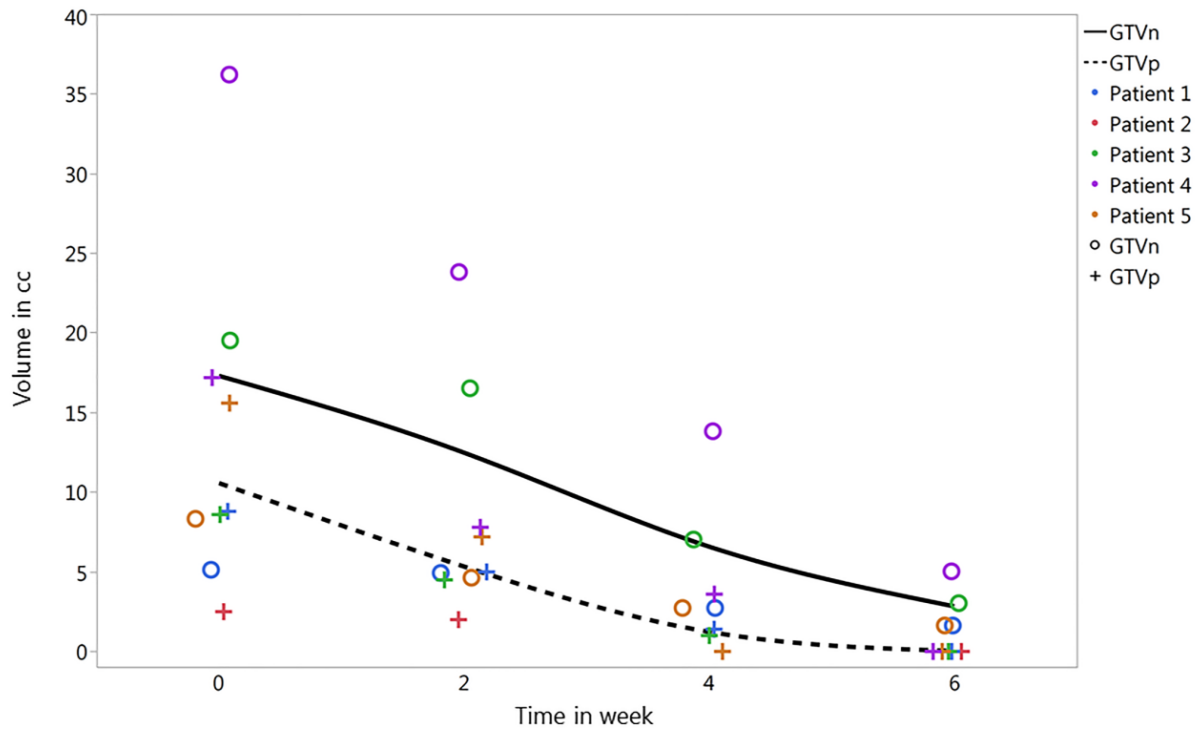
Figure 3. 3: Volumetric response of target volumes.

Details of volumetric response of target volumes for all patients at each time point, over the course of therapy. Patient 2 had an excisional biopsy prior to definitive IMRT and, therefore, had no GTVn at radiation start.

Results demonstrated that the vast majority of OARs showed a decrease in dosimetric parameters when adaptive plans were used compared with standard plans, particularly for swallowing related structures, as illustrated in Table 3.2. Regarding target volumes, the average dose to 95% of $PTV_{initial}$ volume was 70.7 Gy (SD, 0.3) for standard plans versus 58.5

Gy (SD, 2.0) for adaptive plans. Details of dose parameters for target volumes are presented in

Table 3.3.

Table 3. 2: Dosimetric criteria of organs at risk using standard vs adaptive plans.

Organ at risk (OAR)	Mean dose Standard IMRT in Gy	Standard Deviation Standard IMRT Gy	Mean dose Adaptive IMRT in Gy	Standard Deviation Adaptive IMRT Gy
Supraglottic larynx	52.7	10.7	45.8	10.4
Glottic larynx	33.8	21.7	31.0	18.9
Superior pharyngeal constrictor	62.8	6.7	58.1	5.0
Middle pharyngeal constrictor	51.6	16.4	48.4	12.5
Inferior pharyngeal constrictor	34.7	23.3	32.0	18.6
Cricopharygeous muscle	30.0	19.0	27.5	17.5
Mylo/geiohyoid muscle	37.8	10.5	33.4	11.2
Intrinsic tongue muscles	44.7	14.5	40.1	12.9
Genioglossus muscle	51.8	13.5	47.4	11.0
Oral cavity	42.1	11.3	38.0	10.8
Soft palate	55.0	10.7	49.2	10.6
Ipsilateral ant. Diagastric muscle	44.4	6.9	40.6	7.1
Contralateral ant. Diagastric muscle	29.9	10.2	26.0	12.7

Ipsilateral parotid gland	30.2	11.3	26.9	8.3
Contralateral parotid gland	17.4	8.6	16.5	8.4
Ipsilateral submandibular gland	69.7	3.6	65.0	6.0
Contralateral submandibular gland	40.9	20.3	39.9	19.6
Esophagus	19.2	12.3	16.8	9.9
Brain Stem	10.8	1.9	8.3	2.7
Spinal cord	21.8	6.5	21.2	8.0
Thyroid gland	36.1	23.2	32.8	20.7

Table 3. 3: Dosimetric parameters of target volumes using standard vs. adaptive plans.

Patient	PTV mean dose (Standard)	PTV mean dose (Adaptive)	PTV max dose (Standard)	PTV max dose (Adaptive)	PTV D95% (Standard)	PTV D95% (Adaptive)
Patient 1	71.61	62.2	74.88	72.6	70.56	56.02
Patient 2	71.47	61.68	73.61	65.31	70.46	59.08
Patient 3	71.86	66.25	76.02	72.16	70.61	57.42
Patient 4	72.7	69.38	76.4	73.4	71.12	61.8
Patient 5	72.1	65.2	75.7	72.6	70.98	58.1

Using NTCP models, the average reduction of the probability of developing dysphagia ≥ grade 2 and feeding tube persistence at 6-month post-treatment using adaptive strategy was 11% (37% vs 26%, odds ratio (OR) = 0.6, 95% CI 0.2-1.5) and 4% (10% vs 6%, OR = 0.5, 95% CI 0.1-3), respectively as depicted in Figure 3.4.
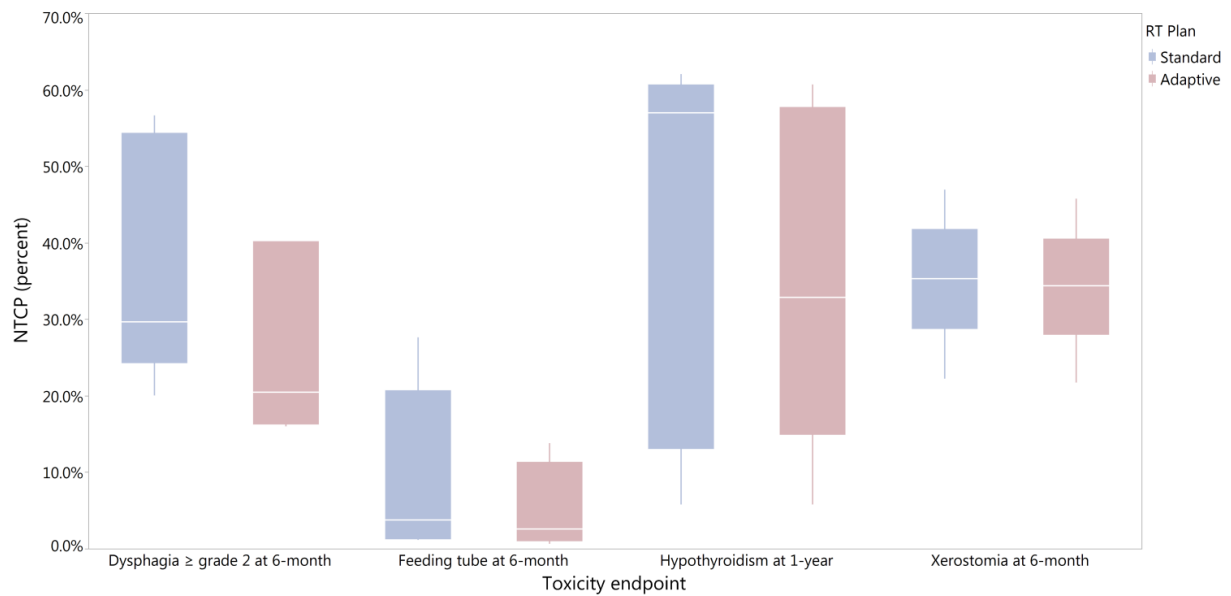
Figure 3. 4: NTCP of standard versus adaptive methods.

Boxplots depicting the comparison of normal tissue complication probability (NTCP) between standard and adaptive methods.

The probability of developing hypothyroidism at 1-year post-treatment was also reduced by average 5% (41% vs 36%, OR= 0.8, 95% CI 0.3-2) while the probability of xerostomia at 6-month was only reduced by average 1% for adaptive plans compared with standard IMRT (35% vs 34%, OR= 0.95, 95% CI 0.4-2.5).

3.4 Discussion

In this study, we report the feasibility of an MRI-guided IMRT dose-adaption workflow for HPV+ OPC. To our knowledge, this is the first study reporting on the dosimetric advantage of MRI-based adaptive radiation de-intensification in head and neck cancers. The proposed

approach was associated with an average reduction in the dose to the PTV of 12 Gy. Adaptive replanning was associated with reduction of dose to the OARs, in particular to the swallowing musculature, which translated into a reduction of the odds of dysphagia ≥ grade 2, feeding tube persistence at 6-months, and hypothyroidism at 1-year post-treatment.

HPV+ OPC has been shown to be a favorable subtype of head and neck cancer with improved prognosis compared to non-HPV+ OPC (4, 101). The distinctive epidemiologic, clinical and molecular characteristics (102) of HPV+ OPC are now reflected in the new cancer staging proposed in the American Joint Committee on Cancer 8th edition (103). Given the excellent outcomes of HPV+ OPC, it is increasingly considered that many patients with HPV+ OPC may be over-treated with current standard chemoradiation. It is, in fact, recognized that current standard treatment is associated with high rates of toxicities that were shown to adversely impact patients' health-related quality of life (104). Given the high probability of long-term survival and typical young age of patients with HPV+ OPC, treatment de-intensification aiming at reducing long-term toxicities and improving survivorship has become a central concern in the management of these patients (105). To this end, multiple clinical trials are currently on-going to assess various treatment de-escalation strategies in this group (106, 107).

The overall goal of all treatment de-intensification strategies is to maintain excellent cancer outcomes while reducing morbidity. Current evaluated strategies include the use of targeted therapies versus systemic chemotherapy (106), reduced radiation dose based on response to induction chemotherapy response (108-110), or modulation of radiation dose in the context of chemoradiation (111, 112). Proton therapy may be also an alternative way to reduce

normal tissue toxicity and is currently investigated in randomized trial (NCT01893307) comparing IMPT versus standard IMRT. A recent study by Blanchard et al. demonstrated the validity of a set of NTCP models for head and neck cancer patients treated with proton therapy. However, improvement in model performance remains to be required for better selection of patients for proton therapy(113). Furthermore, minimally invasive surgery such as trans-oral robotic surgery (TORS) has been also introduced as alternative approach to avoid radiation toxicity with equivalent oncologic outcomes(114). An ongoing randomized clinical trial (NCT02984410) is currently assessing the patient-reported swallowing function over the first year after randomization to either IMRT or TORS in OPC patients.

It is fairly well established that radiation dose is closely related to radiation-induced long-term toxicities, notably to rates and severity of dysphagia as well as rates of stricture formation, feeding tube dependence and aspiration (115-117). In a recent systematic review by Duprez et al., mean dose to pharyngeal constrictors was the strongest predictor of late swallowing dysfunction, with clinical reduction of swallowing dysfunction observed with dose of 52-55 Gy vs. 61-64 Gy, suggesting that even mean OAR dose reduction of less than 10 Gy could translate into clinically impactful toxicity reduction (118). In this context, de-escalation strategies aiming at reducing radiation dose are particularly appealing. Chera et al. (111) recently investigated rates of complete response of a de-intensified chemoradiation strategy in favorable risk HPV+ OPC. Treatment de-escalation consisted of delivery of 60 Gy to the gross disease and reduced cisplatin dose (30 mg/m^2 weekly). The reported clinical complete response rates reached 98% and 60% at the primary and regional sites respectively, suggesting that dose de-escalation may be suitable in selected patients. However, optimal

strategy for patients' selection, notably the potential role of adaptive de-escalation based on individual response, remains to be investigated.

The principle of adaptive radiotherapy planning relies on monitoring temporal and spatial anatomical changes over the course of radiotherapy, and modulating radiation dose based on observed changes. These changes can include changes in target volumes, OAR volume or shape, weight loss, alteration in muscle mass, or edema (92, 119, 120). Several previous studies have assessed the role of per-treatment imaging response during the course of radiotherapy for head and neck cancer, including CT (92, 93, 121, 122), PET-CT (123), anatomic MRI and functional MRI (diffusion weighted or dynamic contrast enhanced) (124), with tumor changes observed in the majority of patients, as early as by fraction 11 (125). Using CT-on-rails image guidance in patients undergoing head and neck radiotherapy, Schwartz et al. at reported that all patients benefited from at least one re-plan and 36% required a second re-plan to account for weight loss, CTV and normal tissue changes (92, 93). More recently, Lee et al. (112) reported outcomes of an adaptive approach consisting of 10 Gy dose de-escalation to involved lymph nodes based on early treatment hypoxia assessment using 18F-fluoromisonidazole-PET. Among 33 patients, 30% received reduced radiation dose; 2-year locoregional control rate was as high as 100%. This study suggests that functional imaging may play an important role in guiding adaptive radiation strategies. The increasing use of MRI for head and neck radiotherapy planning has the advantage of improved soft-tissue visualization (94), which allows to more confidently assess anatomical tumor changes during treatment. In addition, MRI also offers the possibility of frequent per-treatment functional

assessment, without addition of ionizing radiation. The recent introduction of the MR-Linac technology holds the promise to facilitate such adaptive IMRT workflows by mean of daily on-line MRI during radiation treatment (38).

This *in silico* study is limited by its small sample size. However, the aim of this study was to establish the feasibility and the dosimetric advantage of this proposed MRI-guided IMRT dose-adaption workflow for HPV+ OPC, in preparation for future clinical application. In addition, this study used only anatomical MR-sequences for treatment adaption. However, although the role of functional MRI certainly seems promising for assessment and prediction of tumor response (124), observed functional changes require further investigation to establish clear thresholds to be used clinically for treatment adaptation. Finally, the safety, in terms of cancer control outcomes, as well as the toxicity advantages of this workflow will be validated in an upcoming clinical trial by our institution. The results of this study guided the sample size calculation of this upcoming phase II clinical trial designed to validate the superiority of MRI-guided radiotherapy dose adaptation for improving the toxicity profile of HPV+ oropharyngeal cancers without compromising the outcomes.

3.5 Conclusions

This *in silico* results showed the suggested MRI-guided adaptive approach is technically feasible, safe (with no normal tissue exceeding modeled dose constraints), and advantageous in reducing dose to OARs, especially swallowing musculature, thus reducing the NTCP of dysphagia ≥ grade 2, feeding tube persistence at 6-month post-treatment, and hypothyroidism at 1-year post-treatment.

48

Chapter 4: Diffusion-weighted MRI as a biomarker for tumor response and disease control

4.1 Introduction

Radiation therapy (RT) is a cornerstone of head and neck cancer (HNC) treatment both in the definitive (i.e., organ preserving) and the adjuvant post-operative setting. The goal of RT is to maximize the dose to cancer cells while minimizing the dose to adjacent normal tissues. However, tumors have variable sensitivity to RT leading to different disease response rates.(29) Current RT dose and fractionation are largely driven by empirical data rather than tumor-specific information regarding potential radiosensitivity or radioresistance.(5-7, 126) The ability to predict tumor response before and/or during the RT course can allow for the adaptation of RT doses and potentially achieve better treatment outcomes for patients.

Non-invasive imaging such as magnetic resonance imaging (MRI) can provide important information related to tumor characteristics and response to RT. The development of MRI correlates of RT response would be critical for implementing adaptive RT strategies that maximize therapeutic ratios. Specifically, patients with aggressive non-responsive tumors may require RT dose escalation (5, 7), while patients with radiosensitive tumors may benefit from dose de-escalation to spare normal tissues with equivalent tumor control.(6) This represents a significant unmet clinical need since patients with radiosensitive tumors are over-treated and patients with radio-resistant tumors are under-treated. A leading-edge solution to the anatomic adaptive therapy problem has been to integrate MRI into radiation delivery devices (e.g., MR-Linear accelerators).(38) The richer data of MRI compared with standard of care CT images, enables computer-driven identification of tumors and normal tissues and allows radiation plans

49

to be adapted on a daily basis with limited human intervention. (39, 40) Yet, gross anatomic changes represent only one dimension of patient response to RT. Having incorporated high-field MRI into delivery devices, there is now the potential to monitor the biologic changes within the patient using functional MRI sequences without excess radiation, contrast exposure, or excess burden on patients' time.

The central hypothesis of this study is that quantitative MR diffusion-weighted imaging (DWI) can be used as a predictive biomarker of treatment response and oncologic outcomes in HNC. Functional changes in a tissue (e.g., a reduction in cellular density through RT-induced apoptosis) is reflected in an alteration in the detected diffusion measures, using a metric known as the apparent diffusion coefficient (ADC). The ADC component of DWI has been previously used to detect treatment response in HNC.(50, 127, 128) Specifically, DWI has been shown to predict response to induction chemotherapy(41, 42), RT(42-50), and tumor recurrence(51). Preliminary data from a prospective trial at our institution(52), supported by other group's data(42, 44-46, 49, 53, 54), has demonstrated that DWI was able to discriminate patients who will have a complete response at mid-RT. Additionally, recent data from our group demonstrated that early tumor regression rate ≥25% at fraction 15 (i.e., mid-RT) in HNC patients is associated with better local control and overall survival.(55) These low-risk patients represent suitable candidates for RT dose de-escalation if dose could be coupled to a quantitative marker of tumor response probability (i.e., ADC). However, these findings remain to be validated in larger prospective studies with more mature follow-up data to correlate with oncologic outcomes and overall survival. To this end, we aim to determine DWI parameters

associated with tumor response and oncologic outcomes in a prospective cohort of HNC patients treated with definitive RT.

4.2 Methods

4.2.1 Patient selection

HNC patients enrolled in an active prospective imaging study (NCT03145077) from January 2017 to March 2021 were included after institutional-review board approval and study-specific informed consent. Patients in this cohort had MRIs at pre-RT, mid-RT, and post-RT. Inclusion criteria were adult patients with histologic evidence of malignant head and neck neoplasm obtained from the primary tumor or metastatic lymph node; indicated for curative-intent treatment with radiotherapy with or without chemotherapy (induction or concurrent); good performance status (ECOG score 0-2); and with no contraindications to MRI.
Patients evaluated in this study received RT using standard daily fractionation for a period of 6-7 weeks. Tumor staging was based on clinical imaging consisting of contrast (CE) CT prior to treatment initiation using current AJCC 8th edition staging criteria.

4.2.2 MR Imaging

All patients enrolled in the study had imaging acquired using individualized immobilization devices. Head immobilization was performed to decrease motion artifacts during the imaging study, according to the methodology presented previously by our group.(84) Patients were scanned using a MAGNETOM Aera 1.5T MR scanner (Siemens Healthcare, Erlangen, Germany) with two large four-channel flex phased-array coils. After the scout scan,

an anatomic T2-weighted (T2w) fast spin-echo sequence (TR/TE = 4.8 s/80 ms; echo train length = 15, pixel bandwidth = 300 Hz, slice thickness= 2 mm, matrix= 512 x 512) was performed. One hundred and twenty axial slices with a field of view (FOV) of 25.6 cm were selected to cover the primary tumor and neck nodes. Acquisition parameters for DWI MRI were multi shot radial turbo spin-echo (i.e., BLADE), axial acquisition; TR = 6.5 s; TE = 50 ms; pixel bandwidth = 1220 Hz; FOV = 25.6 x 25.6 cm^2; echo train length = 15; EPI factor = 7, acquisition matrix = 128 x 128; voxel size = 1 x 1 x 2 mm^3; 24 contiguous slices; two b-values = 0 and 800 (sec/mm^2) for each orthogonal diffusion direction. DWI acquisition of patients scanned after 2018 was performed with multi shot spin-echo echo-planar imaging (i.e. readout segmentation of long variable echo-trains, RESOLVE), axial acquisition; TR = 3.5 s; TE = 65 ms; pixel bandwidth = 780 Hz; FOV = 25.6 x 25.6 cm^2; acquisition matrix = 128 x 128; slice thickness = 4 mm; reconstruction voxel size = 1 x 1 x 2 mm^3, 48 contiguous slices; number of average = 8; two b-values = 0 and 800 (sec/mm^2) for each orthogonal diffusion direction. ADC maps were subsequently autogenerated using a scanner specific on-line software during image generation. RESOLVE was selected because of shorter scan time (3:30 vs. 7:03 minutes for BLADE) and relatively higher signal-to-noise ratio. Our quality assurance study using phantom, volunteer, and patient images showed that both methods display similar ADC values with no differences in repeatability studies.

4.2.3 Image Segmentation/Registration

The regions of interest (ROIs) for the primary gross tumor volume (GTV-P) and the nodal gross tumor volume (GTV-N) were manually segmented by an expert radiation oncologist

52

(ASRM) using the pre-RT T2w images. Deformable image registration (DIR) was used to register MR sequences at different time points (i.e., baseline and mid-RT) using the benchmarked commercially available image registration software (Velocity AI, version 3.0.1, Atlanta, GA). All baseline GTV-P ROIs were then propagated to the mid-RT T2w images (i.e., mid-RT GTV-P) which represent the same three-dimensional (3D) volume of the original GTV-P on mid-RT images and include both responding and non-responding voxels. This was followed by quality assurance (QA) review and manual editing whenever needed to exclude air gaps or non-anatomically relevant parts in case of massive tumor shrinkage. Residual GTV-N ROIs, on the other hand, were all manually segmented on mid-RT images. Subsequently, DWI images were co-registered with the corresponding T2w of each time point and finally all ROIs were propagated to extract corresponding ADC values. Additional ROIs were created on mid-RT images for patients with non-complete GTV-P response at mid-RT to assess DWI differences between responding and non-responding sub-volumes within the mid-RT GTV-P. The first sub-volume was labeled mid-RT GTV-P-RD which represents the residual disease and the second sub-volume was labeled mid-RT GTV-P-RS which represents the area of response. Figure 1 illustrates the workflow process for image registration and segmentation.
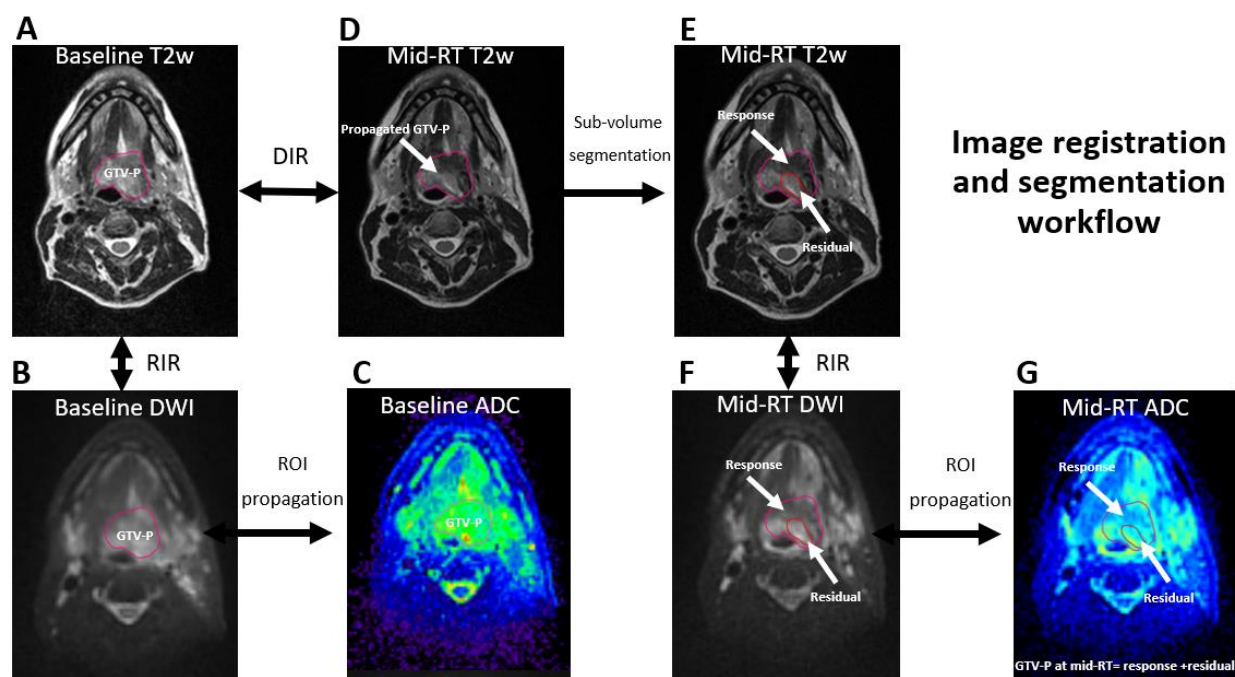
Figure 4. 1: Workflow process of the study.

Illustration of the workflow process for image registration and segmentation in the study using an example of a patient with T4N1 tumor of the base of tongue. Panel (A) shows the GTV-P segmentation on baseline T2w MRI followed by rigid co-registration (RIR) and contour propagation to baseline DWI (B) and then ROI propagation to corresponding ADC map (C). Panel (D) shows mid-RT T2w image with partial response. The image was co-registered to baseline T2w using deformable image registration (DIR) and baseline GTV-P was propagated. Subsequently, the residual and response sub-volumes were segmented (E), then contours were propagated to mid-RT DWI after RIR (F), and finally to the corresponding mid-RT ADC map (G).

4.2.4 Outcome definition

Treatment response was assessed at mid-RT and at 8-12 weeks post-RT using RECIST 1.1 criteria and was defined as: complete response (CR) vs. non-complete response (non-CR). All patients had complete physical examination, fiberoptic endoscopy, MRI, and CECT or FDG PET-CT performed 8-12 weeks after RT completion to assess the final treatment response. Oncologic outcomes included two-year local control (LC), regional control (RC), freedom from distant metastasis (FDM), recurrence-free survival, and overall survival.

4.2.5 Statistical analysis

Continuous data were presented as mean ± standard deviation (SD), and categorical data were presented as proportions. The Kolmogorov–Smirnov test was used to assess the difference in baseline ADC in BLADE vs. RESOLVE DWI sequences. The ADC values for all voxels included in GTV-P and GTV-N ROIs were assessed by histogram analysis and the following parameters were extracted using in-house MATLAB script (MATLAB, MathWorks, MA, USA): ADC mean, 5th, 10th, 20th, 30th, 40th, 50th (i.e. median), 60th, 70th, 80th, 90th, 95th percentile. Pre-RT ADC parameters were correlated with RT response (CR vs. non-CR) at mid- and post-RT time points using the non-parametric Mann-Whitney U test to compare ADC values between the mid-RT CR and non-CR groups. The non-parametric Wilcoxon signed-rank test was used to compare the mid-RT versus baseline ADC. Delta ADC (Δ ADC) were calculated as the percent change of ADC relative to baseline value for each parameter

(i.e., $\frac{midRT\ ADC - PreRT\ ADC}{PreRT\ ADC} \times 100$). Delta volumetric changes for both GTV-P and GTV-N at mid-RT were also calculated and the non-parametric Spearman's Rho test was used to determine the relationship between Δ ADC and Δ volume changes. Recursive partitioning analysis (RPA) was performed to identify Δ ADC threshold associated with relapse. Oncologic and survival endpoints were calculated using the Kaplan-Meier method and the statistical significance was determined using a p-value <0.05. Uni- and multi-variable analyses for oncologic and survival endpoints were performed using Cox regression. For multivariable analysis, we tested the impact of including the ADC parameter of choice compared with baseline models of standard clinical variables. We subsequently compared the new model using Bayesian information criteria (BIC).(129) A lower BIC indicates improved model performance and parsimony, using the BIC evidence grades presented by Raftery (130) with the posterior probability of superiority of a lower BIC model, where a BIC decrease of < 2 is considered "Weak" (representing a 50–75% posterior probability of being superior model), 2–6 denoted "Positive" (posterior probability of 75–95%), 6–10 as "Strong" (posterior probability of > 95%), and > 10, "Very strong" (posterior probability > 99%). In addition, Cox proportional hazards models were constructed using the Lifelines Python package (DOI: 10.21105/joss.01317) using Python version 3.9.7. Clinical models that includes T stage, HPV status, and Smoking pack-year for LC and AJCC stage 8th edition, Age at Diagnosis, and Smoking pack-year for RFS were done. Additive models that include the clinical parameters plus the addition of ADC changes were then constructed to assess the potential additive value. Models were only constructed for patients with a GTV-P. C-

index values were derived from fitted models. All other analyses were executed with JMP Pro version 15 software (SAS Institute, Cary, NC).

4.3 Results
4.3.1 Patients

Eighty-six patients were enrolled. Five patients were excluded from this analysis because of lack of visible GTVs after induction chemotherapy (n = 3) and loss to follow-up (n = 2) leaving a total of 81 patients in the final analysis. At pre-RT, 53 patients had both baseline GTV-P and GTV-N, 6 patients had baseline GTV-P without GTV-N, and 22 patients had GTV-N with no GTV-P (i.e., total GTV-P=59 and total GTV-N=74). Patients with no visible GTV-P at baseline had either carcinoma of neck nodes of unknown primary (CUP; n=12), tonsillectomy prior to RT (n=6), or CR to induction chemotherapy (n=4). The majority of patients were men (n=74, 93%) and the median age was 61 years (range 33-78). Most patients had human papillomavirus (HPV) positive disease (n= 73, 90%). A summary of patient demographic, disease, and treatment criteria is presented in Table 4.1.

Table 4. 1: Patient demographic, disease, and treatment characteristics.

Characteristic	Patients No. (%)
Age (years)	
median (range)	61 (33-78)
Sex	

Male	75 (93)
Female	6 (7)
Smoking status	
Never	37 (46)
Former	35 (43)
Current	9 (11)
Smoking pack-year	
mean (SD)	15 (26)
Disease subsite	
Base of tongue	29 (36)
Tonsil	38 (47)
CUP	12 (15)
Others	2 (2)
T stage	
T0	12 (15)
Tx	6 (7)
T1	13 (16)
T2	24 (30)
T3	9 (11)
T4	17 (21)
N stage	

N0	6 (7)
N1	42 (52)
N2	31(38)
N3	2 (3)
AJCC 8th ed. Stage	
I	38 (47)
II	20 (25)
III	17 (21)
IVa	6 (7)
HPV status	
Positive	73 (90)
Negative	8 (10)
Radiation Dose	
Mean in Gy (SD)	69.6 (1.3)
Radiation Fractions	
Mean (SD)	33 (0.9)
Radiation technique	
IMRT/VMAT	55 (68)
IMPT	26 (32)
Chemotherapy	
None	16 (20)

Induction	1 (1)
Concurrent with RT	54 (67)
Induction + Concurrent	10 (12)

Abbreviations: CUP, carcinoma of unknown primary; SD, standard deviation; Gy, Gray; IMRT, intensity-modulated radiotherapy; VMAT, Volumetric Modulated Arc Therapy; IMPT, intensity modulated proton therapy.

4.3.2 Treatment outcomes

For patients with GTV-P at baseline (n=59), 18 (31%) had mid-RT CR at the primary site which increased to 53 (90%) post-RT. Only 6 patients (10%) had persistent local disease as assessed by imaging at post-RT. Amongst the 6 patients, all had subsequent pathological confirmation of residual/recurrent disease. For patients with GTV-N at baseline (n=75), no patient had CR at the neck at mid-RT while 65 patients (87%) had CR as assessed by imaging at post-RT. Upon further pathological assessment, 6 out of 10 patients with non-CR at the neck had residual/recurrent disease while the reminder had necrotic non-active tissue.

The median follow-up time was 31 months (IQR, 18-38). The 2-year LC, RC, and FDM for the entire cohort were 91%, 92%, and 91%, respectively. While the 2-year RFS and OS were 83% and 94%, respectively. The total number of recurrence events was 15 (18%). Two, three, and five patients had an isolated local, regional, and distant recurrence events, respectively. While one, two, and two patients had combined local & distant, locoregional, and locoregional & distant recurrences, respectively.

4.3.3 DWI correlates of outcomes
4.3.3.1 Baseline ADC parameters

Baseline mean, median, and different histogram percentile ADC values for BLADE vs.
RESOLVE were not significantly different for both GTV-P and GTV-N ROIs (p >0.05 for both,
Figure 2). There was no statistically significant correlation between pre-RT ADC parameters
and CR at mid-RT and post-RT time points for GTV-P. Similarly, there was no significant
correlation between pre-RT parameters and CR at post-RT for GTV-N (p >0.05 for all).
Univariable analysis also did not show a significant correlation between pre-RT ADC
parameters and all oncologic and survival endpoints.
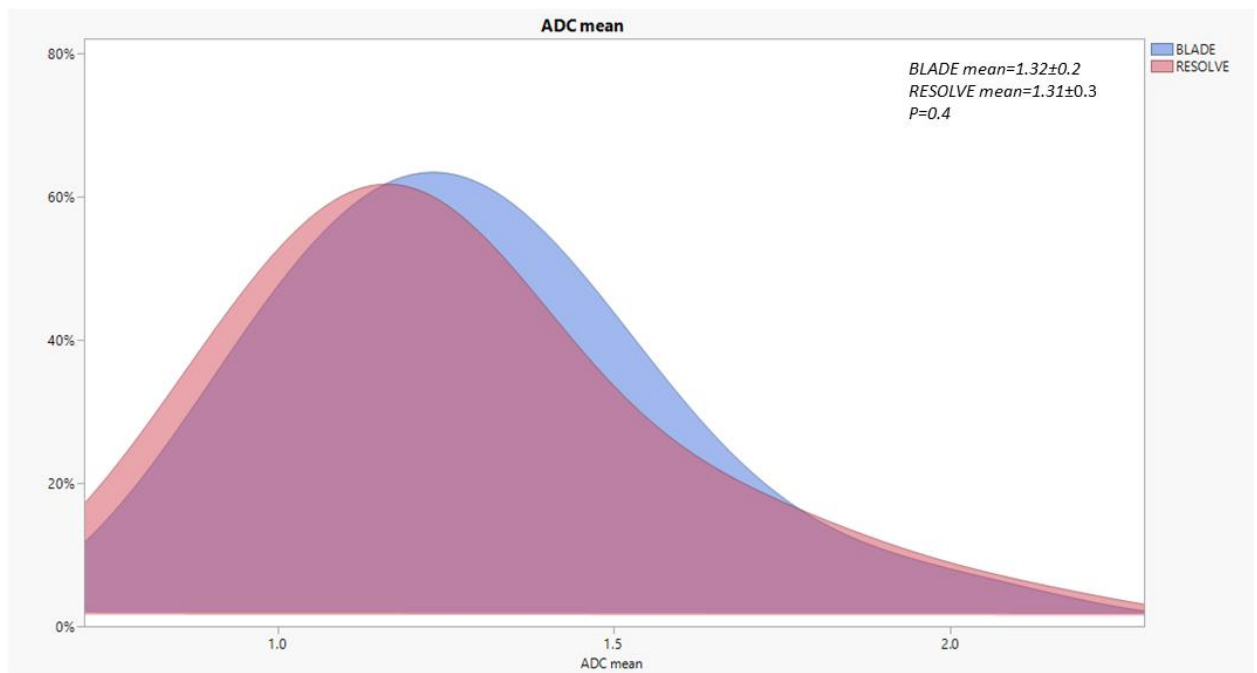
Figure 4. 2: BLADE vs. RESOLVE histograms

Histogram illustration of the distribution of tumor and nodal volumes' ADC mean at baseline using the BLADE vs. RESOLVE DWI acquisition methods in the study. The RESOLVE in pink is overlaid on BLADE in light blue. There were no statistically significant differences using the Kolmogorov–Smirnov test (p=0.4).

4.3.3.2 Mid-RT and delta ADC parameters

There was a statistically significant increase in all mid-RT GTV-P ADC parameters compared to baseline values (p <0.0001 for all, Table 2). Additionally, there was a statistically significant increase in all mid-RT GTV-N ADC parameters compared to baseline values (p <0.0001 for all, Table 2). For patients with CR of the primary tumor at the end of RT, there was a significant increase in GTV-P ADC_{mean} at mid-RT compared to baseline (($1.8 \pm 0.29) \times 10^{-3}$ mm^2/s *versus* $(1.37 \pm 0.22) \times 10^{-3}$ mm^2/s, $p < 0.0001$). On the other hand, patients with non-CR had no statistically significant increase in GTV-P ADC_{mean} (p>0.05). All other studied ADC parameters also had a significant increase at mid-RT for patients with CR of the primary tumor at the end of RT compared to non-CR. However, there was a significant increase in GTV-N ADC parameters at mid-RT for both patients with CR and non-CR at the end of RT.

RPA analysis identified GTV-P Δ ADC_{mean} <7% at mid-RT as the most significant parameter associated with worse LC and RFS (p =0.01). The 2-Year LC and RFS for patients with Δ ADC_{mean} <7% compared to patients with ≥7% at mid-RT were 48% and 42% versus 96% and 87%, respectively (p <0.0001 and 0.001, Figure 3). Δ GTV-N ADC parameters at mid-RT, however, were not significantly associated with any of the studied endpoints (P>0.05).

Table 4. 2: ADC parameter changes at mid-RT versus baseline values.

ADC parameter (x10^{-3} mm^2/s)	End-RT response	Baseline GTV-P	Mid-RT GTV-P	P value	Baseline GTV-N	Mid-RT GTV-N	P value
ADC Mean	CR	1.37±0.2	1.8±0.3	<0.0001	1.27±0.3	1.6±0.4	<0.0001
	Non-CR	1.3±0.2	1.6±0.4	0.07	1.28±0.3	1.54±0.3	0.01
ADC 5th percentile	CR	0.87±0.3	1.2±0.3	<0.0001	0.76±0.2	1.04±0.3	<0.0001
	Non-CR	1.1±0.6	1.3±0.5	0.4	1.02±0.4	1.19±0.3	0.2
ADC 10th percentile	CR	0.97±0.3	1.32±0.3	<0.0001	0.86±0.2	1.16±0.3	<0.0001
	Non-CR	1.2±0.5	1.42±0.4	0.3	1.06±0.3	1.26±0.2	0.02
ADC 20th percentile	CR	1.1±0.3	1.47±0.3	<0.0001	0.97±0.3	1.3±0.4	<0.0001
	Non-CR	1.2±0.4	1.47±0.3	0.4	1.11±0.3	1.34±0.2	0.01
ADC 30th percentile	CR	1.17±0.3	1.58±0.3	<0.0001	1.06±0.3	1.4±0.4	<0.0001
	Non-CR	1.2±0.3	1.5±0.3	0.3	1.16±0.2	1.4±0.1	0.009
ADC 40th percentile	CR	1.25±0.3	1.68±0.3	<0.0001	1.14±0.3	1.5±0.4	<0.0001
	Non-CR	1.22±0.3	1.56±0.3	0.	1.21±0.2	1.45±0.2	0.01
ADC Median	CR	1.35±0.2	1.8±0.3	<0.0001	1.22±0.3	1.58±0.4	<0.0001
	Non-CR	1.25±0.2	1.6±0.2	0.07	1.25±0.3	1.51±0.2	0.009
	CR	1.42±0.3	1.9±0.4	<0.0001	1.32±0.4	1.67±0.4	<0.0001

ADC 60th percentile	Non-CR	1.3±0.2	1.68±0.5	0.1	1.3±0.3	1.57±0.3	0.009
ADC 70th percentile	CR	1.52±0.3	1.95±0.4	<0.0001	1.43±0.4	1.78±0.5	<0.0001
	Non-CR	1.36±0.3	1.7±0.6	0.1	1.36±0.4	1.64±0.4	0.009
ADC 80th percentile	CR	1.6±0.3	2.1±0.4	<0.0001	1.57±0.4	1.91±0.5	<0.0001
	Non-CR	1.4±0.3	1.8±0.7	0.07	1.45±0.4	1.72±0.5	0.01
ADC 90th percentile	CR	1.79±0.4	2.22±0.4	<0.0001	1.76±0.4	2.07±0.5	<0.0001
	Non-CR	1.52±0.4	1.99±0.8	0.03	1.57±0.5	1.84±0.6	0.1
ADC 95th percentile	CR	1.9±0.4	2.36±0.5	<0.0001	1.93±0.4	2.2±0.5	<0.0001
	Non-CR	1.61±0.6	2.09±0.9	0.03	1.65±0.7	1.97±0.8	0.1

A

B

Number at risk

ΔADC$_{mean}$≥7%	48	44	37	15	48	40	35	12
ΔADC$_{mean}$<7%	11	5	4	4	11	5	4	4

64
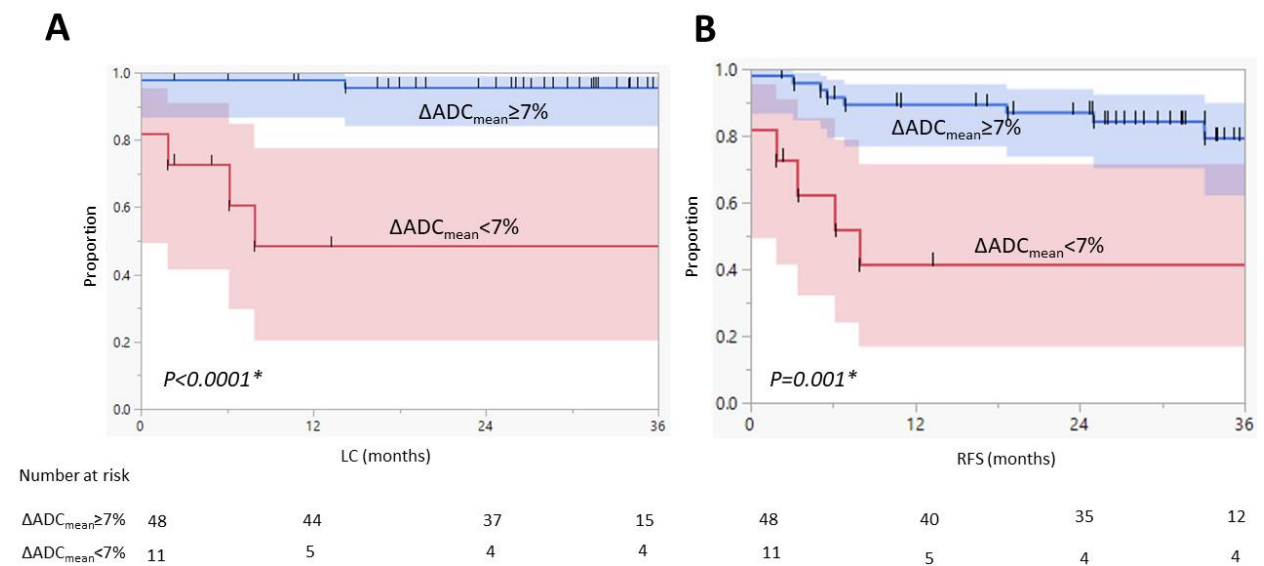
Figure 4. 3: LC and RFS by Δ ADC$_{mean}$.

Kaplan–Meier curves calculated for patients with baseline GTV-P (n = 59) show better (A) local control (LC) and (B) recurrence-free survival (RFS) for patients with ≥7% Δ ADC$_{mean}$ at mid-RT. Shaded colors represent 95% confidence intervals, short vertical lines represent censored data, and asterisks indicate significant log-rank p values.

Univariable analysis of local control showed that GTV-P Δ ADC$_{mean}$ at mid-RT ≥7% was associated with improved LC (hazard ratio (HR), 0.06, 95% CI, 0.01-0.3, p =0.001). In a multivariable model that also included T-stage, smoking pack-year, and HPV status, GTV-P Δ ADC$_{mean}$ at mid-RT remained statistically significant (HR, 0.03, 95% CI, 0.01-0.6, p =0.02) and achieved a better model performance as assessed using BIC criteria (BIC decrease =19.8).

Moreover, univariable analysis of recurrence-free survival showed that GTV-P Δ ADC$_{mean}$ at mid-RT ≥7% was associated with improved RFS (HR, 0.2, 95% CI, 0.06-0.6, p =0.003). In a multivariable model that also included age, AJCC 8th edition stage (i.e., which is based on T-stage, N-stage, tumor site and HPV-status data), and smoking pack-year, GTV-P Δ ADC$_{mean}$ at mid-RT remained statistically significant (HR, 0.3, 95% CI, 0.1-0.9, p =0.04) and also improved the model performance using BIC criteria (BIC decrease =8). Similarly, a univariable analysis of overall survival showed that GTV-P Δ ADC$_{mean}$ at mid-RT ≥7% was associated with improved OS (HR, 0.2, 95% CI, 0.04-0.9, p =0.037). However, it was not statistically significant when added to a multivariable model of age, smoking pack-year, and AJCC 8th edition stage. The clinical LC model yielded a C-index of 0.86 while the additive LC

model yielded a C-index of 0.94 while the clinical RFS model yielded a C-index of 0.73 while the additive RFS model yielded a C-index of 0.78.

4.3.4 Volumetric analysis and ADC

There was a significant decrease in mid-RT residual tumor volumes for both GTV-P and GTV-N compared to baseline pre-RT volumes (3.5 vs. 11.1 mm^3 for GTV-P and 7.4 vs. 11.8 mm^3 for GTV-N, p <0.0001 for both). However, the mean Δ volume decrease at mid-RT was significantly higher in GTV-P compared with GTV-N (69% vs. 30%, p <0.0001). As shown in Figure 4, there was no statistically significant correlation of the Δ volume and Δ ADC$_{mean}$ for both GTV-P (Spearman's Rho=-0.06, p =0.6) and GTV-N (Spearman's Rho=-0.2, p =0.1). Δ volume changes were not significantly correlated with any endpoints (P>0.05). Only baseline GTV-P volume (i.e., a surrogate of T-stage) was significantly correlated with LC on univariable analysis (p =0.03).
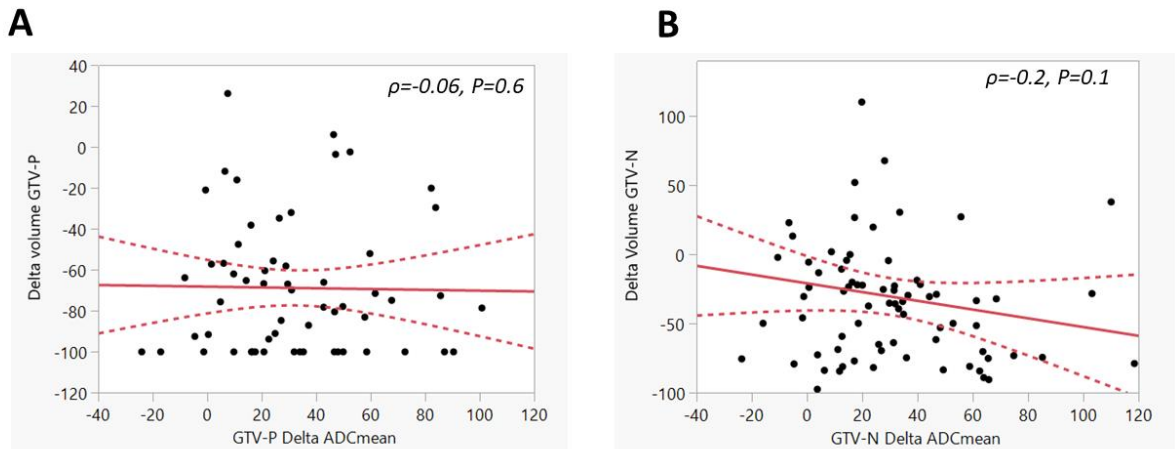
Figure 4. 4: Relationship between delta volume and delta ADC$_{mean}$.

Relationship between Δ volume and Δ ADC$_{mean}$ for both GTV-P (A) and GTV-N (B) at mid-RT. Solid lines represent the linear fit and dotted lines represent the 95% confidence intervals.

4.3.5 ROI subvolume analysis

For patients with mid-RT non-CR at the primary site, there was no statistically significant difference in all ADC parameters between GTV-P-RS and GTV-P-RD (p >0.05 for all). RPA identified Δ ADC$_{mean}$ <5% and <10% as the strongest predictors of local recurrence for GTV-P-RD and GTV-P-RS, respectively (p =0.02 for both). However, for RFS only Δ ADC$_{mean}$ <5% for GTV-P-RD was significantly associated with worse RFS (p =0.01).

4.4 Discussion

Our results show that DWI imaging changes during RT are a significant predictor of oncologic outcomes. The significant increase in mid-RT ADC parameters for both tumor and nodal ROIs reflects a decrease in cellular density in tumor tissue caused by the radiation effect that induces breakdown of cellular membranes which ultimately decrease the restriction of diffusion shown in baseline tumor tissue.(131-133) The increased diffusion in mid-RT images was successfully measured by the studied ADC parameters that showed a higher increase in patients who ultimately developed CR at the end of treatment compared to patients with residual disease.

Our study also identified an ADC biomarker of local control and recurrence-free survival using a Δ GTV-P ADC_{mean} threshold of 7% increase relative to baseline ADC_{mean}. These delta ADC changes were volume independent as our analysis methodology, illustrated in Figure 1, ensured that we use the same 3-D shape and volume of GTV-P propagated from baseline DWIs after image co-registration. We also assessed the effect of subvolume analysis within the subset of patients with non-CR at mid-RT images. In that subset, both Δ ADC_{mean} changes in the residual and responding subvolumes were significantly associated with local control with a 5% and 10% threshold of ADC_{mean} increase. The threshold is lower in residual volumes as expected because of the higher relative tissue density in these subvolumes. This also indicates that quantitative DWI parameter maps can detect the mesoscale cellular changes that could not be otherwise detected using gross visual assessment. Furthermore, this also shows that even within the apparent residual tumors on anatomic imaging at mid-RT, there is a subset that expresses higher ADC changes and those tend to have better LC and RFS. These changes during treatment can serve as a biomarker to predict outcomes and can also be used as a biological tool to adapt therapy dose according to the predicted response during therapy.

An additional significant finding in our study is that pretreatment DWI parameters had no significant association with outcomes, indicating that dynamic information obtained from RT-induced imaging changes during treatment is likely more informative compared to baseline status. Several previous studies matched our findings of no association between pretreatment ADC and outcomes (49, 134, 135) while a prior pilot set from our group as well as other studies showed a significant correlation.(43, 136-138) We believe that pretreatment ADC parameters of

a relatively homogenous cohort with a majority of HPV positive oropharyngeal cancer would be less predictive of outcomes when compared to a more heterogenous group of HNC subsites and/or tumor types. A heterogenous group of tumors will likely have a mixture of well and poorly differentiated tumors with different level of cellularity and stromal contents which thereby lead to a more contrast in the degree of diffusion between different tumor types.(133) Therefore, we think that the pretreatment DWI parameters may be a more prognostic than predictive biomarker as it reflects the nature of the baseline tumor rather than predicts its response to therapy.

In-treatment Δ ADC were investigated in prior studies with a relatively small sample sizes consisting of mixtures of HNC subsites, and in concordance with our results, these studies showed that Δ ADC during RT was a significant correlate of oncologic outcomes.(47, 50, 134) To our knowledge, we present the largest prospective imaging study to date supporting that Δ primary tumor ADC changes during treatment are a strong biomarker of important oncologic outcomes, particularly for local control and recurrence-free survival. The threshold of Δ ADC used should be carefully interpreted according to the nature of the primary tumor subsite, technique of segmentation/image registration, and DWI acquisition parameters (i.e., b values). Notably, delta ADC is a relative rather than an absolute value which could represent a more robust biomarker that is less susceptible to inter-patient and inter-scanner variability and thereby more clinically generalizable. In patients with mainly HPV positive oropharyngeal primary site using 3-D volumetric analysis of GTV-P at mid-RT relative to baseline, Δ ADC$_{mean}$ <7% was shown to be a strong correlate of local failure.

However, our study is not without limitations. Importantly, our study utilized a single-institution cohort without external validation of our findings with multi-institutional data. Another limitation was the use of two DWI sequences during the study (i.e., BLADE and RESOLVE); however, after analyzing the ADC values extracted from both DWI sequences using the Kolmogorov–Smirnov test, no significant differences were found between the two sequences. Lastly, we failed to show any significant correlation between Δ nodal DWI changes and regional control, which could potentially be attributed to the cystic nature of the studied GTV-Ns in our sample. As a future step, we plan to analyze these LNs using a morphologic distinction between solid and cystic component in each node rather than the standard segmentation approach.

4.5 Conclusions

In conclusion, our prospective imaging study of HNC patients demonstrated that Δ ADC parameters at mid-RT represent a strong predictor of local recurrence and recurrence-free survival. Patients with no significant increase of mid-RT ADC at the primary tumor site relative to baseline values are at high-risk of disease relapse. Multi-institutional data are needed for validation of our results.

Chapter 5: Dynamic Contrast-Enhanced MRI for assessment of normal tissue toxicity

This chapter is based upon:

5.1 Introduction

Osteoradionecrosis (ORN) of the mandible is a debilitating complication of external beam radiation therapy (EBRT) for head and neck cancer patients.(139-141) Head and neck squamous cell carcinoma (HNSCC) has an estimated annual incidence of approximately 62,000 cases in the United States.(142) The incidence of Human Papillomavirus (HPV) associated HNSCC continues to rise unabated and is expected to continue to rise for the next two decades until the effects of immunization will begin to impact incidence.(143, 144)

Recent data shows the rate of ORN development in HNSCC patients following EBRT is approximately 7% despite aggressive dental care and close follow up.(145) Even with a

relatively low incidence, the prevalence and burden of ORN is expected to rise because of the excellent prognosis for HPV+ patients (i.e. 5-year overall survival of 80-90% for most patients). Therefore, it is expected that the US will accumulate a large population of adults with a history of mandibular radiation, a nearly 10-fold increase compared to historical trends when prevalence was lower due to higher mortality of non HPV-associated cancers.

Despite the use of more conformal EBRT techniques such as intensity-modulated radiotherapy (IMRT), the mandible remains exposed to significant radiation doses because of its close proximity to target volumes that can eventually lead to the development of ORN especially when coupled with infection and/or dental manipulation.(145, 146) Early-stage ORN can be controlled with conservative measures such as antibiotics, surgical debridement, hyperbaric oxygen (HBO) therapy, pentoxifylline or tocopherol.(147, 148) However, progression to advanced ORN typically requires extensive surgical resection and complex reconstruction and leads to a substantial reduction in the quality of life of HNSCC survivors.(149, 150)

Anatomic imaging using CT or conventional MRI does not identify ORN-related bony changes until relatively late in the process, when the patient is generally already experiencing symptoms. (151, 152) Dynamic contrast-enhanced magnetic resonance imaging (DCE-MRI) is a clinically available imaging method that was shown to detect early-stage idiopathic osteonecrosis of the femur otherwise not visible on conventional MRI.(153) DCE-MRI parameters can be used to monitor bone-healing secondary to trauma or fracture, as well as chronic changes in bone health associated with age-related osteoporotic changes.(154-156)

The most commonly accepted biological mechanism of ORN development remains that summarized by Marx's three H's of hypoxic, hypovascular, and hypocellular tissue. Therefore, we expect that shifts in vascularity may portend development of ORN.(157) Hence, we focused on DCE-MRI as opposed to other imaging modalities. Our group has recently demonstrated that DCE-MRI can be used to detect alterations in bone vascularity following definitive radiotherapy to head and neck cancer patients.(158) However, we do not yet know how early changes in bone vascularity during radiation correlate with subsequent development of ORN. In order to develop a predictive, imaging-based biomarker of ORN development, it is therefore critical to identify DCE-MRI parameters in patients with existing ORN. This will facilitate the discrimination of the quantitative DCE-MRI parameters associated with injured versus healthy mandibular subregions. This characterization will ultimately serve as a guide to monitor temporal DCE-MRI changes following EBRT in attempt to early detect mandibular pathology before the development of symptoms.

Based on existing clinical and preclinical data, we hypothesized that ORN is associated with critical changes in bone vascularity reflected in common DCE MRI parameters namely V_e and Ktrans, as a reflection of overall poor vascular flow and integrity. To this end, we sought to characterize the quantitative DCE-MRI parameters associated with the established diagnosis of advanced mandibular ORN compared with normal mandible in the context of a prospective clinical study with high intrinsic imaging acquisition consistency.

5.2 Methods

5.2.1 Patient selection

Patients with a confirmed diagnosis of advanced ORN developed after curative-intent radiation treatment of head and neck cancer were prospectively enrolled in an observational imaging study (NCT03145077) after institutional-review board approval and study-specific informed consent. Eligibility criteria included age>18 years, pathological evidence of head and neck malignancy with history of curative-intent external beam radiotherapy, patients with clinically confirmed high-grade ORN requiring surgical intervention, good performance status (ECOG score 0-2), and no contraindications to MRI. Clinical staging of ORN was conducted using the Common Terminology Criteria for Adverse Events (CTCAE) version 4.0.

5.2.2 DCE-MRI Imaging

DCE-MRI scans were obtained using GE 3.0T Discovery MR750 scanners with a 6-channel Flex phased-array coil (GE Healthcare Technology, Milwaukee, WI). Prior to DCE-MRI, T1 mapping was performed using six variable flip angles (FA) 3D spoiled gradient recalled echo (SPGR) sequence (FA = 2°, 5°, 10°, 15°, 20°, and 25°; TR/TE = 5.5/2.1 ms, FOV = 25.6 cm, slice number = 30, voxel size = $2 \times 2 \times 4$ mm^3). The DCE-MRI was acquired using a multi-phase 3D Fast SPGR sequence to gain sufficient signal-to-noise ratio (SNR), contrast, and temporal resolution (FA = 15°, TR/TE = 3.6/1 ms, voxel size = 2×2×4 mm3, temporal resolution = 5.5s, number of repetitions = 56, pixel bandwidth = 326 Hz, ASSET acceleration= 2). Gadobutrol (Gadovist, Bayer Healthcare, Germany) was administered at a dose of 0.1

mmol/kg of body weight at 3 ml/s followed by the same amount of saline at 3 ml/s, via a power injector (Spectris MR Injector, MedRad, Pittsburgh Pa).

5.2.3 Computation of the kinetic model

Post-processing of the DCE-MRI images was performed at a workstation running in-house Matlab based pipeline (Matlab, MathWorks, MA, USA). Before quantitative analysis, motion correction and noise suppression were applied using simultaneous spatial and temporal higher-order total variations regularizations (HOTVs) as described by our group and by Chan et al.(159, 160) As shown in Figure 5.1, filtering with HOTVs demonstrated noise suppression as well as motion reduction.(160) To quantify the physiological parameters using DCE-MRI, the arterial input function (AIF) of the contrast agent (CA) entering the tissue was determined individually. T1 map was calculated to convert the signal intensity into concentration time course. Extended Tofts model assumes that the CA resides in and exchanges between two compartments in the tissue: the vascular space and extracellular extravascular space (EES).
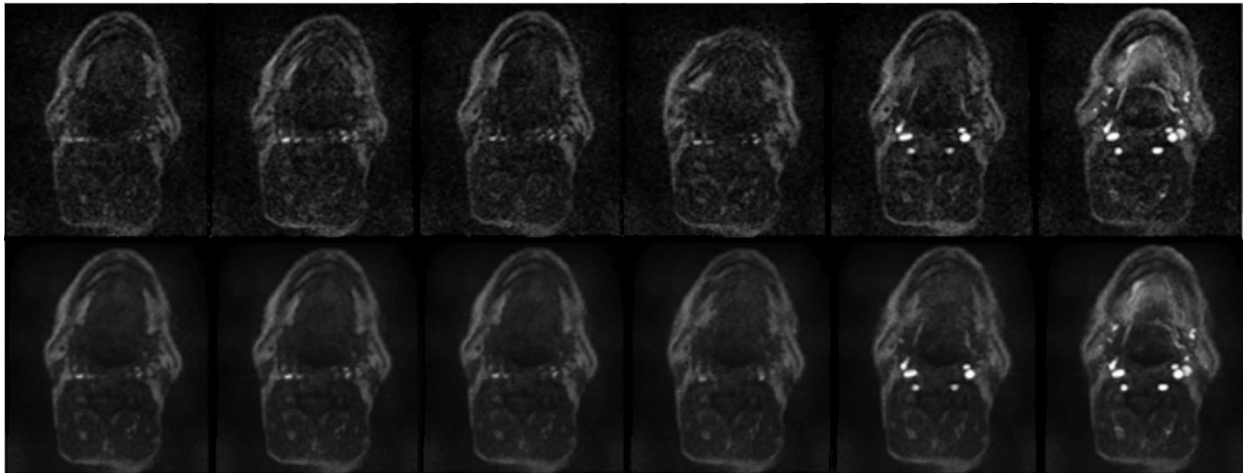
Figure 5. 1: Images before and after HOTVs.

This figure shows consecutive DCE MRI frame time series (from left to right) before (row up) and after (row down) filtering with HOTVs.

When this model is used, the differential equation describing the kinetic behavior of the CA in the tissue of interest is given by:

$$\frac{dC_{TOI}(t)}{dt} = \left(K^{trans} + v_p \cdot k_{ep}\right) \cdot C_p(t) - k_{ep} \cdot C_{TOI}(t) + v_p \cdot \frac{dC_p(t)}{dt} \quad (1)$$

where $C_{TOI}(t)$ and $C_p(t)$ are the concentrations of the CA at time t in the tissue of interest (TOI) and blood plasma, respectively, K^{trans} are the transfer (CA permeability rate) constants between blood plasma and the EES of the TOI. $k_{ep} = K^{trans}/V_e$ is the transfer (CA permeability rate) constant (min^{-1}) from the TOI back to the blood plasma, where V_e is the distribution volume fractions of CA in the EES per unit volume of tissue. When the kinetic model includes a vascular term, V_p that is the capillary plasma volume fractions per unit volume of tissue. Otherwise, by ignoring vascular term, the extended Tofts model is reduced to Tofts model as:

$$\frac{dC_{TOI}(t)}{dt} = K^{trans} \cdot C_p(t) - k_{ep} \cdot C_{TOI}(t) \quad (2)$$

The AIF for the pharmacokinetic (PK) analysis was derived from selected arteries. The relevance of several analytical AIF models in DCE-MRI have been previously extensively investigated.(161) Recently computer simulations were performed to evaluate and compare a population of AIF models with the Parker model.(162) The results demonstrated that a six-parameter linear function plus bi-exponential function AIF model was almost equivalent to the Parker AIF. It should be noted the former is computationally faster and more reliable in functional fitting when compared to the Parker AIF. However, predetermining the arrival time

76

(AT) and time to peak (TTP) of upslope for each AIF time series is usually not accurate in using the above six-parameter model. Therefore, we extended the six-parameter model to a bi-exponential and bi-linear function where the AT and TTP of the upslope are included as parameters to be estimated in AIF fitting.

In order to acquire the corresponding AT and TTP time points of the upslope for each AIF time series, we designed a special cost function, where fitting is performed with global optimization on the AIF model function with seven parameters. The new AIF model function is defined in equation 3 as AIFM where $p1$ to $p7$ are parameters to be determined by functional fitting [23], min is minimal value operator, max is the maximal value operator, abs is absolute value operator; $p4$ and $p5$ is AT and TTP to be determined, while $min(p4, p5)$ give AT, $max(p4, p5)$ is TTP; t is time points, and "$uplimit$" is a constant that is estimated by the maximal possible value of data to be fitted (e.g. twice of the maximum value in the time course).

The new AIF model function (AIFM) was defined as:

$$\text{AIFM} = \min \Big(\max \overbrace{ \Big(p1, p1 + (p2 - p1) \cdot \frac{t - \min(p4, p5)}{abs(p5 - p4)} + (p3 - p1) \cdot \frac{t - \min(p4, p5)}{abs(p5 - p4)} \Big) }^{part\ 1},$$

$$\overbrace{ \min\big(uplimit, p2 \cdot \exp\big(-p6 \cdot (t - \max(p5, p4))\big) + p3 \cdot \exp\big(-p7 \cdot (t - \max(p5, p4))\big)\big) }^{part\ 2} \Big) \ (3)$$

For each given AIF time point, the function can be described in two separate parts as indicated in equation (3). Part one of the function determines the AT and TTP of the upslope as well as the bi-linear functions through a maximization of operations containing parameters $p1$, $p2$, $p3$, $p4$, and $p5$. Here $p1$ (first term in the bracket of part 1) will fit the static signal, and the

second term in the bracket in part 1 will represent the upslope approximated by bi-linear functions. *p*2 and *p*3 represent the end points at TTP of each linear approximation. Moreover, the maximum value at each time point of part 1 represents the approximation of signal, and we therefore apply a *max* operator on the entire set of terms.

Part two of the function determines the signal approximation after TTP of the upslope with bi-exponential functions through a minimization of operations containing parameters *p*2, *p*3, *p*4, *p*5, *p*6, and *p*7, and the *uplimit*, which can be seen as a constant larger than the ceiling value the curve can take. Opposite to the implementation in part 1, the bi-exponential functions should always below *uplimit*, so there is *min* operator applied to the set of terms in part 2. Since the *min* operator in part 2, we can efficiently restrict the parameter estimation of the bi-exponential functions.

Since part 1 is strictly increasing while part 2 is strictly decreasing, we applied a *min* operator on the combination of part 1 and part 2. Subsequently, the minimum of part one and part two is noted to be AIFM as in equation (2). By enforcing these settings, the original complicated constrained (multiple) optimization problems in data fitting is changed into an unconstrained problem. Finally, the fitting cost function is implemented by optimization on ||DATA - AIFM||, where DATA could be DCE concentration or DCE signal. The fitting cost function is implemented by optimization on ||DATA - AIFM||, where DATA could be DCE concentration or DCE signal. By using this extended AIF model function, the AIF fitting can be completed in a more precise and reliable manner. Figure 5.2 shows the fitting process as well as the fitting results where a 56 time point AIF time series is presented. The PK modelling was

done on a pixel-by-pixel basis using a linearization equation of the models used (i.e. Tofts and extended Tofts) as described by Kenya Murase.[25] Subsequently, we implemented the linear least-squares method to acquire the PK parameters.(163, 164) This method is preferred to the conventional nonlinear least-squares method(165), because it is faster and it does not require initial estimation, and has no local optima problems.
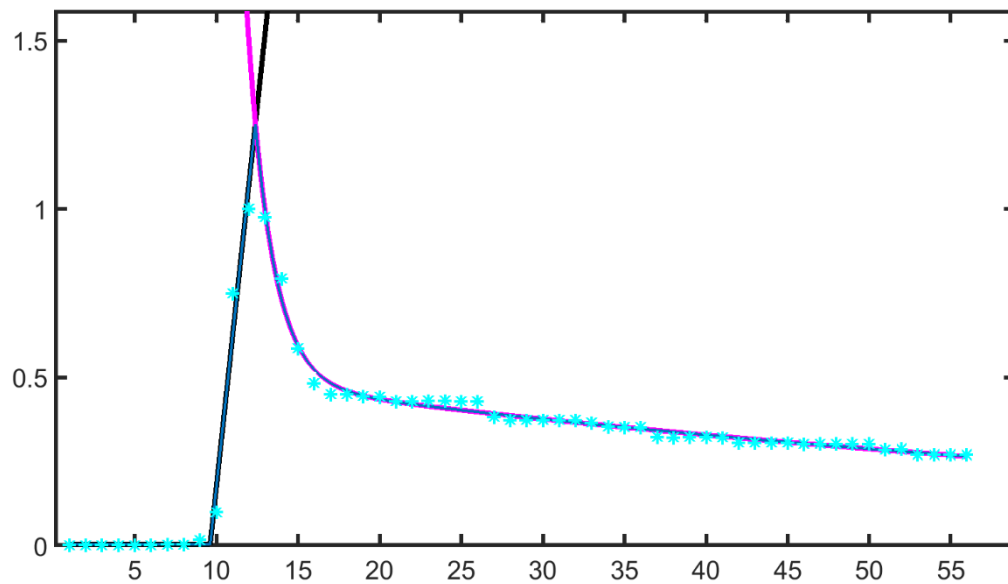
Figure 5. 2: AIF fitting.

The fitting process and fitting results where a 56 time point AIF time series (in Cyan) is presented.

5.2.4 Image segmentation and registration

Manual segmentation of mandibular volumes harboring ORN was done by an expert radiation oncologist (ASRM) and reviewed by expert neuroradiologist (JMJ). The segmentation was done using the MRI anatomical sequences (T1, T2, and T1+contrast) as well as co-registered contrast enhanced CTs (i.e. aquired within two weeks of the MRI with no interval therapy) to create ORN volumes of interest (ORN-VOIs) for all included patients. The segmentation included abnormal signal intensity or irregular gadolinium enhancement of bone marrow and soft tissues seen on MRIs(166, 167) as well as cortical erosions, sequestrations, and/or fractures seen on CTs(168). Subsequently, normal mandibular VOIs were created on the contralateral healthy mandible of similar volume and anatomical location (i.e. mirror image) to create self-control VOIs. Finally, the MRI anatomical sequences were co-registered to the DCE-MRI sequences and then the contours were propagated to the respective quantitative parameter maps. This workflow is graphically summarized in Figure 5.3. For dosimetric correlation, the original planning CTs and dose grids were retrieved when available to extract mandibular dose parameters (mean and maximum dose). In addition, ORN depicting CTs were co-registered to planning CTs using a validated commercial image registration software (Velocity AI 3.0.1). Finally, ORN-VOIs were mapped to planning CTs and dose grid and dosimetric parameters were extracted for each VOI. The RT dose parameters included minimum, mean, dose to 95% volume (D95%) and maximum dose to ORN-VOIs in Gray (Gy).
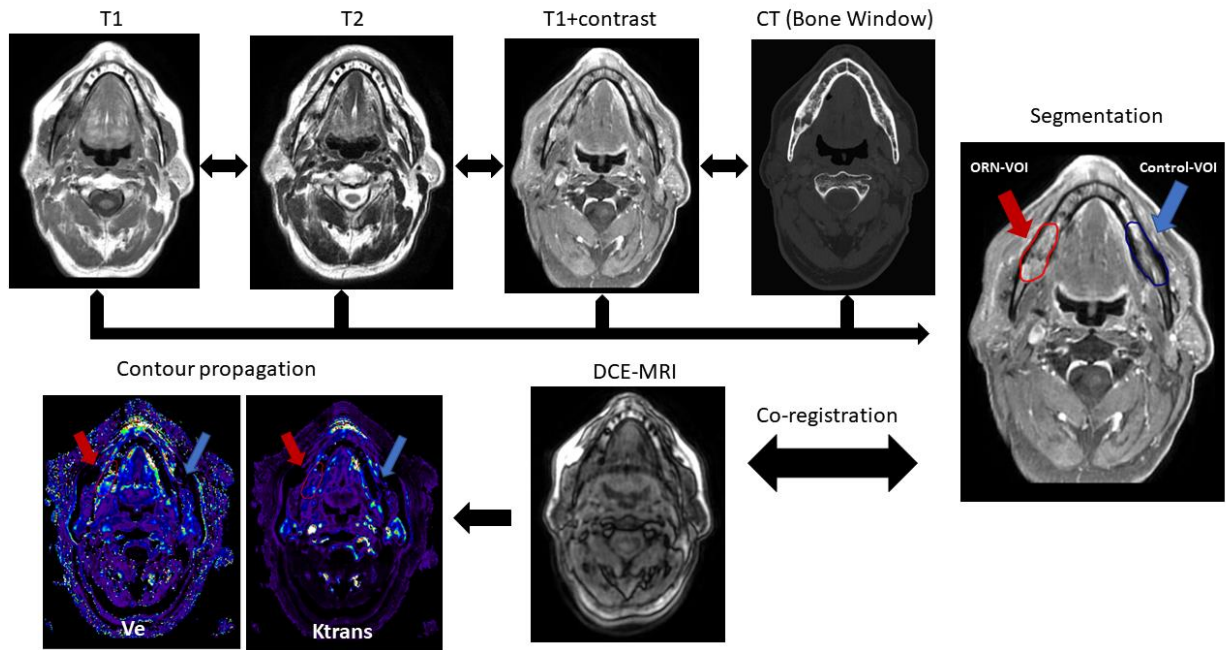
Figure 5. 3: Workflow of advanced ORN analysis.

5.2.5 Statistical analysis

Continuous data were presented as mean ± standard deviation, while categorical

data were presented as proportions. The comparison of quantitative DCE-MRI parameters

between ORN and Control VOIs was assessed using the non-parametric Wilcoxon signed-rank

test. The effect size was calculated and the magnitude of the effect size was determined using

Cohen's criteria where r of 0.1=small effect, 0.3=medium effect and 0.5=large effect.(169) The

non-parametric Spearman's Rho test was used to measure the correlation between radiation

dose to ORV-VOIs and DCE-MRI parameters. P values <0.05 were deemed statistically

significant. All statistical analyses were performed using JMP 14 Pro (SAS Institute, Cary, NC).

81

5.3 Results:

5.3.1 Patients

Thirty patients with grade 3 ORN requiring surgery were included. Median age at diagnosis was 58 years (range 19-78), and 83% were men. The site of tumor origin was in the oropharynx, oral cavity, salivary glands, and nasopharynx in 13, 9, 6, and 2 patients, respectively. IMRT was the radiation technique for all patients. The median IMRT prescription dose was 68 Gy in 32 fractions. The median time to ORN diagnosis after completion of IMRT was 38 months (range 6-184) while the median time to ORN progression to advanced grade after initial diagnosis of ORN was 5.6 months (range 0-128). Table 5.1 summarizes patient, disease, and treatment criteria.

Table 5. 1: Patient, disease, and treatment characteristics.

Characteristic	patients (n=30)
	No. (%)
Age*	
median (range)	58 (19-78)
Sex*	
Male	25 (83)
Female	5 (17)
Ethnicity*	
Caucasian	29 (97)

African American	1 (3)
Smoking status*	
Never	11 (37)
Former	13 (43)
Current	6 (20)
Smoking pack-year	
Mean (SD)	14.7 (24)
Disease subsite	
Nasopharynx	2 (7)
Oropharynx	13 (43)
Oral Cavity	9 (30)
Salivary glands	6 (20)
T stage	
T1	7 (23.33)
T2	7 (23.33)
T3	9 (30)
T4	4 (13.33)
Recurrence	3 (10)
N stage	
N0	9 (30)
N1	3 (10)

N2	15 (50)
Recurrence	3 (10)
HPV status (p16 IHC)	
Positive	8 (26.66)
Negative	2 (6.66)
Unknown	20 (66.66)
Pre-RT dental status	
No dental procedures	32 (47)
Dental extractions	35 (51.5)
Edentulous	1 (1.5)
Radiation Dose	
Mean in Gy (SD)	66.1 (4.7)
Radiation Fractions	
Mean (SD)	32 (2.8)
Chemotherapy	
None	11 (36.66)
Induction	1 (3.33)
Concurrent with RT	14 (46.66)
Induction + Concurrent	4 (13.33)
Surgery	
Yes	14 (46.66)

No	16 (53.33)

5.3.2 Radiation Dose

The RT dosimetric data were available for 21 patients (70%). The average of mean and maximum doses to the entire mandibular volumes were 51.4 Gy (range 35-64) and 69.4 Gy (range 52-76), respectively. The average of minimum doses to ORN VOIs (i.e. the isodose line that covers 100% of the ORN volume) was 46.7 Gy (range 26-66). The average of mean and maximum doses to ORN VOIs were 62.2 Gy (range 44-75) and 67.9 Gy (range 51-76), respectively; the average D95% was 55.6 Gy (range 32-69).

5.3.3 DCE-MRI parameters

The median volume of segmented VOIs was 5.2 cm^3 (range 1.8-10.9). Using the extended Tofts model, the average K^{trans} values in ORN-VOIs were significantly higher compared with controls (0.23±0.25 vs 0.07±0.07 min^{-1}, p<0.0001). The average relative increase of K^{trans} in ORN-VOIs was 3.2 fold those the healthy mandibular control VOIs (range 1.2-10.3). The effect size was large with r=0.52.

Likewise, the average V$_e$ values in ORN-VOIs was significantly higher compared with controls (0.34±0.27 vs 0.15±0.15, p<0.0001). The average relative increase of V$_e$ in ORN-VOIs

was 2.7 fold those the healthy mandibular control VOIs (range 1.1-6.9). The effect size was also large with r=0.69.

Using combined K^{trans} and V_e parameters, 27 patients (90%) displayed at least double the increase of either of the studied parameters in the ORN-VOIs compared with their healthy mandible control VOIs.

V_p was also significantly higher in ORN-VOIs compared with controls (0.17±0.2 vs 0.07±0.12, p<0.0001). However, K_{ep}, as expected, did not show a significant difference between ORN-VOIs versus controls (0.5±0.19 vs 0.46±0.13 min^{-1}, p=0.2) because of the increase of both K^{trans} and V_e parameters. Figure 5.4 depicts the comparison of K^{trans}, V_e, K_{ep}, and V_p values in ORN-VOIs compared with controls. Detailed histograms of patients' ORN versus Control VOI DCE-MRI parameters are presented for the entire cohort as Appendix A. 1.
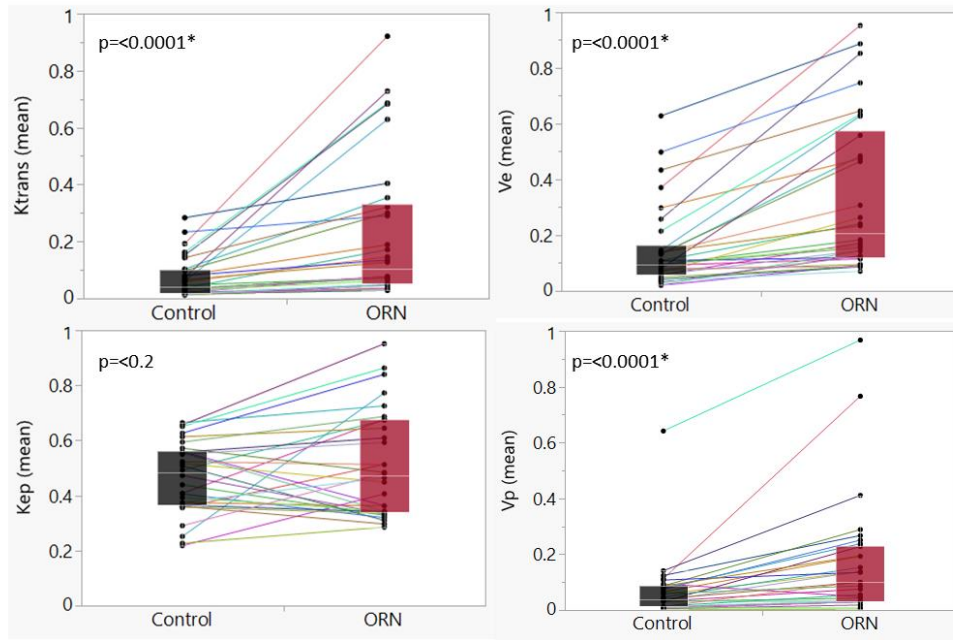
Figure 5. 4: ORN versus control Boxplots.

Boxplots showing the comparison of DCE-MRI parameters between ORN and Control volumes-of-interest (VOI). * indicates statistically significant p values. Connected lines represent each patient parameter value changes in ORN versus Control VOIs.

Using the Tofts model, the mean K^{trans} values in ORN-VOIs were, likewise, significantly higher compared with controls (0.27 ± 0.29 vs 0.08 ± 0.08 min^{-1}, p<0.0001). The average relative increase of K^{trans} in ORN-VOIs was 3.4-fold of the control VOIs (range 1.5-12.3). In addition, the mean V_e values in ORN-VOIs was significantly higher compared with controls (0.34 ± 0.28 vs 0.13 ± 0.13, p<0.0001). The average relative increase of V_e in ORN-VOIs was 4.04 fold of the healthy mandibular control VOIs (range 1.2-15.3). Using combined K^{trans} and V_e parameters,

also showed that 90% of patients had more than two-fold increase of either of the studied parameters in the ORN-VOIs compared with their healthy mandible control VOIs. Using the Spearman's Rho test, there were no significant correlations between any of the dosimetric parameters of ORN-VOIs (minimum, mean, D95% and maximum doses) and any of the DCE-MRI parameters ($P>0.05$ for all) for patients with available dose data (70%). The bivariate correlation between RT dose and DCE-MRI parameters is detailed in the Appendix material (Appendix A.2).

5.4 Discussion

Nearly four decades ago, R.E. Marx postulated a theory for development of ORN predicated in large part on altered bone vascularity, resulting in poor regenerative capacity and a decreased ability to resist mechanical and microbial insults.(157) Although this remains the most likely mechanism for ORN, to date scientists and clinicians have lacked the means to study bone vascularity with sub-centimeter spatial resolution in a non-invasive manner and have largely been forced to infer mechanisms of ORN development by combining limited pre-clinical studies, with static anatomic imaging and histologic evaluation of ORN specimens. For the first time, we now have the opportunity to leverage a clinically available imaging approach to provide real-time, non-invasive information about bone vascularity in the context of ORN (Figure 5.5). This represents a breakthrough both in our ability to study this devastating disease and to begin to develop clinical trials designed to ameliorate the disease using objective, quantitative measures. In addition, implementation of this approach can generate utility in the context of surgical extractions post-radiation, as well as in the context of real-time image-

guided surgical planning for resection of necrotic bone by distinguishing injured/poorly

vascularized bone from viable bone.
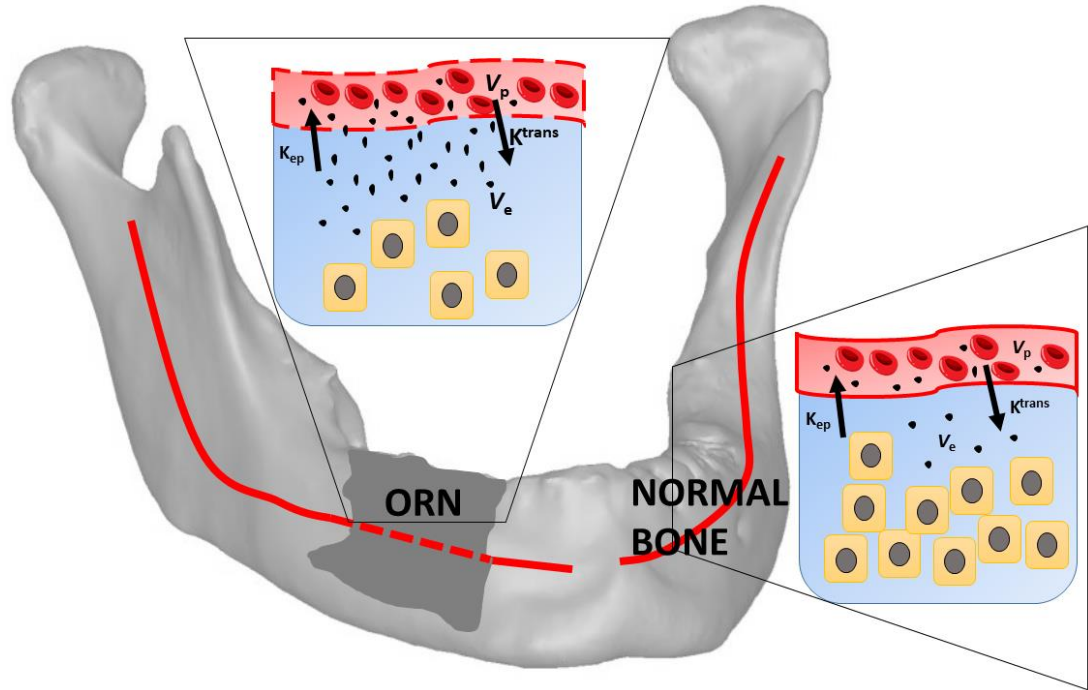
Figure 5. 5: Mechanistic vascular changes of ORN.

Schematic cartoon of the suggested mechanistic changes of ORN. Right mandibular body with

area of ORN and associated altered vascularity; contralateral body with normal body and

vascularity. Normal blood vessels have intact walls (continuous red lines) with well-regulated

fractional volume plasma (V_p) and appropriate contrast exchange (black dots) across the vessel

wall (K^{trans}) to extracellular extravascular compartment in blue (V_e) and normal mandibular

cellularity in yellow. Vessels associated with ORN demonstrate higher V_p with increased

leakiness (K^{trans}) through fragile vessels (dotted red lines) that leads to increased V_e and hypocellularity.

Our findings demonstrated a distinct profile of DCE-MRI parameter maps in mandibular volumes harboring ORN as compared to the normal mandible. DCE-MRI parameters indicating vascular compromise showed a significantly higher degree of leakiness in mandibular vasculature as measured using K^{trans} and V_e of areas affected with advanced grade of ORN versus healthy mandible. The fractional volume of plasma (V_p) was also higher in ORN-ROIs. We were able to measure significant increases in quantitative parameters with an average increase of approximately three-fold of both K^{trans} and V_e compared to values from the healthy mandibular bone. The vast majority of patients (90%) had at least doubling of the values of either K^{trans} or V_e for ORN-VOIs as compared with control VOIs. We also demonstrated a clear separation of parameter histogram distribution for the majority of patients with higher median and interquartile range of K^{trans}, V_e and V_p parameter values of ORN versus control VOIs as detailed in Appendix A. 1.

The quantitative perfusion characteristics of mandibular injury after radiation treatment of the head and neck cancer have never, to our knowledge, been assessed before. One study has previously investigated the qualitative nature of contrast enhancement of DCE-MRI in patients with mandibular ORN.(166) That study showed that all patients with ORN had marked contrast enhancement of the osteoradionecrotic bone marrow, which was reduced after treatment with HBO treatment.(166) DCE-MRI has also shown the ability to detect early-stage idiopathic osteonecrosis of the femur not otherwise visible on conventional MRI as reported by

Chan et al.(153) In addition, DCE-MRI parameters were also used to monitor bone healing secondary to trauma or fracture, as well as chronic changes in bone health associated with age-related osteoporotic changes.(154-156) DCE-MRI was also reported to identify changes related to the development of bony metastasis and tumor response to treatment.(170, 171)

We have recently demonstrated that DCE-MRI can be used to detect radiation-induced changes in mandibular bone vascularity and showed dose-dependent changes in both K^{trans} and V_e in a subset of patients.(158) Unlike the findings of our previous study that showed variability in the dose-dependent changes of vascular parameters where a percentage of patients had a decrease in the measured parameters after treatment, the current study demonstrated only an increase of these parameters. The increased fractional plasma and vascular leakiness in ORN areas reflects fragile vasculature that may be attributed to a process of neovascularization following the post-radiation chronic hypoxia in high-dose areas. A serial imaging study of the natural history of vascular changes of the mandible is currently ongoing to determine at which time point this phenomenon of neovascularization begins to develop and to what extent this development could be correlated with early ORN symptoms development. However, our findings suggest that a two-fold increase in either K^{trans} or V_e parameters is an alarming sign of ORN development if detected in patients with otherwise clinically apparent normal mandible after radiation treatment especially in areas exposed to higher doses of radiation due to tumor proximity.

Our group and others have previously demonstrated the dependency of DCE-MRI quantitative output on the nature of PK models used for analysis.(172, 173) Thereby, we used

the most widely accepted models such as Tofts and extended Tofts models. We also used the patients' contralateral mandible as an internal control to alleviate this model dependency. Additionally, we have recently shown, using multi-institutional comparison of patient-derived DCE-MRI data that quantitative values may not be reliably compared across different patients due to the difference in patient's specific imaging parameters, pre-processing, and post-processing factors.(172) Our results also confirmed that inter-patient DCE-MRI parameter variations were independent of the variation of the RT doses received by the ORN-VOIs as shown in Appendix A. 2. Because of this limitation, in the current study we did not use the absolute values of the parameters associated with ORN but instead compared the relative changes of these parameters to respective controls in the same image for each patient using the contralateral healthy mandibular VOIs. Therefore, our results may be more reproducible and generalizable as they represent the relative changes measured in the irradiated mandibular areas compared with the normal non-irradiated bony area and hence we avoided the inter-subject variability of the parameter absolute values.

The thirty patients included in this study may be perceived as a limited sample size. However, to date this represents the largest prospective quantitative imaging study of ORN ever reported. Furthermore, this study represents the initial characterization of quantitative vascular parameters driven from DCE-MRI for head and neck cancer patients treated with IMRT and affected by radiation-induced advanced ORN toxicity.

5.5 Conclusion

Our results confirmed higher degree of vascular leakiness in the mandibular areas of ORN as measured using DCE-MRI parameters as compared with healthy mandible. Additional efforts will be required to develop DCE-MRI parameter into viable non-invasive biomarkers useful for the early detection of subclinical cases of ORN.

Chapter 6: Methodology for analysis and reporting patterns of failure after radiation therapy

This chapter is based upon:

6.1 Introduction

Intensity-modulated radiation therapy (IMRT) is one of the most important innovations in modern radiation therapy and represents a paradigm shift in the treatment of head and neck cancers (HNCs). However, there are certain hazards that may increase the risk of loco-regional failure (defined as tumor persistence or recurrence) including inadequate definition of the tumor extension and clinically important target volumes (TVs), uncertainties related to daily positioning, weight loss or deformation of tumor and normal tissues during the course of treatment, and uncertainties in plan optimization, dose calculation and treatment delivery(25, 31-34).

The accurate and specific definition of the exact site of failure, in addition to the radiation dose given to this site is, therefore, mandatory to identify the possible cause(s) of failure. The classic definition of failures as "local", or "regional", was appropriate in the setting of

conventional radiotherapy using large homogeneous dose-volumes, but is no longer helpful nor descriptive of distinct types of failure in patients treated with IMRT(35-37).

Several previous efforts have addressed the importance of studying the patterns of failure after IMRT treatment of HNCs,(25, 32, 174-178) with most reporting failures as "infield", "marginal" or "outfield" based on the percentage of overlap between the failure volume and the respective TV on the treatment planning CT (pCT)(25, 174, 175, 177, 178).

The ability to accurately describe the relation of failure to original TVs and dose mandates a fairly precise method to co-register the diagnostic CT documenting recurrence (rCT) to the original pCT. However, the majority of the previous studies implemented mainly rigid image registration techniques (RIR)(25, 32, 175, 177, 178). RIR is simple, quick and widely used but it allows only for 6 degrees of freedom and doesn't account for changes in the shapes or relative positions of different regions-of-interests (ROIs)(179). Emerging data demonstrate the superiority of deformable image registration (DIR) compared to RIR in registering pCT to on-treatment CT or conebeam CT in the setting of image guided radiotherapy (IGRT) for HNCs(180-182). However, very few studies addressed DIR software implementation for the purpose of registering the diagnostic rCT to the original pCT(35, 36).

Our group has recently validated different registration techniques used for co-registering diagnostic contrast enhanced head and neck CT to non-contrast planning CT and showed DIR was superior for this application(183). As a continuation of these efforts and to validate DIR as a tool to improve accurate definition of the patterns of loco-regional failure in the era of IMRT for HNCs, we sought to undergo the following specific aims:

95

1) Develop a workflow methodology to standardize the analysis of HNCs patterns of failure using both geometric and dosimetric parameters.

2) Assess the impact of registration (rigid vs. deformable) techniques on patterns of failure quantitative analytic parameters.

3) Develop a granular classification and nomenclature to optimize the accurate reporting of distinct failure typology.

6.2 Material and Methods

6.2.1 Patients

Tumor registry data for patients diagnosed with head and neck squamous cell carcinoma, whom were treated by IMRT at The University of Texas, MD Anderson Cancer Center between 2006 and 2009, were retrospectively reviewed under an institutional review board approval. 600 patients were identified, of those 103 had a documented recurrence. A total of 21 cases were randomly selected from the recurrence dataset based on the following eligibility criteria: IMRT given for curative intent; treatment of intact tumor (i.e. post-operative cases were excluded); equal distribution of various head and neck subsites (i.e. nasopharynx, oropharynx, hypopharynx, and lateral neck "i.e. neck nodes of unknown primary site"); radiological evidence of local and/or regional failure; available CT scan of failure site prior to any salvage therapy; and pathologic and/or radiologic evidence of recurrence (i.e. biopsy, or high SUV on PET).

6.2.2 IMRT Treatment Planning and Delivery

All patients had been positioned supine in an individualized thermoplastic head and shoulder mask for CT simulation and treatment and a custom dental stent used as an intraoral immobilization device(184, 185). A treatment pCT scan was used for defining TVs. Target volume definition was done in Pinnacle treatment planning system (Pinnacle, Phillips Medical Systems, Andover, MA), with rigorous multi-physician target delineation and quality assurance(186, 187).

Treatment was uniformly delivered using Varian (Varian Medical Systems, Palo Alto, CA) linear accelerators delivering 6-MV photons. Three clinical target volumes (CTVs) were typically defined. CTV definitions and dose prescriptions are summarized in Table 6.1. Treatment was delivered in a conventional fractionation scheme (average 33 fractions). Patients were treated using a monoisocentric technique with an antero-posterior low-neck supraclavicular field matched to the IMRT fields or using whole neck IMRT for cases where gross nodes are located at the match line.

Table 6. 1: IMRT target volume definitions and dose prescription.

Target Volume	Definition	Dose prescription
High risk clinical target volume (CTV1)	gross tumor volume (GTV) plus margin, GTV included all known gross disease (primary tumor plus grossly enlarged lymph nodes)	66-69.96 Gy

	mucosal, bony, and nodal	
Intermediate risk clinical target volume (CTV2)	volumes at intermediate risk of harboring microscopic disease	57-63 Gy
Low risk clinical target volume (CTV3)	mucosal, bony, and nodal volumes at low risk of harboring microscopic disease	54-57 Gy
Planning Target Volume (PTV)	CTV plus 3-4 mm margin, with daily image guidance	

6.2.3 Post-treatment follow-up

Initial post-treatment evaluations were made at 8-12 weeks after therapy completion and subsequently every 2-3 months for the first year, every 3-4 months for the second year, and at least twice a year up to 5 years.

6.2.4 Loco-regional Failure

Cases where local and/or regional recurrence was recorded had their immediate post-failure diagnostic images exported as DICOM files from the clinical PACS system to the treatment planning system, where radiological evident recurrent gross disease (rGTV) was manually contoured by a radiation oncologist (ASRM) and reviewed by a head and neck service-specific attending radiation oncologist (CDF).

6.2.5 Image registration

For each patient, the rCT or rPET-CT was co-registered with pCT using both rigid and deformable image registration techniques. DIR was performed using a commercial software (ADMIRE, Elekta AB, 2015) validated previously by our group for the registration of contrast-enhanced diagnostic CT to non-contrast enhanced planning CT(183). Deformation vector fields were obtained from DIR algorithm, mapping the deformation of the rCT onto the pCT.

Subsequently, in a custom written Matlab routine (MATLAB R2013a, The MathWorks Inc., Natick, MA, 2013), pCT; dose grid; original plan TVs; rCT; and rGTVs were imported. The deformation fields were then applied to rGTVs segmented on the rCT to convert them into 'deformed rGTVs' on the pCT.

Evaluation of deformed rGTVs relative to original planning TVs was done using both centroid-based method that assumed the center of mass of rGTV was the origin of the recurrence volume and its location was compared relative to planning TV after applying deformation vector fields (DVF). Simultaneously, RIR was performed using the rigid co-registration tool available in the Pinnacle planning system to rigidly align rCT to pCT, following that rGTVs where exported to patient's plan where dose volume histograms (DVHs) and rGTV centroids were generated and analysis metrics were calculated. Figure 6.1 illustrates the workflow process of our registration methodology.
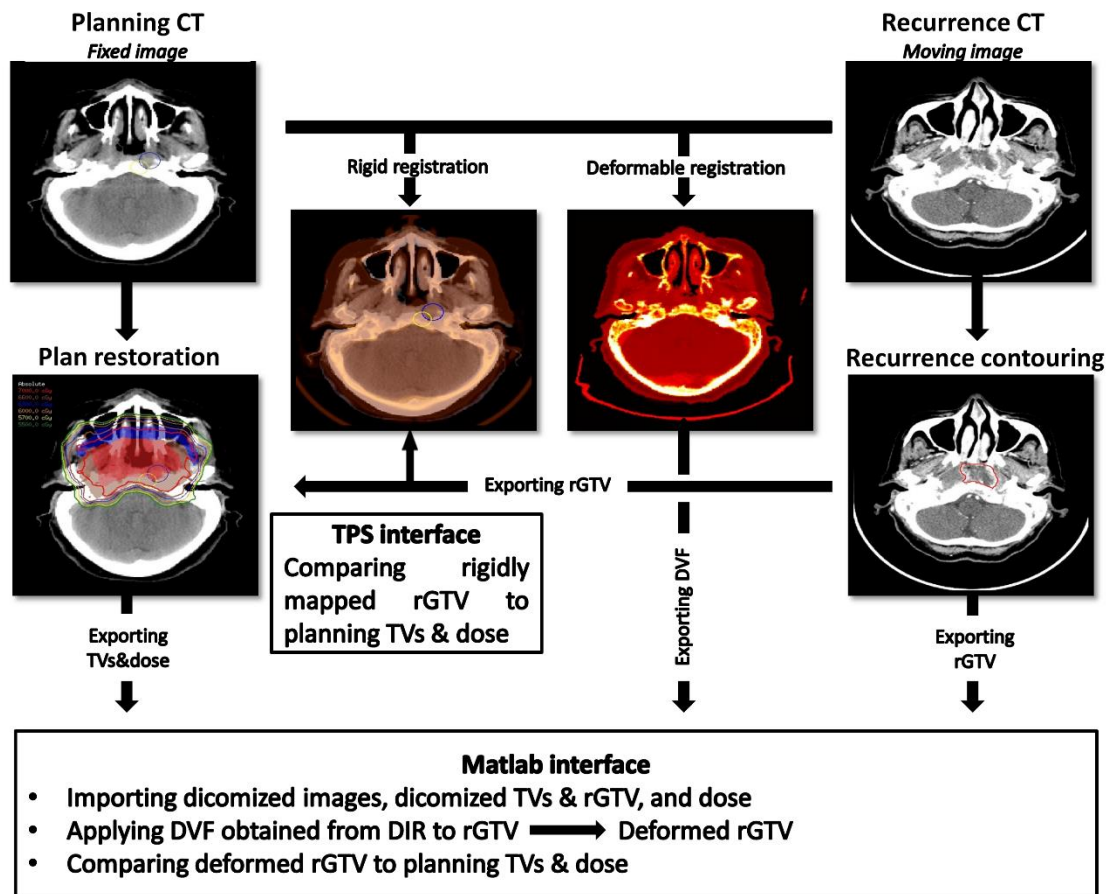
Figure 6. 1: Workflow process of patterns of loco-regional failure registration process.

6.2.6 Analysis of failure metrics

For both RIR and DIR mapped rGTVs the following metrics were evaluated:

1) Recurrence volume, 2) Location of the centroid relative to planning TV: Centroid is the

central voxel of the recurrence volume plus added 2mm margin to account for registration error,

3) Spatial relationship of rGTV centroids to IMRT/supraclavicular match line and ipsilateral

100

parotid in case of peri-parotid failure, and 4) Mean and maximum dose to rGTVs, dose to 95%

failure volume (fD95%), and mean dose to centroid volume.

6.2.7 Classification of failure

In order to refine our reporting and quality assurance practices using a standard

nomenclature, we developed a granular typology of failure categories relative to the planning

TV and dose. As illustrated in Figure 6.2, failures were classified into five types based on

combined spatial and dosimetric criteria:

- Type A: Central high dose failure, where the mapped failure centroid originates in high

  dose TV and the dose to 95% failure volume (fD95%) is ≥95% dose prescribed to

  corresponding TV of origin.

- Type B: Peripheral high dose failure, where the mapped failure centroid originates from

  high dose TV but its fD95% receives <95% dose prescribed to this TV.

- Type C: Central elective dose failure, where the failure centroid originates from elective

  dose TV and its fD95% receives ≥95% dose prescribed to the respective TV.

- Type D: Peripheral elective dose failure, where the failure centroid originates from

  elective dose TV and its fD95% receives <95% dose prescribed to the respective TV.

- Type E: Extraneous dose failure, where the failure centroid originates outside all TVs.

For patients treated with low-neck supraclavicular field matched to the IMRT fields, two

additional types were added:

- Type F: Junctional failures at the site of IMRT/supraclavicular match line.

- Type G: Low neck failures at the site of low-neck supraclavicular field.

Type of failure	A. Central high dose failure	B. Peripheral high dose failure	C. Central elective dose failure	D. Peripheral elective dose failure	E. Extraneous dose failure
Traditional/historic nomenclature	• "Full hit"/"In-field"	• "Partial hit"/ "Marginal"	• "In-field"	• "Partial hit"/ "Marginal"	• "Full miss"/ "Out of field"
Centroid location of origin	• High dose TV	• High dose TV	• Intermediate or low dose TV	• Intermediate or low dose TV	• Outside all TVs
Dose to 95% failure volume (fD95%)	• ≥95% of the dose prescribed to TV of origin	• <95% of the dose prescribed to TV of origin	• ≥95% of the dose prescribed to TV of origin	• <95% of the dose prescribed to TV of origin	• N/A
Possible causes of failure	• Biological failure	• Target delineation error • Dosimetric failure • Overgrown recurrence (rapidly progressive disease or neglected late diagnosed recurrence)	• Improper risk assessment	• Target delineation error • Dosimetric failure • Overgrown recurrence (rapidly progressive disease or neglected late diagnosed recurrence)	• Improper risk assessment • Aberrant areas of recurrence
Potential technical interventions	• Non-technical/non-operator dependent	• Increase CTV1 margin • QA target delineation • QA dose delivery • Increase surveillance frequency	• Prescribing higher doses (shifting to higher CTV levels)	• Increase CTV2/CTV3 margin • QA target delineation • QA dose delivery • Increase surveillance frequency	• Non-technical/non-operator dependent

Figure 6. 2: Classification scheme of IMRT patterns of failure

This diagram illustrates the classification of the patterns of failure using combined centroid based geometric method coupled with the dosimetric parameters.

6.2.8 Statistical analysis

Non parametric statistics were used to compare analysis metrics for centroid locations and dosimetric parameters of failures mapped using RIR versus DIR registration techniques. A

p-value ≤ 0.05 was deemed significant. Statistical assessment and data tabulation was performed using JMP v 11Pro (SAS institute, Cary, NC).

6.3 Results
6.3.1 Patients

A total of 21 patients with HNSCC were included in this pilot methodology/workflow development study. Median age was 58 years (range 30-75), and 86% were men. Patient, disease, and treatment characteristics are presented in table 6.2. Recurrences were delineated using diagnostic contrast-enhanced CT in 16 patients and using PET-CT in 5 patients.

Table 6. 2: Patient demographics, disease, and treatment characteristics

Characteristic	Total	
	n=21	(%)
Age (years)		
Median	58	
Range	30-75	
Time to Failure (months)		
Median	12	
Range	5-69	
Sex		
Male	18	(86)
Female	3	(14)
Origin		
Nasopharynx	6	(28)
Oropharynx	5	(24)
Hypopharynx	5	(24)
Unknown primary	5	(24)
T-category		
T0	5	(24)
T1	1	(5)
T2	7	(33)
T3	5	(24)
T4	3	(14)
N-category		
N0	1	(5)
N1	5	(24)

N2	12	(57)
N3	3	(14)
Treatment		
Radiation alone	4	(19)
Concurrent ChemoRadiation	9	(43)
Induction Chemotherapy + Radiation	1	(5)
Induction Chemotherapy + Concurrent ChemoRadiation	7	(33)
Radiation dose		
Mean (SD)	69.2	(1.7)
Radiation fractions		
Mean (SD)	33	(2)

6.3.2 Spatial/dosimetric failure mapping

6.3.2.1 Spatial mapping

A total number of 26 rGTVs were delineated. Mean rGTVs volume was 12.5 cm^3 (range 1-105). The registration method independently affected the spatial location of mapped failures. Failures mapped using DIR were significantly assigned to more central TVs compared to failures mapped using RIR. 38% of centroids (n= 10) mapped using RIR were located peripheral to the same centroids mapped using DIR (p= 0.0002). Table 6.3 illustrates the sites and geometric details of all failures mapped to the pCT.

Table 6. 3: Geometric details of failed rGTVs.

	n.	(%)
N. of recurrences	26	
Recurrence Volume		
Mean (SD)	12.5	(23)
Location of centroid using		
RIR		
GTV	12	(46)
CTV1	7	(27)
CTV2	1	(4)
CTV3	1	(4)
PTV1	4	(15)
Supraclavicular field	1	(4)

Location of centroid using DIR		
GTV	22	(84)
CTV1	1	(4)
CTV2	1	(4)
CTV3	1	(4)
Supraclavicular field	1	(4)

Abbreviations: NPX = DIR = Deformable image registration, RR = Rigid Registration, GTV= gross tumor volume, CTV= clinical target volume, PTV= planning target volume.

6.3.2.2 Dosimetric mapping

rGTVs mapped using DIR had statistically significant higher mean doses when compared to rGTVs mapped rigidly (mean dose 70 vs. 69 Gy, p = 0.03) while comparison of mean fD95% was not statistically significant (mean fD95% 68 vs. 66 Gy, p = 0.07), and comparison of maximum, and centroid doses showed no-significant differences between both registration methods (p = 0.7 and 0.4, respectively). Table 6.4 shows the dosimetric details of all failures.

Table 6. 4: Dosimetric patterns of failure.

rGTVs dose metrics using RIR	**Mean Dose in Gy. (SD)**
Mean	69 (6)
fD95%	66 (7)
Max.	71 (6)
Centroid	69 (6)
rGTVs dose metrics using DIR	
Mean	70 (5)
fD95%	68 (6)
Max.	72 (5)
Centroid	70 (5)

Abbreviations: DIR = Deformable image registration, RIR = Rigid Image Registration, fD95%= Dose to the 95% failure volume, Max.=Maximum, SD= standard deviation.

6.3.3 Classification of failure

Based on the proposed classification of failure using both the spatial location of the centroids of the mapped failure volumes coupled with the dosimetric parameters (as illustrated

105

in Figure 6.2), 22 (84.6%) out of the 26 failures mapped using DIR were of type A, one of type

B, 2 of type C, and one of type G. Whereas, 18 (69%) out of the 26 failure mapped using RIR

were of type A, 5 of type B, 2 of type C and one of type G. Figure 6.3 illustrates the difference

in classification using both registration methods. There was no type F (junctional) failures in

patient subset treated using anteroposterior low-neck supraclavicular field matched to the IMRT

fields. Additionally, no peri-parotid failures were detected.

Failure Classification

Type A   Type B   Type C   Type G

RIR	18	5	2 1
DIR	22	1 2 1	
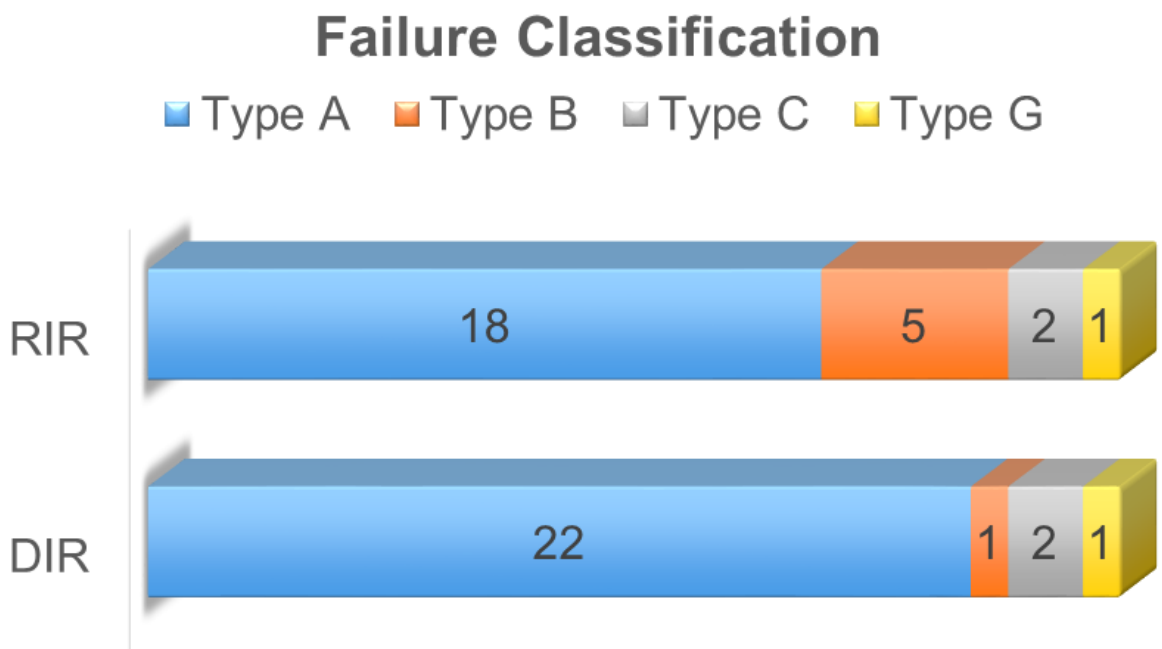
Figure 6. 3: Bar chart of the differences in failure classification.

Bar chart illustrating the difference in failure classification using rigid (RIR) vs. deformable (DIR)

image registration methods.

This combined spatial/dosimetric analysis shows that while 10 centroids (38%) of RIR mapped rGTVs were located peripheral to the same centroids mapped using DIR as shown in Table 6.3. However, after adding the dosimetric component of analysis, only 4 of those 10 RIR mapped rGTVs were peripheral high dose failures (type B) and the other 6 were central high dose failure (type A) because despite the centroids were spatially peripheral in location to the respective DIR ones but dosimetrically, the rGTVs 95% volumes still had ≥95% dose. Figure 6.4 shows an example of the differences in spatial and dosimetric parameters for a DIR versus RIR mapped failure. Those 4 rGTVs were seen in the following patients: two nasopharyngeal (one primary "Figure 6.4" and one nodal site); one oropharyngeal (primary site); and one unkown primary (nodal site). The secondary qualitative review by expert radiation oncologists (CDF, DIR) of those 4 patients agreed with DIR classification that those recurrences are actually central rather than peripheral in origin.
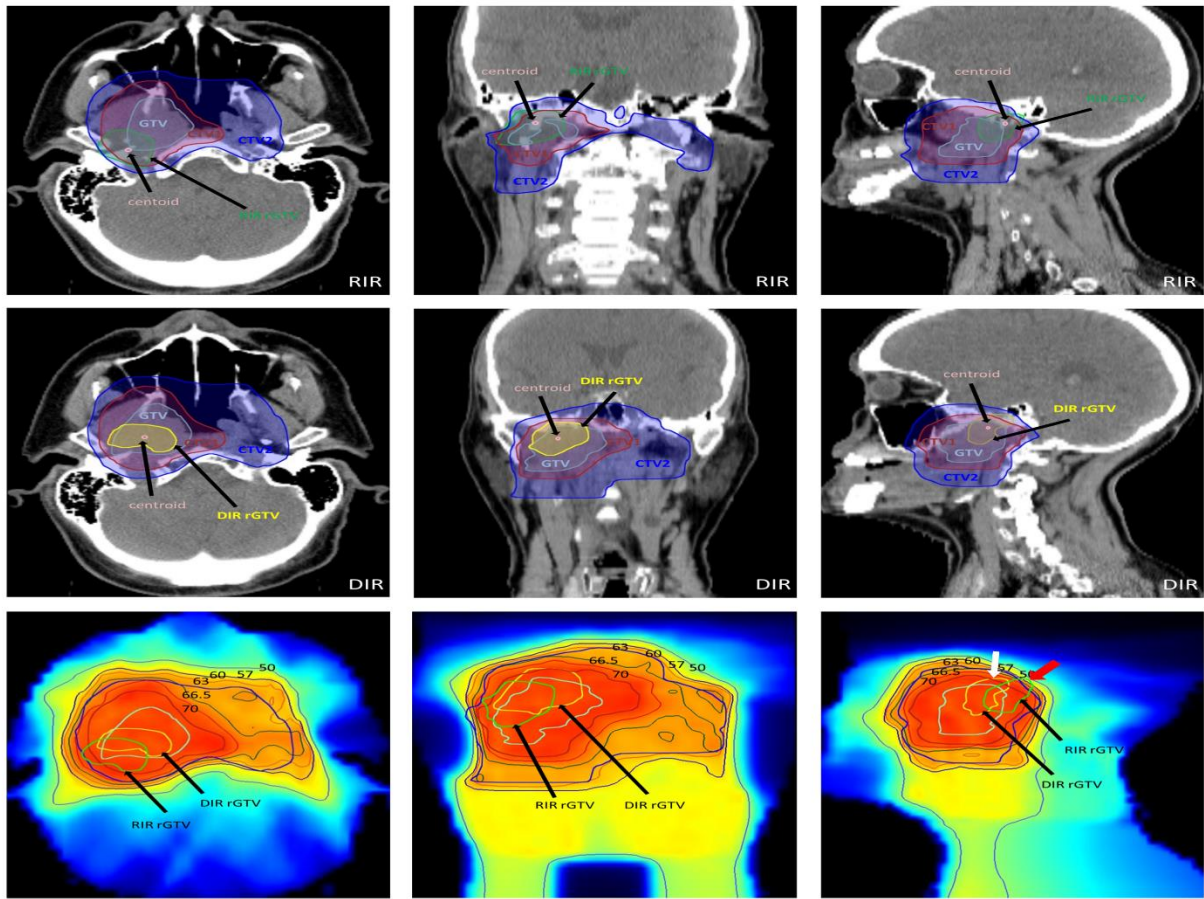
Figure 6. 4: A case illustration.

A case of T2N0 Nasopharyngeal carcinoma recurred 63 months after IMRT. The upper panel

shows the axial, coronal and sagittal images of a RIR mapped rGTV on the original pCT where

its centroid is located at CTV1and the 95% rGTV volume contained on more peripheral PTV2

(contour not shown). The middle panel shows DIR mapped rGTV on the original pCT where its

centroid located at GTV and the 95% rGTV volume contained on more peripheral CTV2. The

lower panel shows RIR and DIR mapped rGTVs overlaid to plan isodose line. Note that RIR

rGTV fD95% extends beyond the 95% isodose line "66.5 Gy" (red arrow in sagittal image) which would erroneously characterize it as type B failure, while in fact DIR shows it as a type A failure (i.e. the fD95% of DIR mapped rGTV is completely encapsulated with 95% isodose line, shown by white arrow in sagittal image).

6.4 Discussion

Traditionally, failure reporting for HNCs has simply classified disease as "local", "regional", or "locoregional", thus relating location of failure to a crude anatomic reference. However, such a reporting language gives no information regarding radiation fields/volumes or delivered dose. In the pre-IMRT era, when large fields of homogenous dose were used, the definition of "in-field" failure (i.e. within the field borders) or "marginal" failure (i.e. adjacent to the block edges) were intuitive descriptors relating treatment parameters to sites of failure. However, in the current era of conformal therapy(188, 189), dose gradients, and multiple TVs make relating spatially accurate information about dose and recurrence far more complicated for IMRT plans. In the same way that a standardized method for analysis and reporting for TVs has been undertaken successfully (188-190), a similar effort is desirable for pattern of failure reporting. In our opinion, reporting failure using only anatomic/field referents is insufficient for complex multi-volume/multi-dose plans, and obscures clinically useful information which might lead to improvements in future studies.

Likewise, the requirement of rigorous assurance for correctly localizing disease after-therapy is increased in terms of required spatial accuracy. The steep dose gradients of modern IMRT plans and proximate transition from high-risk CTVs to intermediate- or lower-risk CTVs

109

implies inaccurate registration will erroneously assign the location of failure to incorrect dose/prescription volume. We, in fact, show RIR for IMRT plans resulted in incorrect localization relative to prior TVs and dose in 16% of failures in the current pilot dataset. Consequently, this study presents a methodology and workflow that involves the application of quality assured DIR software as a tool to standardize co-registration and to correctly attribute sites of loco-regional failure.

Almost all previous studies have used RIR to describe the patterns of loco-regional failure after IMRT(32, 175, 177, 178). Chao *et al* (175) reported 17/126 loco-regional failures treated by definitive or postoperative IMRT; 53% of failures were inside CTV1, 12% marginal to CTV1, 6% marginal to CTV2, and 28% were out of field. Eisbruch et al (32) reported on 21 recurrences in 133 patients with non-nasopharyngeal HNCs treated with parotid-sparing IMRT; 17/21 were in-field. Daly et al (177) reported on 69 HNCs treated with parotid-sparing IMRT; 8 patients developed a loco-regional failure, 7 relapsed within the high-dose CTV, with one junctional failure observed. Sanguineti et al (178) described the patterns of failure for 50 patients with IMRT for oropharyngeal SCC; 5 recurrences were related to high dose regions while 4 were at the low dose regions. All these reports relied on RIR, known to be less spatially accurate than DIR(183); it is conceivable these results might be altered if DIR methods were used. Due et al(36) reported that DIR showed slightly better reproducibility in identification of the site of recurrence origin compared to RIR. Our previous work(183), as well as the current study, confirm the qualitative superiority, in HNC applications, of DIR for CT-CT registration.

In our classification scheme, we designed a combined geometric/dosimetric typology definition to avoid the drawbacks of using each method separately. Centroid only method suppose a single point of origin and ignore the dose given to the whole area of recurrence while the dosimetric only analysis is agnostic to the geometric recurrence origin. Due et al(36) previously reported that focal methods, such as the centroid method we used, are more accurate to localize the origins of loco-regional recurrences than volume overlap methods, which may incorrectly assign recurrences to more peripheral TVs. Raktoe et al(37) further confirmed the superiority of focal methods like centroid expansion to the volumetric method in identifying the origin of loco-regional recurrences. The combined method we used identify the estimated site of recurrence origin relative to the respective TV in the planning CT and then compare the dose to the mapped recurrence volume with the dose prescribed to the TV of origin. Using this method, our results showed that DIR significantly assigned failures to more central TVs and doses compared to RIR concordant with the results of Due et al.(36).

Our proposed nomenclature allows granular reporting of different types of failure. In our classification, type A "central high dose" failures, are considered to be biological failures, as they likely represent resistance to maximal therapy, and thus could not conceivably be prevented by technical/operator dependant processes including IMRT QA or delineation alteration. Type A failures motivate future investigation of alternative treatment stratgies (e.g. integration of novel targeted drug therapies or dose escalation to identifiable biologically aggressive subvolumes). Likewise, type E "extraneous dose" failures cannot be modified by IMRT QA processes. They represent a possible diagnostic or decision error rather than a target

delineation error (i.e. "One will never hit what one does not aim at."). However, type B, C, and D failures are of a special concern since they entail potential technical or radiotherapy process failures. Type C "central elective (intermediate or low) dose" failures may be prevented by prescribing higher doses (i.e. shifting to higher CTV levels). Importantly, type B "peripheral high dose" or D "peripheral elective dose" failures necessitate a rigorous QA process including triple DIR registration of pre-therapy diagnostic imaging (diagnostic CT, MRI, and/or PET-CT) to pCT and the earliest rCT, to assess the potential causes: potential target delineation or dose delivery error (modifiable) versus overgrown recurrence that represents actual type A or C failure which is converted to type B or D, respectively, due to rapidly progressive disease or neglected late diagnosed recurrence (not modifiable). This involves multi-physician review of planning and recurrence contours, and review of IGRT data (i.e. set-up error, adaptive replanning datasets), as well as examination of the follow-up interval between surveillance images. By cataloging type B/D errors, we can then address the relevant issues dynamically for future patients. For instance, the only type B patient (i.e. using DIR methodology), was noted on secondary review of diagnostic imaging to have subsequent intracranial extension, route of failure, despite optimum delineation and dose coverage.

The secondary qualitative review by expert radiation oncologists (CDF, DIR) of all the clinical and imaging data of the four additional recurrences that were classified as peripheral high dose (type B) using RIR while were type A using DIR, concurred with DIR classification that those recurrences are actually central rather than peripheral in origin.

In this dataset, our results showed the majority (84.6%) of DIR mapped failures were of type A indicating, that biological, non-technically/non-operator dependant explanations for failure predominated. However, using RIR type A failures would have been erroneously reported as comprising only 69%. These results assert the need for a robust, quality assured image registration technique, as error in the registration process would invalidate subsequent results and thus might deceptively indicate a greater rate of technical/operator-attributable therapy failures than DIR demonstrates. The current study, while underpowered to make clinical extrapolations due to limited number of patients, nonetheless serves as a benchmark to describe our standardized analytic and reporting method. Already, RTOG 1216, for example, contains provisions regarding collection of imaging data post-failure(191), which will allow careful analysis, and process quality improvement for future trials and large scale datasets.

6.5 Conclusions

Rigid image registration method tends to assign failures more peripherally compared with deformable method. Using DIR, the vast majority of failures in the presented pilot study originated in the high dose target volumes and received full prescribed doses suggesting biological rather than technology-related causes of failure. We heavily recommend a validated DIR-based registration technique in addition to granular combined geometric- and dosimetric-based failure characterization using novel typology-indicative taxonomy as a standard part of large-scale patterns of failure reporting in the IMRT era.

Chapter 7: Patterns of locoregional failure following post-operative intensity-modulated radiotherapy

This chapter is based upon:

Mohamed ASR, Wong AJ, Fuller CD, Kamal M, Gunn GB, Phan J, Morrison WH, Beadle BM, Skinner H, Lai SY, Quinlan-Davidson SR, Belal AM, El-Gowily AG, Frank SJ, Rosenthal DI, Garden AS. Patterns of locoregional failure following post-operative intensity-modulated radiotherapy to oral cavity cancer: quantitative spatial and dosimetric analysis using a deformable image registration workflow. Radiat Oncol. 2017 Aug 15;12(1):129. doi: 10.1186/s13014-017-0868-y. PMID: 28806994; PMCID: PMC5557312.

7.1 Introduction

Surgery is often the treatment of choice for oral cavity squamous cell carcinoma (OCSCC). Post-operative radiotherapy is indicated for OCSCC of advanced stages or with adverse prognostic factors(192-194). Intensity-modulated radiotherapy (IMRT) enables conformal therapy and reduction of complications to surrounding normal tissue, and for many centers has become the standard radiation approach for head and neck cancer(195).

Generally, OCSCC patients demonstrate relatively worse loco-regional control compared to other head and neck subsites (e.g. oropharynx and larynx).(196-198) Studies that have specifically examined cohorts of OCSCC patients receiving postoperative IMRT (PO-

IMRT) have consistently reported only fair locoregional control rates, as low as 53% at 3 years in some series(199-204).

Moreover, most report failures as "infield", "marginal", or "outfield" based on percentage overlap between failure volume and respective target volumes. However, these studies applied non-uniform spatial methods for failure analysis, mainly utilizing non-validated rigid or manual image registration tools and without including the dosimetric component in the analysis(199-204). We have recently shown the potential impact of patterns of failure analysis methodology using a validated image registration software paired with combined spatial and dosimetric analysis of failure, in improving the accuracy of reporting the patterns of failure in the era of IMRT(205-207). As a continuation of these efforts we sought to apply this unique analytic methodology to our institutional large scale oral cavity cancer dataset of patients receiving PO-IMRT with documented treatment failure to achieve the following specific aims: 1) characterize distinct spatial and dosimetric patterns of failure after PO-IMRT, 2) identify clinical risk features associated with each failure type, 3) identify patterns of failure based target volume contouring recommendations, and 4) generate hypotheses for future clinical trials.

7.2 Material and Methods
7.2.1 Patient Selection

Two hundred eighty-nine patients with pathological diagnosis of OCC who received PO-IMRT at the University of Texas MD Anderson Cancer Center from 2000-2012 were retrospectively reviewed under an approved institutional review board protocol. Patients with distant metastases or concurrent malignancies at the time of diagnosis, or treatment with chemotherapy prior to staging at MDACC were excluded. Patients with prove of recurrence

after PO-IMRT with available imaging documenting recurrence were included in the current analysis.

7.2.2 Treatment Planning and Delivery

Treatment planning and delivery is described in details in previously published work, which examines the outcomes for this same patient cohort.(208)

7.2.3 Clinical Data Collection

Diagnostic contrast-enhanced CT and/or PET/CT documenting the initial evidence of local and/or regional recurrence (rCT) was identified. Recurrences were confirmed via radiologic imaging (i.e. progression in subsequent CT imaging or high SUV on PET imaging) or pathology specimens (i.e. from surgical biopsy). Radiologically evident recurrent gross disease (rGTV) was manually segmented and reviewed by two experienced radiation oncologists (ASRM, CDF). Corresponding original planning CTs (pCT) were also identified and original plans were restored. Patient, disease, and treatment characteristics were gathered during chart review.

7.2.4 Image Registration and Dosimetric Analysis

rCT was co-registered with pCT using a previously validated deformable image registration (DIR) methodology (VelocityAI 3.0.1, Velocity Medical Solutions, Atlanta, GA, 2004-2013). (205, 206) rGTVs on the rCT were subsequently deformed to co-registered pCT (Figure 7.1). The centroid, assumed as the origin of tumor recurrence, is represented as the calculated center of mass of the deformed rGTV. Dosimetric and volumetric parameters were obtained from the dose-volume histogram.
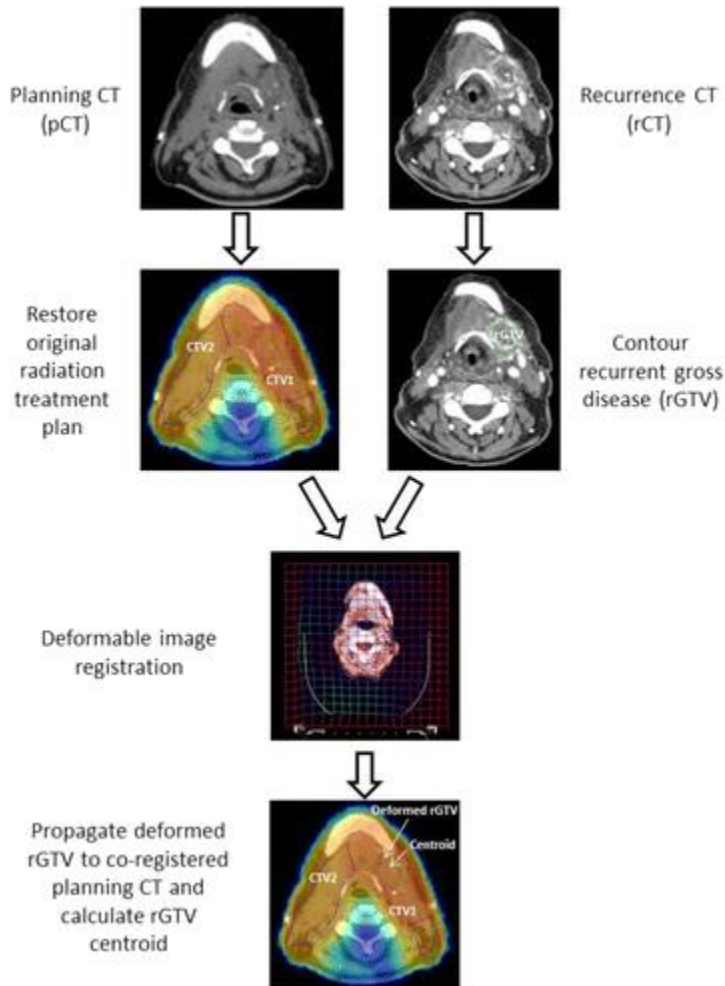
Figure 7. 1: Study workflow.

7.2.5 Patterns of Failure Classification

Failures are classified according to both spatial and dosimetric criteria as previously

described. (207) Briefly, for spatial mapping of recurrence origin, the centroid of each rGTV

was mapped to the corresponding TV in the planning CT. Subsequently, the dosimetric

characteristics were assessed by calculating the dose to 95% of the failure volume (fD95%)

then comparing it relative to the dose prescribed to the corresponding TV of origin as

117

determined by the spatial mapping. Finally, failures were classified into five major types: Type A (central high dose where the mapped failure centroid originates in high dose TV and fD95% is ≥95% dose prescribed to corresponding high dose TV of origin), Type B (peripheral high dose where the failure centroid originates from high dose TV but its fD95% is <95 % dose prescribed to corresponding high dose TV of origin), Type C (central elective dose where the failure centroid originates in lower dose TV and fD95% is ≥95% dose prescribed to corresponding lower dose TV of origin), Type D (peripheral elective dose where the failure centroid originates in lower dose TV but the fD95% is <95% dose prescribed to corresponding lower dose TV of origin), and Type E (extraneous dose where rGTV centroid originates outside all TVs). Type F describes junctional failures at the IMRT/supraclavicular match line, and Type G describes low neck failures at the low-neck supraclavicular field. Type G is analogous to type C if the fD95% is ≥95% dose prescribed to the low-neck and analogous to type D if the fD95% is <95%. Examples demonstrating failure type definitions are illustrated in Figure 7.2.
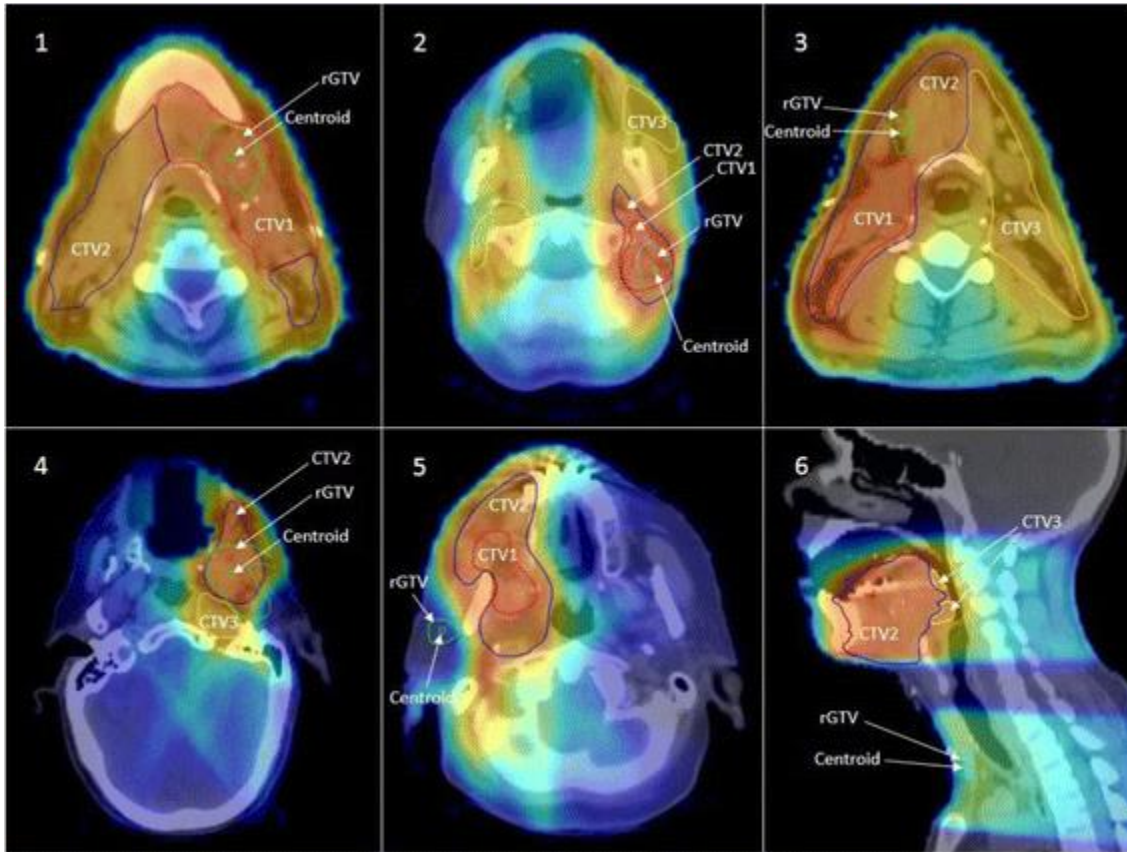
Figure 7. 2: Examples of Failure Types.

1) Type A (central high dose) failures. Centroid is mapped inside high dose TV and dose to 95% rGTV volume ≥ 95% dose prescribed to high dose TV. 2) Type B (peripheral high dose) failure. Centroid is mapped inside high dose TV, but dose to 95% rGTV volume < 95% dose prescribed to high dose TV. 3) Type C-int (central intermediate dose) failure. Centroid is mapped inside intermediate dose TV and dose to 95% rGTV volume ≥ 95% dose prescribed to intermediate dose TV. 4) Type D-int (peripheral intermediate dose) failure. Centroid is mapped inside intermediate dose TV but dose to 95% rGTV volume < 95% dose prescribed to intermediate dose TV. 5) Type E (Extraneous dose failure) where rGTV centroid originates

119

outside all TVs. 6) Type G (low neck failure) where rGTV centroid is located at the low-neck

supraclavicular field.

Patients were then classified according to the predominant mode of failure. Patients

with more than single recurrence lesion were classified as the following: 1) for patients with

type A recurrence and concurrent non-type A lesions, the overall pattern of failure was defined

as type A because we believe type A for such patients is the true recurrence rather than

reseeding from the non-type A recurrence, 2) for patients whom exhibited more than one failure

type of non-type A simultaneously, pattern of failure of each patient was classified according to

the predominant type as determined by the most commonly encountered failure type (i.e.

higher number or higher volume).

7.3 Results
7.3.1 Patient and Treatment Characteristics

Sixty-three patients (22%) developed locoregional recurrences. Median time to

recurrence was 4 months (range 0 – 71). For spatial and dosimetric analysis of the patterns of

failure, 9 patients were excluded: 4 with post-surgical recurrence prior to initiation of IMRT, 3

with no retrievable IMRT plan, and 2 with no available imaging documenting recurrence. This

left 54 patients for the current analysis.

Patient, disease, and treatment characteristics for the analyzed 54 patients are

summarized in Table 7.1. The most common primary site was the oral tongue (39%). The most

common pathologic T and N staging were T2 (37%) and N2 (36%). Forty-seven (87%) patients

had Stage III-IV disease.

Table 7. 1: Patient, Disease, and Treatment Characteristics.

Characteristic	N (%)
Age	
Median (range)	59.5 years (22-87)
Gender	
Female	20 (37)
Male	34 (63)
Tumor Site	
Oral Tongue	21 (39)
Buccal Mucosa	10 (18.5)
Floor of Mouth	2 (4)
Hard Palate	3 (5)
Gingiva	10 (18.5)
Retromolar Trigone	8 (15)
Histologic Differentiation	
Poor	13 (24)
Moderate	36 (67)
Well	5 (9)
Clinical T stage	
T1	8 (15)
T2	19 (35)
T3	9 (17)
T4	18 (33)
Clinical N stage	
Nx	2 (4)
N0	23 (43)
N1	11 (20)
N2a	0 (0)
N2b	14 (26)
N2c	4 (7)
Pathological T stage	
ypT0	2 (4)
T1	8 (15)
T2	20 (37)

T3	7 (13)
T4	17 (31)
Pathological N stage	
No dissection	7 (13)
N0	12 (22)
N1	12 (22)
N2a	0 (0)
N2b	19 (36)
N2c	4 (7)
Overall stage	
Stage I	1 (2)
Stage II	6 (11)
Stage III	7 (13)
Stage IV	40 (74)
Primary Surgery Margin Status	
Negative (>5 mm)	41 (76)
Close (≤ 5 mm)	9 (17)
Positive	4 (7)
Depth of invasion	
≤1.5 cm	33 (61)
>1.5 cm	18 (33)
Unspecified	3 (6)
Perineural invasion	
Yes	22 (41)
No	32 (59)
Lymphovascular invasion	
Yes	14 (26)
No	30 (56)
Unspecified	10 (18)
Extracapsular extension	
Yes	17 (31)
No	37 (69)
IMRT dose and fractionation	
Median Dose (Range), in Gy	60 (56-70)
Median Fractionation (Range)	30 (28-33)
Laterality of Neck radiation	

Unilateral	13 (24)
Bilateral	41 (76)
Chemotherapy	
Induction	5 (9)
Concurrent	13 (24)
Induction and concurrent	2 (4)
No chemotherapy	32 (59)

Surgical margins were positive and close (defined as ≤5 mm) in 4 (7%) and 9 (17%) patients, respectively. Perineural invasion or lymphovascular invasion was present in 22 (41%) and 14 (26%) patients, respectively. Depth of invasion was ≥1.5 cm in 18 patients (33%). Forty-seven patients (87%) had neck dissections, and of those 17 patients had nodal extracapsular extension.

Mean RT dose was 60±7 Gy and mean number of fractions was 30±3. One patient did not complete the full course of IMRT, discontinuing therapy after 6 fractions. Thirteen (24%) and 41 (76%) patients received unilateral and bilateral neck irradiation, respectively. Mean overall treatment package time, defined as time interval from date of surgery to last day of irradiation, was 12.3±1.7 weeks.

7.3.2 Recurrence Characteristics

For patients included in the current analysis; 26 (48%) had local recurrence, 19 (35%) had regional recurrence, and 9 (17%) had both local and regional recurrence. A total of 82 rGTVs were delineated. Median rGTVs volume was 3.7 cm^3 (IQR 1.4-10.6). Figure 7.3 shows the distribution of the predominant type of failure for the entire dataset using the proposed classification schema. Thirty patients (55.5%) were classified as type A. Non-type A failures

123

were distributed as follows: 2 (3.7%) type B, 10 (18.5%) type C, 1 (1.8%) type D, 9 (16.7%) type E, and 2 (3.7%) type G. Because type A "central high dose" failures, are considered to resistance to maximal therapy, and thus could not conceivably be prevented by technical/operator dependent processes, however, non-type A failures represent a major goal for IMRT quality assurance and improvement. Table 7.2 illustrates the details of the characteristics for all non-type A failures.
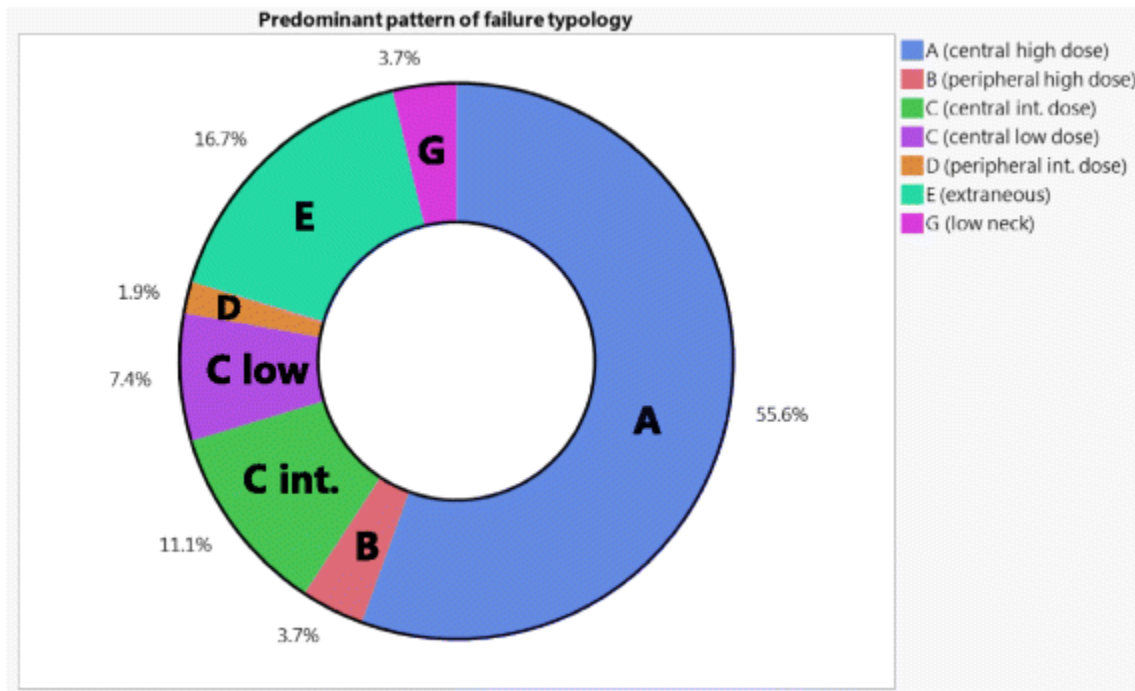
Figure 7. 3: Ring chart of the predominant typology of failure.

Table 7. 2: Failure Sites for non-type A Failures.

Pa tie nt	Local vs Region al	Predomina nt Failure Type	Primary Tumor Site	Patholog ic TN Stage	Surgic al margin s	Neck dissection status and laterality	ECE	Neck Irradiati on Laterali ty	DOI	PNI	LVI	Chem other apy	CTV1 Dose (Gy/n. of Fracions)	Failure Site

1	L	B (peripheral high dose)	gingiva	T2N0	-ve	-ve Ipsilat	-ve	Ipsilat	≤1.5 cm	+ve	-ve	No	60/30	Ipsilat RMT&Maxilla
2	L	B (peripheral high dose)	FOM	T1N2c	-ve	+ve Bilat	+ve	Bilat	>1.5 cm	-ve	-ve	No	13/6†	FOM
3	L	C (central int. dose)	RMT	yT4ayN0	-ve	-ve Ipsilat	-ve	Bilat	≤1.5 cm	-ve	U/S	I+C	60/30	Ipsilat Masticator Space
4	L	C (central int. dose)	tongue	T4aN2b	-ve	+ve Bilat	-ve	Bilat	>1.5 cm	-ve	-ve	No	60/30	FOM
5	L	C (central int. dose)	FOM	T4aN1	-ve	+ve Bilat	-ve	Bilat	>1.5 cm	-ve	-ve	No	60/30	BOT
6	L	A*	RMT	T4aN1	+ve	+ve Ipsilat	-ve	Ipsilat	>1.5 cm	+ve	-ve	No	70/33	Flap recurrence + Ipsilat Parotid &Masticator Space
7	L	D (peripheral int. dose)	gingiva	T4aN1	+ve	+ve Ipsilat	-ve	Bilat	≤1.5 cm	+ve	+ve	No	63/30	Ipsilat Masticator Space
8	L	E (extraneous)	FOM	T1N1	-ve	+ve Bilat	-ve	Bilat	≤1.5 cm	+ve	+ve	No		Mandibular gingiva
9	L	E (extraneous)	gingiva	T4aN1	-ve	+ve Ipsilat	-ve	Ipsilat	≤1.5 cm	-ve	-ve	No	60/30	Contralat mandibular gingiva
10	L	E (extraneous)	gingiva	T4aN2b	close	+ve Ipsilat	-ve	Ipsilat	≤1.5 cm	+ve	-ve	C	60/30	Ipsilat masticator space
11	L	E (extraneous)	Buccal	yT2yN0	-ve	-ve Ipsilat	-ve	Ipsilat	>1.5 cm	-ve	-ve	I+C	60/30	Ipsilat perineural spread along V2&V3
12	LR	C (central int. dose)	tongue	T1N1	-ve	+ve Ipsilat	+ve	Bilat	≤1.5 cm	-ve	-ve	C	60/30	FOM&Contralat level IIa
13	LR	C (central low dose)	tongue	T2N0	-ve	-ve Ipsilat	-ve	Bilat	≤1.5 cm	-ve	+ve	C	64/30	Contralat tongue&level II
14	R	C (central low dose)	Hard palate	T3N0	-ve	-ve Ipsilat	-ve	Bilat	≤1.5 cm	-ve	-ve	No	60/30	Contralat level IIa
15	R	C (central low dose)	gingiva	T4aNx	-ve	No dissection	N/A	Ipsilat	≤1.5 cm	-ve	-ve	No	64/32	Ipsilat level Ib
16	R	C (central int. dose)	RMT	T2N1	-ve	+ve Ipsilat	-ve	Ipsilat	≤1.5 cm	-ve	-ve	No	60/30	Ipsilat level Ib
17	R	C (central low dose)	tongue	T2N1	-ve	+ve Ipsilat	-ve	Bilat	≤1.5 cm	-ve	-ve	No	60/30	Contralat level Ib
18	R	C (central int. dose)	tongue	T1N1	-ve	+ve Ipsilat	-ve	Bilat	≤1.5 cm	-ve	-ve	No	56/28	Level Ia
19	R	A*	tongue	T3N2b	-ve	+ve Ipsilat	+ve	Bilat	>1.5 cm	+ve	+ve	C	60/30	Ipsilat level III (A) Contralat level IIa (C)
20	R	A*	RMT	T4aN2b	close	+ve Ipsilat	-ve	Bilat	≤1.5 cm	-ve	U/S	C	60/30	Ipsilat level IIb (A) Ipsilat retropharyngeal node (D)
21	R	E (extraneous)	Buccal	yT3yN0	close	-ve Ipsilat	-ve	Ipsilat	≤1.5 cm	+ve	-ve	I	60/30	Contralat Pterygoid plates& maxilla
22	R	E (extraneous)	Buccal	T2N2b	close	+ve Ipsilat	-ve	Ipsilat	≤1.5 cm	-ve	+ve	No	60/30	Ipsilat parotid node
23	R	E (extraneous)	Buccal	T2N2b	-ve	+ve Ipsilat	+ve	Ipsilat	≤1.5 cm	-ve	-ve	C	60/30	Ipsilat parotid node
24	R	E (extraneous)	Buccal	T1N2b	close	+ve Ipsilat	+ve	Ipsilat	U/S	-ve	U/S	C	63/30	Contralat levels II, III, IV
25	R	E (extraneous)	gingiva	T2Nx	+ve	No dissection	N/A	Ipsilat	≤1.5 cm	-ve	U/S	No	65/30	Contralat level II
26	R	G (low neck)	tongue	T1N2b	-ve	+ve Ipsilat	-ve	Bilat	≤1.5 cm	+ve	+ve	No	60/30	contralat levels III, IV
27	R	G (low neck)	gingiva	yT4ayN0	close	-ve Ipsilat	-ve	Ipsilat	>1.5 cm	+ve	U/S	I	60/30	Ipsilat level VIb

125

*Indicates type A failure with multifocal recurrence that includes non-type A lesions as well. †This patient had received only 6 fractions and failed to appear for the remainder of her treatments. Abbreviations. L: local; R: regional; LR: locoregional; FOM: floor of mouth; RMT: retromolar trigone; -ve: negative; +ve: positive; Ipsilat: ipsilateral; Contralat: contralateral; Bilat: bilateral; U/S: unspecified; I: induction chemotherapy; C: concurrent chemotherapy; I+C: induction followed by concurrent chemotherapy; No; No chemotherapy.

7.3.3 Local Failure typology

Of the 26 patients with local disease failure without synchronous regional recurrence, 16 (62%) were type A central high dose failures. Ten patients (38%) had non-type A local failure; two (8%) were type B, three (11%) were type C (intermediate dose), one (4%) was type D (intermediate dose), and four (15%) were extraneous type E failure. Three of patients with type A failure had multifocal recurrence; two patients with two foci of recurrences (both within the central high dose region), and one had four foci of recurrences (three in the intermediate dose and one in the high dose).

For the two patients with type B failure, one had a primary tumor in the left mandibular gingiva and developed recurrence involving the left maxillary sinus, with erosion of its lateral wall and extension along the buccal mucosa to the retromolar trigone. The second patient had a primary tumor in the floor of mouth with rapid disease progression subsequent to discontinuing radiation treatment after six fractions.

Regarding patients with type C failure, one patient had his primary tumor in the retromolar area and recurrence in the ipsilateral masticator space. The second patient had the primary tumor in the floor of mouth with recurrence involving the base of tongue, while the third patient had a primary tumor in the oral tongue with recurrence involving the floor of mouth.

The single type D failure had the primary tumor in the left mandibular gingiva and recurred along the left masticator space allowing the rGTV to partially grow outside the CTV2 boundaries, however the centroid was still located inside CTV2.

For patients with type E failure, one had the primary tumor in the right mandibular gingiva and the recurrence in the contralateral mandibular gingiva approximately 2 years following treatment. The second patient had the primary tumor in the left buccal mucosa; the recurrence manifested as retrograde perineural spread that extended to the left pterygopalatine fossa, foramen rotundum, foramen ovale, cavernous sinus, and through the superior orbital fissure into the left orbit (Figure 7.4). The third patient had T1 primary tumor in the central floor of mouth and the recurrence in the left alveolar mandibular ridge approximately 3 years following treatment. Lastly, the fourth patient had the primary tumor in the left mandibular gingiva and the recurrence in the ipsilateral masticator space at the first follow up following treatment.
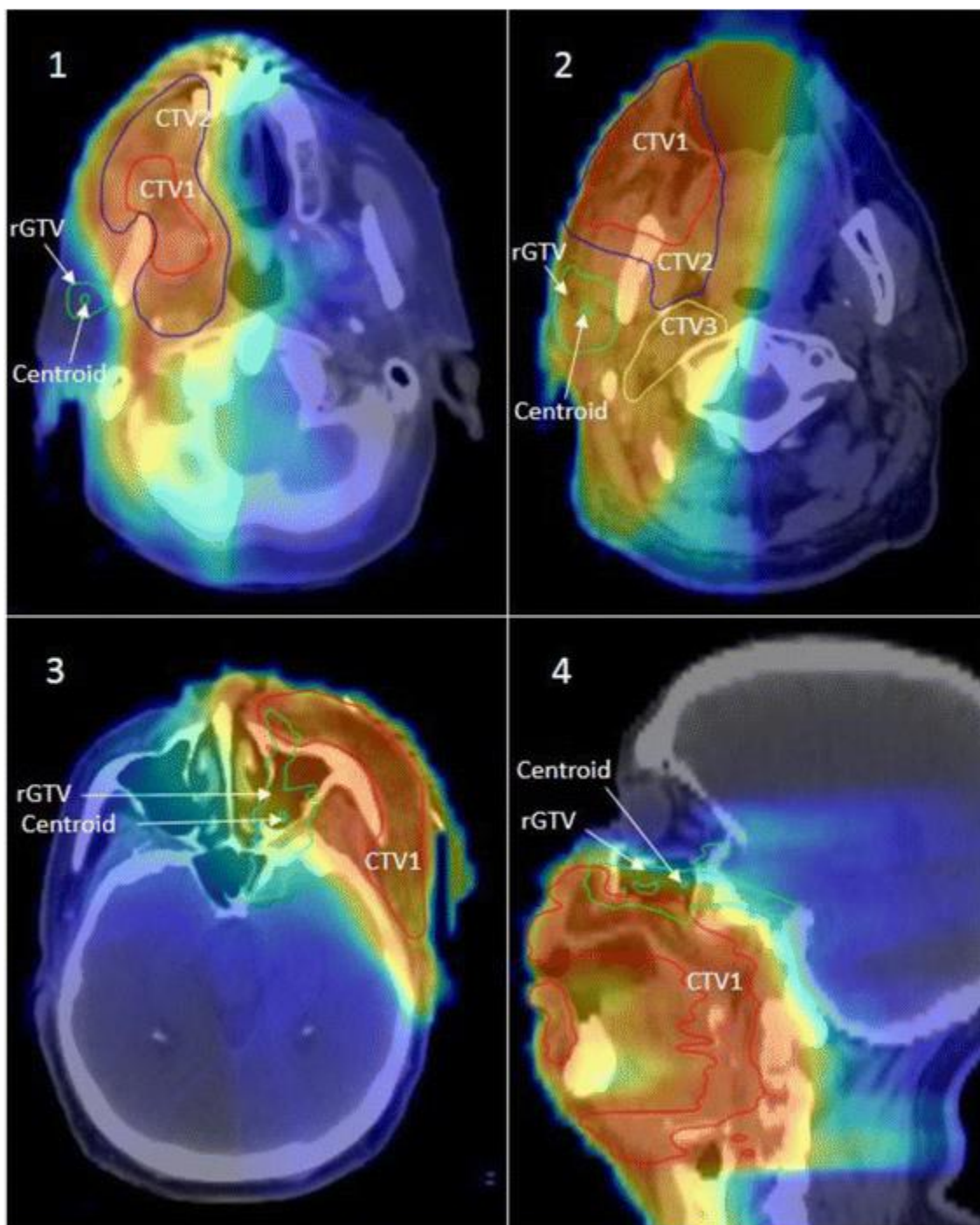
Figure 7. 4: A Case illustration.

The top panel depicts two patients with type E recurrence in the ipsilateral parotid nodal area following parotid sparing IMRT. Both patient*s* were diagnosed with T2N2b right sided buccal mucosa primaries and subsequently failed at the ipsilateral parotid area outside all target volumes. The lower panel depicts another example of type E failure in a patient diagnosed with T3N2b at the buccal mucosa with post-IMRT ipsilateral perineural spread along the maxillary and mandibular nerves (*bottom left, bottom right)*.

7.3.4 Regional Failure typology

Of the 19 patients with regional disease failure without synchronous local recurrence, only 7 patients (37%) were type A central high dose failures. Twelve patients (63%) had non-type A local failure; 5 (26%) were type C (intermediate or low dose), five (26%) were extraneous type E, and 2 (11%) were type G low neck failure. Two of patients with type A failure had multifocal recurrence. One patient with a left oral tongue primary developed synchronous ipsilateral type A recurrence at level III and contralateral type C (low dose) recurrence at level IIa. The second patient had the primary disease in the right retromolar trigone with multi-nodal recurrence at ipsilateral neck level IIb and an ipsilateral retropharyngeal lymph node (type D).

For the five patients with type C failure, one patient had a right hard palate primary with multifocal type C (low dose) failure with two foci of recurrence, both at contralateral level IIa. The second patient had the primary tumor in the left maxillary ridge and recurred in the low dose region at the ipsilateral level Ib. The third and fourth patients had primary tumors of the oral tongue with recurrences in levels Ia (intermediate dose) and contralateral Ib (low dose),

129

respectively. The fifth patient had a primary tumor in the right retromolar trigone and recurrence in the ipsilateral level Ib (intermediate dose).

Four of the five patients with type E extraneous failure had their primary tumor in the buccal mucosa. Two patients had ipsilateral parotid nodal recurrence in the area of spared parotid gland (Figure 7. 4) while the other two patients had recurrences in the un-irradiated contralateral side. The fifth patient had the primary tumor in the left maxillary alveolar ridge with recurrence in the un-irradiated contralateral level II.

Regarding the two patients with type G low neck failure, one had the primary tumor in the left mandibular with negative dissection of ipsilateral neck levels II, III, and IV, however, the patient then recurred in the ipsilateral level VIb (i.e. pre-tracheal recurrence). This failure is analogous to type D as fD95% for this patient was 10 Gy (i.e. fD95% had less than 95% of the dose prescribed to left supraclavicular region which was 58 Gy). The second patient had the primary tumor in the left oral tongue with positive neck dissection of ipsilateral levels I, II, and V then recurred in the contralateral levels III and IV. This failure is analogous to type C as fD95% for this patient was 48.75 Gy (i.e. fD95% had higher than 95% of the dose prescribed to contralateral supraclavicular field that encompassed both contralateral levels III and IV with a prescription dose of 50 Gy).

7.3.5 Locoregional Failure typology

Nine patients had synchronous local and regional failure. The predominant typology for each patient was determined according to the local failure component. Seven (78%) had type A failure and two (22%) had type C. For patients with type A failure, 3 had synchronous non-type-A failure at the neck (2 had synchronous type C and one had synchronous type G). Both

patients with type C failure had their primary tumor in the oral tongue. The first had recurrence in the contralateral side of the tongue and neck level II (both at low dose CTV) while the second had recurrence in the floor of mouth (intermediate dose CTV) and contralateral neck level IIa (low dose CTV).

7.4 Discussion

Our results demonstrate that nearly half of the patients with local and/or regional failure included in the current study had non-central high dose recurrence. We applied our novel patterns of failure analysis and classification methods to further analyze those recurrences of non-central high dose nature. Recurrences in operated tissues are less prone to present concentrically as do recurrences that occur following definitive radiation. The likelihood of a recurrence manifesting in the epicenter of origin disease that is removed surgically is unlikely, particularly when large volumes of tissue are removed and replaced by free flaps, creating significant variations in the irradiated anatomy compared to the presurgical anatomy. Furthermore, the new tissue planes can create differing paths for tumor to spread through. Thus, in the postoperative setting we essentially create a crude probabilistic model of where microscopic disease may be hiding.

While concentric central recurrences occurred less commonly than we noted in the definitive setting, over 75% of recurrences did occur within targeted tissues, the majority of which were in the high dose tumor bed target (Type A), while the remainder were in subclinical (Type C and G) targets. No technical or operator-dependent processes could conceivably prevent such failures. Whether dose intensification to Type A targets would minimize these recurrences is unclear. To date, the benefits of treatment intensification seem small. There is a

paucity of data demonstrating that increasing radiation dose is beneficial, and even concurrent chemoradiation only seems to benefit those at highest risk(196, 209). Type C failures may be prevented by prescribing higher doses (i.e. shifting to higher TV levels), but it is unclear if these relatively small dose increments (as the differences between dose to each CTV was < 10%) would be beneficial, and also increasing dose to larger volumes can potentially increase the risk: benefit ratio. Non-IMRT failure in the matching low-neck supraclavicular field was very uncommon and only seen in two patients. Also, no failures were noted at the IMRT-supraclavicular field match-line confirming the safety of this technique.

Types B (peripheral high dose), D (peripheral elective dose) and E (extraneous) failure are potentially dependent on technical or radiotherapy processes. Type B and D recurrences are analogous to what has been described as "marginal miss". Peripheral misses (type B) were seen only in 4 patients (of whom one didn't complete the prescribed radiation dose). Three of these were in primary tumor sites, and more likely reflect the tumors finding pathways more amenable for spread and growing out of the dose region rather than originating at the periphery. Similarly, the one peripheral nodal failure was in a retropharyngeal node that is typically not targeted but fell into a D type failure rather than E due to the proximity to the primary tumor bed. The paucity of these peripheral type recurrences reflects an adequate CTV delineation strategy, appropriate PTV margins, and precise dose delivery.

Type E extraneous recurrences were seen in approximately 17% of failures. Type E failures are analogous to traditionally defined "out of field" recurrences. This pattern of failure was mainly in patients who had primary tumors of the buccal mucosa or gingiva. Four patients

had primary type E recurrence, and 5 had nodal type E recurrences. Two patients with type E failure at the primary site had recurrences in sites relatively separate from the primary disease, and so these "recurrences" may represent second primary tumors.

Retrograde ipsilateral perineural spread was the cause of Type E recurrence in two patients (Figure 7.4) and was also observed in two other patients (1 Type C and 1 Type D) as seen in Table 7.2. Daly et al. had reported on a patient who had developed failure at the ipsilateral masseter due to presence of perineural invasion and retrograde tracking along the mandibular nerve(202). Yao et al. had previously reported on two patients with extensive perineural invasion and retrograde tracking who had developed failure within the infratemporal fossa(199). We would also recommend that "nerves at risk in the tumor bed should undergo biopsy and be covered in a retrograde fashion within the RT field"(202).

Three patients had recurrence in the contralateral undissected/unirradiated upper neck. Prior studies have reported that positive ipsilateral lymph nodes are a predictive factor for contralateral recurrence; conversely, contralateral lymph node metastases never occurred in patients without ipsilateral lymph node involvement(210, 211). While these studies demonstrated the association of ipsilateral lymph node involvement with contralateral recurrence, the majority of patients in these studies were predominantly patients with oral tongue cancer, and few patients had buccal cancer. We continue to favor comprehensive bilateral radiation for patients with tumors in central oral cavity sites, such as the oral tongue and floor of mouth. Yao et al. recommended that patients with ipsilateral lymph node involvement in OCC should receive bilateral neck irradiation(199). Moreover, Chan et al.

133

suggested that bilateral neck irradiation should be administered to patients with N2b disease(204). However, again these studies were heavily weighted with patients with oral tongue, and not buccal cancers. Thus, our approach to buccal and retromolar trigone tumors is individualized. Those patients with low nodal burden are still treated to the ipsilateral neck, but those with bulky nodes, multiple levels of nodes, or who have an epicentered lateral primary site, but the primary disease extends centrally are treated to both sides of the neck.

Two patients had almost identical pattern of recurrence in the ipsilateral parotid nodes as shown in Figure 7.4. Strict dose constraints to the parotid have been recommended to avoid long-term risks of xerostomia(201). In our cohort, two patients with T2N2b buccal mucosa primaries had recurrences in the ipsilateral parotid gland which was spared during PO-IMRT. This phenomena has been also reported in previous studies(204). The proximity of buccal and retromolar trigone tumors to the parotid bed makes ipsilateral parotid avoidance challenging. We therefore recommend limiting the extent of radiation-induced xerostomia by focusing on sparing the contralateral glands.

To date, a limited number of studies have exclusively investigated failure following PO-IMRT in OCC patients. **Tables 7.3 and 7.4** tabulate our study's patient/treatment and failure characteristics compared to extant literature. Loco-regional control of our study are consistent with that of previous studies(199-204, 212). Although Sher et al. reported low loco-regional failure rates (7%), they acknowledged that it may have reflected the greater proportion of early T and N staging in their cohort(203). Other disease characteristics are noted but are not directly comparable as the subset of reported patients varied from study to study.

134

Table 7. 3: Published Reports Describing Patterns of Failure Following Post-Operative IMRT for Oral Cavity Cancer, Patient Characteristics.

Author	Time period	Patients with PO-IMRT for OCC (n)	LRC (%,at x years)	Patients with LRF following PO-IMRT for OCC (n,%)	Median RFS in months (range)	T3-T4 (%)	pN+ (%)	Positive margin (%)	ECE (%)	PNI (%)	LVI (%)	CRT (%)
Yao et al. (9)	2001-2005	49	82 (2y)	8 (16%)	4.1 (3.0-12.1)	56[a]	69[a]	NR	NR	NR	NR	4[b]
Studer et al. (10)	2002-2007	28	92 (2y)	NR	NR	32[b]	75[b]	NR	NR	NR	NR	85[b]
Gomez et al. (11)	2000-2006	35	84 (2y)	6 (17%)	6.1 (4.1-26.0)	40[b]	63[b]	17[b]	36[b]	54[b]	26[b]	29[b]
Daly et al. (12)	2002-2009	30	53 (3y)	11 (37%)	8.1 (2.4-31.9)	45[c]	60[c]	10[c]	35[c]	50[c]	NR	60[c]
Sher et al. (13)	2004-2009	30	91 (2y)	2 (7%)	NR	26[c]	54[c]	0[c]	20[c]	43[c]	17[c]	77[c]
Chan et al. (17)	2005-2010	180	78 (2y)	38 (21%)	8 (2-39)	40[b]	68[b]	17[b]	34[b]	61[b]	5[b]	26[b]
Metcalfe et al. (20)	2007-2012	45	89/94[d] (2y)	2 (4%)	6 (2-34)	43[e]	73[e]	24[e]	38[e]	45[e]	38[e]	28[e]
Current report	2001-2012	289	79 (2y)	63 (22%)	4 (0-71)	44[c]	65[c]	7[c]	31[c]	41[c]	26[c]	41[c]

Abbreviations: PO-IMRT - post-operative intensity-modulated radiotherapy; OCC - oral cavity cancer; LRC - locoregional control; LRF - locoregional failure; RFS - recurrence free survival; ECE - extracapsular extension; PNI - perineural invasion; LVI - lymphovascular invasion; CRT - chemoradiation; NR - not reported
a - % of all patients in the study (n = 55, 49 with PO-IMRT to OCC)
b - % of all patients who had received PO-IMRT
c - % of only patients who had failed following PO-IMRT
d - local control was 89% and regional control 94% at 2 years
e - % of all patients in the study (n = 106, 45 with PO-IMRT to OCC)

Table 7. 4: Published Reports Describing Patterns of Failure Following Post-Operative IMRT for Oral Cavity Cancer, Failure Characteristics.

Author	LRF following initiation of PO-IMRT (n)	Spatial Classification Method	In Field Recurrences (n)	Marginal Recurrences (n)	Out Field Recurrences (n)
Yao et al. (9)	11	Binary volume overlap with CTV	10	0	1
Studer et al. (10)	NR	NR	NR	NR	NR
Gomez et al. (11)	6	Binary volume overlap with target volume	4[a]	0	0
Daly et al. (12)	11	Percentage volume overlap with 100% isodose CTV[b]	7	2	2
Sher et al. (13)	2	Percentage volume overlap with 95% isodose CTV[c]	2	0	0
Chan et al. (14)	38	Percentage volume overlap with 95% isodose CTV[d]	26	7	5
Metcalfe et al. (20)	2	Percentage volume overlap with 95% isodose CTV[d]	0	0	2
Current report	54	Spatial/dosimetric classification	30->A,10->C,2->G	2->B,1->D	9->E

Abbreviations: CTV – clinical tumor volume; NR – not reported
a - Study reported 4 local failures (all within treatment volume) and 2 regional failures (spatial classification not specified)
b - Per Chao et al. (20), >95% of recurrent tumor falling within CTV is infield, 20-95% is marginal, and <20% is outfield
c - Per Popovtzer et al. (21), >50% of recurrent disease present within 95% isodose line is infield and <50% is marginal
d - Per Dawson et al. (22) ≥95% of recurrence volume within 95% isodose of intended treatment dose is infield, 20 to <95% is marginal, and <20% is outfield

To classify failures using a spatial component, several prior studies (199, 200, 202-204)

used varying volume overlap approaches (213-215). Here we highlight two limitations in these

prior studies: 1) volume overlap methods for spatial characterization and 2) the lack of a

dosimetric component in failure analysis. Given enough time, recurrence volumes can outgrow

TV margins. Thus, the spatial characterization of "infield" vs. "outfield" is volume dependent and biased by elapsed time. As the spatial component of our failure classification, we apply a centroid-based approach. This approach has demonstrated to be more superior and accurate than volumetric overlap approaches, as the latter tends to assign failures more peripherally(216, 217). Moreover, the spatial component alone is insufficient for accurate and specific reporting of failures. Without a dosimetric component, failures that are "infield" but in fact did not receive the prescribed dose (i.e. Types B and D in our classification) could be erroneously assumed to be biological failures. Subsequently, such "infield" failures are not investigated further despite a potentially rectifiable technical or radiotherapy process.

As a retrospective series, the standard caveats apply. However, although patients were not selected nor treated prospectively, all patients were reviewed by a multidisciplinary team. This data was collated as a secondary analysis of part of a larger programmatic evaluation of PO-IMRT outcomes for OCC; the reader is encouraged to peruse the clinical/oncologic report previously published(208). Likewise, as a single institute series from a high-volume tertiary center, the generalizability/scalability of our findings to facilities which do not utilize our systematic quality assurance methods (e.g. multi-physician direct physical examination and consensus review of target delineation) would be suspect(95, 218).

Nevertheless, despite these limitations, our study is the largest, to our knowledge, systematic assessment of patterns of failure to OCC following PO-IMRT using a quality-controlled image-registration pipeline for methodologically rigorous pattern of failure investigation.(207) Similarly, our study is the first to incorporate a dosimetric component in

136

failure classification for OCC following PO-IMRT, in addition to utilizing a centroid-based spatial component and a validated DIR method which is critical for accurate failure analysis(205-207). We hope that by utilizing a standardized typology for reporting patterns of failure in OCC following PO-IMRT, which can be adopted by multiple institutions, we can encourage other comparable reporting practices for PO-IMRT, in a manner that allows improved detection of possible modes of preventable error. This could allow for pooling of data to infer differences in treatment approaches and subsequent outcomes amongst different institutions.

7.5 Conclusions

Prior studies have assessed loco-regional control following PO-IMRT to OCC in manner which elides the reality of dosimetric gradients inherent in IMRT and precludes identification of systematic sources of modifiable error which might impact these recurrences. A standardized typology with both spatial and dosimetric components allows for more accurate and specific reporting of the patterns of failure over traditional "infield" vs. "marginal" vs. "outfield" failure classification schemes. Our study incorporates a dosimetric component in addition to utilizing a centroid-based spatial component and a quantitatively validated DIR method. Approximately half of the patients with local and/or regional failure included in the current study had non-central high dose recurrence. Thus, contrary to non-OCC sites, a substantial proportion of failures in our series, despite rigorous multiphysician quality assurance, are not definitive biological failures and, as potentially modifiable risk-events, necessitate further investigation and potential practice modification. Other groups are encouraged to undertake similar efforts as single-site or pooled analyses for OCC following PO-IMRT.

Chapter 8: Patterns-of-failure guided biological target volume definition: FDG-PET and dosimetric analysis of dose escalation candidate subregions

This chapter is based upon:

Mohamed ASR, Cardenas CE, Garden AS, Awan MJ, Rock CD, Westergaard SA, Brandon Gunn G, Belal AM, El-Gowily AG, Lai SY, Rosenthal DI, Fuller CD, Aristophanous M. Patterns-of-failure guided biological target volume definition for head and neck cancer patients: FDG-PET and dosimetric analysis of dose escalation candidate subregions. Radiother Oncol. 2017 Aug;124(2):248-255. doi: 10.1016/j.radonc.2017.07.017. Epub 2017 Jul 31. PMID: 28774596; PMCID: PMC5600500.

8.1 Introduction

Despite recent advances in radiation therapy (RT), such as intensity modulated radiotherapy (IMRT) and image guided radiotherapy (IGRT), local and/or regional tumor recurrence is still the major mode of therapy failure for head and neck squamous cell cancer (HNSCC) patients.(25, 27, 32, 219) Identifying areas at higher risk of recurrence within gross target volume (GTV) with subsequent dose escalation represents a promising strategy towards reducing the rate of locoregional disease failure.(220-227)

Dose escalation in HNSCC is, nonetheless, limited by the proximity of multiple critical normal tissues. A strategy to target smaller radio-resistant subvolumes of the gross disease with higher radiation dose would be safer and more successful if the precise identification of

these subvolumes is feasible. Biological imaging modalities are promising for the creation of more spatially accurate maps of radio-resistant sub-regions of the disease compared with standard anatomical modalities. 18F-fluorodeoxyglucose positron emission tomography (FDG-PET) is the most widely utilized biological imaging modality in the clinical setting. Dose escalation strategies based on FDG-PET imaging are emerging in multiple cancer subsites.(228)

However, only a few HNSCC dose escalation clinical trials have been undertaken. In those early phase trials, the definition of FDG-PET guided dose escalation sub-volumes had been variable. The authors of the ARTFORCE phase II study designed their dose escalation sub-volumes based on 50% of the maximum uptake in the primary tumor plus a 3 mm margin to create a final PTV-FDG-PET.(229) Investigators from Ghent University Hospital implemented different strategies in two phase I dose escalation studies, using focal dose painting by contours based on the source-to-background ratio in one study (226) and dose painting by number in the second study.(222)

The rationale of defining distinct FDG-PET standard uptake value (SUV) levels as a threshold to dose escalate GTV subvolumes in HNSCC trials has not been validated in large scale datasets and mainly has been extrapolated from non-head and neck subsites (e.g. a non-small cell lung cancer study showed that the 50% SUV high FDG uptake area of the pre-radiotherapy scan overlapped significantly with the residual metabolically active areas post-treatment). (230) The identification of "evidence-based" pretreatment FDG-PET sub-volumes to guide future dose escalation studies is still an unmet need in HNSCC.

139

To this end, we aim to map the spatial location of the origin of posttreatment tumor recurrence to the pretreatment FDG-PET/CT in a large scale post-IMRT HNSCC failure dataset using a quality assured deformable image registration methodology. We sought the following specific aims:

1)   Identify the geometric origin of local and/or nodal recurrence relative to the pretreatment FDG-PET scan and relative to the original treatment target volumes.

2)   Identify FDG-PET SUV thresholds that overlap with the majority of tumor recurrences' origin.

3)   Determine the most feasible FDG-PET boost volume with the most overlap with recurrences' origin and with the smallest size relative to high dose clinical target volumes (CTVs).

4)   Generate hypotheses for future FDG-PET based dose escalation clinical trials in HNSCC.

8.2 Materials and Methods
8.2.1 Patient population
Patients with local and/or regional recurrence after curative-intent IMRT for HNSCC between January 2006 and August 2010 were identified under an institutional review board (IRB) approved protocol. Conditions for patient eligibility included:

1)Pathologically (histologically/cytologically) proven diagnosis of HNSCC.

2)Pathologic and/or radiologic evidence of local and/or regional recurrence after treatment.

140

3)Available pre-IMRT FDG PET/CT scan and retrievable IMRT plans.

4)Available CT scan of failure site prior to any salvage therapy.

5)Patients with previous radiation to the head and neck area or synchronous cancer were excluded.

8.2.3 IMRT Treatment Planning and Delivery

All patients had been positioned supine in an individualized thermoplastic head and shoulder mask for CT simulation and treatment and a custom dental stent used as an intraoral immobilization and displacement device. A treatment planning CT (pCT) scan was used for defining target volumes (TVs). TV definition was done in the Pinnacle treatment planning system (Pinnacle, Phillips Medical Systems, Andover, MA), with rigorous multi-physician quality assurance.(231)

Treatment was uniformly delivered by linear accelerators using 6-MV photons. Three clinical target volumes (CTV) had been defined: CTV1, which included gross tumor volume (GTV) plus margin, where GTV included all known gross disease (primary tumor plus grossly enlarged lymph nodes); CTV2, which included the mucosal, bony, and nodal volumes at intermediate risk of harboring microscopic disease; CTV3, which included the mucosal, bony, and nodal volumes at low risk of harboring microscopic disease. IMRT was delivered in 33-35 fractions. The dose prescribed to CTV1 was 66-70Gy, the dose prescribed to CTV2 ranged from 60-63 Gy and the dose prescribed to CTV3 ranged from 56-57 Gy. The prescribed dose to the uninvolved low- neck field was 50 Gy in 25 fractions. Each Planning Target Volume (PTV) was defined as the CTV plus 3-4 mm margin, with daily IGRT.(232) Patients were treated using

a monoisocentric technique with an antero-posterior low-neck supraclavicular field matched to the IMRT fields or using whole neck IMRT for cases where gross nodes were located at the match line.

8.2.4 Loco-regional Recurrence

Cases where local and/or regional recurrent disease were recorded had their post-failure/pre- salvage diagnostic images exported as DICOM files from the clinical PACS system to Pinnacle, where radiological evident recurrent gross disease (rGTV) was manually delineated by a radiation oncologist (ASRM) and reviewed by a head and neck service-specific attending radiation oncologist (CDF). The date of failure was defined as the date of first follow-up study indicating recurrent disease.

8.2.5 Image registration

Planning CT (pCT), target volumes, and dose maps were restored for this analysis. The metabolic tumor volume was identified on the pre-radiotherapy FDG-PET scan using an in-house auto-segmentation algorithm (PET-GTV$_{AS}$) (233), which has been optimized and validated for HNSCC.(234) For each patient, both pretreatment FDG-PET/CT and recurrence depicting CT (recCT) were co-registered with pCT scan using a prior validated atlas-based deformable image registration commercial software, ADMIRE version 1.13.5 (ELEKTA, Stockholm, Sweden 2016).(235, 236)

Subsequently, planning CTs; dose grids; original plan target volumes; recurrence CTs; rGTVs; PET-CTs; PET-GTVAS; and deformation vector fields were all imported in a custom written Matlab routine (MATLAB R2014b, The MathWorks Inc., Natick, MA, 2014). The deformation vector fields were then applied to PET-GTVAS segmented on PET/CT and rGTV

142

segmented on the recurrence CT to convert them into a deformed PET-GTVAS and a deformed rGTV on the planning CT, respectively. Figure 8.1 depicts the workflow methodology described above.
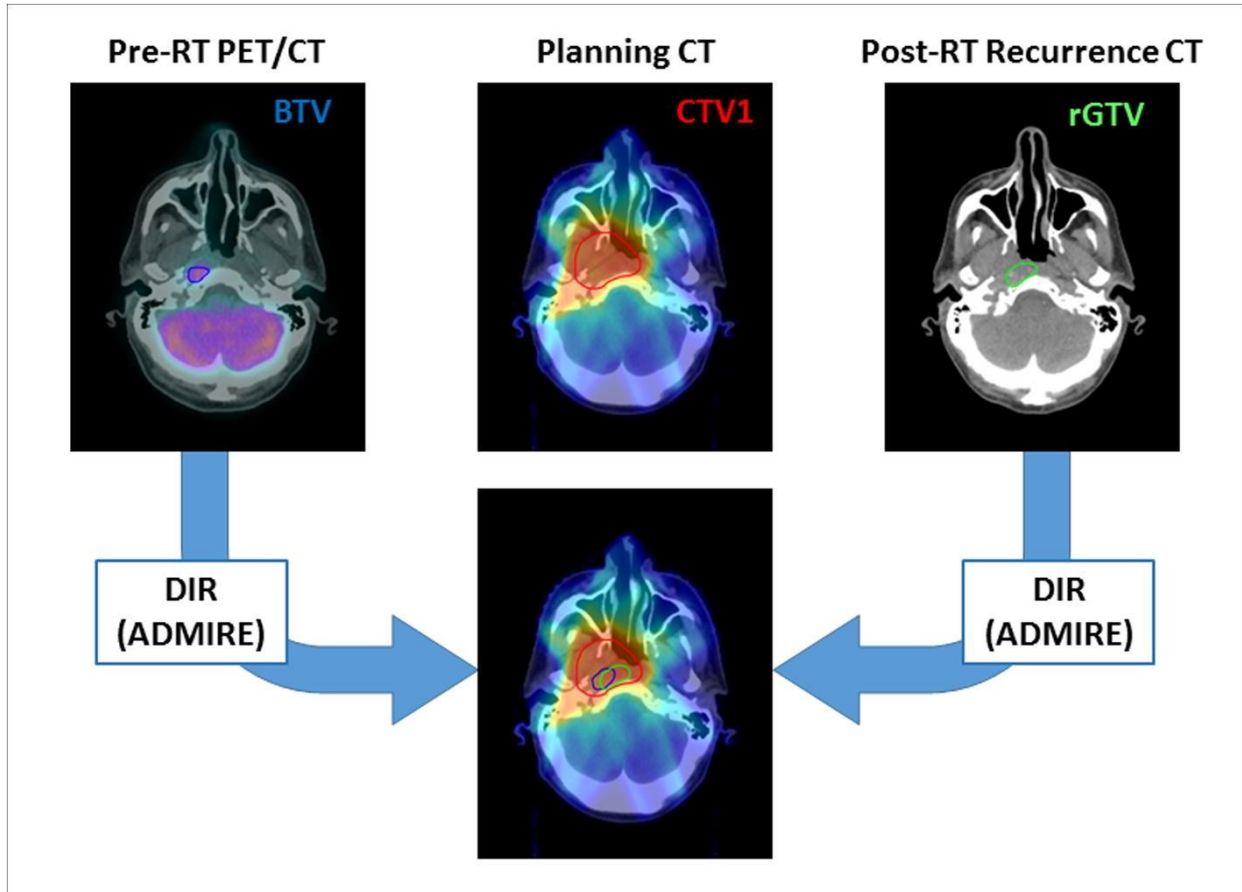
Figure 8. 1: Workflow methodology of the study.

8.2.6 Recurrence Origin Mapping

The center of mass of the registered rGTV was identified as the origin from where failure expanded (i.e. nidus of the recurrence) and a nidus volume (NV) was created by adding a 4 mm radius to account for uncertainties in registration and delineation. A margin of 4 mm

143

was decided using error propagation (Eq. 1) (237) of the known uncertainties (2 mm for registration and 3 mm for delineation) providing an overall uncertainty of 3.6 mm that was rounded to 4 mm. Additional nidus volumes were generated by increasing the radius from 0 to 10 mm, in 2 mm increments, for a comprehensive evaluation of the uncertainty of the nidus (origin of the recurrence). The location of deformed NVs was then compared relative to the deformed PET- GTVAS contours location as well as the original plan target volumes and dose.

Eq. 1

$$\delta E = \sqrt{(\delta r)^2 + (\delta d)^2}$$

Where *δr* is the uncertainty in registration and *δd* is the uncertainty in delineation.

8.2.7 Patterns of loco/regional recurrence

Failures were classified according to both geometric and dosimetric criteria as previously described by our group.(235) In brief, the geometric mapping of recurrence origin was done by correlating the NV of each rGTV to the corresponding TV in the planning CT. Subsequently, the dosimetric characteristics were assessed by calculating the dose to 95% of the failure volume (fD95%) then comparing it relative to the dose prescribed to the corresponding TV of origin as determined by the geometric mapping. Finally, failures were classified into five major types: Type A (central high dose where fD95% is ≥95% dose prescribed to corresponding high dose TV of origin), Type B (peripheral high dose where fD95% is <95 % dose prescribed to corresponding high dose TV of origin), Type C (central elective dose where fD95% is ≥95% dose prescribed to corresponding lower dose TV of origin), Type D (peripheral elective dose where fD95% is <95% dose prescribed to corresponding

144

lower dose TV of origin), and Type E (extraneous dose where rGTV centroid originates outside all TVs). Type F describes junctional failures at the IMRT/supraclavicular match line, and Type G describes low neck failures at the low-neck supraclavicular field. The overall pattern of failure for patients with type A recurrence and concurrent non-type A recurrence was defined as type A. While patients who had more than one non-type A at the same time, pattern of failure of each patient was classified according to the most predominant type based on rGTV volume.

5.2.8 PET boost volumes

For this analysis the 30%, 40%, 50%, 60% and 70% of the maximum SUV volumes were identified on the pre-radiotherapy FDG-PET images and an isotropic margin of 0-20mm (in an iterative increments of 2mm) was added around each iso-intensity volume to create boost tumor volumes (BTV30+0, BTV30+2, …., BTV70+20). For each deformed BTV, the overlap with the 4 mm NV of all recurrence lesions of type A nature was recorded. The BTV was considered adequate to capture the nidus of recurrence if the overlap was greater than 95% provided that BTV volume is less than CTV1 volume. All BTVs with volume ≥ CTV1 volumes were excluded. For primary site recurrences, additional analysis was done to identify the best possible BTV candidate by calculating the percent volume of the selected BTV relative to the high dose CTV (thus minimizing the necessary boost volume). Because the generated margins around BTVs were isotropic in nature, we also calculated the percent of voxels of each boost volume that were outside the high dose CTV (0% is the best and 100% is worst). Lastly, differences in the percent of lesions covered between the 0 and 10 mm margin nidus volumes were used to assess each BTV's robustness to uncertainty in the identification of the nidus. To

145

identify the best possible boost tumor volume, an arbitrary score function (Eq. 2) was

determined and scores were calculated for each volume.

Eq. 2

$$Score = [\% \ of \ patients \ covered \ + \ (Robustness) + (100 - \% \ of \ Boost \ Volume \ outside \ CTV1)$$
$$+ \ (100 \ - \ \% \ of \ CTV1 \ covered \ by \ boost \ volume)]/4$$

Where Robustness = 100 − (% of 10 mm NVs covered − % of 0 mm NVs covered)

8.2.9 Statistical analysis
Statistical assessment and data tabulation were performed using JMP v 11Pro (SAS

institute, Cary, NC).

8.3 Results
8.3.1 Patients and tumor characteristics
A total of 47 patients were eligible for this analysis. Median age was 59 years (range

33-93). Median time from end of radiation treatment to recurrence was 8 months (range 1-58).

The PET-GTVAS had a median volume of 24 cm3 (range: 3-197) and SUVmax for these

volumes were found to have a median value of 16 (range 6 – 41). Patient, disease, and

treatment characteristics are summarized in table 8.1.

Table 8. 1: Patient, disease, and treatment characteristics.

Variables	No. of patients (%)
Gender	

Male	42 (89%)
Female	5 (11%)
Smoking Status	
Smoker	32 (68%)
Non-smoker	15 (32%)
Primary Site	
Oropharynx	30 (64%)
Hypopharynx	7 (15%)
Oral cavity	1 (2%)
Nasopharynx	3 (6%)
Sinonasal	2 (4%)
Larynx	4 (9%)
T stage	
T1	7 (15%)
T2	18 (38%)
T3	9 (19%)
T4	13 (28%)
N stage	
N0	2 (4%)
N1	6 (13%)
N2a	4 (8%)
N2b	17 (36%)
N2c	13 (28%)
N3	5 (11%)
HPV status	
Positive	17 (36%)
Negative	4 (9%)
Unknown	26 (55%)

IMRT dose & fractionation	
Mean Dose (SD), in Gy	69.5 (1.5)
Mean n. of Fractions (SD)	33 (1.6)
Chemotherapy	
Induction	5 (11)
Concurrent	17 (36)
Induction and concurrent	20 (42)
No chemotherapy	5 (11)

8.3.2 Patterns of failure

Patients included in this analysis had failure at the primary site in 19 patients (40.4%), at the nodal site in 18 patients (38.3%), and in both the primary and nodal sites in 10 patients (21.3%). Forty-two patients (89.4%) were classified as type A failure. Five patients (10.6%) were of non- type A failure; two were type C, one type D, and one type E.

A total of 66 rGTVs were identified. Median rGTV volume was 3.7 cm3 (IQR 2-9). Of these, 54 (82%) were of type A, 5 (7.5%) were type C (i.e. central low dose), 1 (1.5%) was type D (i.e. peripheral low dose), 5 (7.5%) were type E (i.e. out of field), and 1 (1.5%) was type G (i.e. in the low neck supraclavicular field). For type A's rGTVs, 26 (48%) were at the primary site and 28 (52%) were at the nodal site. The mean (SD) of mean doses of all rGTVs' originating in high dose regions was 71 Gy (2) and the mean of dose to 95% rGTVs' volume

148

was 69 Gy (3). Figure 8.2 depicts the patterns of failure classification per patient and per individual recurrence lesion.
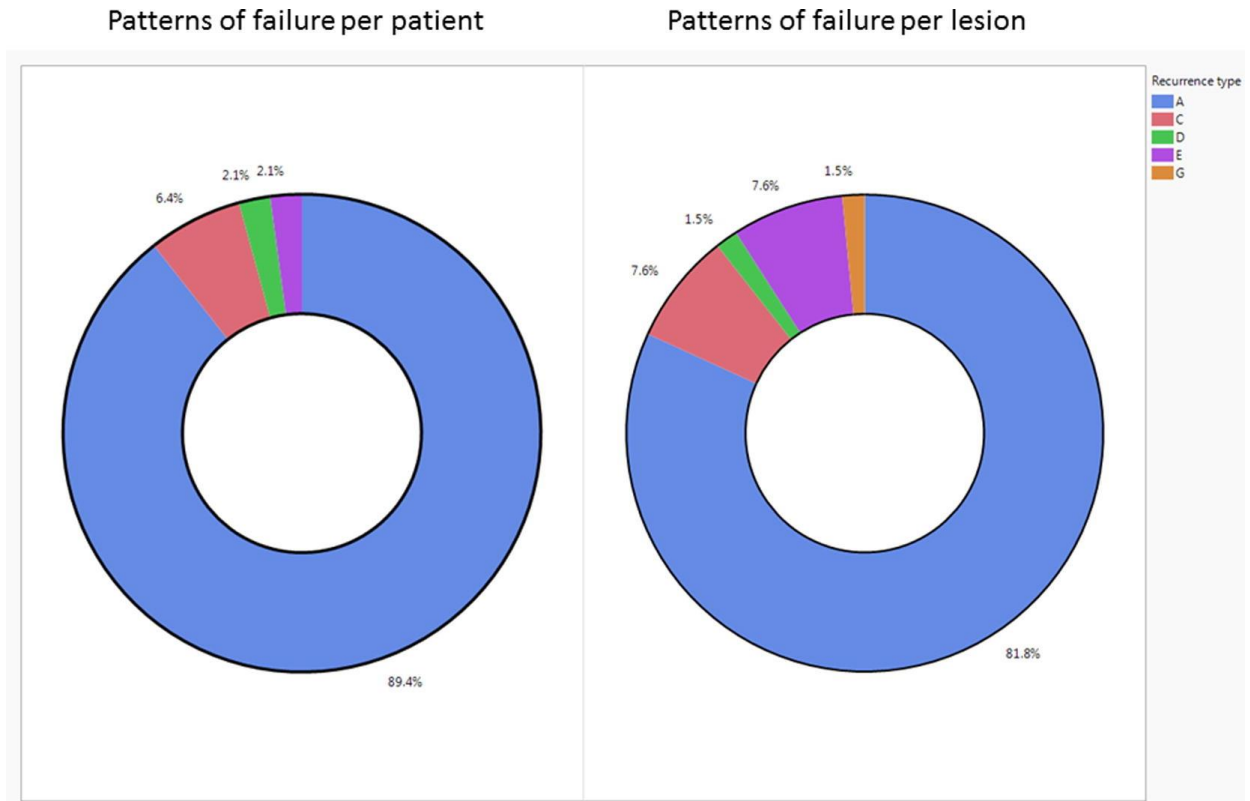
Figure 8. 2: Pie charts of the patterns of failure classification.

8.3.3 PET boost volumes

The range of BTVs that encompasses the recurrence origin (i.e. nidus volume) of all type A rGTVs is listed in Figure 8.3. PET-GTVAS overlapped with 38% of NVs of the primary sites and 32% of NVs of the nodal sites. With no added margins, the examined SUV thresholds did not overlap with most of NVs. For example, when no margin expansion is included, BTV50 (i.e. BTV50+0) covered less than 20% of type A primary site's nidus volumes, while lowering

149

the threshold BTV30 only resulted in 50% coverage of primary site recurrence origin. However, with additional margin expansion, more than one BTV alternative resulted in the coverage of ≥90% of the primary site nidus volumes as well as the coverage of ≥75% of all type A nidus volumes as shown in Figure 8.3.
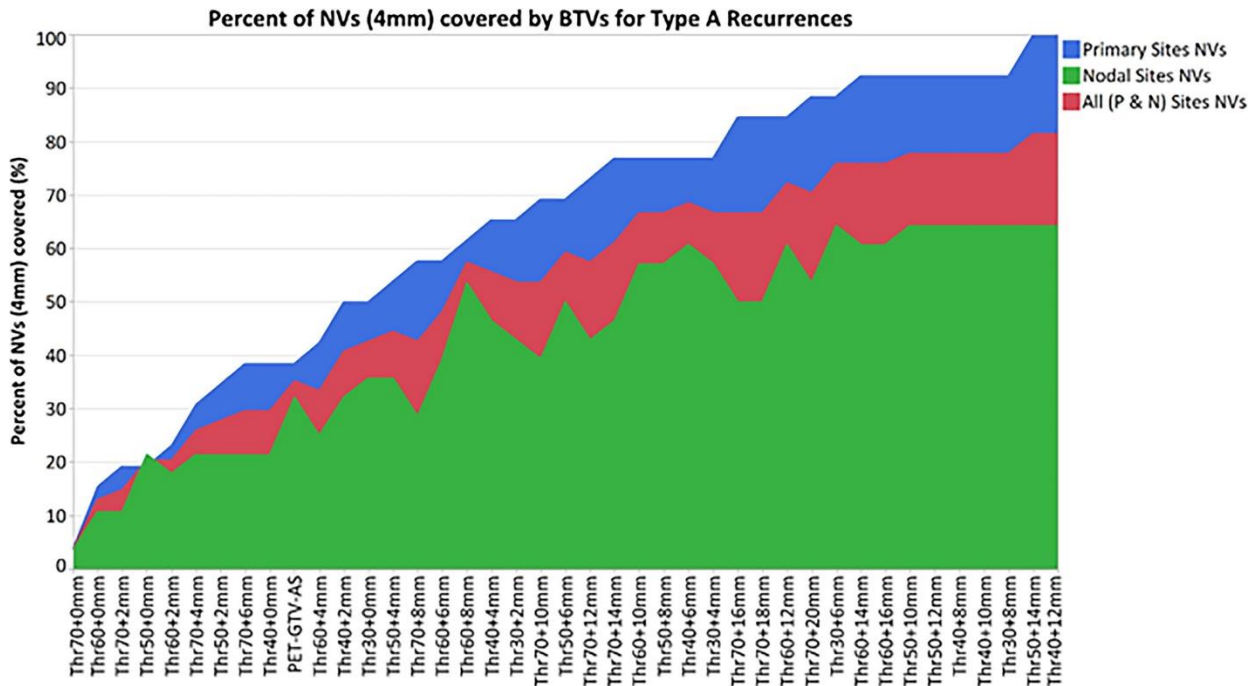
Figure 8. 3: Percent of NVs covered by BTVs for type A recurrences.

This figure shows the percent of type A recurrences' origin covered by Boost Volume when considering the nidus volume created by adding a 4 mm radius. Boost volumes with an average volume greater than 100% of CTV1 are not shown as per our criteria, BTV volume must be less than CTV1 volume. Recurrent lesions were classified per their anatomical location, and coverage per class (n. of primary rGTVs=26, n. of nodal rGTVs=28, total type A's rGTVs=54) are shown in this figure.

Nevertheless, as shown in Figure 8.4, the candidate BTVs with ≥90% of the primary site nidus volumes coverage did not achieve equivalent performance when using the other metrics of best BTV selection (i.e. the percent of BTV volume inside CTV1 relative to the entire CTV1 volume and the percent of voxels outside CTV1). BTV50+10mm had the best collective performance with high NV coverage (92.3%), low average relative volume to CTV1 (41%), least average percent voxels outside CTV1 (19%), and high average robustness metric (i.e. increasing the margin expansion around the rGTV centroid from 0 to 10 mm led to a minor drop in the percent of overlap [27%]). Appendix B figure B1 shows the overall performance score for all BTVs whose volume did not exceed the size of CTV1. As depicted in figure B1, BTV50+10mm outperformed all other volumes based on this criterion. Appendix figures B2, B3, and B4 show percent of NVs covered per BTV as a function of NV margins. Figure 8.5a clearly demonstrates that BTV50+10mm encompasses the vast majority of primary tumor recurrence's origin. While Figure 8.5b-d depicts a case demonstration of the candidate boost volume relative to recurrence and planning target volumes.
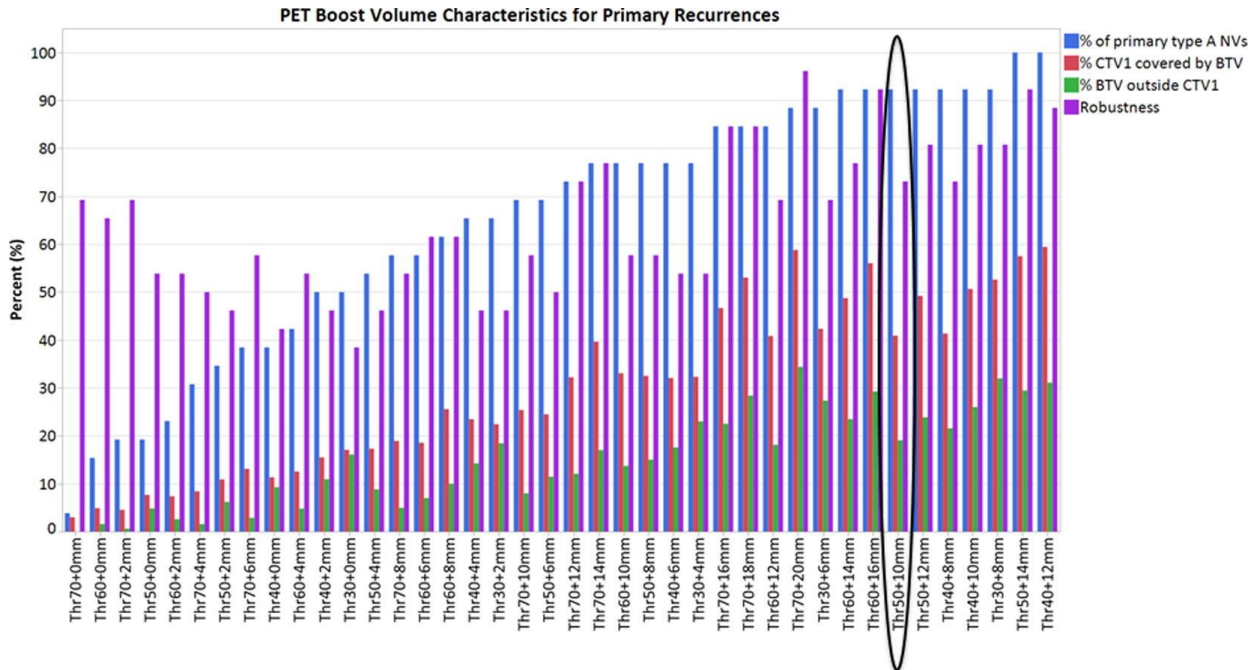
Figure 8. 4: PET boost volume characteristics.

This figure shows the PET boost volume metrics used for determining the "best" boost volume. The blue bars show % of primary site nidus volumes covered per boost volume (100% is best, 0% is the worst). The red bars show the % of CTV1 that are being covered by BTV (less is better, we don't want the whole CTV1 to be boosted). The green bars show the % of voxels of each boost volume that are outside the CTV1 (the idea is that we want the boost volume to be mostly inside the CTV1, so 0% is best and 100% is worst). Lastly, the purple bars represent each boost volume's robustness. Robustness is calculated per volume by looking at the difference in coverage for different nidus radius. The higher the number the more robust the volume is. Boost volumes that are greater than CTV1 have been excluded. Volumes are ordered by increasing % of patients covered. BTV50+10mm had the best collective

performance with highest possible NV coverage (92.3%), least relative volume to CTV1 (41%), least percent voxels outside CTV1 (19%), and reasonable robustness score (73%).
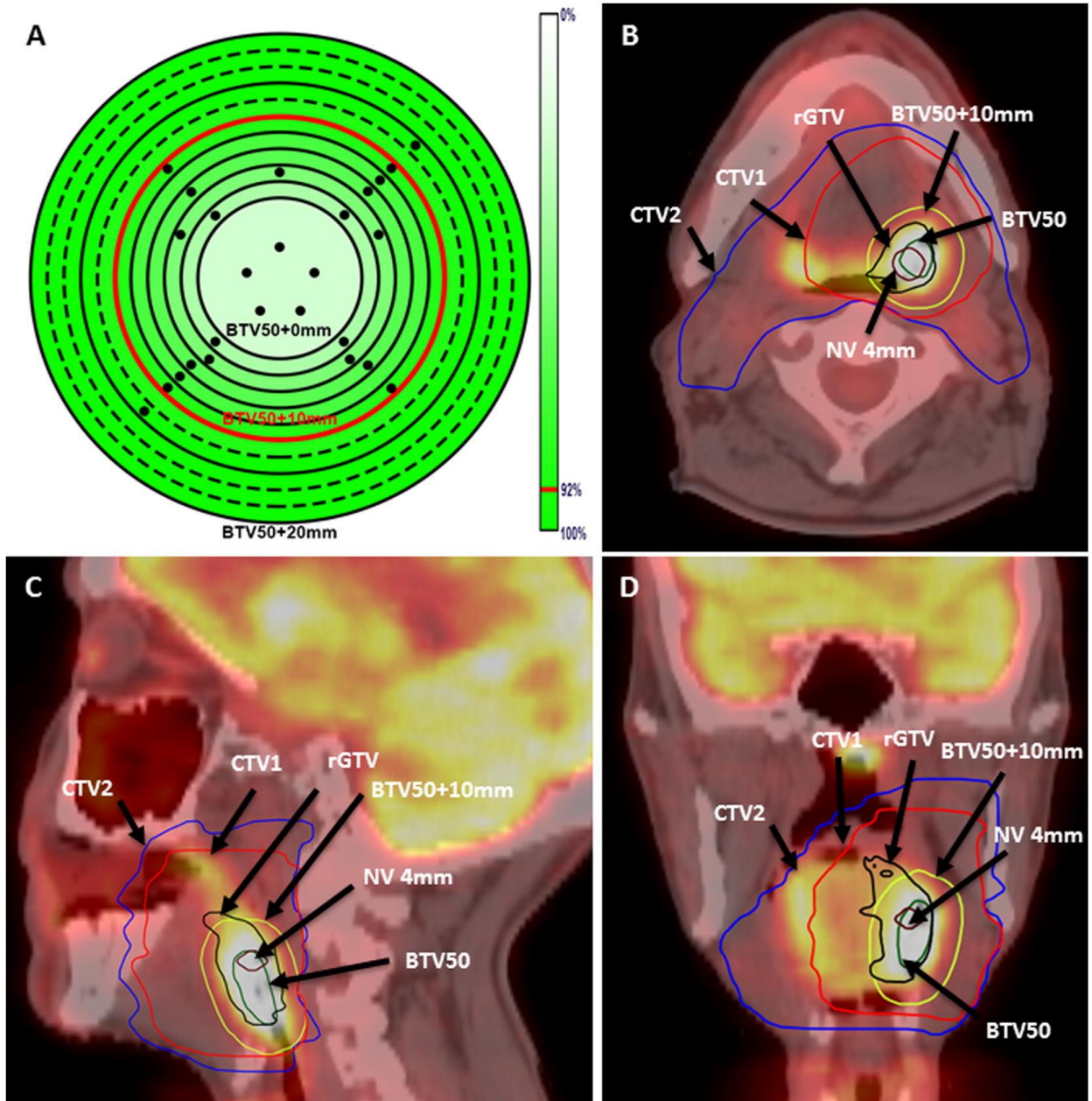
Figure 8. 5: Heat map of recurrences and case illustration.

Panel A shows a heat map of percent of lesions covered (4mm nidus) for volumes segmented using a 50% of SUVmax threshold value. The dots on Panel A represent patients with primary recurrences, whereas the different rings represent the different margins increasing from the center to the outer most ring by a 2 mm interval. Panels B-D show an example of a T2N2b left tonsillar patient with local recurrence at the primary site. The 4mm nidus volume (magenta), primary recurrence (black), BTV50 (green), BTV50+10mm (yellow), CTV1 (red), and CTV2 (blue) are highlighted.

8.4 Discussion

The strategy of increasing radiation dose to be delivered to subvolumes of gross tumor with supposed higher radio-resistance while keeping surrounding normal structures at similar or lower dose levels, appears promising as a step towards improving locoregional control and consequently survival in multiple cancer sites. (220, 228, 230) The deployment of such strategy requires optimal integration of spatially accurate biological imaging in radiation treatment paradigms. FDG-PET/CT is a very attractive solution in this context because it is a widely used tracer and a standard of care imaging modality that provides both anatomical as well as biological aspects of tumors (e.g. tumor metabolism).(238-240) FDG-PET/CT has been successfully used for HNSCC radiation treatment planning purposes,(241) however, its effective use for dose escalation requires a validation of the geometric correlation between the origin of posttreatment disease failure, pretreatment FDG-PET uptake, planning target volumes, and radiation dose, which is the main aim of the current study. The uncertainties and

154

limitations of PET are well known.(242) However, they were carefully considered and taken into account in this analysis.

A few prior studies have attempted to address the correlation of patterns of failure to pretreatment FDG-PET for head and neck squamous carcinomas.(124, 243) These studies, however, lacked the validation of the exact spatial correlation between the recurrence's origin and the pretreatment FDG uptake. Such knowledge is required to be able to define the appropriate subvolumes to target in FDG-PET-guided dose escalation clinical trials. In addition, the number of failures examined in these studies were few. A large scale failure dataset is required to ensure a realistic representation of different patterns of failure encountered clinically. A single previous study by Due et al. (244) was the first to attempt to spatially correlate the patterns of failure relative to pretreatment FDG-PET on a cohort of 39 HNSCC recurrences after IMRT. Their results showed that 54% of recurrences were originated inside the FDG-positive volume delineated by the nuclear medicine physician.

In the current study, we used a previously validated deformable image registration software for CT-CT registration in HNSCC (235, 236) to map the segmented recurrence volume in post-failure diagnostic CT back to the simulation CT scan, planning target volumes, and dose grid. Simultaneously, the CT of the pretreatment FDG-PET-CT was also registered to the simulation CT. We used the failure's centroid mapping method proven by prior work from our group and by others (36, 37) as a more discriminative and accurate manner to localize the origins of loco- regional recurrences than volume overlap methods, which may potentially and incorrectly assign recurrences to more peripheral target volumes regions. We added a 4 mm

margin expansion of the centroid of the mapped failure volume to create the nidus volume, as the closest approximation of the 3D volume of the recurrence origin and to account for registration and delineation uncertainties.

Our results showed that the majority of patients (89%) failed at the central high dose regions. Surprisingly, as shown in figures 8.3, 8.4, and 8.5a the majority of type A recurrence origin's did not necessarily fall in voxels with the highest uptake of FDG and an additional 10 mm isotropic margin expansion around the 50% of the maximum SUV was required to create a BTV that cover 92% of type A's recurrences at the primary site. Other BTV volumes, though, overlapped with the majority of recurrences. However, those volumes were considered inappropriate for having either larger relative volume compared to CTV1 or higher percent of voxels outside CTV1. BTV50+10mm, on the other hand, had the best collective performance with the highest overlap with a recurrence's origin, the smallest relative volume compared to CTV1 (i.e. realistic boost subvolume), and the least percent of voxels outside CTV1.

These findings show a boost subvolume of 50% of the maximum FDG uptake would cover less than 20% of primary site recurrence's origin. Also, the voxels of highest FDG uptake are not ineluctably the voxels of highest radio-resistance. Thereby, strategies of selective targeting of the voxels of highest uptake by higher dose (e.g. dose painting by number) seem to underestimate the recurrence risk in nearby voxels within the BTV50+10mm which have relatively lower uptake. Consequently, subvolume definition strategies for FDG-PET-guided dose escalation studies should be revised in the context of these findings.

Critically, if we plan to identify regional sub-volume dependent dose modification (e.g.

PET- tracer-, MR parameter- or CT-texture-identified "boost" volumes) as a potential modifier of

local/regional tumor response, it is imperative that the underlying nomenclature and

methodology for defining said events be fully detailed and reproducible. Our attempt, within this

dataset, is to not only generate a definitive recommendation for "boostable" subvolume

identification, but a methodologic benchmark and process overview for additional

functional/biological/radiomic applications. Conceivably, PET SUV in this manuscript could be

replaced in an equivalent analytic framework with multiparametric MRI or radiomic texture

profiles. The imperative first step in any of these efforts would be a representational framework,

as detailed herein, which adequately describes with known spatial precision quantifiable event

probabilities.

Our study, however, does not go without caveats. Being retrospective in nature, the

typical limitations of any retrospective study apply. Also, we have assumed that isovolumetric

expansion of the recurrence from the center of mass of the recurrence volume would localize

the origin of recurrence, which may not be true in all head and neck cancer cases. However,

this is the best possible estimation based on empirical findings. We also did a robustness

analysis to address the effect of nidus volume on our findings as shown Appendix B figure B1-

B4. Because of the uncertainties related to non-rigid registration as well as inter-observer

contouring variability, we expanded the centroid of recurrence by 4 mm radius as detailed

above. This analysis provided additional depth in determining the best available BTVs since it

took into consideration the inherent uncertainties presented by arbitrarily choosing a NV with a

157

4 mm radius. There are many uncertainties associated with the use of FDG-PET.(242) Some of the ones that can influence the identification of the BTV the most are the voxel size (5.5x5.5x3.7mm3), the uncertainties related to the reproducibility of SUVmax (i.e. 1-6%) (245), as well as blurring due to potential patient motion inherent from the length of the scan. In this work we decided to account for those uncertainties with the combination of different thresholds as a percent of SUVmax with different isotropic margins, guided of course as was described in detail by the patterns of failure analysis, combined with an additional robustness analysis of the recurrence centroid. This robustness analysis showed that even with a 10 mm margin expansion around the centroid, BTV50+10mm still covers the majority of primary site recurrences (i.e. >73%).

Nevertheless, this is, to our knowledge, the largest series of HNSCC failure following curative- intent IMRT to robustly and simultaneously characterize the spatial, biological, and dosimetric foci of recurrence in an integrated spatial frame, using a validated pattern of failure methodology. Our data serve to define a candidate BTV volume that appropriately covers the subvolumes of highest radio-resistance based on objective patterns of failure mapping using rigorous image-processing to afford increased spatial certainty as a prior for further investigation and extra-institutional validation.

8.5 Conclusions
To conclude, we present 47 HNSCC patients with recurrence following curative intent IMRT. Our results showed that the majority of recurrences occurred in the central high dose regions. When correlated with pretreatment FDG-PET, the majority of these type A recurrences originated in an area that would be covered by a 10 mm margin on the volume of 50% of the

maximum FDG uptake. A validation of these findings is needed in multi-institutional and

prospective HNSCC treatment failure databases.

Chapter 9: Associations between imaging phenotypes and genomic mechanisms

This chapter is based upon:

Mohamed ASR*, Zhu Y*, Lai SY, Yang S, Kanwar A, Wei L, Kamal M, Sengupta S, Elhalawani H, Skinner H, Mackin DS, Shiao J, Messer J, Wong A, Ding Y, Zhang L, Court L, Ji Y, Fuller CD. Imaging-Genomic Study of Head and Neck Squamous Cell Carcinoma: Associations Between Radiomic Phenotypes and Genomic Mechanisms via Integration of The Cancer Genome Atlas and The Cancer Imaging Archive. JCO Clin Cancer Inform. 2019 Feb;3:1-9. doi: 10.1200/CCI.18.00073. PMID: 30730765; PMCID: PMC6874020.

*Equal contribution.

The permission for reuse of this material was obtained from Wolters Kluwer Health, Inc.

9.1 Introduction

Head and neck squamous cell carcinomas (HNSCCs) prevail as the sixth most common cancer worldwide with over 500,000 expected newly diagnosed cases reported annually(246). In the United States, 40,000 new HNSCC cases are reported with approximately 7,890 deaths per year(247). HNSCCs encompass a diverse array of cancers that can originate from subsites within the oral cavity (44%), larynx (31%) or pharynx (25%)(248). Viral infections, specifically human papilloma virus (HPV) primarily type 16 and Epstein-Barr virus, are associated with higher risk of oropharynx and nasopharynx cancers respectively(249, 250). Protracted tobacco and alcohol use as well as UV light exposure are among the traditional risk factors for development of HNSCC(251). There has been a dramatic change in the affected patient cohort as risk factors

has changed, represented by a decrease in tobacco use and concomitant increase in HPV-associated disease. This was reflected as a substantial rise in the incidence of HPV-associated oropharynx cancers as compared to a decline in cancers of the larynx and hypopharynx(252). Given the high morbidity and mortality associated with HNSCC, this type of cancer represents a major health burden.

The refinement in head and neck irradiation techniques, specifically introduction of intensity-modulated radiotherapy about 15 years ago, was a paradigm shift HNSCC management that resulted in improvement of treatment outcomes(253). Continued efforts have been made to investigate potential prognostic and predictive biomarkers to establish the conceptual framework for precision medicine in management of HNSCC(254). One example is the exploration of the correlation between disruptive alteration of the gene encoding the tumor-suppressor protein p53 (TP53) and treatment failure with subsequent decreased survival in HNSCC patients(255).

Radiographic images, such as Computed Tomography (CT), have been routinely used for diagnosis and treatment of HNSCC. However, the relationship between tumor imaging phenotypes and underlying tumor genomic mechanisms remains underexplored. Precise and effective treatment of cancer requires the integration of disease information from multiple sources. Imaging-genomics research combines radiographic image analysis with genomic research to improve disease diagnosis and prognosis, discover novel biomarkers, and identify genomic mechanisms associated with phenotype formation(59-63). Such imaging-genomics studies have been performed for multiple cancer types, including breast invasive carcinoma(59-63), lung cancer(64, 65), glioblastoma multiforme(256), and clear cell renal cell carcinoma(257).

161

To our knowledge, there are very few existing imaging-genomics studies for HNSCC. One of the earliest studies from 2003 by Yang et al. investigated the correlation between temporal changes in T1- and T2-weighted contrast-enhanced magnetic resonance imaging and genomic analysis using oligonucleotide microarrays in murine squamous cell carcinoma tumor models(258). Aerts et al. developed a multi-feature radiomic signature capturing intratumoural heterogeneity that was linked to gene-expression patterns, validated in three independent data sets of lung and head-and-neck cancer patients(259). Recently, Pickering et al. correlated radiologist-selected CT imaging features of 27 oral cavity squamous cell carcinomas with the expression of cyclin D1, angiogenesis-related genes, and epidermal growth factor receptors(260).

In the current study, we innovatively investigated the comprehensive relationship between the multi-layer tumor genomic system and the multiple aspects of tumor imaging phenotype for HNSCC. We integrated multi-omics, whole-genome measurements from The Cancer Genome Atlas (TCGA)(261) with radiomic data derived based on CT images from The Cancer Imaging Archive (TCIA)(262) for matched patients, and identified statistically significant associations between them. We also explored the potential of using CT imaging as a non-invasive marker predicting the tumor molecular status for HNSCC.

9.2 Materials and Methods

Clinical, radiological, and genomic data (Appendix Information Sections C1-C2) for 126 HNSCC patients from TCGA and TCIA were integrated and analyzed. CT images of the patients were downloaded from TCIA and processed using Imaging Biomarker Explorer

(IBEX)(263), an automatic medical image analysis software pipeline that generates tumor radiomic features. The radiomic features were grouped into five categories: (1) gray level co-occurrence matrix, (2) gray level run length matrix, (3) neighbor intensity difference, (4) intensity direct, and (5) size/shape(259). Appendix Information Section C. 1 introduces how the radiomic features were generated. Multi-omics genomic data and patient clinical information were acquired from TCGA using the open-source R software tool TCGA-Assembler(264). Appendix Information Section C. 2 introduces the collection and processing of genomic data. Genomic data, clinical data, and radiomic data were integrated to form the imaging-genomics data (Table 9.1) for subsequent analysis. A total of 126 patient samples were used for analysis, representing all matched cases in TCGA and TCIA HNSCC database(s).

Table 9. 1: Summary of the integrative imaging-genomics data used in the analysis.

Number of features and tumors in different data platforms		
Data platform	**Number of features**	**Number of Tumors**
Radiomics	187 radiomic features	126
miRNA expressions	1046 miRNAs	125
Mutated genes	16573 genes	122
Gene expressions	20531 genes (179 pathways)	125
Copy number variations	19921 genes (179 pathways)	126
Promoter region DNA methylation	19325 genes (179 pathways)	126

Numbers of tumors/patients in different categories	
AJCC tumor stage	Stage I (n = 4), stage II (n = 14), stage III (n = 22), stage IV (n = 86)
Tumor site	Oral cavity (n = 69), larynx (n = 36), oropharynx (n = 21)
Smoking behavior	Current smoker (n = 52), former smoker (n = 45), never smoker (n = 29)
Sex	Male (n = 97), female (n = 29)
HPV status	HPV+ (n = 29), HPV−(n = 96), not measured (n = 1)
Disruptive TP53 mutation	With disruptive TP53 mutation (n = 33), without disruptive TP53 mutation (n = 89), not measured (n = 4)

CT parameters

CT scanner manufacturer	GE (n = 61), Siemens (n = 33), Philips (n = 26), Toshiba (n = 5), Picker (n = 1)
Slice thickness: median (IQR)	2.5 (1.25-3)
Contrast	All are contrast-enhanced
Tube voltage (kVp)	120 (n = 98), 130 (n = 7), 135 (n = 1), 140 (n = 20)
Tube current (mA): range	59-600
Data collection diameter (mm): median (IQR)	500 (320-500)
Reconstruction diameter (mm): median (IQR)	250 (242-268)

Others

Age (years)	Mean = 59.81, std = 11.28

The number of tumors for radiomics (i.e. 126) is the number of tumor cases with radiomic features. For genomic data platforms, the number of tumors is the number of tumor cases with both radiomic features and genomic data of the specific platform, which were used in our study.

A multi-step informatic and statistical pipeline was built to perform integrative data processing and analysis (Figure 9.1). First, linear regression was used to identify statistically significant associations between radiomic features and gene-level genomic features including expressions of miRNAs and somatic mutations summarized at the gene level, adjusting for patient age, tumor grade, tumor subsite, and patient smoking status (Appendeix Information Sections C. 7 and C. 8). Second, for the whole-genome measurements, including gene expressions, copy number variations (CNVs), and promoter region DNA methylation, we investigated their associations with tumor radiomic features at the pathway level using a modified Gene Set Enrichment Analysis (GSEA)(265) scheme that was also adjusted for the confounding factors mentioned above (Appendix Information Sections C. 4-6). The genetic

164

pathways in consideration are from the Kyoto Encyclopedia of Genes and Genomes

(KEGG)(266) database charactrerizing various aspects of the biomolecular system. Third,

based on radiomic features, random forest classifers(267) were used to predict patient HPV

status and TP53 mutation status in HNSCC (Appendix Information Section C. 9).
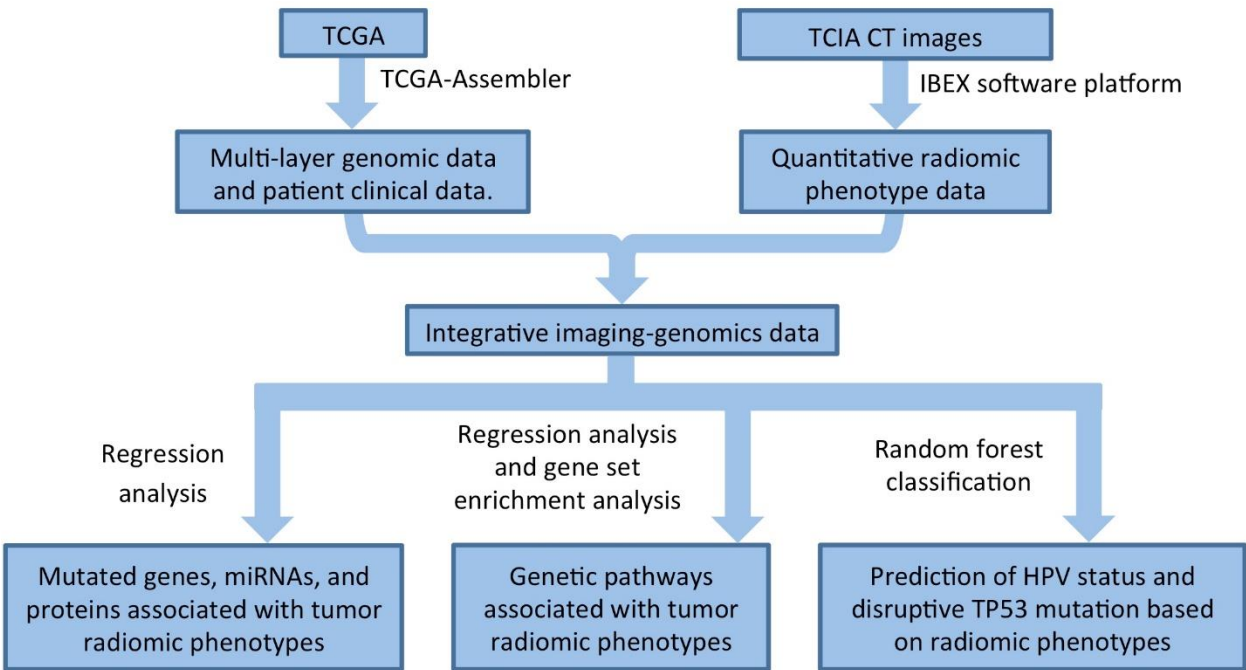
Figure 9. 1: Flowchart of processing the data.

9.3 Results

A total of 5,347 statistically significant associations (adjusted p-value ≤ 0.05) were

identified between various radiomic and genomic features. Appendix figure C.1 is a graphical

presentation of the identified associations. Table 9. 2 shows the numbers of identified

associations between different categories of genomic features and radiomic features, based on

which Fisher's exact test (268, 269) indicates that the frequency of statistically significant

associations depended on the feature category (p-value < 0.0001), meaning some feature

categories have more associations than others. The identified associations are statistically

significantly enriched among pathway transcriptional activities and all five categories of

radiomic features with adjusted p-values < 0.0001 (Appendix table C3). This implies that

transcriptional activities of genetic pathways modulate various aspects of tumor imaging

phenotype.

Table 9. 2: Numbers of statistically significant associations between genomic features of different platforms and radiomic features of different categories.

Feature Category	Gray Level Co-occurrence Matrix	Gray Level Run Length Matrix	Neighbor Intensity Difference	Intensity Direct	Size / Shape
Transcriptional activity of pathway	1709	304	131	1413	884
Copy number variation of pathway	196	37	28	161	62
Promoter region DNA methylation change of pathway	156	30	15	119	29
miRNA expressions	6	0	0	10	0
Mutated genes	16	5	0	36	0

9.3.1 Associations between Radiomic Features and Genetic Pathways

Appendix C include all identified associations involving transcriptional activities, gene

CNVs, and promoter region DNA methylation changes of all KEGG pathways. Figure 9.2

specifically presents that radiomic features are associated with cancer-related KEGG pathways(266) that cover multiple aspects of the cancer molecular system, such as signal transduction, cell growth and death, immune system, and cellular interactions and community. Figure 9.2a, 2b, and 2c show the associations of transcriptional activities, gene CNVs, and promoter region DNA methylation changes of cancer-related KEGG pathways, respectively. There are many interesting findings in Figure 9.2a indicating pathway transcriptional activities are correlated with and modulate multiple aspects of tumor imaging phenotype, and we elaborate on them below.

Figure 9. 2: Heatmap of associations between genomic and radiomic features.

This figure depicts statistically significant associations between radiomic features and (a)

transcriptional activities of cancer-related genetic pathways, (b) gene CNVs of cancer-related

genetic pathways, (c) gene promoter region DNA methylation changes of cancer-related

genetic pathways. In each heatmap, only genetic pathways and radiomic features with

statistically significant associations were shown. Each of the gray level co-occurrence matrix

features can be calculated using different offset parameter values, i.e. 1, 2, 3, 4, and 5, which

168

results in 5 different instances of a feature. Because the 5 instances of a feature were usually correlated, the directions (i.e. positive or negative) of the associations between a cancer-related pathway and the different instances of a radiomic feature were always the same. Thus, in the heatmaps, associations between different instances of a radiomic feature and a pathway could be collapsed into one association. If a pathway had an association with at least one instance of a radiomic feature, the association between the pathway and the radiomic feature was included in the heatmap. Percentile and quantile radiomic features from the intensity direct category were not included in the heatmaps for simplicity, because they have many instances with different percentile or quantile values.

9.3.2 Cell Growth and Death

Multiple associations related to cell growth and death are identified in our analysis. Transcriptional activities of ribosome genes are correlated with multiple aspects of tumor imaging phenotype, including (1) tumor texture heterogeneity characterized by positive association with *entropy* and negative associations with *energy 1*, *homogeneity*, and *homogeneity 2*, (2) tumor size features, including *convex hull volume*, *convex hull volume 3D*, *mass*, *maximum 3D diameter*, *mean breadth*, *number of voxel*, and *surface area*, and (3) tumor shape irregularity, characterized by negative associations with *roundness*, *sphericity*, and *convex*, and positive association with *spherical disproportion*. Ribosome genes support protein synthesis and are important for various cellular processes, such as cell proliferation and growth. Our result shows that they are more transcriptionally active in larger, more irregular and heterogeneous tumors. The apoptosis pathway takes a tumor suppressive role by eliminating damaged or redundant cells through activating caspases. Disruption or evasion of apoptosis

169

can lead to tumor initiation, progression or metastasis(270). Consistently, we find that the

transcriptional activity of apoptosis pathway is negatively associated with tumor size

(characterized by *convex hull volume*, *convex hull volume 3D*, *maximum 3D diameter*, *mean*

breadth, and *surface area*) and tumor shape irregularity (characterized by its positive

associations with *convex* and *sphericity*, and negative association with *spherical disproportion*).

9.3.3 Immune System

Pathways related to immune regulation, including pathways of natural killer cell

mediated cytotoxicity, T cell receptor signaling, B cell receptor signaling, antigen processing

and presentation, and chemokine signaling, are all negatively associated with tumor size

features. One possible explanation is that patients with larger tumors have a less active

immune system and therefore are unable to effectively destroy tumor cells and curb tumor

growth. Similarly, we find a correlation between immune system activity and tumor shape

regularity, as the pathway activities are positively associated with *sphericity* and *convex*, and

negatively associated with *spherical disproportion*.

9.3.4 Cellular Interactions and Community

Pathways related to cell adhesion molecules, cytokine-cytokine receptor interaction,

ECM-receptor interaction, adherens junction, gap junction, and focal adhesion regulate cell-cell

interaction and signaling acting as intercellular regulators and mobilizers of cells, and maintain

cell and tissue architecture that limits cell movement and proliferation, which are two important

factors in cancer progression. Aberrant activities of these pathways can lead to the

development and metastasis of many types of cancer, including HNSCC(271). We find that

their activities are negatively associated with multiple tumor size features, indicating smaller

tumors tend to have stronger activities of these pathways than large tumors. Activities of all these pathways, except gap junction, are also correlated with tumor shape regularity characterized by their positive associations with *sphericity* and negative associations with *spherical disproportion*.

9.3.5 Signal Transduction

The transcriptional activities of several molecular signaling pathways, including MAPK signaling pathway, TGF-beta signaling pathway, JAK-STAT signaling pathway, VEGF signaling pathway, WNT signaling pathway, and ERBB signaling pathway, are negatively associated with tumor size features, indicating that they are more active in small tumors than large tumors. Previous report (272) has suggested TGF-beta signaling as a potent tumor suppressor in HNSCC, which is supported by its negative association with tumor size identified in the current study. The activities of MAPK, TGF-beta, JAK-STAT, and VEGF signaling pathways are positively associated with tumor shape regularity.

Compared to pathway transcriptional activities, CNVs of cancer-related pathways have much fewer statistically significant associations with radiomic features (Figure 9.2b). CNVs of JAK-STAT signaling pathway, cytokine-cytokine receptor interaction, natural killer cell mediated cytotoxicity, and antigen processing and presentation genes are correlated with tumor shape regularity characterized by their positive associations with *convex* and *sphericity,* and negative associations with *spherical disproportion*. CNVs of apoptosis genes are positively associated with tumor texture homogeneity characterized by *homogeneity* and *homogeneity 2*, indicating tumors with heterogeneous texture may have fewer copies of apoptosis genes than tumors with homogeneous texture.

Figure 9.2c shows the statistically significant associations between radiomic features and promoter region DNA methylation changes of cancer-related pathways. DNA methylation changes of ribosome genes have the largest number of associations with radiomic features (first row in Figure 9.2c), including negative associations with two tumor size features *maximum 3D diameter* and *surface area*, and positive associations with tumor shape regularity (characterized by positive association with *sphericity* and negative association with *spherical disproportion*). The directions of these associations are opposite of those for the transcriptional activities of ribosome genes, which is expected, since methylation at promoter region usually negatively affects gene expression. In addition, we find that DNA methylation changes of three immune related pathways, i.e. natural killer cell mediated cytotoxicity, T cell receptor signaling pathway, and chemokine signaling pathway, are negatively associated with tumor shape regularity (Figure 9.2c). These are new results that may shed lights on the connection between immune pathways with radiomic phenotypes. We report the analysis scheme and more findings in Appendix Information Sections C4-6.

9.3.6 Associations between Radiomic Features and miRNA Expressions and Mutated Genes
9.3.6.1 MiRNA

Table S7 presents statistically significant associations between miRNA expressions and radiomic features. *MiR-320a* has been reported as a negative regulator of tumor invasion and metastasis(273). Its expression correlates with tumor texture homogeneity characterized by positive associations with *homogeneity* and *homogeneity 2* and negative associations with *entropy* and *global entropy*. The radiomic feature *global uniformity* measures the overall homogeneity of tumor pixel intensity(259) and is positively associated with the expressions of 8

miRNAs including both antitumorigenic/*antimetastatic* and oncogenic miRNAs. The

antitumorigenic/*antimetastatic* miRNAs include *miR-101*(274)*, miR-15b*(275)*,* and *miR-320a*;

the oncogenic miRNAs include *miR-106b* and *miR-25*(276), *miR-155*(277)*,* and *miR-378*(278);

the last miRNA *miR-7* is involved in multiple cancer-related signaling pathways and has been

reported with both oncogenic and antitumorigenic roles(276).

9.3.6.2 Somatic Mutation

Table S8 shows statistically significant associations between radiomic features and genes with

somatic mutations in at least 10 patients. *EP300* encodes the E1A binding protein p300, a

histone acetyltransferase regulating the transcription of genes involved in cell proliferation and

differentiation. Mutations in *EP300* have been reported for HNSCC and may contribute to the

disease initiation and progression(279). Our analysis shows somatic mutations in *EP300* are

negatively associated with *inverse variance* and positively associated with *median absolute*

deviation. *COL11A1* encodes one of the two alpha chains of type XI collagen that is an

essential component of the interstitial extracellular matrix. *COL11A1* may contribute to HNSCC

tumorigenesis and be a potential therapeutic target(280). We find mutations in *COL11A1* are

negatively associated with *inverse variance*.

We report the analysis schemes and more details about the identified associations

involving miRNAs and somatic mutations in Appendix Information Sections 7 and 8.

9.3.7 Predictions of Patient HPV Status and Disruptive TP53 Mutation Using Radiomic Features

We applied the random forest classifier(267) to predict the patient HPV status based on

tumor radiomic features. A two-tier five-fold cross-validation was used to tune the classifier

parameters and evaluate the generalization prediction performance. Predictive radiomic

173

features were selected through a recursive feature elimination scheme. Table 9. 3 shows the

mean and standard deviation of the Area Under the receiver operating characteristic Curve

(AUC) across 30 cross-validation trials, which measures the prediction accuracy. There is no

significant difference between the average AUCs obtained using different numbers of features

for prediction. The highest average AUC achieved is 0.71, while the average AUC using only

five features in each cross-validation trial still reaches 0.706. Using the same classification and

feature selection scheme, we predicted whether a tumor possessed any disruptive TP53

mutation, a biomarker in HNSCC development and treatment(255). Loss-of-function alterations

are dominant among the TP53 mutations in the cancer cases. All disruptive TP53 mutations

are loss-of-function alterations and only one of the non-disruptive TP53 mutations is a gain-of-

function alteration. Table 9. 3 shows the mean and standard deviation of obtained AUCs. The

highest average AUC is 0.641 with five features selected for prediction in each cross-validation

trial. See the Appendix Information Section C. 10 for details of the prediction and feature

selection scheme, and additional details of results, such as the most frequently selected

features for prediction and their frequencies.

Table 9. 3: Model performance.

Mean (standard deviation) of AUCs obtained through a two-tier five-fold cross-validation scheme that includes 30 cross-validation trials when different numbers of radiomic features were selected for prediction in each cross-validation trial.

Prediction target	All features	100 features	50 features	20 features	10 features	5 features
HPV status	0.701(0.13)	0.71(0.127)	0.697(0.133)	0.7(0.137)	0.71(0.133)	0.706(0.146)
Disruptive TP53 mutation	0.587(0.071)	0.594(0.095)	0.624(0.087)	0.627(0.111)	0.62(0.102)	0.641(0.112)

9.4 Discussion

Using TCGA and TCIA data, we conducted an exploratory yet comprehensive imaging-genomics study. To our knowledge, this is the first study that integrates radiomic features of CT images with whole-genome measurements depicting multiple layers of tumor molecular system for HNSCC. We report statistically significant associations between radiomic features characterizing multiple aspects of the tumor imaging phenotype and various genomic features (including transcriptional activity, CNV, DNA methylation, miRNA expression, and somatic mutation). The identified associations support existing knowledge related to HNSCC pathogenetic mechanisms and provide evidence for novel hypotheses on the relationship between tumor genomic mechanisms and subsequent tumor phenotypes that can be validated in future studies. Also, we attempted to use radiomic features to predict important molecular biomarkers in HNSCC, such as HPV status and disruptive TP53 mutation, with decent AUC values. These results provide basis for future investigations to establish the potential of using non-invasive imaging approach to probe the genomic and molecular status of HNSCC.

Compared to pathway transcriptional activities, much fewer statistically significant associations have been identified for pathway CNVs and DNA methylation changes (Table 9. 2 and Figure 9.2). There could be two reasons for this. First, transcriptional activity is closer to phenotype formation than CNV and DNA methylation in the process of molecular system regulating the development of phenotype. Basically, transcriptional activities can more directly influence the generation of various phenotypes, while CNVs and DNA methylation changes may have to function through transcription. Secondly, DNA mutation events, such as CNVs and

175

somatic mutations, are rarely shared across many patients, resulting in a small number of samples with the same mutation event that limits the statistical power for identifying potential associations.

Our study is based on CT images of 126 HNSCCs and their multi-layer whole-genome genomic data, which form a unique imaging-genomics dataset that was not available before TCGA/TCIA era. This unique dataset enables our novel investigation of associations between tumor phenotypes and multiple molecular layers for HNSCC. To our best knowledge, there is no other dataset including matched imaging data, multi-omics genomic data, and clinical data for HNSCC as our dataset does, on which we can repeat our analysis for validation. Our findings have been uploaded to http://www.compgenome.org/Radiogenomics/ as a public resource to facilitate future research on HNSCC imaging-genomics. Future studies can either use our results as evidences to support their hypotheses or validate our findings through new analyses and experiments. Although unique and novel, our imaging-genomics dataset is not large. Its sample size might limit the statistical power for identifying imaging-genomics associations and the accuracy of predicting tumor molecular status based on radiomic features. Nonetheless, we believe our study will pave ways for future HNSCC imaging-genomics investigation using more samples and advanced imaging technologies.

Bogowicz et al. also used radiomic features to predict HPV status for HNSCC and achieved an AUC of 0.78(281), which is in a similar range but higher than our HPV prediction accuracy (average AUC = 0.71). Multiple factors, such as different patient cohorts, can contribute to the difference of prediction performance in the two studies. Considering the cohorts used in both studies are not large (sample size < 150), the obtained prediction performances indicate the

176

potential of using imaging to probe tumor molecular status in the future, with the accumulation of imaging-genomics data and the development of imaging techniques.

More imaging-genomics analyses have been planned for HNSCC. One particularly interesting approach is to integrate genomics, epigenomics, and proteomics data simultaneously with imaging data to provide a more comprehensive depiction of how the multi-layer molecular system regulates and produces various tumor imaging phenotypes. Graphical models can be powerful tools for studying such complex relationship, due to their ability to model conditional dependence and competing regulatory factors(282).

This chapter is based upon:

10.1 Introduction

Thyroid cancer is the most common endocrine malignancy and its incidence continues to rise in both men and women (142). Estimated new thyroid cancer cases in women is 32,130 in 2021 compared to 9,100 in 1992 and 12,150 compared to 3400 in men, respectively (283, 284). The age adjusted incidence of thyroid cancer increased more than 3.8-fold to near 14 per 100,000 between 1973 and 2015 (285). Papillary (PTC) and follicular thyroid carcinomas are well-differentiated tumors and represent the most common thyroid cancer subtypes with good overall prognosis and response to treatment (286). However, a subset of these well-

differentiated tumors progress to more aggressive poorly differentiated (PDTC) and anaplastic thyroid cancer (ATC). PDTC and ATC represent a major clinical challenge due to the poor therapeutic outcomes with a median survival of less than 12 months in the majority of patients, despite the use of aggressive multimodality treatment (i.e. surgery, radiation, chemotherapy, and/or targeted therapy) (287, 288).

The identification and development of novel systemic agents is rarely driven by focusing on ATC alone; rather ATC is routinely incorporated into basket trials based on genomic and epigenetic events (289). This is precisely how the BRAF-MEK combination gained clinical traction in the context of ATC (67). However, despite substantial initial anti-tumor activity, most patients develop resistance to treatment over time, consistent with findings in other solid tumors such as melanoma (66). This presents a significant problem because translational efforts in basket trials cannot proceed with sufficient focus to identify novel and effective ATC targets.

Multiple studies published over the last decade have now provided a comprehensive picture of the genomic, epigenetic and transcriptional program which accompanies ATC development (290, 291). Unfortunately to date, ATC tumors have not demonstrated targetable mutations sufficiently distinct from other tumors (292, 293). Thus, we must re-assess and re-orient translational efforts for ATC. One approach is to evaluate the broad array of currently available agents with anti-solid tumor activity, which may demonstrate substantial efficacy in PDTC and ATC with already established safety profiles (i.e., drug repurposing).

Most previous drug identification and preclinical testing efforts in the context of ATC have been restricted by several deficiencies including: 1) limited availability of validated human cell lines with a known genomic and epigenetic background, 2) limited utilization of orthotopic models, and 3) limited availability of relevant patient derived xenograft (PDX) models (68). All three of these factors can severely impact the ability to identify promising systemic agents, both due to false positive and false negative results. For example, when targeted therapies such as inhibitors of BRAF, EGFR, or ALK are tested in cancer cells lacking BRAF, EGFR, or ALK alterations respectively, they are ineffective. However, these inhibitors are markedly effective in cancer cell lines, animal models, and human patient tumors bearing the corresponding genomic alteration. This is demonstrated by the distinct efficacy of BRAF inhibitors in tumors that harbor *BRAF* mutations. Evaluating such inhibitors in a limited panel of wild-type *BRAF* expressing cell lines would have easily generated a false negative result.

The increasing availability of both well-characterized PDTC and ATC human cell lines as well as increasing stocks of PDX models, allows us to effectively identify drugs for the deadly diseases. In this study, we utilized high-throughput drug screening (HTS) as an initial filter for subsequent preclinical testing and drug validation in PTC, PDTC, and ATC.(69). Our group has generated and authenticated a large panel of PTC, PDTC, and ATC cell lines along with two ATC PDX models (70-72). They were used to perform a hierarchical preclinical drug screen and validation, leveraging the complexity built into these preclinical models.

10.2 Materials and Methods

10.2.1 Cell lines

Twelve human thyroid cancer cell lines were included in this study (ATC n=7, PDTC n=1, PTC n=4). MDA-T85 (ATCC Cat# CRL-3354, RRID:CVCL_QW84) (70), MDA-T178, MDA-T187 (RRID:CVCL_A1CS), MDA-T192 were generated from tumors obtained from patients who underwent surgical treatment at The University of Texas MD Anderson Cancer Center (MDACC). MDA-T178 and MDA-T187 were derived from 78- and 74-year-old women, respectively, with a histopathologic diagnosis of ATC. MDA-T192 was derived from a metastatic paratracheal lymph node in a 65-year-old woman with PDTC. The surgical specimens were tested histopathologically to confirm the diagnosis, and single-cell suspension was generated as previously described (70). Genomic DNA was extracted from frozen tissue and cell lines using the Gentra Puregene kit (Qiagen # 158667). STR analysis for each cell line and its matching tissue was performed at the Characterized Cell Line Core Facility at MDACC. These STR profiles were then compared with those in the ATCC, the DSMZ, the JCRB, the RIKEN (RRID:SCR_001065), and the MDA databases for possible matches. The TPC-1 cell line (RRID:CVCL_6298) was kindly provided by Dr. Jerome Hershman (VA Greater Los Angeles Healthcare System, Los Angeles, CA). The K2 cell line was provided by Dr. D. Wynford-Thomas (Cardiff University, Cardiff, United Kingdom). Hth7 (RRID:CVCL_6289**)**, Hth104 (RRID:CVCL_A427), SW1736 (CLS Cat# 300453/p463_SW-1736, RRID:CVCL_3883), and U-Hth83 (RRID:CVCL_0046) were kindly provided by Dr. Jeffrey Myers (MDACC). The BCPAP cell line (DSMZ Cat# ACC-273, RRID:CVCL_0153) was purchased from DSMZ

(Braunschweig, Germany). The 8505C cell line (TKG Cat# TKG 0439, RRID:CVCL_1054) was purchased from ECACC. Cells from TPC-1, MDA-T85, MDA-T178, MDA-T187, MDA-T192, U-Hth83, and Hth104 were maintained in RPMI1640 medium (Sigma-Aldrich R8758) containing 10% fetal bovine serum (Sigma-Aldrich F0926), nonessential amino acid mixture (Cambrex BioScience MT25025CI), 1 mM sodium pyruvate (Fisher Scientific MT25000CI), and 2 mM L-glutamine in a 37°C incubator supplied with 95% air and 5% CO_2. K2 cells were maintained in DMEM/F12 medium (Sigma-Aldrich D8062) containing 10% fetal bovine serum and 2 mM L-glutamine. BCPAP cells were maintained in RPMI1640 medium containing 10% fetal bovine serum and 2 mM L-glutamine. Hth7 and SW1736 cells were maintained in MEM medium (Cambrex BioScience MT10010CV) containing 10% fetal bovine serum, nonessential amino acid mixture, 1 mM sodium pyruvate, and 2 mM L-glutamine. 8505C cells were maintained in MEM medium containing 10% fetal bovine serum, nonessential amino acid mixture, and 2 mM L-glutamine.

10.2.2 Screening Library

HTS of 257 agents was performed at the Gulf Coast Consortium's Combinatorial Drug Discovery Program at the Institute of Biosciences and Technology (IBT), Texas A&M University Health Science Center. The library includes 112 agents from the National Cancer Institute Approved Oncology Set V (NCI_AOD5) collection; the remaining 145 agents were acquired from commercial suppliers and assembled by IBT scientists to cover a wide range of potential targets. These agents were predominantly FDA-approved agents and investigational

compounds. All agents were prepared in 100% DMSO (Sigma–Aldrich D2650) at a stock concentration of 10 mM.

10.2.3 High-throughput screening assay

As performed previously (294), a total of 500-1000 cells of each cell line were suspended in 50 µl of medium per well and seeded into Greiner Black 384-well µClear plates using a Multidrop Combi liquid dispenser (ThermoFisher Scientific). The plates were kept at room temperature after seeding for 40-60 minutes prior to placing them into a cell culture incubator to form a monolayer overnight at 37°C in a humidified chamber with 95% air and 5% CO_2. After recovery, 50 nl of the agent was transferred into the wells using an Echo 550 acoustic dispensing platform (Labcyte). Cells from an untreated plate were fixed with 0.4% paraformaldehyde (Fisher Scientific #31901) and cell nuclei were stained with 4′,6-diamidino-2-phenylindole (DAPI, Sigma-Aldrich MBD0015) at the time of agent addition (Day 0) to provide the number of cells present per well at the time of treatment. In the primary screen, three concentrations were tested (0.01, 0.1, and 1 µM) with a fixed volume of DMSO (0.1% v/v) in replicates. Each assay plate contained a fixed concentration of the agents in addition to a negative control (0.1% DMSO), two positive controls (10 µM of cisplatin, Pharmachemie B.V #2962769 and carboplatin, Selleckchem S1215), and an 8-point dose response curve of the positive controls. After a 72-hour incubation with the agents, cells were fixed and nuclei were stained with DAPI using an integrated Hydrospeed plate washer (Tecan Life Sciences) and Multidrop Combi dispenser. Plates were imaged on an IN Cell Analyzer 6000 laser-based

confocal imaging platform (General Electric Healthcare Bio-Sciences) and nuclei counted using the algorithms developed using the IN Cell Developer Toolbox software (ver. 1.6).

10.2.4 Statistical analyses

Statistical analysis of assay performance was performed in accordance with the National Center for Advancing Translational Sciences (NCATS) Assay Guidance Manual (295). Briefly, a running statistical evaluation was performed on each plate throughout the course of the screening campaign to evaluate the consistency of results. Metrics evaluated included the rate of growth of the negative controls, the coefficient of variance of the positive and negative controls, and assay robustness determined from the Z' statistic. Assay reproducibility and experimental drift were determined using the minimum significance ratio calculated from the standard deviation of IC_{50} values of the on-plate positive control dose response curves. Pharmacologic data was normalized using the growth adjustment formula proposed by the Hafner *et al.* (296)

$$GR(c) = 2^{\frac{\log_2(x(c)/x_0)}{\log_2(x_{neg}/x_0)}} - 1$$

where *x(c)* was defined as the observed cell count at the end of the assay, x_0 was the median cell count at the time of treatment (Day 0), and x_{neg} the median cell count of the negative control at the end of the assay. This method of normalization effectively removed alterations in the rate of growth, allowing for more effective comparisons between cell lines, and differentiated cytotoxic from cytostatic effects.

To identify the most effective agents in each individual cell line, we selected those agents with maximal growth inhibition at each dose level (top 25th percentile) and subsequently used the non-parametric Mann–Whitney U test to compare the normalized index with other agents and controls. *P* values less than 0.05 were considered statistically significant. Furthermore, pharmacologic dose response data was summarized as an area under the curve (AUC) value calculated by numerically integrating growth-adjusted values described in the concentration-response curves. The data were fitted against a cascade of nonlinear regression models, each with different initialization criteria, to identify the best fit using a combination of R (Pipeline Pilot, RRID:SCR_014917, Dassault Systemes/Biovia, Vélizy-Villacoublay, France) software platforms. Mechanistic clustering was performed by merging pharmacologic data with an in-house database of mechanistic annotations. The core maintains a MySQL database of all compounds used. All our collections are from commercial sources. When a collection is purchased, the vendor supplies a file that contains the identification and location of every compound purchased; that is how we know which compounds match to which result, making it a 1:1 relationship. Most commercial vendors supply additional information such as known targets for each of the compounds when known. When this information is available, we include it within our internal database. We have, for certain projects, manually curated the metadata for the compounds screened through a literature review using PubMed and other on-line data sources such as the PubChem, PubChem Identifier Exchange Service, Drug Bank, ChEMBL, ChemSpider, FDA, and DTP. All of this information can be found in the 'mechanistic annotations' referred to in this work. We have attempted to record literature or vendor supported Target Class, Target(s), Process, and Pathway information to help us cluster

185

compounds into particular drug classes or signaling pathways. These data were then used to generate a factorized adjacency matrix that was subsequently rendered as a minimum spanning tree using the cluster, visNetwork, and Intergraph packages in R package implementing methods. Subsequent to the identification of agents with maximal growth inhibition in each cell line, we performed a confirmatory test for these agents using eight-point dose-response curves.

10.2.5 IC_{50} and Colony formation analysis

To determine the IC_{50} of each agent, cells (0.3-1×10^4) were plated in 48-well plates (Fisher Scientific #12-565-322) with 1 mL of medium in a $37°C$ incubator supplied with 95% air and 5% CO_2. Docetaxel (Accord Healthcare #00955-1020-01), LBH-589 (Selleckchem S1030), and pralatrexate (Selleckchem S1497) were added to cells 24 hours later and incubated for 72 hours at varying concentrations (6 replicates). We selected these three drugs because of successful growth inhibition in the tested cell lines used in the initial high throughput screening assay as well as the potential for future clinical implementation. MTT (Thiazoyl Blue Tetrazolium Bromide, VWR # 97062-380) dissolved in 0.8% NaCl solution (Sigma–Aldrich D8537) at 2 mg/mL was added to each well (0.1 mL) and incubated at $37°C$ for 4 hours. The liquid was then aspirated from the wells and discarded. Stained cells were dissolved in 0.5 mL of DMSO and their absorption at 570 nm was measured using a SPECTROstar or CLARIOstar plate reader. IC_{50} was determined using Prism 8.0 software.

For colony formation analysis, 100 or 200 cells were plated in 6-well plates (Fisher Scientific #087721B) in triplicate. The test agents were added to wells after 24 hours and was

186

then further incubated for 72 hours. Fresh media were then added to cells and incubated for an additional 5-7 days in an incubator supplied with 95% air and 5% CO_2 at 37°C. Colonies were stained with 0.05% crystal violet (Sigma-Aldrich C6158) in 10% buffered formalin (Fisher Scientific SF1004) and counted. Figures were generated using Prism 8.0 software.

10.2.6 *In vivo* testing of selected agents

All animal experiments were performed in accordance with protocols approved by the IRB and the Institutional Animal Care and Use Committee. Immunodeficient athymic *nu/nu* mice (Envigo #069) were used for the orthotopic (297) and PDX models. PDX models were generated from patients' surgical specimens implanted directly in the flank of the mice (G0). Once the tumor reached 1000 mm^3, it was subsequently expanded to additional mice for a total of three times (G1 to G3) to be deemed successfully established. MDA-ATC1 (298) was developed from the same ATC patient specimen used to generate the MDA-T187 cell line. MDA-ATC5 was developed from a 59-year-old man with ATC. Tumors were STR analyzed to confirm match to DNA from patient's tissues. Once tumors were established, mice were randomized into groups. Five treatments with 5 mg/kg docetaxel diluted in 0.8% NaCl and 20 mg/kg pralatrexate dissolved in 2% DMSO and 48% polyethylene glycol (PEG) 300 (Sigma-Aldrich #202371) were given once every three days by intraperitoneal injection. LBH-589 (dissolved in 2% DMSO + 48% PEG 300) was given daily for 5 days at 20 mg/kg (first cycle), followed by a rest period of 2 days, and then daily for 5 days at 10 mg/kg (second cycle), by intraperitoneal injection (299). Control mice for docetaxel were treated with 0.8% NaCl, while the LBH-589 and pralatrexate control mice were treated with 2% DMSO + 48% PEG 300.

Tumor growth was monitored by Xenogen (IVIS 200 imaging system, Caliper Life Sciences, Hopkinton, Massachusetts) in the presence of D-luciferin (Fisher Scientific L2912) using Living Image 3.0 software for orthotopic models. Tumor volume was measured by caliper for PDX models and calculated using the formula (V = length × width × depth).

10.2.7 Mitotic count and immunohistochemistry

The tumor specimens from orthotopic and PDX models were collected and fixed in 10% neutral buffered formalin. Fixed tissues were processed into 5 µm thick sections, stained with hematoxylin and eosin (H&E), and examined microscopically by a head and neck pathologist using a BX41 Olympus microscope (Olympus, Tokyo, Japan) and an Aperio (Leica Biosystems, Wetzlar, Germany) digital image scanner. Mitotic count was determined as described previously (300). Briefly, 10 high-power fields were examined under microscope from H&E stained slides and mitotic cells were counted. Immunohistochemistry (IHC) analyses were performed against human-specific Ki-67 (DAKO #M7240 or Cell Signaling Technology #9027) and cleaved caspase 3 (Cell Signaling Technology #9579). Diaminobenzidine was used as a chromogen for antigen localization. Ki-67 and cleaved caspase 3 positive cells were counted manually from 6 and 4 high-power fields, respectively. The percentage of positive cells was calculated using the following formula: Total number of positive cells/(Total number of positive cells + Total number of negative cells) * 100. Graphs were generated using Prism 8.0.

10.3 Results

10.3.1 Relative drug effectiveness as a function of dose and tumor mutational status

Twelve human thyroid cancer cell lines were used in this study including seven ATC, one PDTC, and four PTC lines ($BRAF^{V600E}$ and $TP53$ mutational status summarized in Table 10.1). After HTS of 257 agents, we were able to identify the most effective compounds (based on their inhibition categories) for each cell line by a tree-structure analysis (Figure 10.1A). Using this analysis, we identified relationships between thyroid cancer type, individual agent dose, and $BRAF^{V600E}$ and $TP53$ mutational status. For example, at 0.1 µM, the most effective classes of agents against ATC cell lines were anti-metabolites, inducers of reactive of oxygen species (ROS), proteasome inhibitors, microtubule inhibitors, heat shock protein (HSP90) inhibitors, and Polo-like kinase 1 (Plk1) inhibitors (Figure 10.1B). At the lower, 0.01 µM dose, only anti-metabolites, proteasome inhibitors, and microtubule inhibitors remained effective. Similar to ATC, all tested PTC cell lines demonstrated sensitivity to proteasome inhibitors, microtubule inhibitors, ROS inducers, HSP90 inhibitors, targeted kinase inhibitors, and histone deacetylase (HDAC) inhibitors at 0.1 µM. However, only proteasome inhibitors and microtubule inhibitors remained effective at 0.01 µM. Several classes of agents including targeted kinase inhibitors, proteasome inhibitors, and microtubule inhibitors demonstrated activity regardless of $BRAF^{V600E}$ and $TP53$ mutational status. In addition, several classes including antimetabolites, HSP90 inhibitors, and ROS inducers exhibited activity regardless of the $BRAF$ mutational status, while anthracenediones and HDAC inhibitors had preferential activity in wild-type (non-mutated) $BRAF$ (Figure 10.1C). HDAC inhibitors were effective in cell lines that exhibited wild-type $TP53$ status while anti-metabolites and vinca alkaloids were most effective in the context of $TP53$ mutations.

Table 10. 1: Summary of cell lines and PDX models with their *BRAF* and *TP53* mutational status.

Cancer type	Cell line/PDX	Name	*BRAF*	*TP53*
PTC	Cell line	TPC-1	WT	WT
	Cell line	K2	V600E	WT
	Cell line	BCPAP	V600E	D259Y
	Cell line	MDA-T85	V600E	WT
PDTC	Cell line	MDA-T192	WT	WT
ATC	Cell line	MDA-T178	WT	WT
	Cell line	U-Hth83	WT	Y236C & P153fs
	Cell line	Hth7	WT	G245S
	Cell line	MDA-T187	V600E	K132N
	Cell line	SW1736	V600E	No expression, Q192*
	Cell line	Hth104	V600E	No expression
	Cell line	8505C	V600E	R248G
	PDX	MDA-ATC1	V600E	K132N
	PDX	MDA-ATC5	WT	WT

The mutation status of *BRAF* and *TP53* was determined by whole exome sequencing, Sequenom, or Sanger sequencing. The expression of *TP53* in Hth104 cells was determined by Western blot analysis after failed Sanger sequencing. MDA-ATC1 was generated from the same patient who gave rise to MDA-T187 cell line and carrying the same BRAF and TP53

mutations as determined by whole exome sequencing. Abbreviations: WT: wild-type; PTC: papillary thyroid carcinoma; PDTC: poorly differentiated thyroid carcinoma, ATC: anaplastic thyroid carcinoma; fs: frame shift; *: nonsense mutation.

Figure 1A

Figure 1 B

C

192
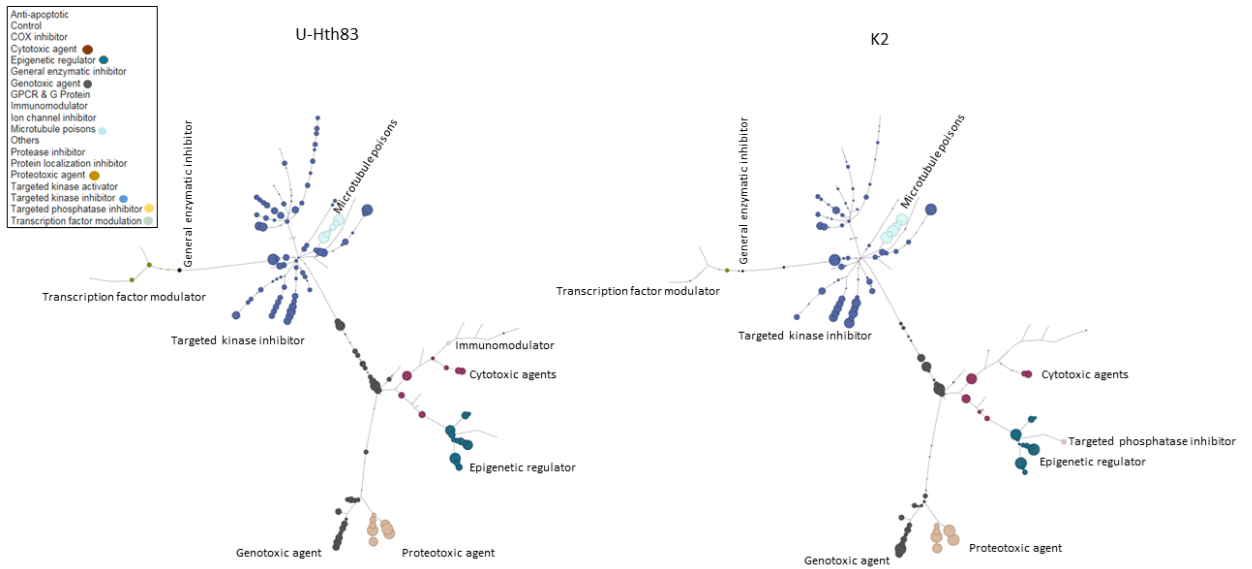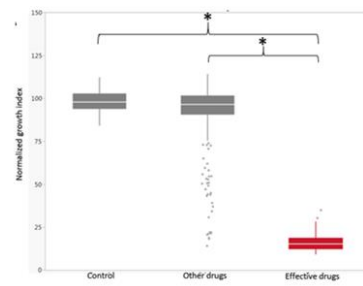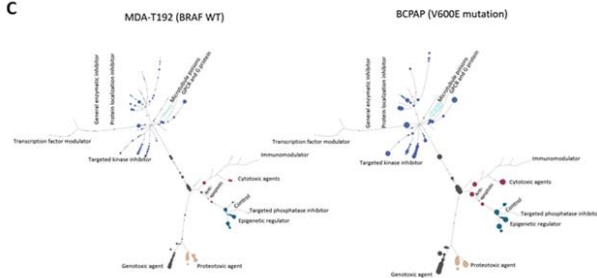
Figure 10. 1: HTS analysis.

Analysis of HTS. **A**, Tree analysis for U-Hth83 (left) and K2 (right) cells after HTS where the size of the colored data point dots represents relative effectiveness of each individual agent. A larger the dot indicates an increased effect. Each class with major effects were color coded for easier identification. **B**, Boxplots of effective drugs in the initial screen at 0.1 μM concentration compared with DMSO (Control), other ineffective drugs, and the effective drugs. * indicates statistical significance $P<0.0001$ for both. **C**, A comparison of the activities of different classes of agents using tree analysis in a *BRAF*^{WT} (MDA-T192) versus *BRAF*^{V600E} mutated BRAF cell line (BCPAP).

We selected seventeen agents (Table 10.2) for further efficacy testing in all twelve cell lines (sample outputs for U-Hth83 and K2 cell lines can be found in Figures 10.2A and 10.2B, respectively). The selection criteria included the level of agent activity in the tested cell lines as well as persistent activity at lower concentrations. Most of the seventeen agents selectively inhibited cell growth in a dose-dependent manner, except for cabazitaxel which did not show any change in the rate of cell growth in both the U-Hth83 and K2 cell lines. Vinblastine sulfate did not change the growth rate of U-Hth83 cells under any of the tested doses, while pralatrexate did not change the growth rate of K2 cells. All were consistent with the results from the initial screening.

Table 10. 2: Agents selected for retesting.

Inhibition category	Agents
Antifolates	Pralatrexate

HDAC Inhibitor	JNJ-26481585, LBH-589, NVP LAQ824
HSP90 Inhibitor	NVP AUY922
Microtubule inhibitor	Cabazitaxel, Docetaxel, Paclitaxel, Vinblastine sulfate, Vincristine sulfate
PLK1 inhibitor	BI 2536
Proteasome inhibitor	BORTEZOMIB, Carfilzomib
Protein kinases inhibitor	STAUROSPORINE
Pyrimidine analog	Gemcitabine hydrochloride
ROS inducer	ELESCLOMOL
Topoisomerase inhibitor	Mitoxantrone

Agents were selected after stringent statistical analysis from 257 potential candidates. They were listed by their inhibitory mechanisms.
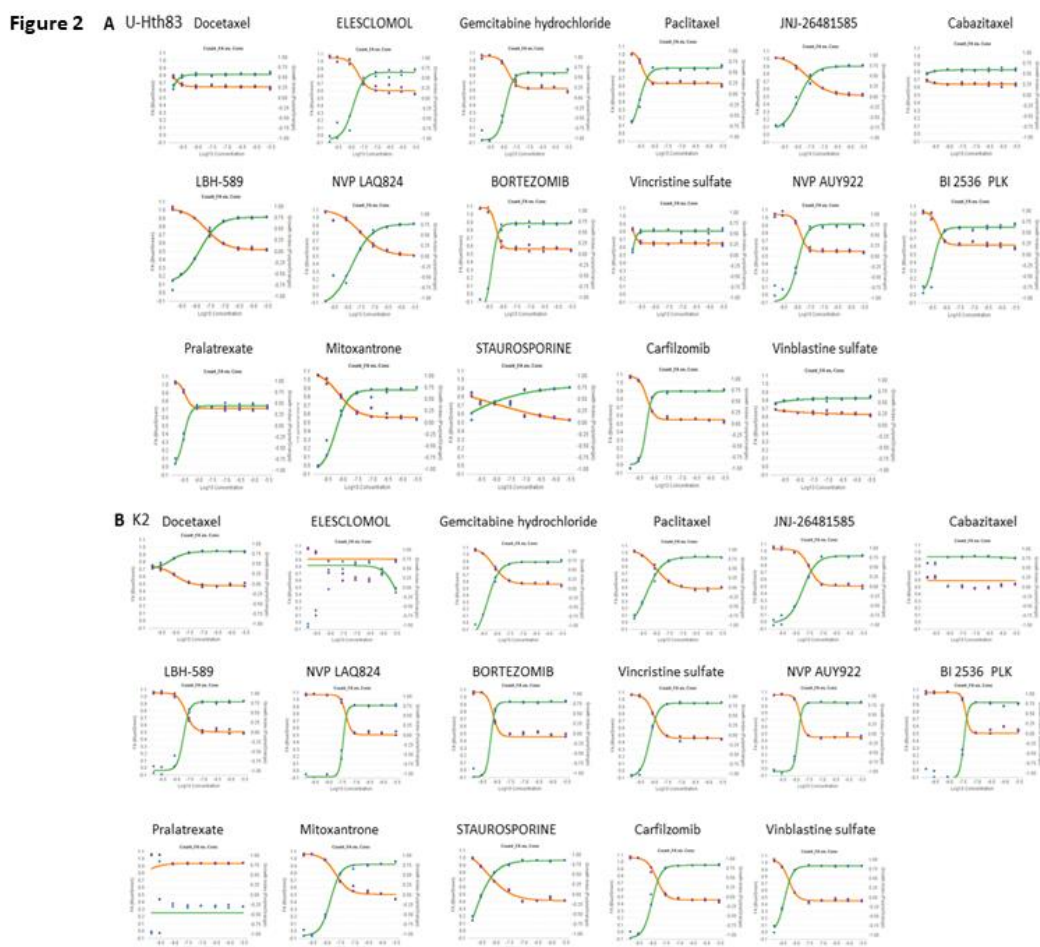
Figure 10. 2: Dose-response curves.

Confirmatory eight-point dose-response curves for selected agents against U-Hth83 (**A**) and K2 (**B**) cell lines. The green curves indicated the fraction of cells affected (FA) by the agents and the orange curves indicated the cell growth index (GI).

195

10.3.2 *In vitro* validation of selected compounds

Three agents, consisting of a microtubule inhibitor (docetaxel) (301), an antifolate (pralatrexate) (302), and a HDAC inhibitor (LBH-589/panobinostat) (303), were chosen to be further analyzed based on the screening data and their existing FDA approval for other non-thyroid cancers. Two thyroid cancer cell lines, U-Hth83 (ATC; $BRAF^{WT}$, $TP53^{P153fs}$) and K2 (PTC; $BRAF^{V600E}$, $TP53^{WT}$), were utilized for IC_{50} measurements which were used to corroborate the HTS data (Table 10.3). To further validate the effects of the three agents in terms of growth inhibition, a colony formation assay was used in the U-Hth83 (Figure 10.3A) and K2 cell lines (Figure 10.3B). We found that all three agents were able to decrease the number of colonies formed in both cell lines in a dose-dependent manner at nanomolar concentrations, with the exception of pralatrexate in K2 cells.

Table 10. 3: IC_{50} of selected agents.

Cancer type	Cell line	Drug	Average IC_{50} (nM)
PTC	K2	Docetaxel	2.12±0.54
		LBH-589	0.79±0.54
		Pralatrexate	n/a
ATC	U-Hth83	Docetaxel	1.02±0.26
		LBH-589	0.06±0.01
		Pralatrexate	1.35±0.11

To determine the IC_{50} of each agent, docetaxel, LBH-589, or pralatrexate were added to cells for 72 hours at varying concentrations (6 replicates). Concentrations were selected based on the initial high throughput screening assay. After drug treatment, MTT was added to stain cells followed by DMSO and

absorption at 570 nm was measured using a SPECTROstar or CLARIOstar plate reader. IC_{50} was determined using Prism 8.0 software. Average IC_{50} was determined from three independent assays. n/a: the IC_{50} was beyond the range of the cell proliferation assays (10 μM).
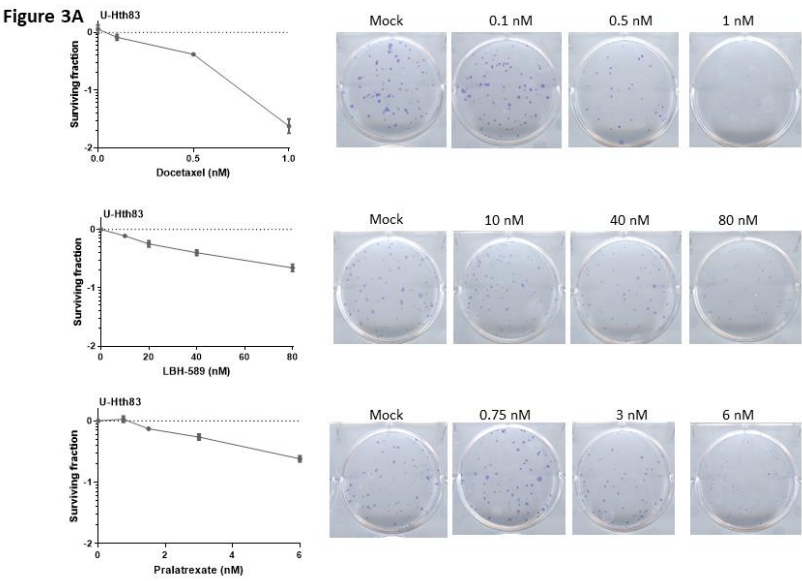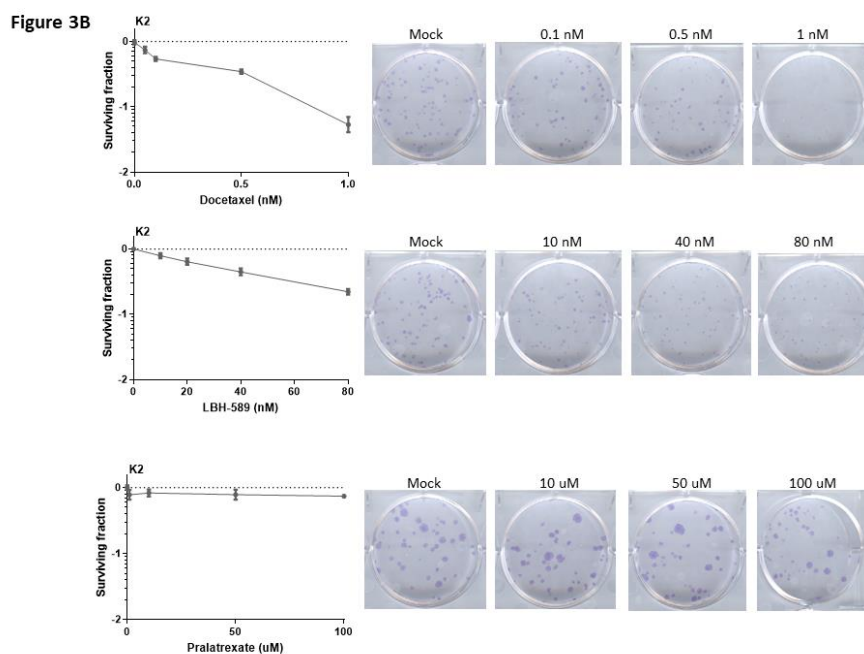
Figure 3A

Figure 10. 3: Colony formation assay.

Detecting cell growth by colony formation assay after docetaxel, LBH-589, and pralatrexate treatments. U-Hth83 (**A**) and K2 (**B**) cells (100 cells/well) were plated in 6-well plates in triplicates and only one well was shown here as an example. Docetaxel, LBH-589, and pralatrexate at different concentrations were added to cells 24 hours later for 72 hours. After 72-hour treatment, agents were removed, and fresh media were added to cells. Cells were then incubated for up to 7 days without disturbance to allow colonies to grow. To visualize colonies, cells were stained with 0.05% crystal violet in 10% formalin. Controls were cells without agent treatment. Colony numbers were converted to surviving fractions by Prism after transforming colony numbers with log.

10.3.3 *In vivo* validation of selected compounds

Docetaxel, pralatrexate, and LBH-589 anti-tumor activity was tested in orthotopic U-Hth83 or K2 tumors. LBH-589 significantly inhibited tumor growth in both U-Hth83 and K2 models (Figures 10.4 and 10.5A). Docetaxel inhibited U-Hth83 tumor growth (Figures 10.4 and 10.5B), while pralatrexate was able to inhibit K2 tumor growth (Figures 10.4 and 10.5C). No significant changes in tumor volumes were detected in K2 mice treated with docetaxel and in U-Hth83 mice treated with pralatrexate. To further reinforce our findings in the orthotopic model, we tested the three agents in two ATC PDX models, MDA-ATC1 ($BRAF^{V600E}$, $TP53^{K132N}$), and MDA-ATC5 ($BRAF^{WT}$, $TP53^{WT}$) (Table 10.1). Significant tumor growth inhibition was detected in MDA-ATC1 and MDA-ATC5 following LBH-589 and pralatrexate treatments (Figure 10.4), while docetaxel led to a significant tumor growth inhibition in MDA-ATC1.
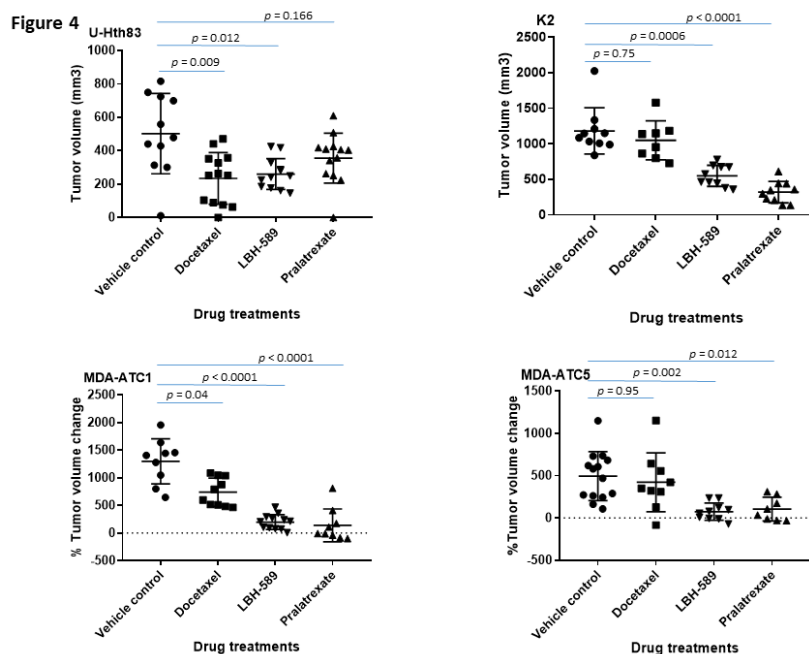
Figure 10. 4: Boxplots of the drug effect on orthotopic and PDX models.

Suppressing tumor growth by docetaxel, LBH-589, and pralatrexate in orthotopic (top) and PDX (bottom) models. **Top**, U-Hth83 (left) and K2 (right) cells carrying luciferase (5×10^5) were injected into nude mice thyroid orthotopically and tumor growth was monitored by Xenogen twice a week. Treatment started on day 7 for vehicle control (12 mice for U-Hth83 and 10 mice for K2), 5 mg/kg docetaxel (13 mice for U-Hth83 and 8 mice for K2), and 20 mg/kg pralatrexate (13 mice for U-Hth83 and 10 mice for K2). Docetaxel and pralatrexate were given once every three days by intraperitoneal injection for total of five treatments. LBH-589 was given once a day for 5 days at 20 mg/kg (first cycle), rested for 2 days, and then once a day for 5 days at 10 mg/kg (second cycle) by intraperitoneal injection (12 mice for U-Hth83 and 10 mice for K2). Tumor volume (*ex vivo*) was calculated after mice were euthanized by caliber and graph was generated by Prism. *P* values were calculated by Student's t-Test. **Bottom**, PDX models of MDA-ATC1 (left) and MDA-ATC5 (right) were treated with docetaxel (10 mice for MDA-ATC1 and 9 mice for MDA-ATC5), LBH-589 (12 mice for MDA-ATC1 and 10 mice for MDA-ATC5), or pralatrexate (9 mice for MDA-ATC1 and 8 mice for MDA-ATC5). Vehicle controls were 10 mice for MDA-ATC1 and 16 mice for MDA-ATC5. The doses and treatment schedules for PDX models were the same as described for the orthotopic models. SubQ tumor was measured by caliber 2-3 times weekly. Percentage of tumor volume change was determined by correction with the starting tumor volume.

Figure 5A

U-Hth83

	Controls		LBH-589	
	791	795	780	800

K2

	Controls		LBH-589	
	830	848	838	850

Before treatment

After 1st cycle

After 2nd cycle

Ex vivo tumor

Figure 5B U-Hth83

	Controls for Docetaxel		Docetaxel		Controls for Pralatrexate		Pralatrexate	
	821	823	781	782	791	795	706	712

Before treatment

After 2 treatments

After 3 treatments

After 4 treatments

After 5 treatments

Ex vivo tumor

201

Figure 10. 5: Images of U-Hth83 and K2 orthotopic tumors by Xenogen and pictures of *ex vivo* tumors.

Tumor cells (U-Hth83 or K2) were inoculated into mice thyroid orthotopically as described in Materials and Methods. Images of Xenogen were shown before treatment and after first and second cycles for LBH-589 or after 2-5 treatments for docetaxel and pralatrexate. Images of *ex vivo* tumors were shown underneath. Two mice from each group were shown here as examples. **A**, LBH-589 treatment in both U-Hth83 and K2. **B**, Docetaxel and pralatrexate treatments in U-Hth83. **C**, Docetaxel and pralatrexate treatments in K2.

Agent toxicity evaluated as a function of changes in animal weight was moderate. LBH-589 significantly reduced mouse weight in all four mouse models by up to 12% after the first cycle of treatment at 20 mg/kg (Figure 10.6), while pralatrexate significantly decreased mouse

weight in the MDA-ATC5 mice. To ensure mice survival and complete our treatment plan, LBH-589 dosage was reduced to 10 mg/kg for the second cycle of treatment.
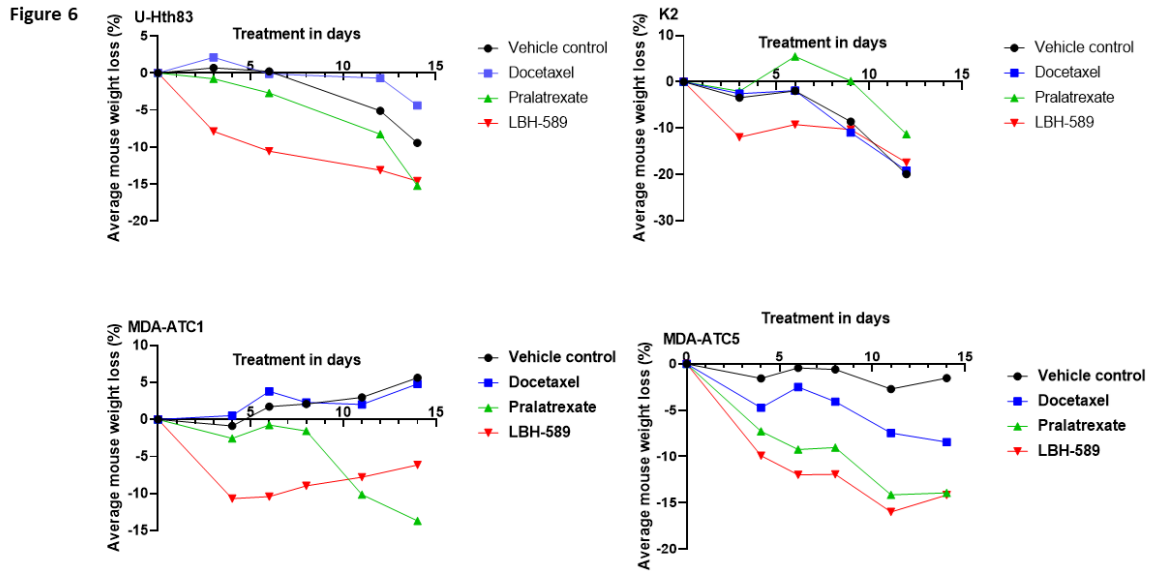
Figure 10. 6: Mice weights as a measurement of drug toxicity.

Mice weights from orthotopic (top) and PDX (bottom) as a measurement of agent toxicity. **Top**, mice inoculated withU-Hth83 (left) and K2 (right) cells orthotopically were weighed before agent treatments, 2-3 times weekly during treatment, and after all treatment. Percentage of average mouse weight loss was corrected with the mouse weight before treatment. **Bottom**, mice weights from PDX models MDA-ATC1 (left) and MDA-ATC5 (right) were shown after correction from weight before treatment.

Orthotopic and PDX models were further examined for apoptosis after drug treatment through IHC of cleaved caspase 3 (Figure 10.7A). Using pralatrexate as an example, we detected an increase in cleaved caspase 3 positive cells in both orthotopic (K2) and PDX (MDA-ATC1) models after drug treatment compared to controls. For proliferation of orthotopic and PDX models after drug treatment, IHC of Ki-67 (Figure 10.7B) and mitotic count (Figure 10.7C) were determined. IHC of Ki-67 demonstrated that the Ki-67 positive cells decreased in both orthotopic (K2) and PDX (MDA-ATC1) models after pralatrexate treatment, compared to controls (Figure 10.7B). Mitotic count identified the number of cells undergoing mitosis and was used as a measurement of cell proliferation. We detected a dramatic decrease in mitotic count in both models after pralatrexate treatment when compared to control tumors (Figure 10.7C). All of these results confirmed that after pralatrexate treatment tumor cells have a decreased proliferation and increased apoptosis in both orthotopic and PDX models and these results supported our observation of a decrease in tumor volume.
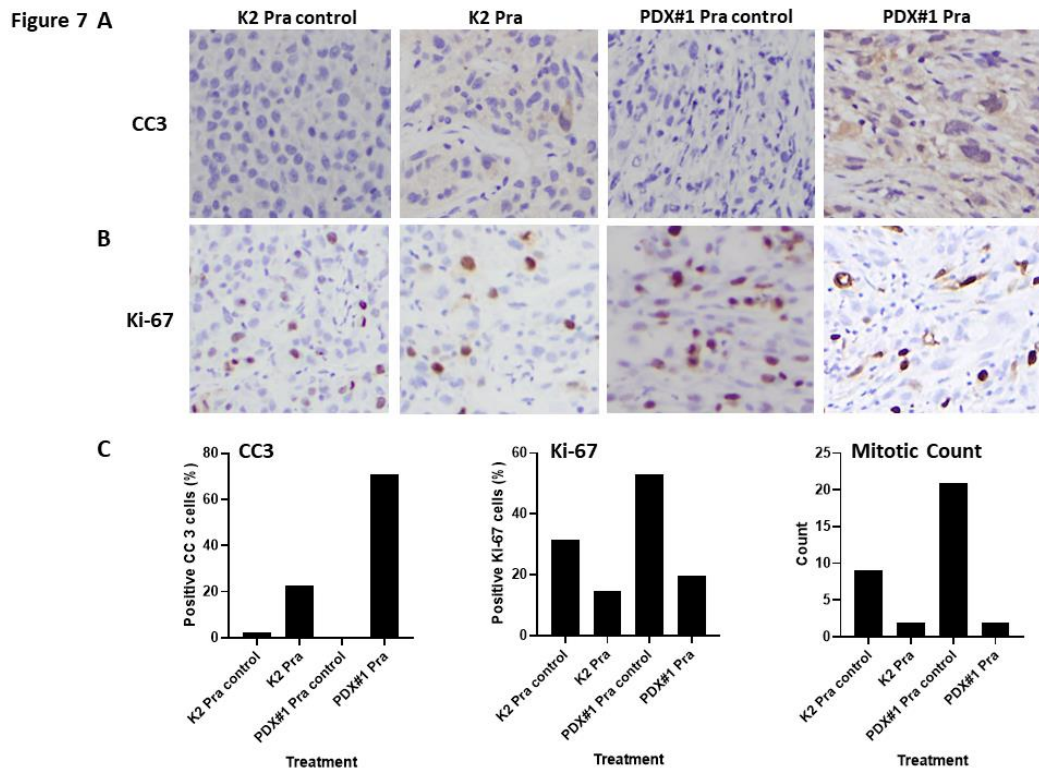
Figure 10. 7: IHC of cleaved caspase 3 and Ki-67.

IHC of cleaved caspase 3 (CC3) as an indicator of apoptosis and IHC of Ki-67 and mitotic count as an indication of proliferation. Tumors from the orthotopic model K2 and the MDA-ATC1 PDX model (PDX#1) after treatment with pralatrexate are shown. All graphs were generated using Prism. IHC staining with CC3 (A) or Ki-67 (B) in K2 and PDX#1. C, percentage of CC3 positive cells (left) was counted from four high power fields and calculated using the following formula: Total number of positive cells/(Total number of positive cells + Total number of negative cells) * 100. Percentage of Ki-67 positive cells (middle) was counted from six high

power fields and calculated using the same formula as for CC3. Mitotic count (right) was determined from ten high power fields.

10.4 Discussion

The potential of precision oncology is maximized in the context of "magic bullets", compounds targeted to a specific protein that ideally is mutated or fused in a manner distinct from the normal variant. These compounds are subsequently matched to tumors demonstrating the target event (i.e., mutation, fusion, amplification). BRAF inhibitors were first shown to have profound anti-tumor activity in the context of melanoma more than a decade ago (304, 305). At the time, the short term efficacy of BRAF inhibitors in the context of *BRAF*-mutant disease provided tremendous advancement in the treatment of a disease without any meaningful systemic option (304, 305). However, tumors developed resistance bypassing BRAF through increased MEK activity (306). The combination of BRAF and MEK inhibitors of FDA approved drugs for ATC (Vemurafenib, Dabrafenib, and Trametinib) attacked this resistance mechanism, and the combinatorial approach has now become standard of care for patients with BRAF-mutated advanced melanoma, with excellent, and fairly durable effects on progression free and overall survival (307).

Variable therapeutic efficacy in a subset of tumors is largely a function of intrinsic tumor biology (308), which provides the principal rationale for basket trials. Although this is primarily applied to targeted agents such as BRAF inhibitors, intrinsic tumor biology can also drive response to conventional cytotoxic agents (309). We sought to leverage a broad preclinical

206

platform for PDTC and ATC to identify and evaluate potentially effective systemic agents. Our findings demonstrate that HTS can effectively identify distinct classes of systemic agents that have a variable effect against thyroid cancer cell lines with variable histopathologic and mutational profiles. Although limited to 12 cell lines, this approach can be rapidly scaled to cell line banks in excess of 40-50 cell lines, providing a robust interface between relative drug effectiveness and molecular background as has been demonstrated by other groups (310). However, this represents simply a first step in a preclinical testing process which must support clinical trial development. *In vitro* screens fail to account for the significant modulatory effects of the tumor microenvironment, potentially generating false positives, and more concerning, false negative results, which could result in loss of potentially effective agent combinations (311-319). Variability of each mouse's individual response to the tested agents was expected (320). In a recent study by Ghosh *et al.*, following HTS, the effect of a BRAF inhibitor with a multitargeting TK inhibitor was analyzed and demonstrated their synergistic effect on 4 cell lines using both *in vitro* and *in vivo* (orthotopic) models. That study was limited to targeting BRAF-mutated disease, which only represents approximately 35% of the ATC population (321), and the HTS was composed of a select 32 drugs. In our study, the goal was to identify novel classes of drugs that would be useful against both *BRAF*[V600E]-mutated and wild-type ATC. HTS was augmented by *in vitro* validation, but most importantly, validation under *in vivo* conditions using the gold standard preclinical approach which combines both orthotopic models with PDX models. Furthermore, 257 agents were used in the initial HTS and we were able to identify the agents that showed potent activity against most cell lines. We validated the activity of a selected set of seventeen agents after stringent statistical analyses that showed the strongest

207

efficacy using a confirmatory eight-point dose-response curve. Three of the seventeen agents were chosen for a more detailed analysis as they were already FDA-approved to treat non-thyroid cancers.

LBH-589 (HDAC inhibitor), approved for the treatment of multiple myeloma (303), was the most effective agent in terms of cell growth inhibition *in vitro* in both tested cell lines, as well as in terms of tumor growth inhibition *in vivo* in all four mouse models (two orthotopic and two PDX models). Combining our current findings with those of Catalano *et al.* we report significant anti-tumor LBH-589 effects in total of 5 distinct ATC cell lines *in vitro*, 3 xenograft models (1 flank and 2 orthotopic), and 2 PDX models, clearly making this agent a strong candidate for clinical trial consideration (322). LBH-589's described effects on cell cycle arrest make it an excellent candidate for combinatorial strategies with radiation, currently a mainstay of ATC multi-modality treatment (323, 324).

Pralatrexate (antifolate/antimetabolite), approved for peripheral T-cell lymphoma (302), significantly inhibited tumor growth in both PDX models (MDA-ATC1 and MDA-ATC5), but did not consistently inhibit *in vitro* and *in vivo* growth in the human cell line models making it potentially less attractive as a clinical agent. Although pralatrexate showed significant cell growth inhibition in U-Hth83 cells *in vitro*, U-Hth83 orthotopic tumor growth was not inhibited *in vivo*. Interestingly, the opposite was seen with the K2 cells where cell growth *in vitro* was not inhibited significantly, while inhibition occurred in the orthotopic tumor model. The selective inhibitory effect of pralatrexate in the K2 orthotopic tumors may be related to differences in the tumor microenvironment. As such, we cannot conclude that the inhibitory effect of pralatrexate

208

was tumor-type specific or *BRAF*/*TP53*-mutation specific. Our results of proliferation and apoptosis after pralatrexate treatment confirmed that tumors have decreased proliferation and increased apoptosis in both orthotopic and PDX models when compared to controls. Since the mechanism of action for pralatrexate involves preferential accumulation in actively dividing cells inhibiting the function of critical enzymes involved in DNA synthesis and inducing cell death (302), these cellular functions are likely associated with other signaling transduction/metabolic pathways and are not dependent on *BRAF* and *TP53*.

Docetaxel (microtubule inhibitor), approved for the treatment of multiple cancers including breast cancer, non-small-cell lung cancer, and squamous cell carcinoma of the head and neck (301), effectively inhibited colony formation in both U-Hth83 and K2 cell lines, but only managed to inhibit growth in the U-Hth83 orthotopic and MDA-ATC1 PDX models. Interestingly, both U-Hth83 and MDA-ATC1 have *TP53* mutations, suggesting that docetaxel may have a selective effect. Functional *TP53* was found to induce apoptosis in docetaxel-treated prostate cancer cells (325). Together with our findings, docetaxel may be targeting p53 signaling transduction pathway and regulating cell survival.

Significant toxicity measured by weight loss was expected in mice treated with LBH-589, as previously reported (303, 322). LBH-589 treatment for our *in vivo* models started at 20 mg/kg for the first five days (first cycle) following the manufacturer's recommendation (299). Significant weight loss was observed after the first cycle of treatment, which prompted us to reduce the dose to 10 mg/kg during the second cycle to ensure study completion and mouse survival. Similar weight loss with LBH-589 (8% at 20 mg/kg and 13% at 30 mg/kg) was also

209

detected by Catalano *et al.* when they treated mice with CAL-62 cells (ATC) injected

subcutaneously (322), while increased mortality was observed at above 10 mg/kg in mice with

graft-versus-host disease (303). Dose adjustments were not required for pralatrexate and

docetaxel. In multiple myeloma patients treated with LBH-589, although weight loss *per se* was

not one of the major side effects, diarrhea was found in 68% of patients *vs* 42% on placebo and

vomiting in 26% of patients compared to 13% on placebo from the Phase III PANORAMA 1 trial

(326).

Although HTS was effective for identifying agents for additional comprehensive testing,

there are known limitations of *in vitro* HTS. Even when using robotic-based assays, there are

technical challenges to screening large libraries of compounds across multiple cell lines, which

is essential to account for genomic and epigenetic heterogeneity. However, these large-scale

screening efforts may identify false-positive candidates. We addressed this possibility by using

four distinct *in vivo* models (two orthotopic and two PDX models), while employing large

numbers of mice per test group (8-16 per group) to minimize potential experimental variations.

Given the breadth of our cell line and PDX model inventory, we could match genetic

backgrounds for the cell lines used *in vitro* and *in vivo* (orthotopic model) with the PDX models,

making our overall agent discovery approach as robust as possible.

In conclusion, we report a comprehensive approach to identifying novel treatments for

thyroid cancer, specifically ATC. Following HTS with 257 agents, we identified three candidate

agents and performed extensive *in vitro* and *in vivo* analyses, culminating with a large-scale

preclinical trial in four mouse models, two orthotopic and two PDX models. HDAC inhibitor,

LBH-589, appeared to have the most effective tumor growth inhibition on thyroid cancer (both ATC and PTC regardless of *BRAF* and *TP53* mutations in all four *in vivo* models). The inhibitory effect of docetaxel *in vivo* was specific for *TP53*-mutated tumors alone, while pralatrexate was effective in both ATC and PTC regardless of *BRAF* and *TP53* mutation status. Our work demonstrates the feasibility of using this systematic approach for preclinical *in vivo* drug testing and potential combination with FDA approved drugs in future. This platform provides an avenue for the identification of novel agents, validation, and resistance evaluation. Utilization of immunodeficient PDX models and immunocompetent murine models in the future facilitates personalized therapeutics development as a strong justification for proceeding to human clinical trials. Our study provides value to the field in two somewhat distinct yet overlapping ways. First, it demonstrates that HTS can identify potentially effective compounds against the PTC-ATC disease spectrum which have already been introduced into a clinical setting for other malignancies. This is important, because it can prompt clinicians to revisit "old" drugs using new combinatorial approaches, particularly by leveraging combinations of targeted (BRAFi) and non-targeted agents (i.e. docetaxel) and through combinations with immune checkpoint inhibitors (ICIs) which is in fact the current clinical strategy at our institution. Second, it identifies existing compounds (i.e. HDAC inhibitors) which, although not currently employed in clinical practice, may be a viable combinatorial strategy for early phase, exploratory clinical trials with a reasonable toxicity profile. Following our methodology, others can employ similar approaches to identify novel classes of systemic agents for the treatment of ATC, as well as other malignancies.

Chapter 11. Discussion

11. 1 General Summary

This work had a clinical and a translational component. In the clinical component, we showed that the currently available clinical imaging modalities can be successfully used to adapt RT dose during treatment according to the tumor response, predict oncologic disease outcomes, characterize RT-induced toxicity, and identify the patterns of disease failure. We used anatomical T2w MRI for the RT dose adaptation purpose. Our findings showed that after proper standardization of the immobilization and image acquisition techniques we can achieve high geometric fidelity of the images. These images can then be used to monitor the shrinkage of the GTV during the RT course and optimize the clinical target volumes accordingly. Our results showed that this MR-guided dose adaptation technique has a dosimetric advantage over the standard of care and was associated with a reduction in normal tissue doses that translated into a reduction of the odds of dysphagia ≥ grade 2 and feeding tube persistence at 6-months, and hypothyroidism at 1-year post-treatment.

In the second aim, we used quantitative MR imaging to interrogate its utility for prediction of oncologic outcomes and characterization of RT-induced normal tissue toxicity. Our findings showed that delta changes of ADC parameters derived from DWI images at mid-RT can be used to predict local recurrence and recurrence free survival. We also showed that K^{trans} and V_e vascular parameters derived from DCE images can characterize the mandibular areas of ORN (i.e. the most devastating normal tissue toxicity in the head and neck after RT) as compared with healthy mandible.

212

In the final clinical aim, we used CT images of recurrence and baseline CT planning images to develop a methodology and workflow that involves the application of deformable image registration software as a tool to standardize image co-registration in addition to granular combined geometric- and dosimetric-based failure characterization to correctly attribute sites and causes of loco-regional failure. We then successfully applied this methodology to identify the patterns of failure following postoperative IMRT for oral cavity cancer patients and following definitive IMRT in HNC patients of different disease subsite. Using this method, we showed that the majority of recurrences occurred in the central high dose regions for patients treated with definitive IMRT compared with mainly non-central high dose recurrences after postoperative IMRT. We also correlated recurrences with pretreatment FDG-PET and identified that the majority of the central high dose recurrences originated in an area that would be covered by a 10 mm margin on the volume of 50% of the maximum FDG uptake. This is a significant finding since the main PET-guided dose escalation studies in the past only used the volume of 50% of the maximum FDG uptake without additional margin which may be the main reason that ultimately led to the failure of these studies.

In the translational component, we integrated radiomic imaging features derived from pre-RT CT images with whole-genome measurements using TCGA and TCIA data. Our results demonstrated a statistically significant associations between radiomic features characterizing different tumor phenotypes and different genomic features such as transcriptional activity, DNA methylation, miRNA expression, and somatic mutation. These findings represent a promising potential towards non-invasively tract genomic changes in the tumor during treatment and use

213

this information to adapt treatment accordingly. In the final project of this dissertation, we developed a high-throughput approach to identify effective systemic agents against aggressive head and neck tumors with poor prognosis like ATC. We successfully identified three candidate drugs and performed extensive *in vitro* and *in vivo* validation using orthotopic and PDX models. Among these drugs, HDAC inhibitor and LBH-589 showed the most effective tumor growth inhibition that can be used in future clinical trials.

11. 2 Specific aim 1:

Determine the feasibility and dosimetric benefits of this MRI-based dose-adaption strategy for HPV positive oropharyngeal cancer patients using serial in-treatment MRIs acquired in radiation treatment positioning and immobilization setup.

We aimed in this part of the dissertation to integrate the anatomic MR images in RT platforms to be able to adapt the RT dose according to treatment response in order to accurately track high risk targets with serially reduced margins during therapy to limit normal tissue dose and subsequent toxicity while maintaining uncompromised high dose to target volumes, without the need of exogenous contrast. In project 1.1, we quantified the geometric distortion in patient images by comparing their in-treatment position MRIs with the corresponding planning CTs, using CT as the non-distorted gold standard. We used the T2w MRs of 21 HNC patient acquired in the same immobilization position as in the RT planning CTs. MRI to CT rigid registration was then done and geometric distortion comparison was assessed by measuring 430 carefully selected anatomical landmarks on both images. The median distortion for all landmarks in all scans was around 1 mm which is a clinically

214

insignificant error compared to the gold standard CT. This ensured a good quality MR image to proceed with the second half of Aim 1 which was to determine the feasibility and dosimetric benefits of using MR-guided RT dose adaption strategy for HPV positive OPC. We designed an in-silico study using the MR images acquired every two weeks during RT for patients with locally advanced disease. For each patient a standard versus an adaptive IMRT plan was created. For adaptive plans, we created an adaptive planning target volume based on detectable tumor shrinkage on T2w images. We kept the standard 70 Gy dose prescription to the adaptive volume to allow for maximum dose to any residual disease but in case of tumor complete response only a floor dose of 50.16 Gy will be received. The average dose to 95% of initial PTV volume was 70.7 Gy for standard plans versus 58.5 Gy for adaptive plans. The results of this project showed that most OARs received lower doses using adaptive plans which is translated to an average reduction in the probability of developing dysphagia ≥ grade2, feeding tube persistence at 6-month post-treatment and hypothyroidism at 1-year post-treatment of 11%, 4%, and 5%, respectively. Since the original hypothesis of that aim was that T2 weighted MRI can be used for MR-guided RT dose adaptation to achieve same tumor control as standard therapy but with additional sparing of surrounding normal tissue, we conclude that the hypothesis for this aim was successfully met.

11. 3 Specific aim 2:

Determine quantitative MRI parameters associated with tumor response, oncologic outcomes, and normal tissue toxicity in head and neck cancer patients treated with definitive radiation therapy.

215

In Aim 2 of this work, we sought to determine the benefits of using quantitative MR imaging parameters as a tool to predict RT outcomes and characterize RT-induced toxicity. In the first project of this aim, we assessed DWI parameters associated with tumor response and oncologic outcomes in HNC patients treated with RT. We enrolled 81 patients in an active prospective imaging study at our institution. Patients had MRIs pre-, mid-, and post-RT completion. Treatment response was assessed at mid-RT and at 8-12 weeks post-RT and local, regional, and distant control as well as recurrence-free and overall survival at 2-year post-RT. Our results showed that primary tumor delta ADCmean <7% at mid-RT is a significant parameter associated with worse local control and recurrence-free survival. Uni- and multi-variable analysis of prognostic outcomes showed that it was an independent predictive factor.

This shows that patients with no significant increase of primary tumor site ADC at mid-RT relative to baseline values are at high risk of disease relapse. In the second project, we aimed to characterize the quantitative DCE-MRI parameters associated with advanced mandibular ORN compared to the contralateral normal mandible. We included patients with the diagnosis of advanced ORN after curative-intent RT of HNC. Thirty patients were included with 38 months median time from RT completion to ORN development. The results of this study showed a statistically significant higher K^{trans} and V_e in ORN volumes-of-interest compared with control volumes of the contralateral healthy mandible. Using combined K^{trans} and V_e parameters, 90% of patients included in the study had at least a two-fold increase of either of the studied parameters in the ORN volumes-of-interest compared with control volumes. These results confirm there is a quantitatively significant higher degree of leakiness in the mandibular

216

vasculature as measured using DCE-MRI parameters of ORN areas compared with healthy

mandible. This also suggests that a two-fold increase in either K^{trans} or V_e parameters is an

alarming sign of ORN development if detected in patients with otherwise clinically apparent

normal mandible after radiation treatment especially in areas exposed to higher doses of RT.

Therefore, our hypothesis that quantitative MRI parameters can be used for prediction of tumor

response, long-term oncologic outcomes, as well as the characterization of RT-induced normal

tissue toxicity was successfully supported by the projects' results.

11. 4 Specific aim 3:

<u>Develop and apply a methodology to standardize the analysis and reporting of the patterns of</u>

<u>failure after radiation for head and neck cancer patients.</u>

This part of the dissertation aimed to develop and apply a novel methodology to

standardize the analysis and reporting of the patterns of loco-regional failure after IMRT/IMPT

of HNC. In project 3.1, we included 21 patients with evidence of local and/or regional failure

following IMRT for HNC and manually delineated recurrent gross disease on the diagnostic CT

documenting recurrence which was co-registered with the original planning CT using both

deformable and rigid image registration. Subsequently, recurrence volumes were mapped to

the planning CT for comparison relative to original planning target volumes and dose using a

centroid-based approaches. Failures were then classified into five distinct types based on

combined spatial and dosimetric criteria. The results of this work showed that rigid image

registration tends to assign failures more peripherally and that DIR-based methods accurately

mapped the vast majority of failures to the high dose volumes suggesting biological rather than

217

technology-related causes of failure. We then applied this methodology to identify spatial and dosimetric patterns of failure for oral cavity cancer patients receiving post-operative IMRT and identify the radio-resistant subvolumes in pretreatment FDG-PET by mapping the spatial location of the origin of tumor recurrence in projects 3.2 and 3.3 respectively. The results of project 3.2 showed that 50% of OCC patients with local/regional failure had non-central high dose recurrence and identified potential causes the increase the intermediate and extraneous dose recurrences in these patients. While patients treated with definitive IMRT in project 3.3, the majority of loco-regional recurrences originated in the regions of central-high-dose. When correlated with pretreatment FDG-PET, these recurrences originated in an area that would be covered by additional 10 mm margin on the volume of 50% of the maximum FDG uptake. Such findings highlight the importance of proper definition of the subvolumes to target in FDG-PET-guided dose escalation clinical trials. Based on these results, we deem the hypothesis of this Specific Aim to be correct.

11. 5 Specific aim 4:

<u>Determine the associations between imaging phenotypes and genomic mechanisms in head and neck tumors and identify effective systemic agents against aggressive tumors with a reasonable toxicity profile to allow for rapid translational development.</u>

In project 4.1 of this translational research component of the dissertation, we aimed to establish if imaging radiomics features of head and neck tumors could be indicative of important genomic biomarkers. We integrated whole-genome multi-omics data from the TCGA with matched CT images from TCIA for a set of 126 HNC patients to identify statistically

218

significant associations between radiomic and genomic features. Our results showed a widespread of statistically significant associations between genomic features (including miRNA expressions, somatic mutations, and transcriptional activities, copy number variations, and promoter region DNA methylation changes of pathways) and radiomic features characterizing the size, shape, and texture of tumor. A model for prediction of HPV and TP53 mutation status using radiomic features was also developed and achieved an AUC of 0.71 and 0.641, respectively. These findings suggest that radiomic features are associated with genomic characteristics at multiple molecular layers in HNC and provides justification for continued development of radiomics as biomarkers for relevant genomic alterations that can be adopted for prognostic and treatment adaptation purposes. For project 4.2, we aimed to identify effective systemic agents against aggressive thyroid carcinoma variants. We used 12 human thyroid cancer cell lines with comprehensive genomic characterization in a high-throughput screening of 257 compounds to select agents with maximal growth inhibition. Cell proliferation, colony formation, orthotopic thyroid models, and patient-derived xenograft models were used to validate the selected agents. Our results identified a selected group of agents that were effective in the initial screen. Subsequently, docetaxel, LBH-589, and pralatrexate were selected for additional *in vitro* and *in vivo* analysis as they have been previously approved by the FDA for other cancers. A significant tumor growth inhibition was demonstrated in all tested models treated with LBH-589, while pralatrexate demonstrated significant tumor growth inhibition in the orthotopic papillary thyroid carcinoma model and two PDX models, and docetaxel demonstrated significant tumor growth inhibition only in the context of mutant TP53. These results confirmed that a high-throughput screening can be used to identify classes of

219

systemic agents which demonstrate preferential effectiveness against aggressive thyroid cancers, particularly those with mutant TP53. Preclinical validation in both orthotopic and PDX models, which are accurate *in vivo* models mimicking tumor microenvironment, may support initiation of early phase clinical trials in non-BRAF mutated or refractory to BRAF/MEK inhibition ATC. Therefore, we find the hypothesis of this aim to be also correct.

11.6 Future research and applications

The results of the projects included in this dissertation support the potential development of many future research protocols and clinical trials. It is worth reporting that the results of Aim 1 project, was the basis of the currently active clinical trial protocol (NCT03224000).(327) In this protocol we use a 2-stage Bayesian phase II study to examine weekly RT dose-adaptation based on MRI-guided tumor response as explained in project 1.2. Individual patient's plan is designed to optimize dose reduction to organs at risk and minimize locoregional failure probability based on serial MRI during RT. The primary aim of the trial is to assess the non-inferiority of MR-guided dose adaptation for patients with low risk HPV-associated OPC compared standard RT. The stage 1 of this study already enrolled 15 patients and LRC at 6 months was found to be sufficiently safe as per the Bayesian model, so stage 2 of the protocol is now active for enrollment to an additional 60 patients, randomized to either MR-guided RT or standard IMRT.

Regarding the future directions based on Aim 2, we are planning to validate the DWI results using external data sets to establish if our delta ADC threshold at mid-RT can be used as a biomarker of high-risk patients for future dose escalation RT clinical trial. In addition, we

are planning to determine if DWI parameters can be also used to predict toxicity outcomes. This will include salivary glands parameters and xerostomia, swallowing muscle parameters and dysphagia, and taste bud bearing tongue mucosa parameters and dysgeusia. In a similar vein, we will assess if the vascular changes in primary tumor volumes as measured by DCE-MRI can be also predictive of oncologic outcomes. If successful, we will be able to build a comprehensive model of multiparametric MR imaging biomarkers of tumor response and disease outcomes that can be used to stratify patients in future HNC clinical trials. Moreover, we plan to use the DCE-MRI vascular signature of ORN to develop a prophylactic clinical trial of pentoxifylline and tocopherol treatment of high-risk patients after RT. The initial results from this Aim will be also included as preliminary data for a programmatic P01 NIH submission named "InHANCE: Imaging Innovation for Head And Neck Cancer Evaluation & Elimination of Toxicity." The central scientific theme of this P01 application will be to improve the therapeutic ratio for HNC by reducing normal tissue injury and the incipient loss of quality of life from locoregional therapies (i.e. surgery and radiotherapy). This will be performed by using patient-specific data acquired via advanced imaging methods with application of statistical learning analytic approaches to effectively predict, detect, prevent and mitigate therapy-related normal toxicity in HNC survivors.

The patterns of failure analysis methodology developed in Aim 3 has been already implemented by different groups and in different cancer sites as the standard methodology for RT patterns of failure analysis.(328-330) We are also in the midst of applying this methodology for the secondary analysis of the patterns of failure in the Australian TROG 07.03 RadioHUM

clinical trial. This will be also applied for the data from a consortium of five international institution from US, Asia, and Middle East as part of the Sister Institution Network Fund (SINF). We will also apply this methodology to identify the origin of tumor recurrence relative to baseline functional MR parameters to allow for better characterization of radioresistant tumor subvolumes.

For Aim 4, we plan to validate the identified radiogenomic associations using a larger dataset of HNC patients. This carry a huge potential for dynamically detect the genomic profiles of evolving tumors and/or recurrences without the need of frequent invasive biopsies. Moreover, our results from the high-throughput approach to identify effective agents for the treatment of aggressive thyroid tumors demonstrate the feasibility of using this approach for preclinical *in vivo* drug testing and potential combination with FDA-approved drugs in future. This platform also provides an avenue for the identification and validation of novel agents. Utilization of immunodeficient PDX models and immunocompetent murine models in the future will allow for the efficient development of personalized systemic treatment of different aggressive tumor types and will constitute a strong justification for proceeding to clinical trials. We also plan to include the effective agents identified in this aim in combination with RT and use MR diffusion parameters as a tool for prediction of multimodality treatment response in mouse models of aggressive head and neck tumors. In this study, we will correlate the imaging findings with spatially co-registered histopathological data of cellular response to treatment at spectrum of tumor models with variable radiation sensitivity. This would identify imaging parameters associated with radioresistent subvolumes for further treatment intensification.

222

11.7 Conclusions

In this work, we were able to integrate anatomic MR images in dose adaptation RT strategies which led to reduction in normal tissue complication probability and subsequent integration in currently active clinical trial. We also successfully demonstrated the utility of quantitative MR parameters as a biomarker for tumor response, disease outcomes, and normal tissue toxicity. In addition, we developed a novel methodology for analysis, reporting, and interpretation of the patterns of disease failure after radiation therapy. Furthermore, we were able to identify association between genomic features and imaging radiomic features representing different head and neck tumor phenotypes. Finally, we identified and validated classes of systemic agents with preferential effectiveness against aggressive thyroid tumors particularly those with mutant TP53.

Appendix A.1 DCE-MRI parameter histograms for all 30 patients included in the analysis.

Patient 1

Parameter	ORN-VOI		Control-VOI	
	Mean	SD	Mean	SD
Ktrans	0.036	0.027	0.020	0.017
Ve	0.127	0.078	0.031	0.027
Kep	0.335	0.165	0.473	0.189
Vp	0.018	0.012	0.005	0.004

Patient 2

Parameter	ORN-VOI		Control-VOI	
	Mean	SD	Mean	SD
Ktrans	0.146	0.089	0.059	0.072
Ve	0.308	0.217	0.137	0.152
Kep	0.512	0.293	0.523	0.354
Vp	0.102	0.084	0.013	0.013
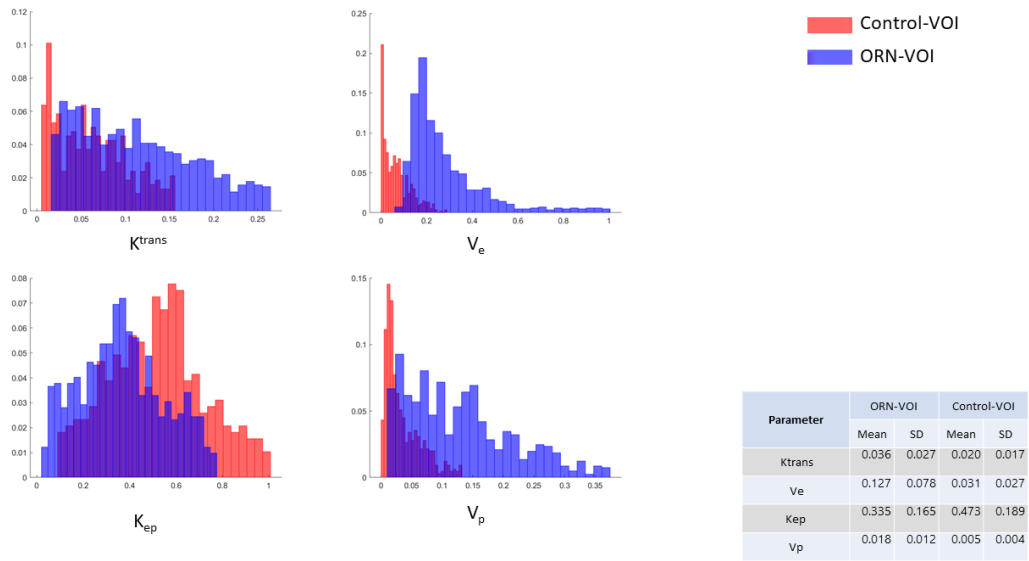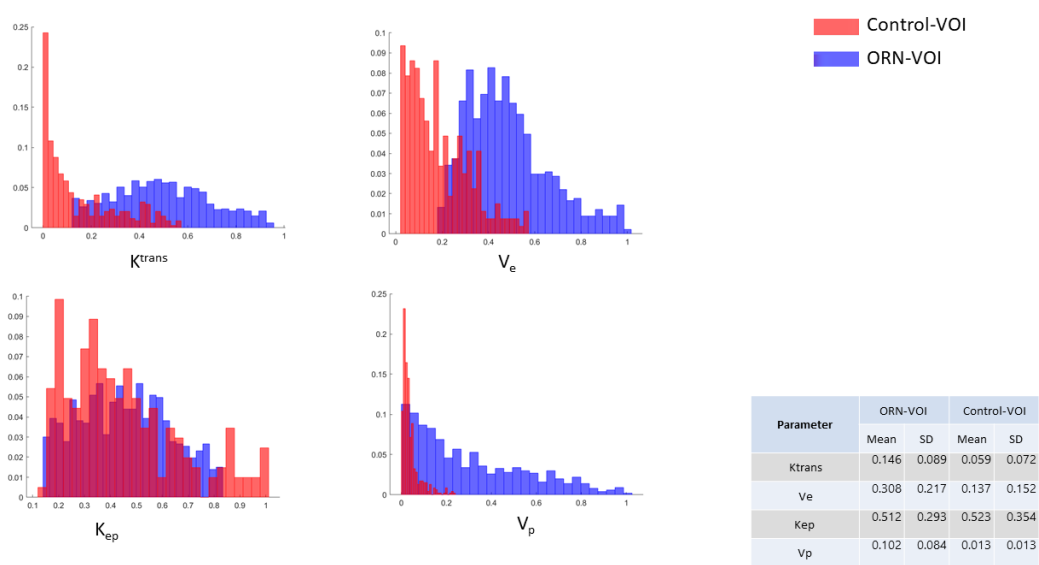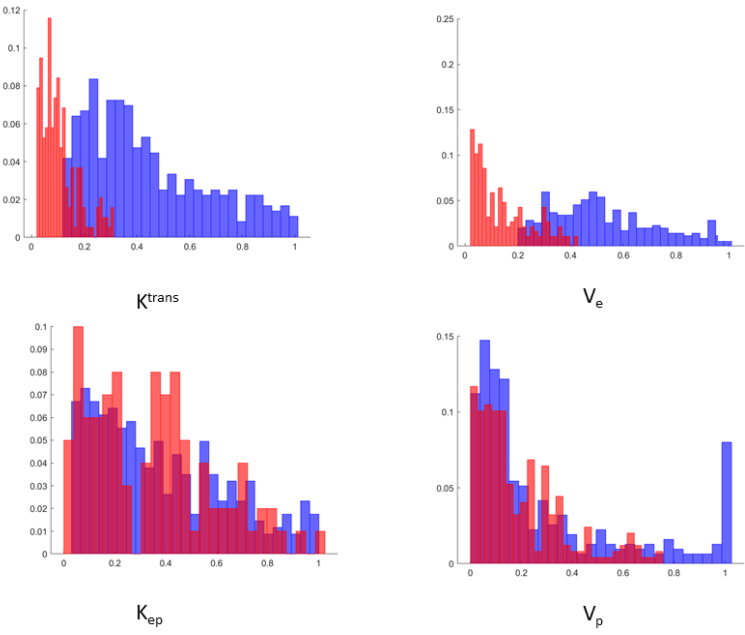
Patient 3

Parameter	ORN-VOI		Control-VOI	
	Mean	SD	Mean	SD
Ktrans	0.686	0.561	0.162	0.155
Ve	0.634	0.382	0.215	0.222
Kep	0.863	0.608	0.651	0.472
Vp	0.967	1.052	0.642	0.596

Patient 4
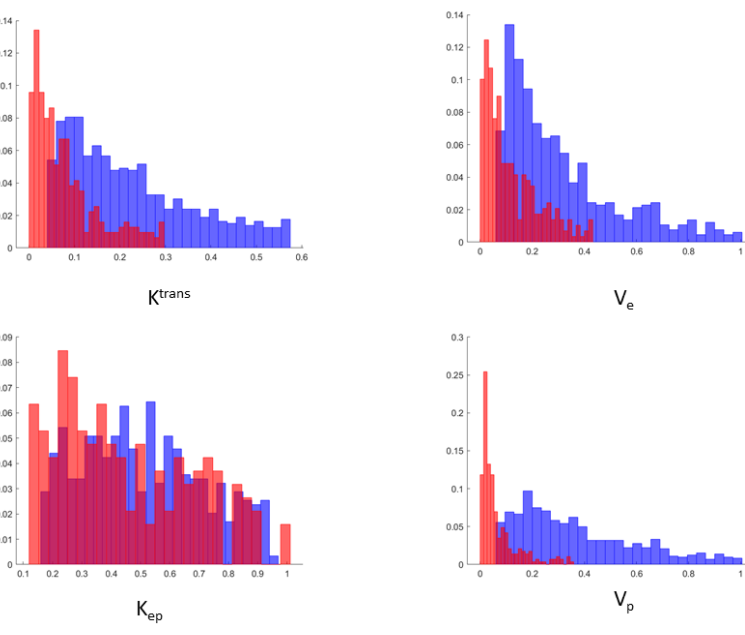
Parameter	ORN-VOI		Control-VOI	
	Mean	SD	Mean	SD
Ktrans	0.076	0.067	0.031	0.037
Ve	0.145	0.162	0.058	0.075
Kep	0.593	0.334	0.550	0.389
Vp	0.138	0.170	0.035	0.058

225
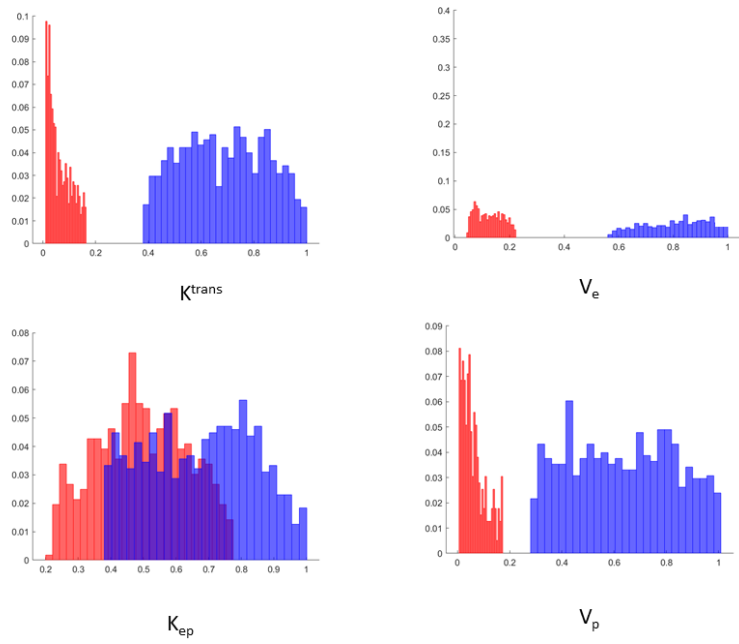
Patient 5

Parameter	ORN-VOI		Control-VOI	
	Mean	SD	Mean	SD
Ktrans	0.728	0.274	0.073	0.063
Ve	0.559	0.140	0.081	0.046
Kep	0.951	0.349	0.656	0.279
Vp	0.228	0.095	0.031	0.027

Patient 6
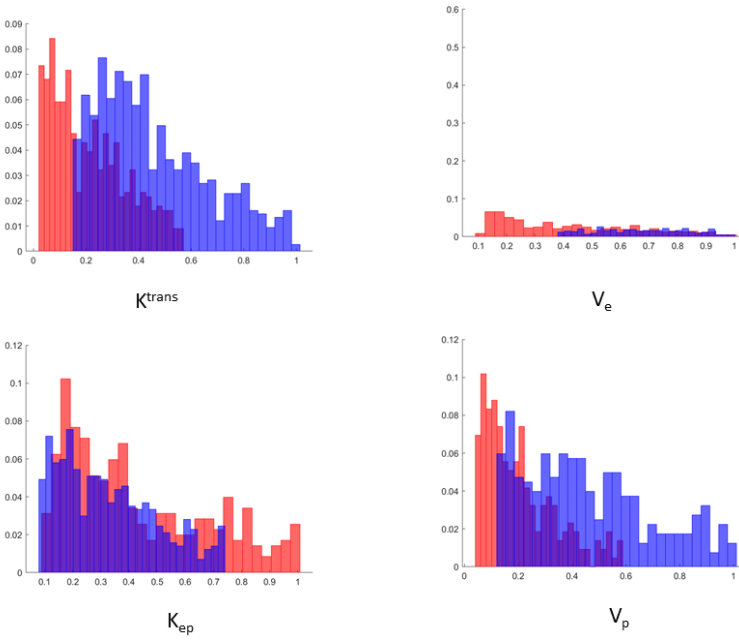
Parameter	ORN-VOI		Control-VOI	
	Mean	SD	Mean	SD
Ktrans	0.321	0.257	0.143	0.132
Ve	0.646	0.386	0.434	0.386
Kep	0.297	0.221	0.361	0.280
Vp	0.100	0.069	0.040	0.030
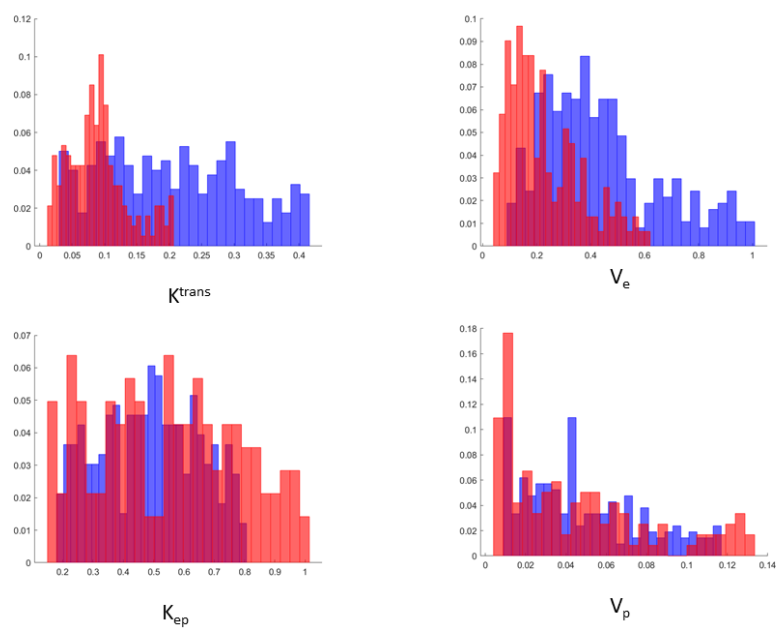
226

Patient 7

Parameter	ORN-VOI		Control-VOI	
	Mean	SD	Mean	SD
Ktrans	0.063	0.045	0.028	0.021
Ve	0.162	0.121	0.095	0.097
Kep	0.343	0.163	0.393	0.233
Vp	0.008	0.006	0.009	0.010

Patient 8

Parameter	ORN-VOI		Control-VOI	
	Mean	SD	Mean	SD
Ktrans	0.029	0.014	0.016	0.018
Ve	0.087	0.047	0.043	0.054
Kep	0.310	0.138	0.508	0.345
Vp	0.029	0.011	0.013	0.011

227
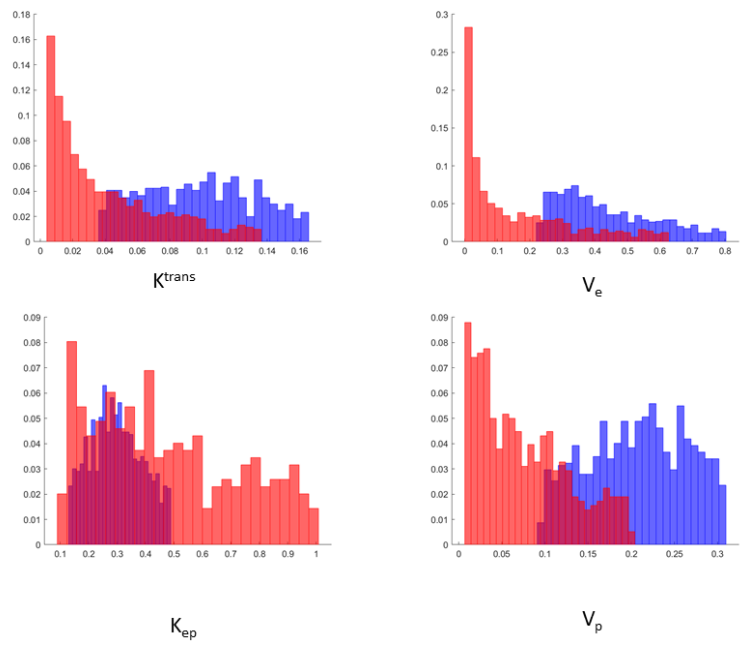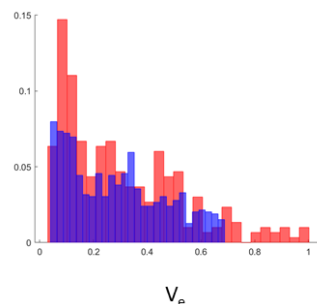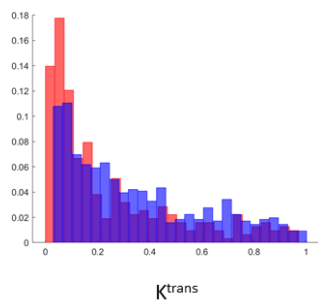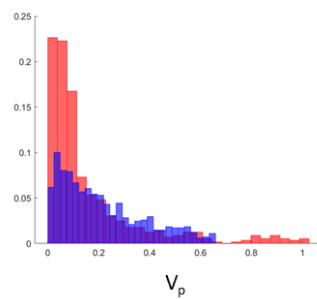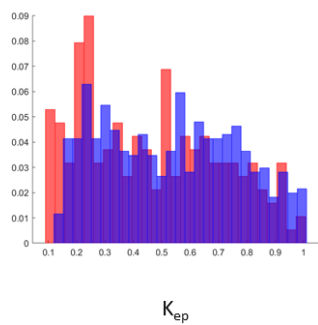
Patient 9

Parameter	ORN-VOI		Control-VOI	
	Mean	SD	Mean	SD
Ktrans	0.135	0.137	0.080	0.098
Ve	0.120	0.102	0.109	0.101
Kep	0.840	0.553	0.626	0.440
Vp	0.135	0.110	0.108	0.112

Patient 10
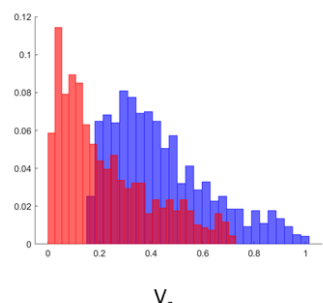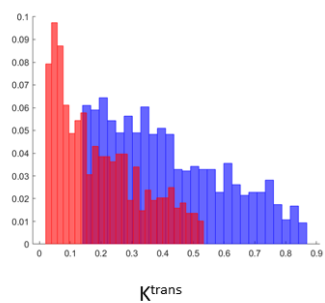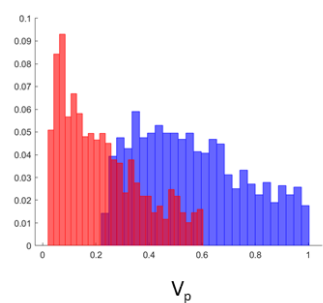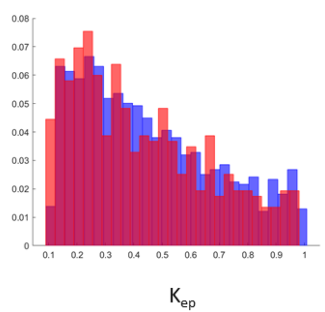
Parameter	ORN-VOI		Control-VOI	
	Mean	SD	Mean	SD
Ktrans	0.127	0.078	0.066	0.060
Ve	0.234	0.185	0.140	0.176
Kep	0.645	0.445	0.613	0.459
Vp	0.195	0.099	0.086	0.077

228
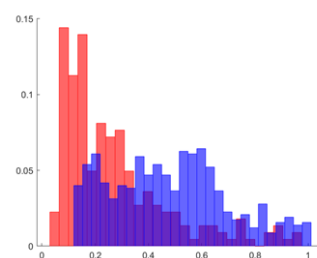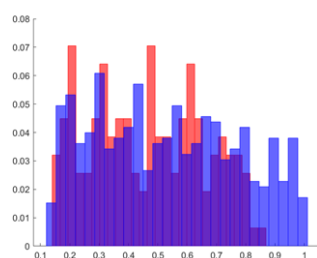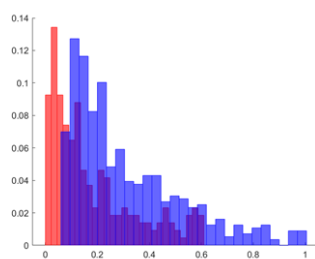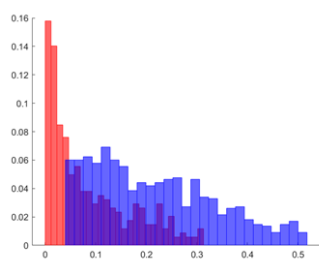
Patient 11

Parameter	ORN-VOI		Control-VOI	
	Mean	SD	Mean	SD
Ktrans	0.071	0.057	0.036	0.046
Ve	0.155	0.185	0.095	0.128
Kep	0.687	0.408	0.594	0.328
Vp	0.087	0.055	0.059	0.059

Patient 12
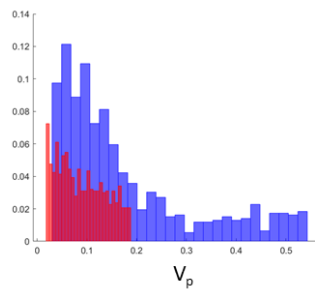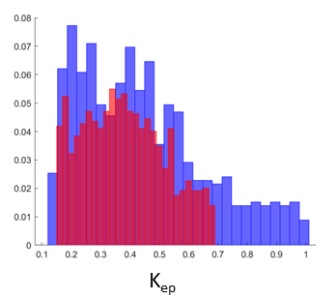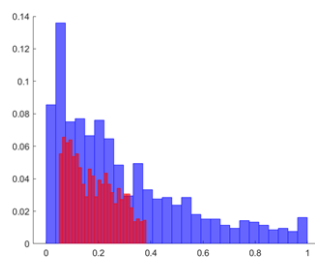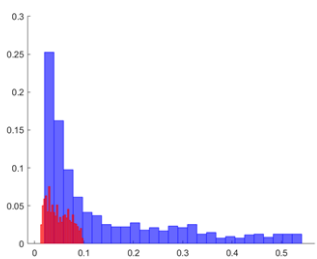
Parameter	ORN-VOI		Control-VOI	
	Mean	SD	Mean	SD
Ktrans	0.052	0.057	0.015	0.009
Ve	0.071	0.085	0.037	0.027
Kep	0.464	0.338	0.376	0.204
Vp	0.033	0.036	0.014	0.009

229
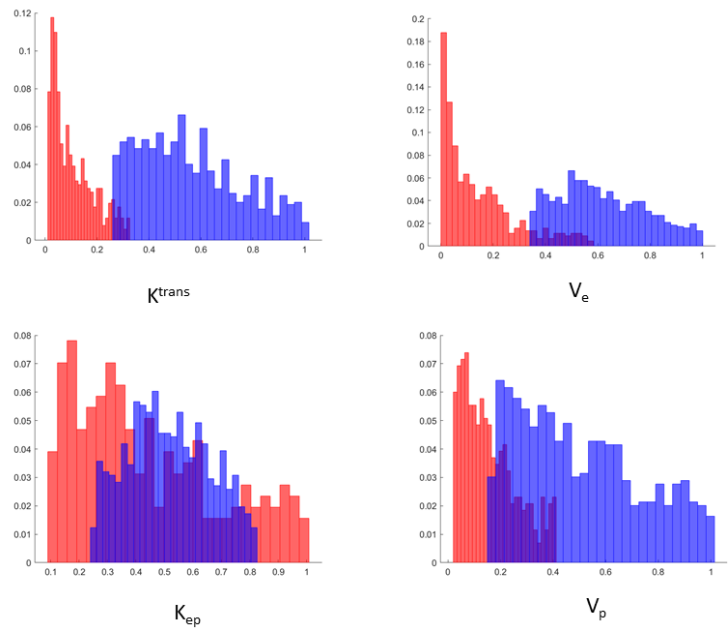
Patient 13

Parameter	ORN-VOI		Control-VOI	
	Mean	SD	Mean	SD
Ktrans	0.683	0.339	0.152	0.150
Ve	0.853	0.308	0.258	0.325
Kep	0.609	0.262	0.557	0.410
Vp	0.411	0.255	0.141	0.119

Patient 14
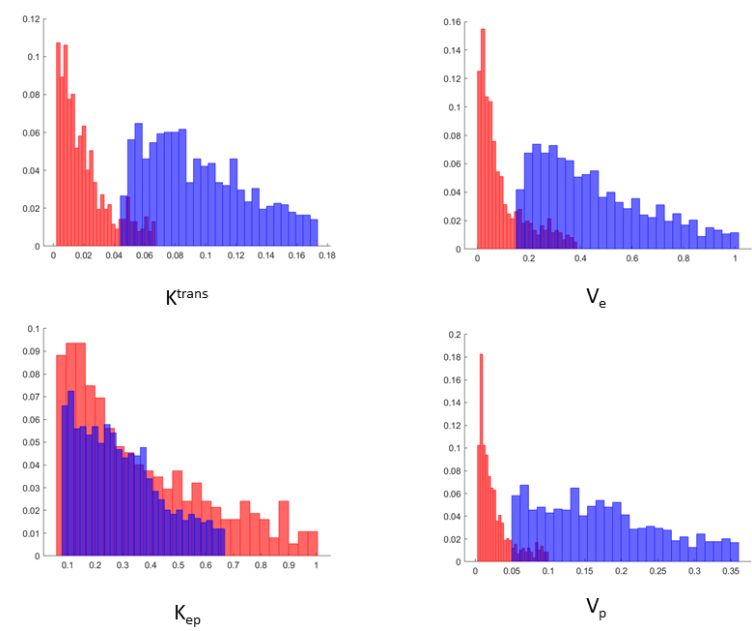
Parameter	ORN-VOI		Control-VOI	
	Mean	SD	Mean	SD
Ktrans	0.921	0.525	0.192	0.223
Ve	0.953	0.421	0.371	0.402
Kep	0.513	0.396	0.355	0.281
Vp	0.766	0.563	0.113	0.127

230
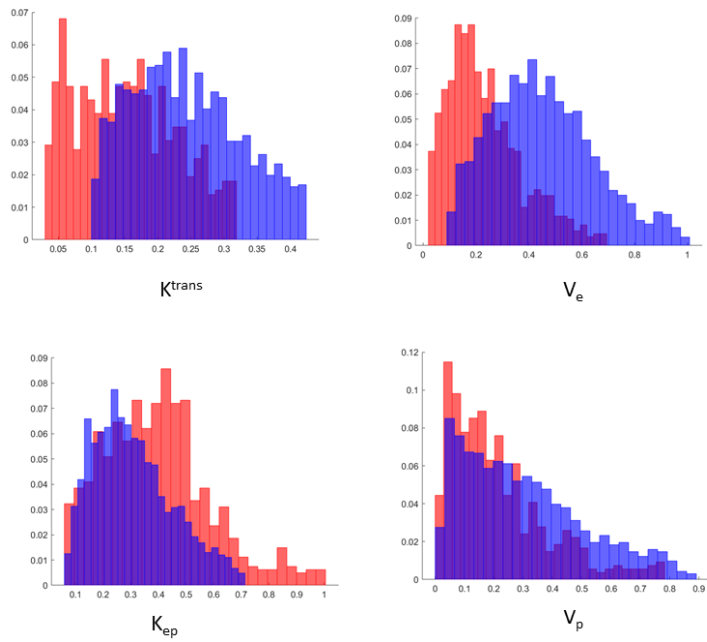
Patient 15

Parameter	ORN-VOI		Control-VOI	
	Mean	SD	Mean	SD
Ktrans	0.072	0.035	0.047	0.031
Ve	0.183	0.079	0.094	0.057
Kep	0.328	0.145	0.439	0.200
Vp	0.043	0.029	0.031	0.024

Patient 16
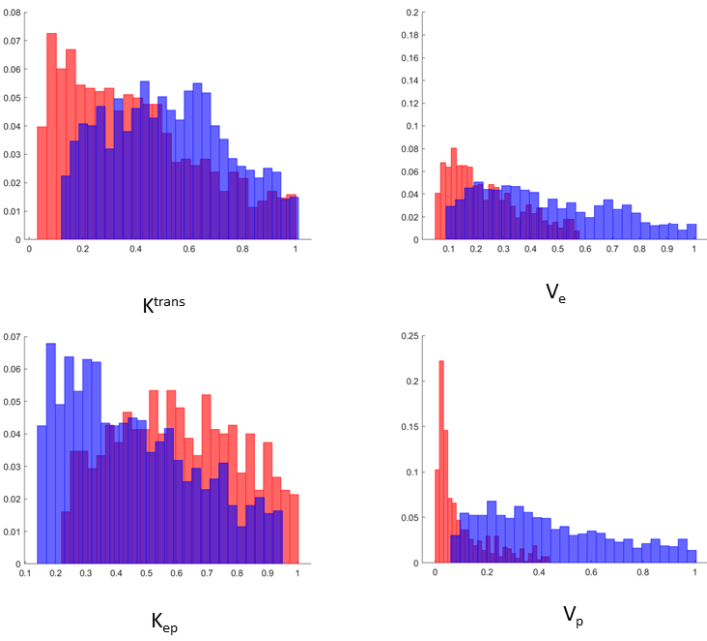
Parameter	ORN-VOI		Control-VOI	
	Mean	SD	Mean	SD
Ktrans	0.291	0.159	0.233	0.152
Ve	0.747	0.379	0.498	0.330
Kep	0.320	0.189	0.406	0.192
Vp	0.251	0.165	0.075	0.070

231
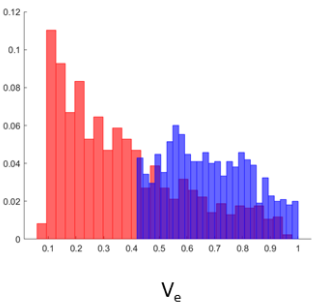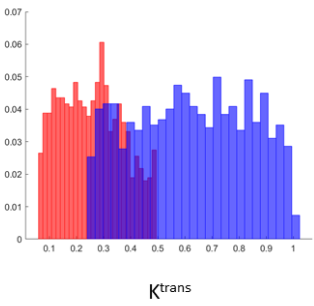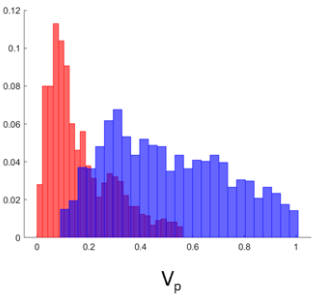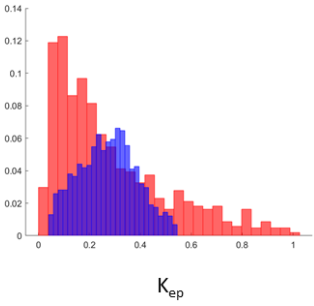
Patient 17

Parameter	ORN-VOI		Control-VOI	
	Mean	SD	Mean	SD
Ktrans	0.189	0.088	0.081	0.049
Ve	0.475	0.174	0.298	0.271
Kep	0.362	0.151	0.374	0.295
Vp	0.193	0.088	0.065	0.049

Patient 18
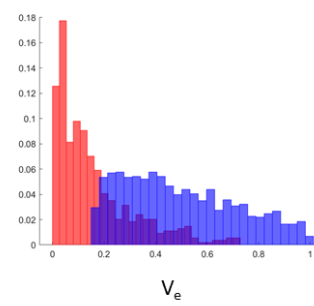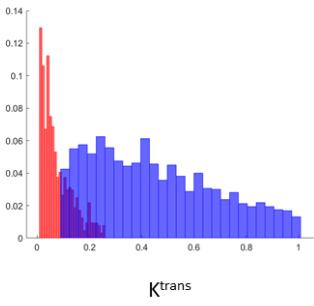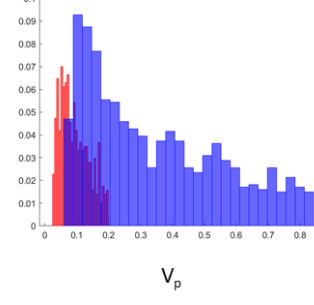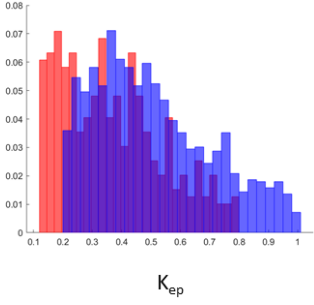
Parameter	ORN-VOI		Control-VOI	
	Mean	SD	Mean	SD
Ktrans	0.172	0.123	0.036	0.043
Ve	0.241	0.160	0.109	0.149
Kep	0.673	0.412	0.492	0.327
Vp	0.056	0.045	0.015	0.009

Patient 19
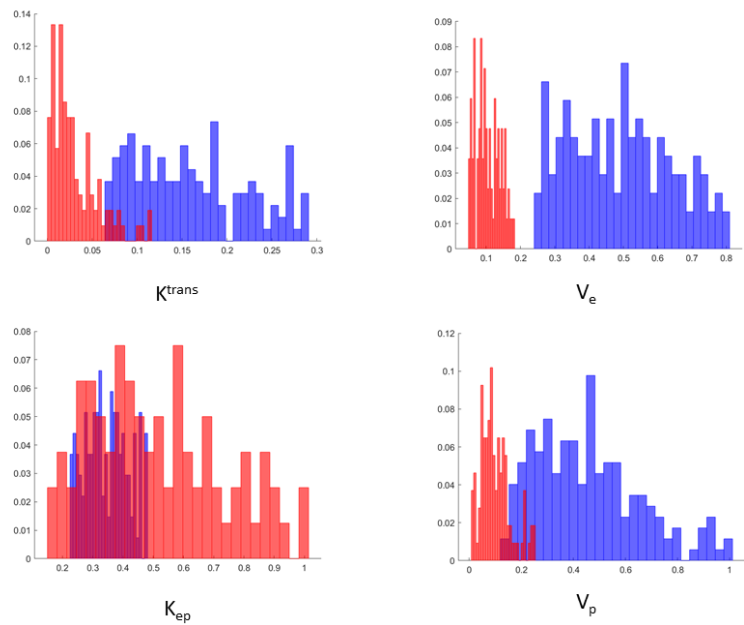
Parameter	ORN-VOI		Control-VOI	
	Mean	SD	Mean	SD
Ktrans	0.047	0.025	0.013	0.015
Ve	0.093	0.041	0.020	0.011
Kep	0.364	0.104	0.558	0.320
Vp	0.031	0.014	0.006	0.009

Patient 20
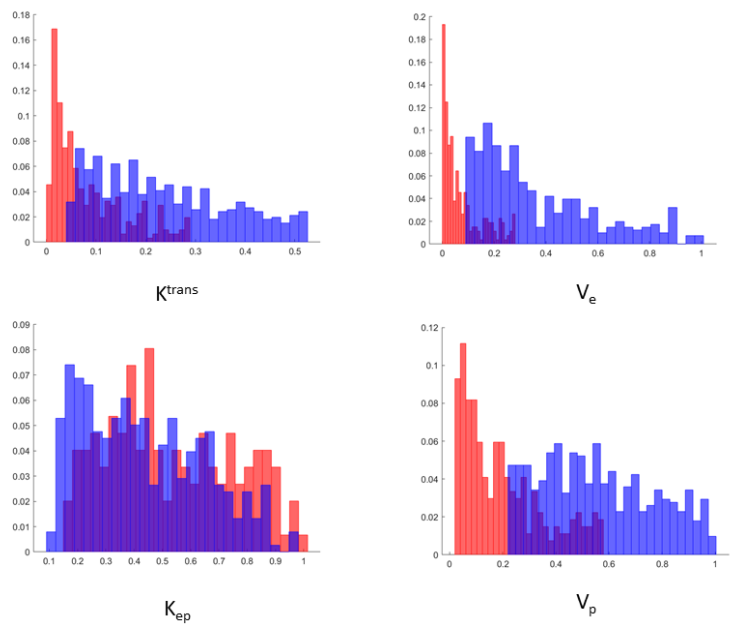
Parameter	ORN-VOI		Control-VOI	
	Mean	SD	Mean	SD
Ktrans	0.074	0.055	0.033	0.040
Ve	0.264	0.271	0.067	0.096
Kep	0.449	0.325	0.517	0.304
Vp	0.137	0.076	0.058	0.058

Patient 21
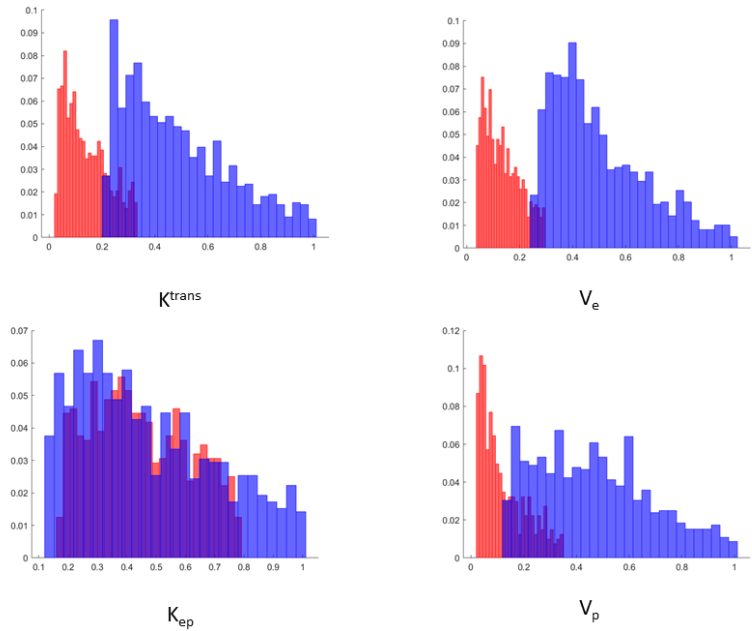
Parameter	ORN-VOI		Control-VOI	
	Mean	SD	Mean	SD
Ktrans	0.354	0.214	0.103	0.079
Ve	0.485	0.276	0.132	0.094
Kep	0.725	0.476	0.664	0.333
Vp	0.153	0.104	0.046	0.047

Patient 22
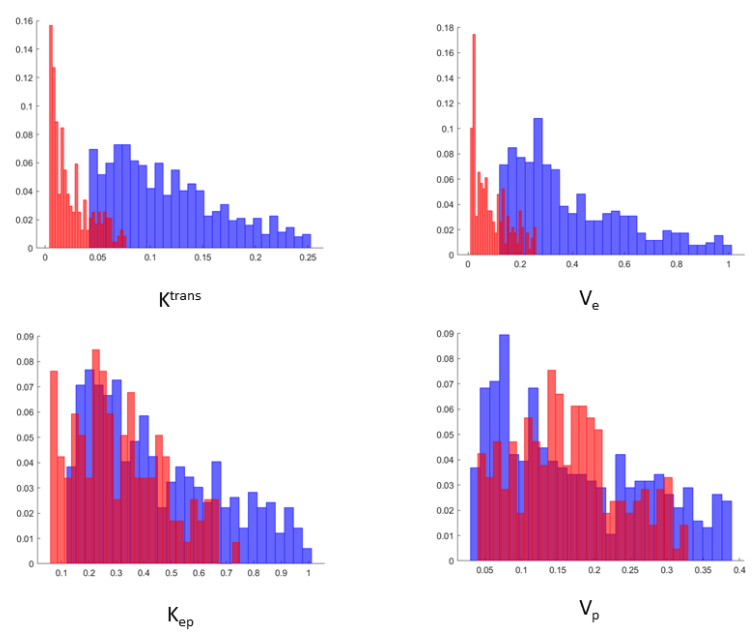
Parameter	ORN-VOI		Control-VOI	
	Mean	SD	Mean	SD
Ktrans	0.078	0.065	0.022	0.026
Ve	0.172	0.144	0.059	0.070
Kep	0.406	0.323	0.218	0.140
Vp	0.048	0.038	0.094	0.075

234
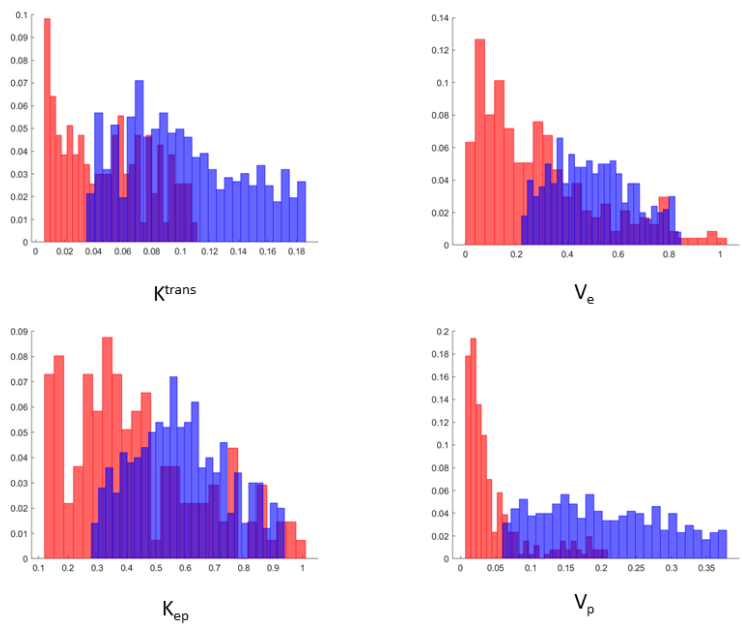
Patient 23

Parameter	ORN-VOI		Control-VOI	
	Mean	SD	Mean	SD
Ktrans	0.030	0.016	0.016	0.012
Ve	0.095	0.047	0.075	0.095
Kep	0.285	0.125	0.227	0.164
Vp	0.030	0.018	0.010	0.012

Patient 24
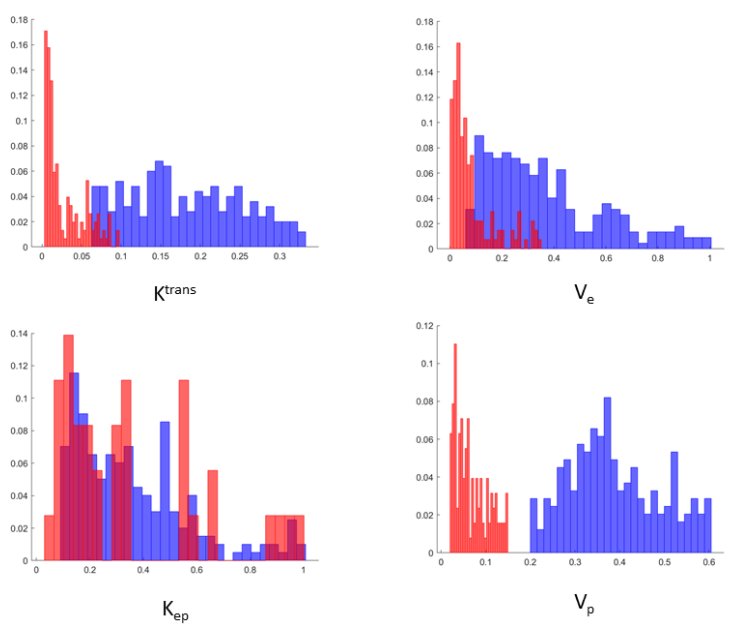
Parameter	ORN-VOI		Control-VOI	
	Mean	SD	Mean	SD
Ktrans	0.629	0.420	0.061	0.072
Ve	0.628	0.398	0.146	0.166
Kep	0.772	0.536	0.252	0.158
Vp	0.238	0.215	0.079	0.050

235
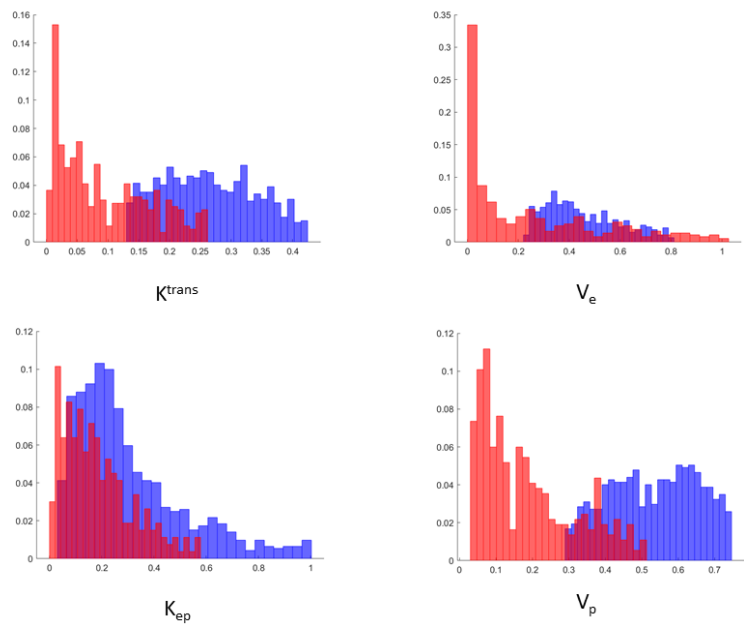
Patient 25

Parameter	ORN-VOI		Control-VOI	
	Mean	SD	Mean	SD
Ktrans	0.077	0.033	0.033	0.030
Ve	0.115	0.061	0.092	0.137
Kep	0.676	0.469	0.408	0.294
Vp	0.075	0.026	0.032	0.029

Patient 26
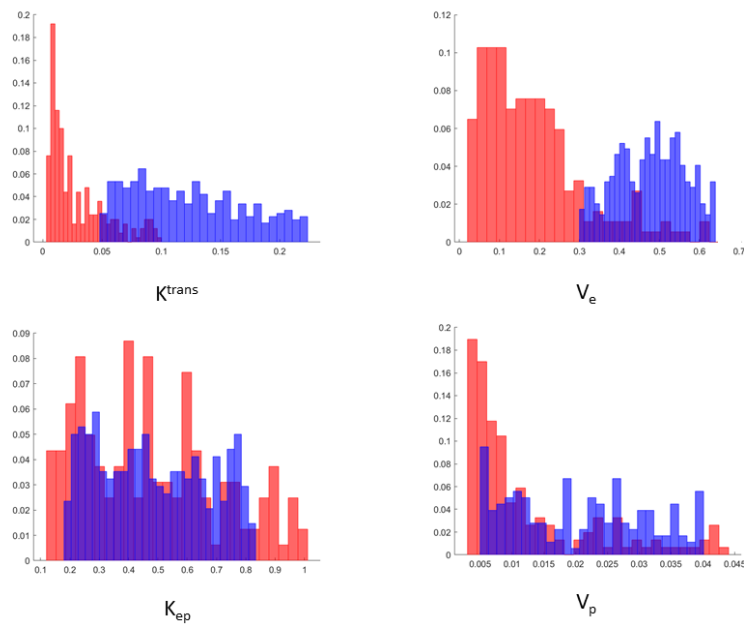
Parameter	ORN-VOI		Control-VOI	
	Mean	SD	Mean	SD
Ktrans	0.037	0.019	0.012	0.015
Ve	0.088	0.027	0.049	0.060
Kep	0.335	0.170	0.359	0.266
Vp	0.003	0.002	0.003	0.005

236
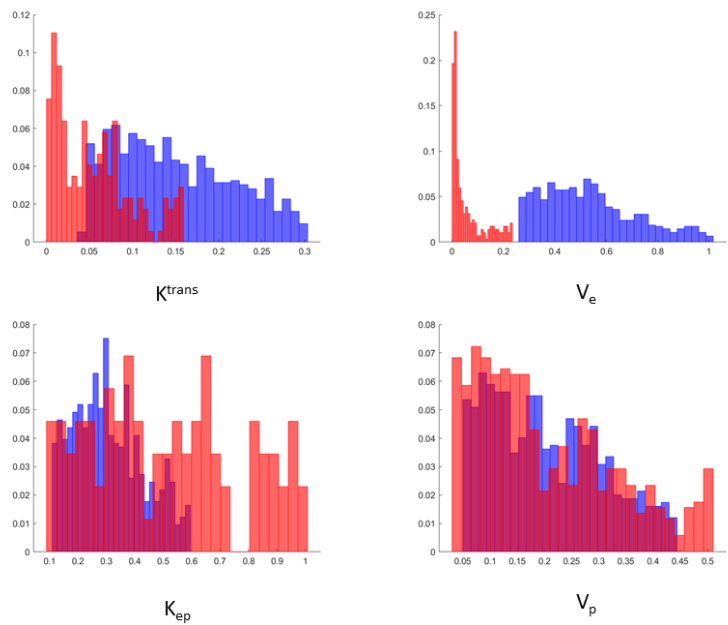
Patient 27

Parameter	ORN-VOI		Control-VOI	
	Mean	SD	Mean	SD
Ktrans	0.046	0.030	0.020	0.021
Ve	0.143	0.085	0.022	0.030
Kep	0.343	0.201	0.555	0.366
Vp	0.032	0.022	0.033	0.027

Patient 28
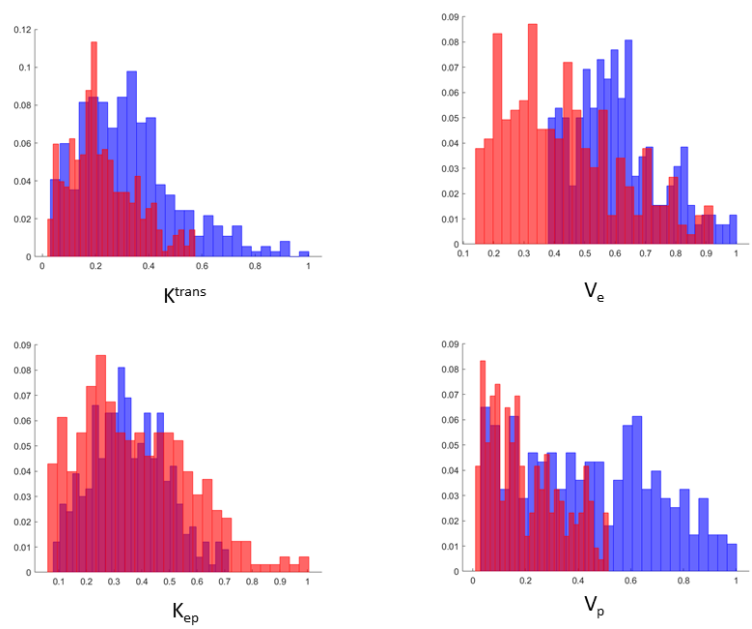
Parameter	ORN-VOI		Control-VOI	
	Mean	SD	Mean	SD
Ktrans	0.404	0.230	0.284	0.157
Ve	0.887	0.266	0.628	0.364
Kep	0.341	0.130	0.365	0.192
Vp	0.267	0.160	0.124	0.084

237
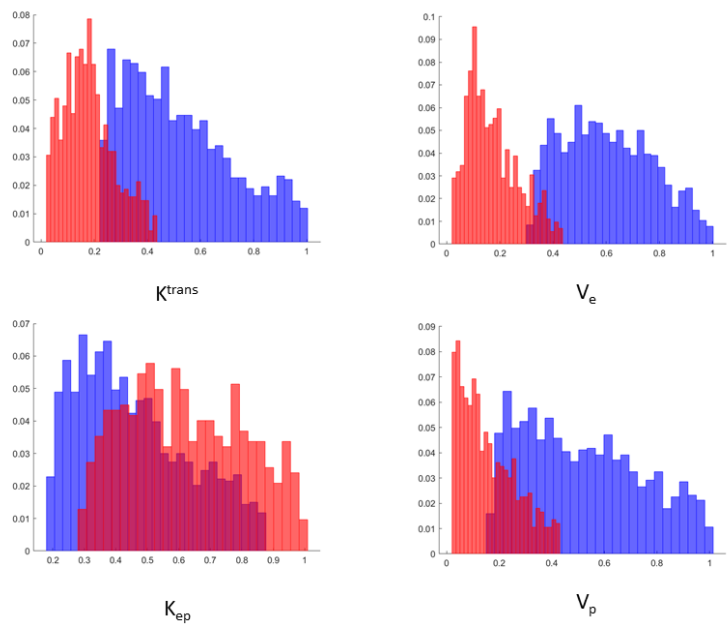
Patient 29

Parameter	ORN-VOI		Control-VOI	
	Mean	SD	Mean	SD
Ktrans	0.300	0.173	0.098	0.082
Ve	0.465	0.209	0.135	0.110
Kep	0.484	0.297	0.572	0.268
Vp	0.289	0.204	0.087	0.080

Patient 30
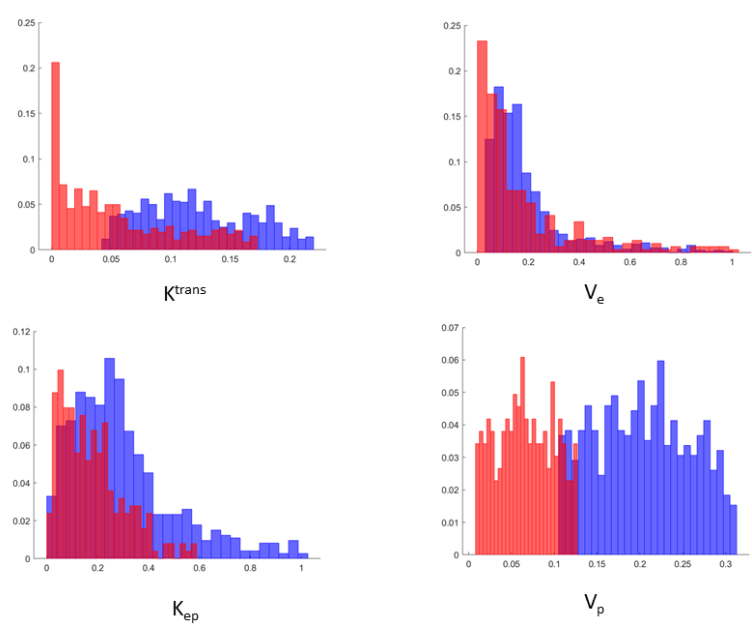
Parameter	ORN-VOI		Control-VOI	
	Mean	SD	Mean	SD
Ktrans	0.035	0.013	0.016	0.014
Ve	0.088	0.075	0.080	0.095
Kep	0.481	0.336	0.290	0.203
Vp	0.029	0.011	0.010	0.007

238

Appendix A.2 Correlation of radiation dose and DCE-MRI parameters.

Radiation dose correlation with Ktrans

r=-0.07, p=0.8 (Ktrans vs Min dose)

r=-0.08, p=0.7 (Ktrans vs Mean dose)

r=0.04, p=0.9 (Ktrans vs Max dose)

r=-0.007, p=0.97 (Ktrans vs Dose to 95% of ORN volume)

Radiation dose correlation with Ve

r=-0.17, p=0.5 (Ve vs Min dose)

r=-0.29, p=0.2 (Ve vs Mean dose)

r=-0.28, p=0.2 (Ve vs Max dose)

r=0.1, p=0.7 (Ve vs Dose to 95% of ORN volume)

239
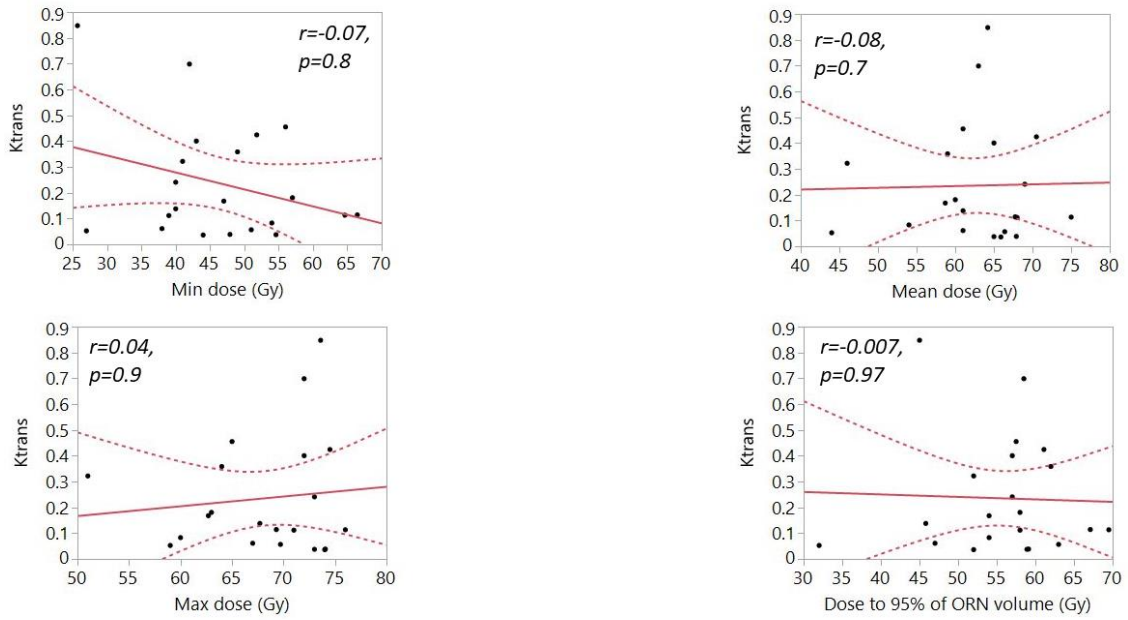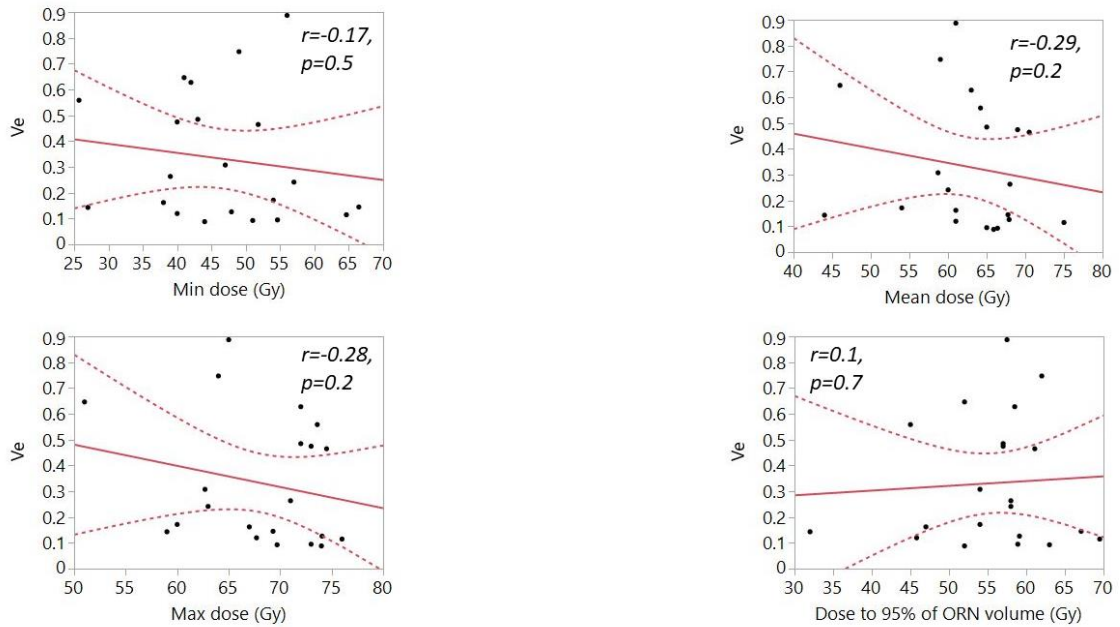
Radiation dose correlation with Kep
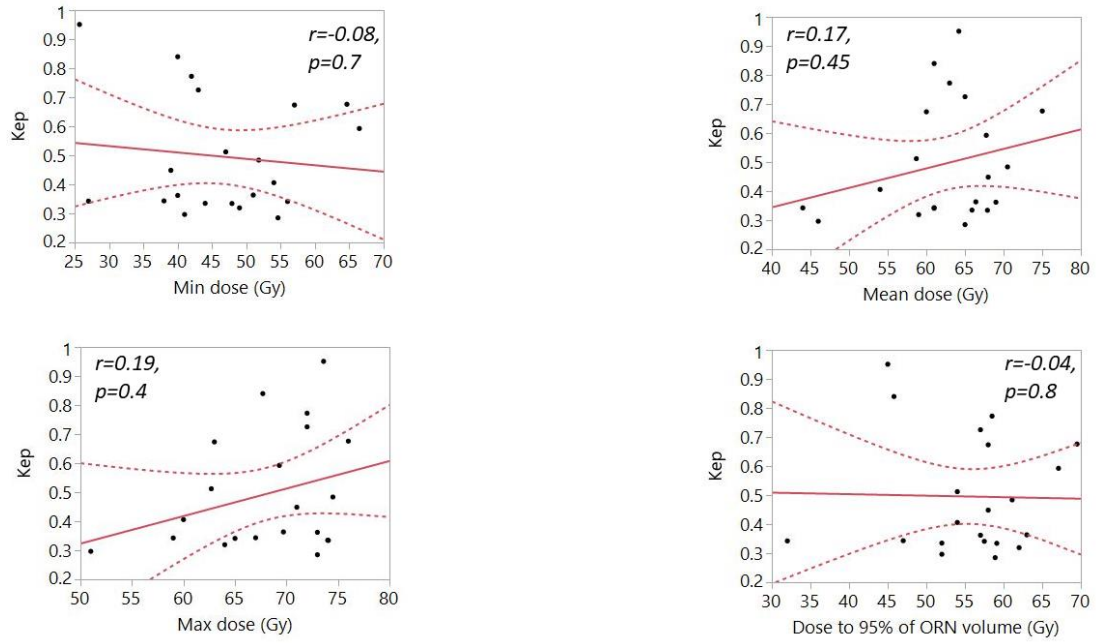
Radiation dose correlation with Vp
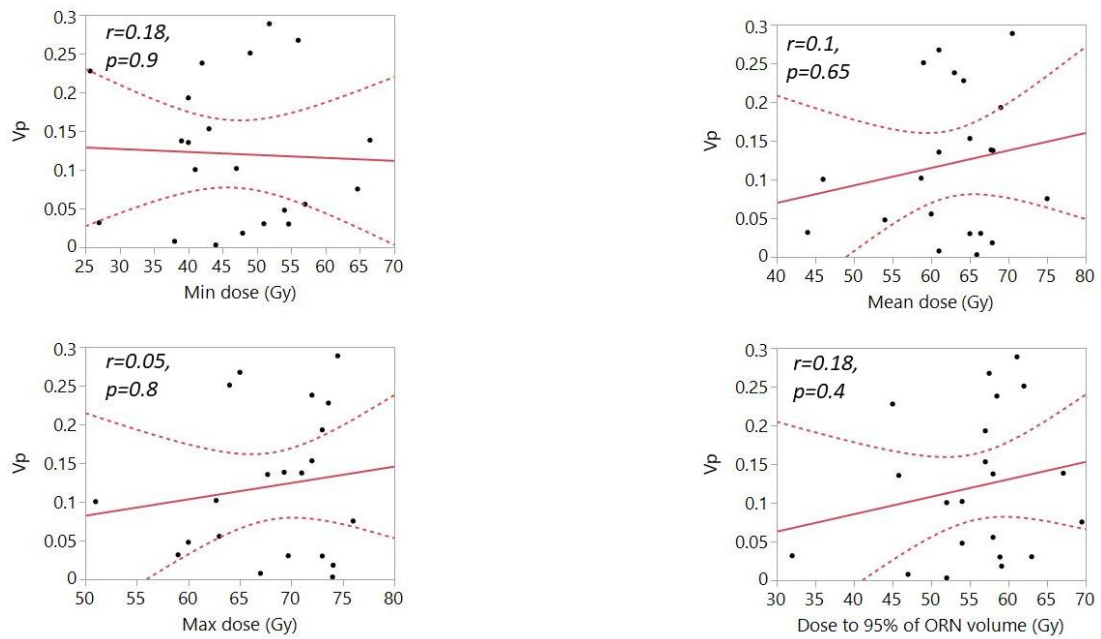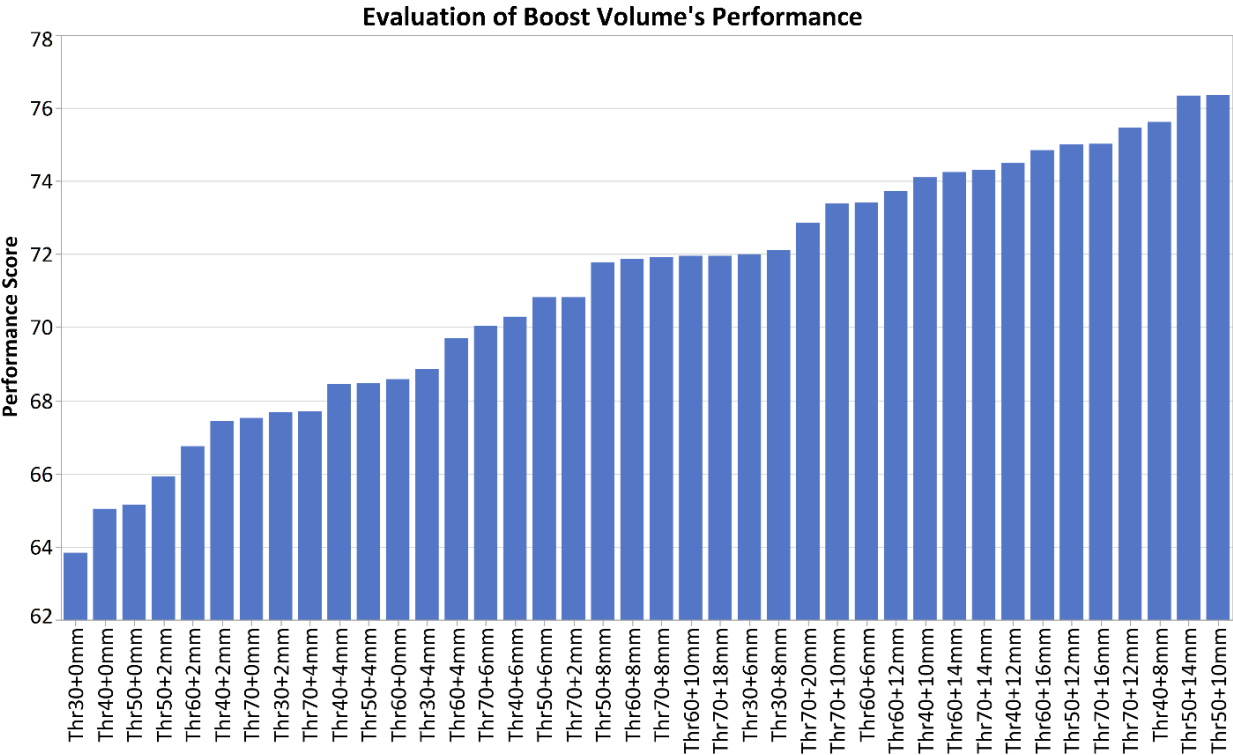
Figure B1. Performance score for each BTV used in this study. Volumes greater than CTV1 were excluded.
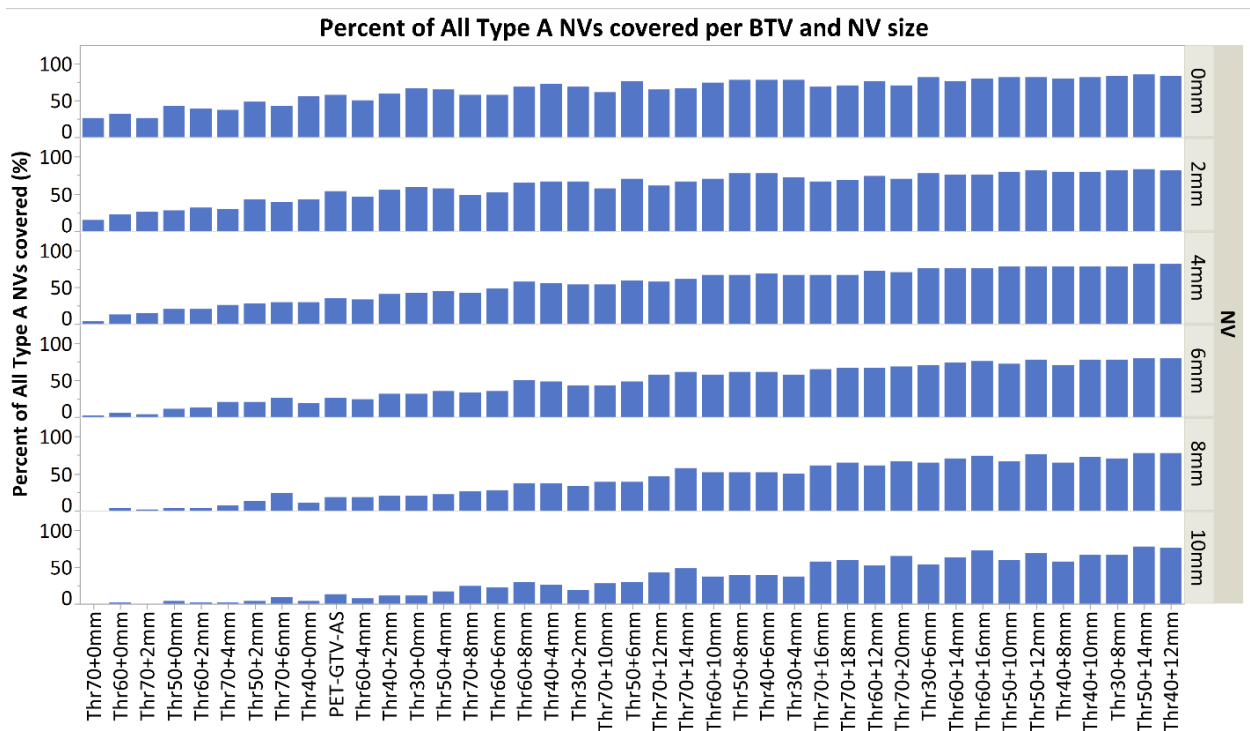
Figure B2 This figure shows coverage data for all recurrent volumes per nidus radius size and boost volume. Boostvolumes are ordered per increasing coverage for 4mm nidus data.
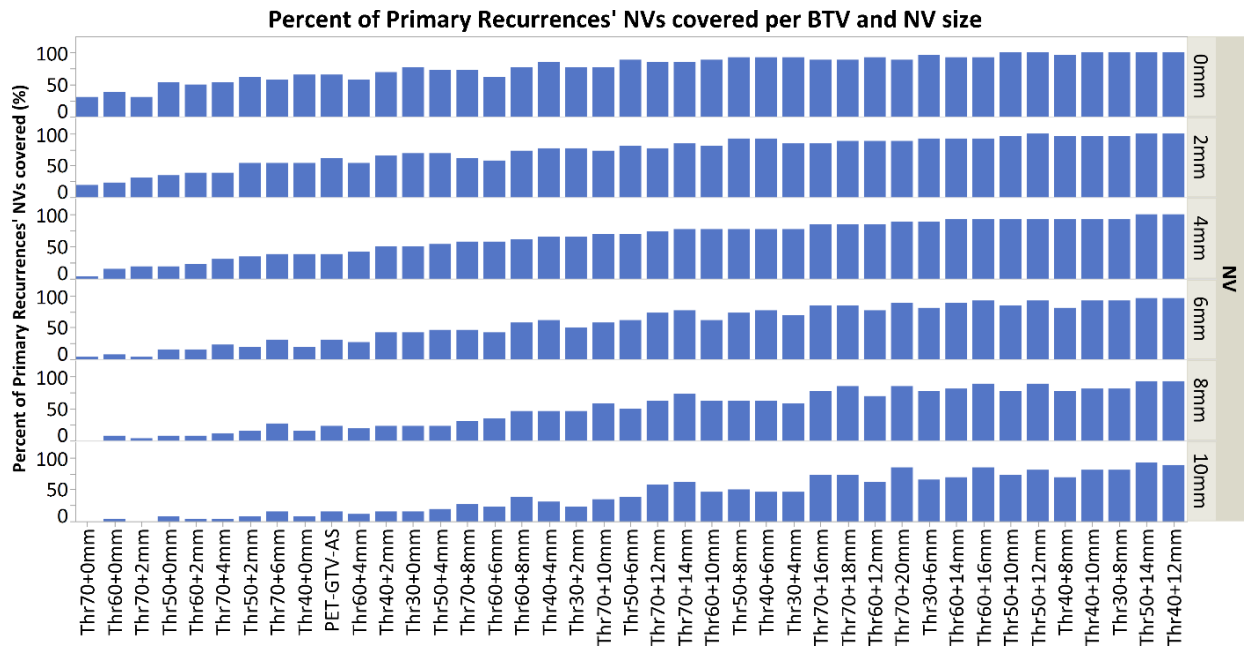
Figure B3 This figure shows coverage data for primary recurrent volumes per nidus radius size and boost volume. Boost volumes are ordered per increasing coverage for 4mm nidus data. In addition, Robustness is included to show the difference per volume between 0mm and 10mm nidus coverage.

Figure B4 This figure shows coverage data for node recurrent volumes per nidus radius size and boost volume. Boost volumes are ordered per increasing coverage for 4mm nidus data.

Appendix C: Supplement to Chapter 9

Section C. 1 Preparation of Radiomic Data.

Imaging Characteristics

Contrast-enhanced Computed Tomography (CT) images were obtained from TCIA with a section thickness ranging from 0.4mm to 5mm. Slice thickness was chiefly 1mm and 3mm in 33.6% and

26.1% of the included scans, respectively. Axial images were acquired by using a matrix of 512×512 pixels and reconstructed with a voxel size of 0.05cm×0.05cm along the x- and y-axis in 85.8% of the scans. Hence, a trilinear interpolation voxel resampling filter was applied to these scans using Imaging Biomarker Explorer (IBEX)(263) software to yield voxel sizes congruent with the mode of the dataset. The contrast-enhanced images were generated after one hundred twenty milliliters of contrast material was injected into patient body at a rate of 3mL/sec, which was followed by scanning after a 90-second delay.

Manual Segmentation of Regions of Interest (ROI)

Gross tumor volumes (GTVs) for primary tumor (GTVp) constituted our regions of interest for this project. GTVs were defined as per ICRU 62/83, specifically, "the gross demonstrable extent and location of the tumor"(331). Tumor volumes were manually segmented on each individual patient's diagnostic contrast-enhanced CT axial images or simulation CT scans by trained personnel independently. They were blinded to relevant clinical meta-data and their segmentation was revised by an expert radiation oncologist, along the regulations we followed for previous projects(332). The segmentation process was governed by the guidelines of the International Commission on Radiation Units and Measurements (ICRU) report 83. Segmentation primarily relied on the findings from physical examination, fiberoptic nasopharyngolaryngoscopy and imaging studies. Manual segmentation was performed by using commercial treatment planning software VelocityAI™ 3.0.1 software. Regions of interest were

then exported in digital imaging and communications and medicine (DICOM) format to IBEX(263) software for further extraction of quantitative imaging features.

Texture Analysis

Texture analysis was performed using IBEX(263), which utilizes the Matlab platform (Mathworks Inc, Natick, VA). Primary tumor GTV contours in DICOM-RTSTRUCT format were imported into IBEX. Features explored in this analysis comprise a group of agnostic imaging features that encompass intensity, shape and texture. These features are typically classified as first, second and higher order texture features(333). First-order features, based on intensity values and the shape of the ROI, are those derived from histogram analysis prior to any mathematical transformation and regardless of spatial configuration. Intensity-based features such as kurtosis and skewness can provide information about the overall distribution of grey levels but due to their nature, are unable to inform about the specific spatial distribution of gray levels within the tumor. To quantify intratumoral heterogeneity incorporating spatial information, textural analysis was employed which constitutes to the second-order statistical output. These include methods such as gray level co-occurrence matrix, gray level run length matrix, and neighbor intensity difference. In these methods, a mathematical transformation is applied to the CT image to create a so-called parent matrix. From this parent matrix, a multitude of calculations for features such as energy, entropy, dissimilarity, and correlation may be performed. Voxel size was resampled in the three dimensions into constant values beforehand, via a trilinear interpolation preprocessing filter. Accordingly, voxel size was set to 0.98 mm in the x-dimension, 0.98 mm in the y-dimension and

246

2.5 mm in the z-dimension. Many of the aforementioned algorithms had various parameters that can be modified to yield drastically different results. To that end, we explored many of these features exhaustively using multiple iterations of filters with varying parameters. Examples of parameters include neighborhood size (measured in voxels) or sigma, among others.

We used IBEX(263) to generate radiomic features of five categories, which are gray level co-occurrence matrix, gray level run length matrix, neighbor intensity difference, intensity direct, and size/shape. Table C1 gives a list of the radiomic features. The information was provided by the developers of IBEX(263). More elaborate definitions of these statistical texture features along with relevant equations were provided by previous literature(259, 334-340).

Table C1. Radiomic features derived from CT images

Feature Category	Features	Definition	References
Gray Level Co-occurrence Matrix	Auto-Correlation	The Correlation texture measures the linear dependency of grey levels on those of neighbouring pixels.	(335)
	Cluster Prominence	A measure of the skewness or asymmetry	(335)

	Cluster Shade	A measure of the skewness or asymmetry	(335)
	Cluster Tendency	Assess if non-random structure exists in the data by measuring the probability that the data is generated by a uniform data distribution	(335)
	Contrast 1	Returns a measure of the intensity contrast between a pixel and its neighbor over the whole image.	(336, 337)
	Correlation	Returns a measure of how correlated a pixel is to its neighbor over the whole image.	(336, 337)
	Difference Entropy	The entropy for the diagonal probabilities	(259, 336)
	Dissimilarity	Dissimilarity is conceptually similar to the Contrast feature in terms of grey level variations	(335)

	Energy 1	Describes the grey level energy	(336, 337)
	Entropy	Entropy is a information-theoretic concept that gives a metric for the information contained within grey level	(335)
	Homogeneity		(259, 336, 337)
	Homogeneity 2		(259, 336, 337)
	Information Measure Correlation 1	The first measure of information theoretic correlation	(259, 336, 337)
	Information Measure Correlation 2	The second measure of information theoretic correlation	(259, 336, 337)
	Inverse Difference Moment Norm	Inverse difference moment after being normalized to	(259, 336, 337)

		improve classification performance of this feature	
	Inverse Difference Norm	Inverse difference after being normalized to improve classification ability of this feature.	(259, 336, 337)
	Inverse Variance		(259)
	Maximum Probability		(335)
	Sum Average	The average for the cross-diagonal probabilities	(259, 336, 337)
	Sum Entropy	The entropy for the cross-diagonal probabilities	(259, 336, 337)
	Sum Variance	The variance for the cross-diagonal probabilities	(259, 336, 337)
Gray Level Run Length Matrix	Gray Level Non-uniformity	This feature assesses the distribution of runs over the grey values	(338)

	High Gray Level Run Emphasis	This is a feature that emphasizes high grey levels,	(338)
	Long Run Emphasis	This feature emphasizes long run lengths	(338)
	Long Run High Gray Level Emphasis	This feature emphasizes runs in the lower right quadrant of the GLRLM, where long run lengths and high grey levels are located	(338)
	Long Run Low Gray Level Emphasis	This feature emphasizes runs in the upper right quadrant of the GLRLM, where long run lengths and low grey levels are located	(338)
	Low Gray Level Run Emphasis	This is a feature where low grey levels are emphasized	(338)
	Run Length Non-uniformity	This feature assesses the distribution of runs over the run lengths	(338)
	Run Percentage	This feature assesses the fraction of the number of	(338)

		realized runs and the maximum number of potential runs	
	Short Run Emphasis	This feature emphasizes short run lengths	(338)
	Short Run High Gray Level Emphasis	This feature emphasizes runs in the lower left quadrant of the GLRLM, where short run lengths and high grey levels are located	(338)
	Short Run Low Gray Level Emphasis	This feature emphasizes runs in the upper left quadrant of the GLRLM, where short run lengths and low grey levels are located	(338)
Neighbor Intensity Difference	Busyness	Textures with large changes in grey levels between neighboring voxels are called busy	(339)
	Coarseness	Summing level differences gives an indication of the	(339)

		level of the spatial rate of change in intensity	
	Complexity	Complex textures are non-uniform and rapid changes in grey levels are common	(339)
	Contrast 2	Contrast depends on the dynamic range of the grey levels as well as the spatial frequency of intensity changes	(339)
	Texture Strength		(339)
Intensity Direct	Energy 2		(259)
	Global Entropy	The intensity entropy among all the voxels	(259)
	Global Maximum	The intensity maximum among all the voxels.	(259)
	Global Mean	The intensity mean among all the voxels.	(259)
	Global Median	The intensity median among all the voxels.	(259)

	Global Minimum	The intensity minimum among all the voxels.	(259)
	Global Std	The intensity standard deviation among all the voxels.	(259)
	Global Uniformity	The intensity uniformity among all the voxels.	(259)
	Inter-Quartile Range	The interquartile range of the intensity values among all the voxels.	(259)
	Kurtosis	Measure the peakedness of all the voxels' intensity.	(259)
	Local Entropy Maximum	First, at each voxel, compute entropy in its neighborhood region. Then, compute the maximum among all the voxel's entropy calculated from step 1.	(259)
	Local Entropy Mean	First, at each voxel, compute entropy in its neighborhood region. Then, compute the	(259)

		mean among all the voxel's entropy calculated from step 1.	
	Local Entropy Median	First, at each voxel, compute entropy in its neighborhood region. Then, compute the median among all the voxel's entropy calculated from step 1.	(259)
	Local Entropy Minimum	First, at each voxel, compute entropy in its neighborhood region. Then, compute the minimum among all the voxel's entropy calculated from step 1.	(259)
	Local Entropy Std	First, at each voxel, compute entropy in its neighborhood region. Then, compute the standard deviation among all the voxel's entropy calculated from step 1.	(259)

	Local Range Maximum	First, at each voxel, compute range value (maximum value-minimum value) in its neighborhood region. Then, compute the median among all the voxel's range value calculated from step 1.	(259)
	Local Range Mean	First, at each voxel, compute range value (maximum value-minimum value) in its neighborhood region. Then, compute the mean among all the voxel's range value calculated from step 1.	(259)
	Local Range Median	First, at each voxel, compute range value (maximum value-minimum value) in its neighborhood region. Then, compute the median among all the voxel's range value calculated from step 1.	(259)

	Local Range Minimum	First, at each voxel, compute range value (maximum value-minimum value) in its neighborhood region. Then, compute the minimum among all the voxel's range value calculated from step 1.	(259)
	Local Range Std	First, at each voxel, compute range value (maximum value-minimum value) in its neighborhood region. Then, compute the standard deviation among all the voxel's range value calculated from step 1.	(259)
	Local Std Maximum	First, at each voxel, compute standard deviation in its neighborhood region. Then, compute the maximum among all the voxel's	(259)

		standard deviation value calculated from step 1.	
	Local Std Mean	First, at each voxel, compute standard deviation in its neighborhood region. Then, compute the mean among all the voxel's standard deviation value calculated from step 1.	(259)
	Local Std Median	First, at each voxel, compute standard deviation in its neighborhood region. Then, compute the median among all the voxel's standard deviation value calculated from step 1.	(259)
	Local Std Minimum	First, at each voxel, compute standard deviation in its neighborhood region. Then, compute the minimum among all the voxel's	(259)

		standard deviation value calculated from step 1.	
	Local Std Std	First, at each voxel, compute standard deviation in its neighborhood region. Then, compute the standard deviation all the voxel's standard deviation value calculated from step 1.	(259)
	Mean Absolute Deviation	The mean absolute deviation of the intensity values among all the voxels.	(259)
	Median Absolute Deviation	The median absolute deviation of the intensity values among all the voxels.	(259)
	Percentile	Percentiles of the intensity values among all the voxels.	(259)
	Quantile	Quantiles of the intensity values among all the voxels.	(259)

	Range	The intensity range (maximum value - minimum value) among all the voxels.	(259)
	Root Mean Square		(259)
	Skewness	Measure the asymmetry of all the voxels' intensity.	(259)
	Variance		(259)
Size/Shape	Compactness 1	Compactness1 = (Volume)/(sqrt(pi)*(SurfaceArea)^(2/3))	(259)
	Compactness 2	Compactness2 = 36*pi*(Volume^2)/((SurfaceArea)^3).	(259)
	Convex	Measure the proportion of the pixels in the convex hull that are also in the region.	(259)
	Convex Hull Volume	The mean volume of the 2D convex hulls that are the convex envelopes of each slice's binary mask.	(259)

	3D Convex Hull Volume	3D volume of the convex hull that is the convex envelope of binary mask.	(259)
	Mass		(259)
	Maximum 3D Diameter	Maximum 3D Diameter = largest pairwise Euclidean distance between voxels on the surface of the tumor volume.	(259)
	Mean Breadth	Denotes integral of mean curvature	(259)
	Number Of Voxels	The number of voxels treating the edge voxels differently.	(259)
	Orientation	Measures the angle between the x-axis and the major axis of the ellipse in 2D.	(259)
	Roundness	Measures how much the binary mask is close to circle in 2D.	(259)

		Measures the deviation of a tumor's shape from a sphere based on its effective diameter	(259)
	Spherical Disproportion		
	Sphericity	Measures how close a tumor's shape is to a sphere	(259)
	Surface Area	The surface area of the binary mask.	(340)
	Surface Area Density	Surface Area Density = (surface area of the binary mask)/(volume of the binary mask).	(259, 340)

For some features in the gray level co-occurrence matrix category and the intensity direct category, multiple feature instances were calculated for a single feature using different parameter settings. For example, for each feature in the gray level co-occurrence matrix category, five feature instances were generated with the offset parameter being 1, 2, 3, 4, and 5, which calculated the feature values over different distances, so the name of a feature from the gray level co-occurrence matrix category usually includes the offset parameter value; for *percentile* and *quantile* in the intensity direct category, feature instances with different percentile and quantile values were calculated. We used IBEX(263) to generate 196 radiomic features based

on the tumor CT images and then removed the features whose values were identical to others. Additionally, two size/shape features, i.e. *voxel size* and *number of objects*, were excluded from analysis, because they did not vary (much) over the tumor cases and thus were not useful for analysis. All tumor cases had the same *voxel size* value equal to 0.002384174. The *number of objects* for all tumor cases was 1, except four of them were 2 and one of them was 3. After removal, 187 radiomic features were kept and used in the analysis. The number of features in each category is shown in Table C2.

Table C. 2   Numbers of features from different radiomic feature categories

Feature category	Gray level co-occurrence matrix	Gray level run length matrix	Neighbor intensity difference	Intensity direct	Size/Shape
Feature number	105	11	5	51	15

Section C. 2 Preparation of Genomic Data.

The genomic data used in this analysis were generated by TCGA(261). All tumor biospecimens were collected according to TCGA protocol. Each tumor biospecimen was extracted from the tissue adjacent to the tissue block where a slide was obtained for disease diagnosis of the patient.

Each tumor sample must pass a pathology review to be qualified for generating genomic data. TCGA protocol required that a tumor sample must contain at least 60% tumor cell nuclei with less than 20% necrosis to be included in the study. The American Joint Committee on Cancer (AJCC) staging system was used to stage all the tumor cases.

All TCGA genomic data and clinical information were retrieved from TCGA data server using TCGA-Assembler[264], an open-source R package that can automatically download, assemble, and process public TCGA data. TCGA used the Illumina HiSeq 2000 sequencing platform to generate RNA-seq data, which were then processed by the MapSplice genome alignment algorithm[341] and the RSEM gene expression estimation algorithm(342). We used the normalized read counts of RNA-seq data for analysis. MiRNA-seq data were generated using the Illumina Genome Analyzer and HiSeq 2000 sequencing platforms and the RPM (Reads Per Million miRNAs mapped) values were used for analysis. In TCGA, the Affymetrix® Genome-Wide Human SNP Array 6.0 and the circular binary segmentation algorithm[343] were used to generate copy number values of DNA fragments, based on which TCGA-Assembler was used to calculate an average copy number for each gene in each sample. Somatic mutation data were generated through exome sequencing using the Illumina Genome Analyzer sequencing platform. Three mutation callers, including VarScan 2 (for SNVs/Indels)[344], SomaticSniper (for SNVs)[345], and GATK IndelGenotyper v2.0 (for Indels)[346], were used to identify candidate mutations. TCGA took the union of the mutations identified by these three callers and additional filtering and processing were taken to ensure the quality of mutation calls[347]. TCGA DNA methylation data were generated using Infinium HumanMethylation450 BeadChip from Illumina, which measures

the methylation level of about 485,000 CpG sites. We used TCGA-Assembler to calculate an average methylation level of CpG sites in the promoter region of each gene, which includes 1500 base pairs upstream of the transcription start site.

Section C. 3 Overview of Identified Associations.

Through linear regression analysis and Gene Set Enrichment Analysis (GSEA)[265, 348], a total of 5350 statistically significant associations (adjusted p-value ≤ 0.05) were identified between various radiomic features and genomic features. Genomic features include miRNA expressions, somatic gene mutations, and transcriptional activities, gene CNVs, and promoter region DNA methylation changes of genetic pathways documented in the Kyoto Encyclopedia of Genes and Genomes (KEGG) database(266). The radiomic features were grouped into five categories, which are gray level co-occurrence matrix, gray level run length matrix, neighbor intensity difference, intensity direct, and size/shape. For details of linear regression analysis and GSEA, see Appendix Information Sections C4-9.

Fig. 2a in the main text is a graphical presentation of the identified associations. Fig. 2b in the main text shows the numbers of identified associations between different categories of genomic features and different categories of radiomic features, based on which Fisher's exact test(268, 269) indicated that the frequency of statistically significant associations depended on the feature category (p-value ≤ $1.0×10^{-8}$), meaning some feature categories had more associations than others.

265

For each pair of genomic feature category and radiomic feature category, we used Fisher's exact test to evaluate the enrichment of associations between them with the resulted adjusted p-value presented in Table C. 3. Take the associations between pathway transcriptional activities and size/shape features as an example to explain how the enrichment significance is evaluated. The total number of genomic features used in the association analysis is 179 (transcriptional activities of pathways) + 179 (copy number variations of pathways) + 179 (promoter region DNA methylation changes of pathways) + 292 (miRNA expressions) + 70 (mutated genes) + 173 (protein expressions) = 1072, so there are 1072×187 = 200464 potential associations, among which 179×15 = 2685 potential associations are between pathway transcriptional activities and size/shape radiomic features. From Figure 9. 2b in the main text, 5350 statistically significant associations have been identified, among which 884 associations are between pathway transcriptional activities and size/shape features. Based on these numbers, Fisher's exact test gives a p-value smaller than 1.0×10 30, after correction over all 30 tests included in Table C. 3 using the Benjamini–Hochberg (BH) procedure.(349) We can see the identified associations were statistically significantly enriched among pathway transcriptional activities and all five categories of radiomic features (adjusted p-values < 1.0×10^{-30}). This implies that transcriptional activities of genetic pathways modulate various aspects of the tumor imaging phenotype.

Table C. 3 Adjusted p-values evaluating the enrichments of statistically significant associations between genomic features of different platforms and radiomic features of different categories

Feature Category	Gray Level Co-occurrence Matrix	Gray Level Run Length Matrix	Neighbor Intensity Difference	Intensity Direct	Size/Shape
Transcriptional activity of pathway	$<1.0 \times 10^{-30}$	$<1.0 \times 10^{-30}$	$<1.0 \times 10^{-30}$	$<1.0 \times 10^{-30}$	$<1.0 \times 10^{-30}$
Copy number variation of pathway	1	1	1	1	1
Promoter region DNA methylation change of pathway	1	1	1	1	1
miRNA expressions	1	1	1	1	1
Mutated genes	1	1	1	1	1

Section C. 4 Associations Between Radiomic Features and Pathway Transcriptional Activities.

We investigated the associations between radiomic features and the transcriptional activities of genetic pathways documented by the KEGG database[266]. Genes with unreliable expressions were removed to avoid significant noise in data or bias in analysis results. A gene was excluded from the analysis, if its read count per million reads mapped was less than 1 in more than a half of the samples. 13562 genes were kept after gene filtering. Their normalized read counts were log2 transformed and used for analysis. The association analysis was performed through two steps, i.e. linear regression analysis and GSEA[265]. The linear regression analysis was performed for each gene and each radiomic feature to examine whether the gene's expression affected the radiomic feature, with adjustments of patient age, tumor stage, tumor subsite, and patient smoke status, which was formulated as

$$x_i = \beta_0 + \beta_1 m_i + \beta_2 a_i + \beta_3 g_{2,i} + \beta_4 g_{3,i} + \beta_5 g_{4,i} + \beta_6 s_{2,i} + \beta_7 s_{3,i} + \beta_8 o_{2,i} + \beta_9 o_{3,i} + \varepsilon, \quad (1)$$

where x_i was the value of the radiomic feature for patient i, m_i was the expression level of the gene in patient i, a_i was the age of patient i, $g_{2,i}$, $g_{3,i}$, and $g_{4,i}$ were three 0/1 indicators coding the patient tumor stage (stage I: $g_{2,i} = 0$, $g_{3,i} = 0$, $g_{4,i} = 0$; stage II: $g_{2,i} = 1$, $g_{3,i} = 0$, $g_{4,i} = 0$; stage III: $g_{2,i} = 0$, $g_{3,i} = 1$, $g_{4,i} = 0$; stage IV: $g_{2,i} = 0$, $g_{3,i} = 0$, $g_{4,i} = 1$), $s_{2,i}$ and $s_{3,i}$ were two 0/1 indicators coding the tumor subsite (larynx: $s_{2,i} = 0$ and $s_{3,i} = 0$; oral cavity: $s_{2,i} = 1$ and $s_{3,i} = 0$; oropharynx: $s_{2,i} = 0$ and $s_{3,i} = 1$), $o_{2,i}$ and $o_{3,i}$ were two 0/1 indicators coding the patient smoke status (current smoker: $o_{2,i} = 0$ and $o_{3,i} = 0$; former smoker: $o_{2,i} = 1$ and $o_{3,i} = 0$; never smoker: $o_{2,i} = 0$ and $o_{3,i} = 1$). A t-value that could be used for evaluating the statistical significance of β_1

was calculated. We then used the Bioconductor R package PIANO[348] to perform GSEA using the t-values as the gene-level statistics. GSEA studies whether the behavior of a set of genes as a whole group correlates with the change of a radiomic feature[265]. It is based on known gene sets that are genetic pathways or functional gene modules. In our analysis, we used the KEGG pathways collected in the Molecular Signature Database[265] that includes 179 genetic pathways covering various genetic and molecular functions. GSEA calculated the gene-set-level statistic and the associated nominal p-value evaluating the statistical significance of the gene-set-level statistic based on 10000 random gene sets. The BH procedure was used to control the False Discovery Rate (FDR) of the identified associations for each radiomic feature among its association tests with all KEGG pathways.[349] An association was statistically significant if the adjusted p-value was no larger than 0.05. Positive association and negative association, i.e. the two different association directions, were tested separately between a gene set and a radiomic feature. Note that because the gene-level statistics (t-values) were obtained through linear regression analysis with adjustments to patient age, tumor grade, tumor subsite, and patient smoke status, our GSEA results were also adjusted to these confounding variables. To our knowledge, this was the first time that GSEA was performed with adjustments to co-variables.

Figure 9.2a in the main text shows the statistically significant associations between radiomic features and transcriptional activities of some cancer-related pathways. One of the pathways was cell cycle and its transcriptional activity was positively associated with tumor texture homogeneity characterized by its associations with *energy 1*, *entropy*, *homogeneity*, and *homogeneity 2*.

269

Section C. 5 Associations Between Radiomic Features and Gene Copy Number Variations of Pathways.

We studied the associations between radiomic features and gene copy number variations (CNVs) of pathways. The analysis procedure followed that of the pathway transcriptional activity associations. First, the linear regression analysis with adjustments to patient age, tumor grade, tumor subsite, and patient smoke status was performed for each pair of gene and radiomic feature following Equation (1), where m_i here was the copy number of the gene in patient i and all other variables in the equation were kept unchanged. Then, GSEA was performed using the t-value of coefficient β_1 obtained in the linear regression analysis as the gene-level statistic. Nominal p-values evaluating the statistical significance of gene-set-level statistics were calculated based on 10000 random gene sets and the FDR was controlled using the BH procedure for each radiomic feature among all its association tests with the 179 KEGG pathways. Before the analysis, genes were ranked according to their standard deviations of copy numbers over the samples from the largest to the smallest. The top 14000 genes were selected for the analysis.

Section C. 6 Associations Between Radiomic Features and Pathway DNA Methylation Changes.

We studied the associations between radiomic features and promoter region DNA methylation changes at the pathway level. The analysis procedure followed those of pathway transcriptional activity and CNVs. The linear regression analysis still followed Equation (1), where m_i here was the DNA methylation value in the promoter region of the gene in patient i and all other variables in the equation were kept unchanged. GSEA was performed using the t-value of coefficient β_1 as the gene-level statistic. Nominal p-values evaluating the statistical significance of gene-set-level statistics were calculated based on 10000 random gene sets and the FDR was controlled using the BH procedure for each radiomic feature among all its association tests with the 179 KEGG pathways. Before the analysis, genes were ranked according to their standard deviations of methylation levels over all patients from the largest to the smallest. The top 14000 genes were selected for the analysis.

Figure 9. 2c in the main text shows the statistically significant associations between radiomic features and promoter region DNA methylation changes of some cancer-related KEGG pathways. Promoter region DNA methylation change of the adherens junction pathway was correlated with tumor shape regularity characterized by its positive association with *sphericity*.

Section C. 7 Associations Between Radiomic Features and miRNA Expressions.

Before the analysis, to select only miRNAs with reliable expression levels for analysis, we removed miRNAs whose RPM values are less than 2 in more than a half of the samples, which resulted in 292 miRNAs for the analysis. Log2 transformation of the RPM data was then taken.

We used the linear regression analysis to identify the associations between radiomic features and miRNA expressions with adjustments to patient age, tumor grade, tumor subsite, and patient smoke status. The linear regression analysis was performed for each pair of miRNA and radiomic feature following Equation (1), where m_i here was the expression level of the miRNA in patient i and all other variables in the equation were kept unchanged. The p-value of coefficient β_1 was obtained in regression analysis and then adjusted using the BH procedure to control the FDR over all association tests of each radiomic feature. Before the analysis, to select only miRNAs with reliable expression levels for analysis, we removed miRNAs whose RPM values are less than 2 in more than a half of the samples, which resulted in 292 miRNAs for the analysis. Log2 transformation of the RPM data was then taken.

Table C. 4 summarizes all statistically significant associations between miRNA expressions and radiomic features. *MiR-320a* has been reported as a negative regulator of tumor invasion and metastasis(273). Its expression correlated with tumor texture homogeneity characterized by positive associations with *homogeneity* and *homogeneity 2* and negative associations with *entropy* and *global entropy*. The radiomic feature *global uniformity* measures the overall homogeneity of tumor pixel intensity(259) and was positively associated with the expressions of 8 miRNAs including both antitumorigenic/*antimetastatic* and oncogenic miRNAs. The antitumorigenic/*antimetastatic* miRNAs include *miR-101* (targeting *EZH2*, a histone-lysine N-methyltransferase enzyme epigenetically silencing tumor suppressor genes(274))*, miR-15b* (targeting *VEGF*, an important factor in the neo-angiogenesis process that is crucial for cells to reach and disseminate through the circulation system(275))*, and *miR-320a*; the oncogenic

miRNAs include *miR-106b* and *miR-25* (both from miR-106b-25 cluster that is over-expressed in HNSCC and promotes cell proliferation(276)), *miR-155* (upregulated in HNSCC and targeting tumor suppressors such as adenomatous polyposis coli(277))*,* and *miR-378* (reported to repress a potential tumor suppressor gene *TOB2* in nasopharyngeal carcinoma(278)); the last miRNA *miR-7* is involved in multiple cancer-related signaling pathways and has been reported mainly as a tumor suppressor, but with the opposite effect also documented(276).

Table C. 4 Statistically significant associations between radiomic features and miRNA expressions

Gene Symbol	Radiomic Feature	Adjusted P-value	Coefficient
hsa-mir-101-2	Global Uniformity	0.03203	0.017687
hsa-mir-106b	Global Uniformity	0.03203	0.01729
hsa-mir-155	Global Uniformity	0.03203	0.019309
hsa-mir-15b	Global Uniformity	0.049439	0.017349
hsa-mir-25	Global Uniformity	0.03203	0.01822
hsa-mir-320a	Entropy (offset = 4)	0.049795	-0.33106

hsa-mir-320a	Entropy (offset = 5)	0.040612	-0.3402
hsa-mir-320a	Homogeneity (offset = 4)	0.045543	0.027079
hsa-mir-320a	Homogeneity (offset = 5)	0.038173	0.028195
hsa-mir-320a	Homogeneity 2 (offset = 4)	0.040392	0.032628
hsa-mir-320a	Homogeneity 2 (offset = 5)	0.03204	0.034094
hsa-mir-320a	Global Entropy	0.024199	-0.17216
hsa-mir-320a	Global Uniformity	0.013523	0.02116
hsa-mir-378	Global Uniformity	0.03203	0.018323
hsa-mir-582	Skewness	0.03015	-1.49173
hsa-mir-7-1	Global Uniformity	0.03203	0.017998

For Coefficient column, positive value indicates positive association and negative value indicates negative association. A radiomic feature from the gray level co-occurrence matrix category can

274

be calculated using different offset parameter values, i.e. 1, 2, 3, 4, and 5, which forms five different instances of a feature.

Section C. 8 Associations Between Radiomic Features and Somatically Mutated Genes.

We used the linear regression analysis to identify the associations between radiomic features and somatically mutated genes with adjustments to patient age, tumor grade, tumor subsite, and patient smoke status. To achieve reliable results, genes with somatic mutations in less than 10 patients were excluded, which resulted in 70 genes for the analysis. The linear regression analysis was performed for each pair of somatically mutated gene and radiomic feature following Equation (1), where m_i here was a 0/1 indicator indicating whether patient i had any somatic mutation in the gene and all other variables kept unchanged. The p-value of coefficient β_1 was obtained in the regression analysis and then adjusted using the BH procedure to control the FDR over all association tests of each radiomic feature.

Table C. 5 summarizes all identified associations between radiomic features and somatically mutated genes. *PCDH15* is a member of the cadherin superfamily that encodes integral membrane proteins regulating calcium-dependent cell-cell adhesion. Mutations in *PCDH15* correlated with the texture homogeneity of HNSCC characterized by *energy 1*. *AHNAK2* has been reported to be over-expressed in pancreatic cancer.[350]

Our analysis indicated that HER3 expression was positively associated with a tumor texture feature named correlation, which measures the correlation between a pixel's intensity and their neighbors' intensities across tumor.

Table C.5 Statistically significant associations between radiomic features and somatically mutated genes

Gene Symbol	Radiomic Feature	Adjusted P-value	Coefficient	Number of Samples With Mutations	Number of Samples Without Mutations
PCDH15	Energy 1 (offset = 2)	0.049784	0.06012	11	111
PCDH15	Energy 1 (offset = 3)	0.042448	0.059314	11	111
PCDH15	Energy 1 (offset = 4)	0.03184	0.059367	11	111
PCDH15	Energy 1 (offset = 5)	0.026395	0.059023	11	111
PCDH15	Maximum Probability (offset = 1)	0.046293	0.108355	11	111
PCDH15	Maximum Probability (offset = 2)	0.044694	0.106199	11	111

PCDH1 5	Maximum Probability (offset = 3)	0.043507	0.1047 75	11	111
PCDH1 5	Maximum Probability (offset = 4)	0.027814	0.1060 42	11	111
PCDH1 5	Maximum Probability (offset = 5)	0.016698	0.1073 1	11	111
LINC00 969	Long Run Low Gray Level Emphasis	0.034502	0.8389 88	12	110
LINC00 969	Global Median	0.041526	- 47.747 8	12	110
LINC00 969	Median Absolute Deviation	0.045561	41.601 47	12	110
LINC00 969	30 Percentile	0.033253	- 98.535	12	110
LINC00 969	35 Percentile	0.03213	- 98.343 2	12	110
LINC00 969	40 Percentile	0.031563	- 97.457 4	12	110

LINC00 969	45 Percentile	0.032072	- 84.927 3	12	110
CUBN	Long Run Low Gray Level Emphasis	0.034502	0.8999 71	10	112
CUBN	Global Median	0.037448	- 52.973	10	112
CUBN	Median Absolute Deviation	0.023872	47.648 97	10	112
CUBN	30 Percentile	0.0248	- 109.32 5	10	112
CUBN	35 Percentile	0.024188	- 109.31 6	10	112
CUBN	40 Percentile	0.024937	- 107.84 9	10	112
CUBN	45 Percentile	0.028463	-93.82	10	112
TUBB8 P7	95 Percentile	0.039029	57.908 78	11	111
AC0245 60.3	Long Run Low Gray Level Emphasis	0.030238	0.9212 28	10	112

AC0245 60.3	Global Median	0.037448	-55.816 3	10	112
AC0245 60.3	Median Absolute Deviation	0.021757	49.368 81	10	112
AC0245 60.3	30 Percentile	0.0248	-113.10 3	10	112
AC0245 60.3	35 Percentile	0.024188	-113.18 1	10	112
AC0245 60.3	40 Percentile	0.02435	-111.88 9	10	112
AC0245 60.3	45 Percentile	0.024681	-97.568 3	10	112
EP300	Inverse Variance (offset = 2)	0.007322	-0.0529 1	10	112
EP300	Inverse Variance (offset = 3)	0.002273	-0.0592 7	10	112

EP300	Inverse Variance (offset = 4)	0.003468	-0.06086	10	112
EP300	Inverse Variance (offset = 5)	0.007857	-0.06122	10	112
EP300	Long Run Low Gray Level Emphasis	0.030238	0.929682	10	112
EP300	Global Median	0.041526	-49.2545	10	112
EP300	Median Absolute Deviation	0.021757	48.69917	10	112
EP300	30 Percentile	0.0248	-107.691	10	112
EP300	35 Percentile	0.024188	-107.363	10	112
EP300	40 Percentile	0.024937	-105.939	10	112

EP300	45 Percentile	0.028463	-91.3924	10	112
COL11A1	Inverse Variance (offset = 2)	0.007322	-0.04203	17	105
COL11A1	Inverse Variance (offset = 3)	0.008623	-0.04275	17	105
COL11A1	Inverse Variance (offset = 4)	0.048034	-0.03945	17	105
COL11A1	Global Median	0.037448	-41.9748	17	105
COL11A1	30 Percentile	0.046828	-79.0511	17	105
COL11A1	35 Percentile	0.040247	-79.889	17	105
COL11A1	40 Percentile	0.040164	-79.0535	17	105

COL11A1	45 Percentile	0.037421	-69.4913	17	105
AHNAK2	Long Run Low Gray Level Emphasis	0.030238	0.920164	11	111
AHNAK2	Global Median	0.037448	-52.6036	11	111
AHNAK2	Median Absolute Deviation	0.021757	47.20461	11	111
AHNAK2	30 Percentile	0.0248	-108.044	11	111
AHNAK2	35 Percentile	0.024188	-109.803	11	111
AHNAK2	40 Percentile	0.02435	-109.176	11	111
AHNAK2	45 Percentile	0.024681	-95.1837	11	111

For Coefficient column, positive value indicates positive association and negative value indicates negative association. A radiomic feature from the gray level co-occurrence matrix category can be calculated using different offset parameter values, i.e. 1, 2, 3, 4, and 5, which forms five different instances of a feature. Percentile and quantile from the intensity direct category can also be calculated using different parameter values resulting in multiple feature instances.

Section C. 9 Associations Between Radiomic Features and Protein Expressions

We used the linear regression analysis to identify the associations between radiomic features and protein (or phospho-protein) expressions with adjustments to patient age, tumor grade, tumor subsite, and patient smoke status. The linear regression analysis was performed for each pair of protein and radiomic feature following Equation (1), where m_i here was the expression level of the protein in patient and all other variables in the equation were kept unchanged. The p-value of coefficient β_1 was obtained in the regression analysis and then adjusted using the BH

procedure to control the FDR over all association tests of each radiomic feature.

Table C. 6 summarizes the identified associations between radiomic features and protein expressions. HER3 (encoded by ERBB3) is a member of the epidermal growth factor receptor (EGFR) family and can function as an oncoprotein. Our analysis indicated that HER3 expression was positively associated with a tumor texture feature named correlation, which

283

measures the correlation between a pixel's intensity and their neighbors' intensities across tumor.

Table C. 6 Statistically significant associations between radiomic features and protein expressions.

Gene Symbol	Radiomic Feature	Adjusted P-value	Coefficient
MAPK1|ERK2-R-C	Maximum 3D Diameter	0.026239	0.86837
ERBB3|HER3-R-V	Correlation (offset = 5)	0.046202	0.045507
TSC2|Tuberin-R-C	Maximum 3D Diameter	0.026239	0.957955

For Gene Symbol column, characters before "|" is the gene encoding the protein and characters after "|" is the antibody used for measuring the protein expression. For Coefficient column, positive value indicates positive association and negative value indicates negative association. A radiomic feature from the gray level co-occurrence matrix category can be calculated using

different offset parameter values, i.e. 1, 2, 3, 4, and 5, which forms five different instances of a feature.

Section C. 10 Prediction of HNSCC HPV Status and Disruptive TP53 Mutation Using Radiomic Features.

We used random forest classifiers(267, 351) to predict HPV status and disruptive TP53 mutation in tumor (i.e. to predict whether a tumor possesses any disruptive TP53 mutation), based on radiomic features. We used CRAN R package "randomForest" (https://cran.r-project.org/web/packages/randomForest/index.html) to implement the classification pipeline. A two-tier nested cross-validation scheme was used to evaluate the generalization prediction performance (see Figure C. 1). The parameters of the random forest algorithm, including the number of features used for decision at each node in a tree and the maximum size of a terminal node (leaf) in a tree were tuned through the inner-tier cross-validation, in which the set of parameters that generated the highest average prediction accuracy on the testing data in the inner-tier cross-validation trials were used to train the classifier on the outer-tier training data and the trained classifier was used to predict the labels of outer-tier testing data. The outer-tier cross-validation evaluated the generalization prediction performance of the whole classification scenario including the parameter tuning. For the maximum size of terminal node, the candidate parameter values were 1 and 2. The candidate values for the number of features used for decision at each node were generated based on the suggestion from the user manual of the randomForest R package by calculating $\text{unique}\big(\text{floor}\big(\text{seq}(f_{min}, f_{max}, 10)\big)\big)$, where $\text{unique}(\cdot)$ was the R function returning the unique elements of an input numeric vector, $\text{floor}(\cdot)$ was the R

function returning a numeric vector containing the largest integers not greater than the corresponding elements of the input vector, and seq(f_{min}, f_{max}, 10) was the R function returning a sequence of eleven equally spanned numeric values starting at f_{min} and ending at f_{max}. f_{min}= max (floor($\sqrt{p}/3$), 1) and f_{max}= min (floor($\sqrt{p} \times 3$), p), where p was the number of features in the data, max($\cdot$, $\cdot$) returned the larger value of the two inputs, and min($\cdot$, $\cdot$) returned the smaller value of the two inputs. Basically, there were eleven candidate values for the number of features used for decision at each node, which were evenly spanned from f_{min} to f_{max}. The number of random trees in the random forest classifier was always set at 10000. Before analysis, all radiomic features were standardized to have a 0 mean and a unit standard deviation.

An importance measure was used to evaluate the prediction power (i.e. importance) of features. It was calculated based on permuting the out-of-bag (OOB) data. OOB data were samples excluded from constructing a tree and used for testing the classification accuracy of the constructed tree. For each tree, the classification accuracy of the OOB portion of the data was recorded. Then the same was done after randomly permuting the values of a feature. The difference between the two classification accuracies were then averaged over all trees, and normalized (divided) by the standard deviation of the difference, which formed the importance measure of feature. Features were ranked according to their importance measure for selecting top predictive features. We applied a recursive feature elimination scheme as shown in Figure C. 1 The prediction performance evaluation was first conducted using all features. Then, for each pair of outer-tier training data and testing data, the features were ranked based on their importance measures obtained on the training data and the top 100 features were selected. Both

286

the training data and the testing data were modified to include only these 100 most important features, while the other features were removed. Then the prediction performance was re-evaluated based on the 100 features. This feature elimination process went on recursively to select the best 50 features out of the 100 features, the best 20 features out of the 50 features, the best 10 features out of the 20 features, and finally the best 5 features out of the 10 features. As a result, the generalization prediction performance was evaluated for the cases of all features, 100 features, 50 features, 20 features, 10 features, and 5 features. The Area Under the Receiver Operating Characteristic (ROC) Curve (AUC) was used as the performance metric for prediction accuracy. Both the outer-tier and inner-tier cross-validation schemes were five-fold cross-validations, with the classification performance summarized over 30 cross-validation trials.

We used the above feature selection and prediction scheme to predict patient HPV status based on radiomic features. When five features were selected in each cross-validation trial for prediction, the top five features most frequently selected for prediction were *global maximum*, *skewness*, *sum variance (offset = 5)*, *sum variance (offset = 4)*, and *local range std*, which were used in 24, 17, 14, 10, and 9 out of the 30 cross-validation trials, respectively. Offset was a parameter used to calculate radiomic features in the gray level co-occurrence matrix category and it took multiple values (i.e. 1, 2, 3, 4, 5), each of which resulted in a different instance of the feature. The most frequently selected feature, i.e. *global maximum*, is the maximum intensity value of all voxels in a tumor; *skewness* measures the asymmetry of the intensity distribution of all voxels in a tumor; *sum variance* is related to the heterogeneity of tumor texture; *local range*

287

std calculates the standard deviation of the intensity range of the neighborhoods for all tumor voxels, forming a feature related to pixel intensity heterogeneity.

Using the same analysis scheme, we predicted disruptive TP53 mutations in tumors using radiomic features and selected predictive ones from them. When five features were selected in each cross-validation trial for prediction, the top five features most frequently selected for prediction were *mean absolute deviation*, *global maximum*, *sum entropy (offset = 5)*, *texture strength*, and *global entropy*, which were selected in 20, 16, 14, 13, and 11 out of the 30 cross-validation trials, respectively. *Mean absolute deviation*, *sum entropy*, and *global entropy* measure the heterogeneity of tumor voxel intensity or texture. *Texture strength* evaluates the saliency of tumor texture primitives. *Global maximum*, the most frequently selected feature for predicting HPV status, is the second most frequently selected feature here for predicting disruptive TP53 mutation.

The frequencies of the most frequently selected features across cross-validation trials are not very high in both prediction tasks. It may be caused by the relatively small sample sizes, i.e. 125 tumor samples for predicting patient HPV status and 122 tumor samples for predicting disruptive TP53 mutations in tumors. Due to the small sample size, the data distribution in each cross-validation trail may substantially vary, thus different features can be selected for prediction across trials.
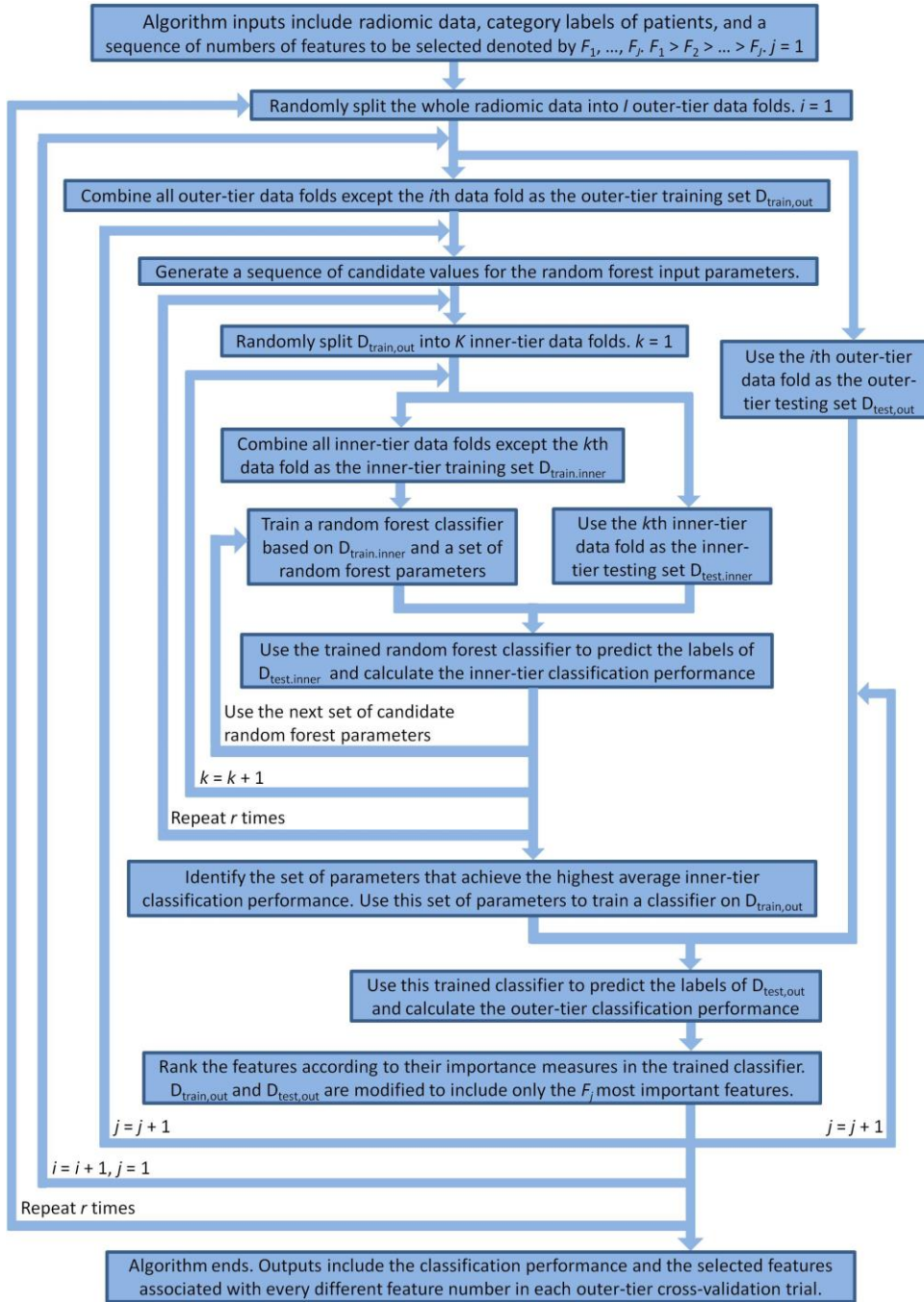
Figure C. 1 A flowchart showing the two-tier nested cross-validation scheme for evaluating the generalization prediction performance.

Bibliography:

1.   Siegel RL, Miller KD, Jemal A. Cancer statistics, 2019. CA Cancer J Clin. 2019;69(1):7-34. Epub

2019/01/09. doi: 10.3322/caac.21551. PubMed PMID: 30620402.

2.   Fakhry C, Westra WH, Li S, Cmelak A, Ridge JA, Pinto H, Forastiere A, Gillison ML. Improved

Survival of Patients With Human Papillomavirus–Positive Head and Neck Squamous Cell Carcinoma in a

Prospective Clinical Trial. JNCI: Journal of the National Cancer Institute. 2008;100(4):261-9. doi:

10.1093/jnci/djn011.

3.   Ang KK, Sturgis EM. Human Papillomavirus as a Marker of the Natural History and Response to

Therapy of Head and Neck Squamous Cell Carcinoma. Seminars in radiation oncology. 2012;22(2):128-

42. doi: https://doi.org/10.1016/j.semradonc.2011.12.004.

4.   Ang KK, Harris J, Wheeler R, Weber R, Rosenthal DI, Nguyen-Tân PF, Westra WH, Chung CH,

Jordan RC, Lu C, Kim H, Axelrod R, Silverman CC, Redmond KP, Gillison ML. Human papillomavirus and

survival of patients with oropharyngeal cancer. N Engl J Med. 2010;363(1):24-35. Epub 2010/06/10. doi:

10.1056/NEJMoa0912217. PubMed PMID: 20530316; PMCID: PMC2943767.

5.   Dahlstrom KR, Calzada G, Hanby JD, Garden AS, Glisson BS, Li G, Roberts DB, Weber RS, Sturgis

EM. An evolution in demographics, treatment, and outcomes of oropharyngeal cancer at a major

cancer center: a staging system in need of repair. Cancer. 2013;119(1):81-9. Epub 2012/06/28. doi:

10.1002/cncr.27727. PubMed PMID: 22736261; PMCID: PMC3469778.

6.   Garden AS, Kies MS, Morrison WH, Weber RS, Frank SJ, Glisson BS, Gunn GB, Beadle BM, Ang

KK, Rosenthal DI, Sturgis EM. Outcomes and patterns of care of patients with locally advanced

oropharyngeal carcinoma treated in the early 21st century. Radiat Oncol. 2013;8:21. doi:

10.1186/1748-717X-8-21. PubMed PMID: 23360540; PMCID: PMC3576243.

7.   Sandulache VC, Hamblin J, Lai S, Pezzi T, Skinner HD, Khan NA, Dioun SM, Hartman C, Kramer J,

Chiao E, Zhou X, Zevallos JP. Oropharyngeal squamous cell carcinoma in the veteran population:

Association with traditional carcinogen exposure and poor clinical outcomes. Head Neck.

2015;37(9):1246-53. doi: 10.1002/hed.23740. PubMed PMID: 24801106; PMCID: PMC4496314.

8.   Nutting CM, Morden JP, Harrington KJ, Urbano TG, Bhide SA, Clark C, Miles EA, Miah AB,

Newbold K, Tanay M, Adab F, Jefferies SJ, Scrase C, Yap BK, A'Hern RP, Sydenham MA, Emson M, Hall E.

Parotid-sparing intensity modulated versus conventional radiotherapy in head and neck cancer

(PARSPORT): a phase 3 multicentre randomised controlled trial. Lancet Oncol. 2011;12(2):127-36. Epub

2011/01/18. doi: 10.1016/s1470-2045(10)70290-4. PubMed PMID: 21236730; PMCID: PMC3033533.

9.   Bernier J, Domenge C, Ozsahin M, Matuszewska K, Lefebvre JL, Greiner RH, Giralt J, Maingon P,

Rolland F, Bolla M, Cognetti F, Bourhis J, Kirkpatrick A, van Glabbeke M. Postoperative irradiation with

or without concomitant chemotherapy for locally advanced head and neck cancer. The New England

journal of medicine. 2004;350(19):1945-52. Epub 2004/05/07. doi: 10.1056/NEJMoa032641. PubMed

PMID: 15128894.

10.   Garden AS, Kies MS, Morrison WH, Weber RS, Frank SJ, Glisson BS, Gunn GB, Beadle BM, Ang

KK, Rosenthal DI, Sturgis EM. Outcomes and patterns of care of patients with locally advanced

oropharyngeal carcinoma treated in the early 21(st) century. Radiation Oncology (London, England).

2013;8:21-. doi: 10.1186/1748-717X-8-21. PubMed PMID: PMC3576243.

11.   Haughey BH, Sinha P. Prognostic factors and survival unique to surgically treated p16+ oropharyngeal cancer. The Laryngoscope. 2012;122(S2):S13-S33. doi: 10.1002/lary.23493.

12.   Licitra L, Perrone F, Bossi P, Suardi S, Mariani L, Artusi R, Oggionni M, Rossini C, Cantù G, Squadrelli M, Quattrone P, Locati LD, Bergamini C, Olmi P, Pierotti MA, Pilotti S. High-Risk Human Papillomavirus Affects Prognosis in Patients With Surgically Treated Oropharyngeal Squamous Cell Carcinoma. Journal of Clinical Oncology. 2006;24(36):5630-6. doi: 10.1200/jco.2005.04.6136.

13.   Mendenhall WM, Amdur RJ, Morris CG, Kirwan JM, Li JG. Intensity-modulated radiotherapy for oropharyngeal squamous cell carcinoma1. The Laryngoscope. 2010;120(11):2218-22. doi: 10.1002/lary.21144.

14.   Sedaghat AR, Zhang Z, Begum S, Palermo R, Best S, Ulmer KM, Levine M, Zinreich E, Messing BP, Gold D, Wu AA, Niparko KJ, Kowalski J, Hirata RM, Saunders JR, Westra WH, Pai SI. Prognostic significance of human papillomavirus in oropharyngeal squamous cell carcinomas. The Laryngoscope. 2009;119(8):1542-9. doi: 10.1002/lary.20533.

15.   Toledano I, Graff P, Serre A, Boisselier P, Bensadoun R-J, Ortholan C, Pommier P, Racadot S, Calais G, Alfonsi M, Favrel V, Giraud P, Lapeyre M. Intensity-modulated radiotherapy in head and neck cancer: Results of the prospective study GORTEC 2004–03. Radiotherapy and Oncology. 2012;103(1):57-62. doi: http://dx.doi.org/10.1016/j.radonc.2011.12.010.

16.   Ang KK, Harris J, Wheeler R, Weber R, Rosenthal DI, Nguyen-Tân PF, Westra WH, Chung CH, Jordan RC, Lu C, Kim H, Axelrod R, Silverman CC, Redmond KP, Gillison ML. Human Papillomavirus and

Survival of Patients with Oropharyngeal Cancer. The New England journal of medicine. 2010;363(1):24-35. doi: 10.1056/NEJMoa0912217. PubMed PMID: PMC2943767.

17.   Eisbruch A, Schwartz M, Rasch C, Vineberg K, Damen E, Van As CJ, Marsh R, Pameijer FA, Balm AJM. Dysphagia and aspiration after chemoradiotherapy for head-and-neck cancer: Which anatomic structures are affected and can they be spared by IMRT? International Journal of Radiation Oncology*Biology*Physics. 2004;60(5):1425-39. doi: http://dx.doi.org/10.1016/j.ijrobp.2004.05.050.

18.   Levendag PC, Teguh DN, Voet P, van der Est H, Noever I, de Kruijf WJM, Kolkman-Deurloo I-K, Prevost J-B, Poll J, Schmitz PIM, Heijmen BJ. Dysphagia disorders in patients with cancer of the oropharynx are significantly affected by the radiation therapy dose to the superior and middle constrictor muscle: A dose-effect relationship. Radiotherapy and Oncology. 2007;85(1):64-73. doi: http://dx.doi.org/10.1016/j.radonc.2007.07.009.

19.   Mortensen HR, Jensen K, Aksglæde K, Behrens M, Grau C. Late dysphagia after IMRT for head and neck cancer and correlation with dose–volume parameters. Radiotherapy and Oncology. 2013;107(3):288-94. doi: http://dx.doi.org/10.1016/j.radonc.2013.06.001.

20.   Wilson JA, Carding PN, Patterson JM. Dysphagia after Nonsurgical Head and Neck Cancer Treatment: Patients' Perspectives. Otolaryngology -- Head and Neck Surgery. 2011;145(5):767-71. doi: 10.1177/0194599811414506.

21.   Bayman E, Prestwich RJ, Speight R, Aspin L, Garratt L, Wilson S, Dyker KE, Sen M. Patterns of failure after intensity-modulated radiotherapy in head and neck squamous cell carcinoma using

compartmental clinical target volume delineation. Clin Oncol (R Coll Radiol). 2014;26(10):636-42. doi:

10.1016/j.clon.2014.05.001. PubMed PMID: 24928558.

22.   Dandekar V, Morgan T, Turian J, Fidler MJ, Showel J, Nielsen T, Coleman J, Diaz A, Sher DJ.

Patterns-of-failure after helical tomotherapy-based chemoradiotherapy for head and neck cancer:

implications for CTV margin, elective nodal dose and bilateral parotid sparing. Oral Oncol.

2014;50(5):520-6. doi: 10.1016/j.oraloncology.2014.02.009. PubMed PMID: 24613544.

23.   Gupta T, Jain S, Agarwal JP, Ghosh-Laskar S, Phurailatpam R, Pai-Shetty R, Dinshaw KA.

Prospective assessment of patterns of failure after high-precision definitive (chemo)radiation in head-

and-neck squamous cell carcinoma. Int J Radiat Oncol Biol Phys. 2011;80(2):522-31. doi:

10.1016/j.ijrobp.2010.01.054. PubMed PMID: 20646862.

24.   Yovino S, Settle K, Taylor R, Wolf J, Kwok Y, Cullen K, Ord R, Zimrin A, Strome S, Suntharalingam

M. Patterns of failure among patients with squamous cell carcinoma of the head and neck who obtain a

complete response to chemoradiotherapy. Head Neck. 2010;32(1):46-52. doi: 10.1002/hed.21141.

PubMed PMID: 19484762.

25.   Schoenfeld GO, Amdur RJ, Morris CG, Li JG, Hinerman RW, Mendenhall WM. Patterns of failure

and toxicity after intensity-modulated radiotherapy for head and neck cancer. International journal of

radiation oncology, biology, physics. 2008;71(2):377-85. doi: 10.1016/j.ijrobp.2007.10.010. PubMed

PMID: 18164838.

26.   Daly ME, Lieskovsky Y, Pawlicki T, Yau J, Pinto H, Kaplan M, Fee WE, Koong A, Goffinet DR, Xing

L, Le QT. Evaluation of patterns of failure and subjective salivary function in patients treated with

294

intensity modulated radiotherapy for head and neck squamous cell carcinoma. Head Neck.

2007;29(3):211-20. doi: 10.1002/hed.20505. PubMed PMID: 17111429.

27.   Chao KS, Ozyigit G, Tran BN, Cengiz M, Dempsey JF, Low DA. Patterns of failure in patients

receiving definitive and postoperative IMRT for head-and-neck cancer. Int J Radiat Oncol Biol Phys.

2003;55(2):312-21. PubMed PMID: 12527043.

28.   Brizel DM, Lydiatt W, Colevas AD. Controversies in the locoregional management of head and

neck cancer. Journal of the National Comprehensive Cancer Network : JNCCN. 2011;9(6):653-62. Epub

2011/06/04. doi: 10.6004/jnccn.2011.0054. PubMed PMID: 21636537.

29.   Perri F, Ionna F, Muto P, Marzo MD, Caponigro F, Longo F, Vittoria Scarpati GD, Lorenzo GD,

Giuliano M, Solla R. Genetics and management of locally advanced carcinomas of the head and neck:

role of altered fractionation radiotherapy. Future Sci OA. 2018;5(1):FSO347-FSO. doi: 10.4155/fsoa-

2018-0058. PubMed PMID: 30652016.

30.   Alsahafi E, Begg K, Amelio I, Raulf N, Lucarelli P, Sauter T, Tavassoli M. Clinical update on head

and neck cancer: molecular biology and ongoing challenges. Cell death & disease. 2019;10(8):540. Epub

2019/07/17. doi: 10.1038/s41419-019-1769-9. PubMed PMID: 31308358; PMCID: PMC6629629.

31.   Gregoire V, Coche E, Cosnard G, Hamoir M, Reychler H. Selection and delineation of lymph

node target volumes in head and neck conformal radiotherapy. Proposal for standardizing terminology

and procedure based on the surgical experience. Radiotherapy and oncology : journal of the European

Society for Therapeutic Radiology and Oncology. 2000;56(2):135-50. PubMed PMID: 10927132.

32.   Eisbruch A, Marsh LH, Dawson LA, Bradford CR, Teknos TN, Chepeha DB, Worden FP, Urba S, Lin A, Schipper MJ, Wolf GT. Recurrences near base of skull after IMRT for head-and-neck cancer: implications for target delineation in high neck and for parotid gland sparing. Int J Radiat Oncol Biol Phys. 2004;59(1):28-42. doi: 10.1016/j.ijrobp.2003.10.032. PubMed PMID: 15093896.

33.   Suzuki M, Nishimura Y, Nakamatsu K, Okumura M, Hashiba H, Koike R, Kanamori S, Shibata T. Analysis of interfractional set-up errors and intrafractional organ motions during IMRT for head and neck tumors to define an appropriate planning target volume (PTV)- and planning organs at risk volume (PRV)-margins. Radiotherapy and oncology : journal of the European Society for Therapeutic Radiology and Oncology. 2006;78(3):283-90. doi: 10.1016/j.radonc.2006.03.006. PubMed PMID: 16564594.

34.   Hong TS, Tome WA, Harari PM. Heterogeneity in head and neck IMRT target design and clinical practice. Radiotherapy and oncology : journal of the European Society for Therapeutic Radiology and Oncology. 2012;103(1):92-8. Epub 2012/03/13. doi: 10.1016/j.radonc.2012.02.010. PubMed PMID: 22405806; PMCID: Pmc3694728.

35.   Shakam A, Scrimger R, Liu D, Mohamed M, Parliament M, Field GC, El-Gayed A, Cadman P, Jha N, Warkentin H, Skarsgard D, Zhu Q, Ghosh S. Dose-volume analysis of locoregional recurrences in head and neck IMRT, as determined by deformable registration: a prospective multi-institutional trial. Radiotherapy and oncology : journal of the European Society for Therapeutic Radiology and Oncology. 2011;99(2):101-7. doi: 10.1016/j.radonc.2011.05.008. PubMed PMID: 21621868.

36.   Due AK, Vogelius IR, Aznar MC, Bentzen SM, Berthelsen AK, Korreman SS, Kristensen CA, Specht L. Methods for estimating the site of origin of locoregional recurrence in head and neck squamous cell

carcinoma. Strahlentherapie und Onkologie : Organ der Deutschen Rontgengesellschaft [et al].

2012;188(8):671-6. Epub 2012/05/15. doi: 10.1007/s00066-012-0127-y. PubMed PMID: 22580623.

37.   Raktoe SA, Dehnad H, Raaijmakers CP, Braunius W, Terhaard CH. Origin of tumor recurrence

after intensity modulated radiation therapy for oropharyngeal squamous cell carcinoma. International

journal of radiation oncology, biology, physics. 2013;85(1):136-41. Epub 2012/05/01. doi:

10.1016/j.ijrobp.2012.02.042. PubMed PMID: 22541959.

38.   Kontaxis C, Bol GH, Lagendijk JJ, Raaymakers BW. Towards adaptive IMRT sequencing for the

MR-linac. Phys Med Biol. 2015;60(6):2493-509. Epub 2015/03/10. doi: 10.1088/0031-9155/60/6/2493.

PubMed PMID: 25749856.

39.   Kontaxis C, Bol GH, Lagendijk JJ, Raaymakers BW. A new methodology for inter- and

intrafraction plan adaptation for the MR-linac. Physics in medicine and biology. 2015;60(19):7485-97.

doi: 10.1088/0031-9155/60/19/7485. PubMed PMID: 26371425.

40.   Bostel T, Nicolay NH, Grossmann JG, Mohr A, Delorme S, Echner G, Haring P, Debus J, Sterzing

F. MR-guidance--a clinical study to evaluate a shuttle- based MR-linac connection to provide MR-guided

radiotherapy. Radiat Oncol. 2014;9:12. doi: 10.1186/1748-717X-9-12. PubMed PMID: 24401489;

PMCID: 3904210.

41.   Ryoo I, Kim JH, Choi SH, Sohn CH, Kim SC. Squamous Cell Carcinoma of the Head and Neck:

Comparison of Diffusion-weighted MRI at b-values of 1,000 and 2,000 s/mm(2) to Predict Response to

Induction Chemotherapy. Magnetic resonance in medical sciences : MRMS : an official journal of Japan

Society of Magnetic Resonance in Medicine. 2015;14(4):337-45. doi: 10.2463/mrms.2015-0003. PubMed PMID: 26104081.

42.   Chen Y, Liu X, Zheng D, Xu L, Hong L, Xu Y, Pan J. Diffusion-weighted magnetic resonance imaging for early response assessment of chemoradiotherapy in patients with nasopharyngeal carcinoma. Magnetic resonance imaging. 2014;32(6):630-7. doi: 10.1016/j.mri.2014.02.009. PubMed PMID: 24703576.

43.   Ng SH, Lin CY, Chan SC, Lin YC, Yen TC, Liao CT, Chang JT, Ko SF, Wang HM, Chang CJ, Wang JJ. Clinical utility of multimodality imaging with dynamic contrast-enhanced MRI, diffusion-weighted MRI, and 18F-FDG PET/CT for the prediction of neck control in oropharyngeal or hypopharyngeal squamous cell carcinoma treated with chemoradiation. PLoS One. 2014;9(12):e115933. Epub 2014/12/23. doi: 10.1371/journal.pone.0115933. PubMed PMID: 25531391; PMCID: PMC4274121.

44.   Noij DP, Pouwels PJ, Ljumanovic R, Knol DL, Doornaert P, de Bree R, Castelijns JA, de Graaf P. Predictive value of diffusion-weighted imaging without and with including contrast-enhanced magnetic resonance imaging in image analysis of head and neck squamous cell carcinoma. European journal of radiology. 2015;84(1):108-16. doi: 10.1016/j.ejrad.2014.10.015. PubMed PMID: 25467228.

45.   Hoang JK, Choudhury KR, Chang J, Craciunescu OI, Yoo DS, Brizel DM. Diffusion-weighted imaging for head and neck squamous cell carcinoma: quantifying repeatability to understand early treatment-induced change. AJR American journal of roentgenology. 2014;203(5):1104-8. doi: 10.2214/AJR.14.12838. PubMed PMID: 25341151.

46.   Lambrecht M, Van Calster B, Vandecaveye V, De Keyzer F, Roebben I, Hermans R, Nuyts S. Integrating pretreatment diffusion weighted MRI into a multivariable prognostic model for head and neck squamous cell carcinoma. Radiotherapy and oncology : journal of the European Society for Therapeutic Radiology and Oncology. 2014;110(3):429-34. doi: 10.1016/j.radonc.2014.01.004. PubMed PMID: 24630535.

47.   Matoba M, Tuji H, Shimode Y, Toyoda I, Kuginuki Y, Miwa K, Tonami H. Fractional change in apparent diffusion coefficient as an imaging biomarker for predicting treatment response in head and neck cancer treated with chemoradiotherapy. AJNR American journal of neuroradiology. 2014;35(2):379-85. Epub 2013/09/14. doi: 10.3174/ajnr.A3706. PubMed PMID: 24029391; PMCID: PMC7965773.

48.   Hong J, Yao Y, Zhang Y, Tang T, Zhang H, Bao D, Chen Y, Pan J. Value of magnetic resonance diffusion-weighted imaging for the prediction of radiosensitivity in nasopharyngeal carcinoma. Otolaryngology--head and neck surgery : official journal of American Academy of Otolaryngology-Head and Neck Surgery. 2013;149(5):707-13. doi: 10.1177/0194599813496537. PubMed PMID: 23884282.

49.   Chawla S, Kim S, Dougherty L, Wang S, Loevner LA, Quon H, Poptani H. Pretreatment diffusion-weighted and dynamic contrast-enhanced MRI for prediction of local treatment response in squamous cell carcinomas of the head and neck. AJR American journal of roentgenology. 2013;200(1):35-43. doi: 10.2214/AJR.12.9432. PubMed PMID: 23255739; PMCID: 3549615.

50.   Vandecaveye V, Dirix P, De Keyzer F, de Beeck KO, Vander Poorten V, Roebben I, Nuyts S, Hermans R. Predictive value of diffusion-weighted magnetic resonance imaging during

chemoradiotherapy for head and neck squamous cell carcinoma. European radiology. 2010;20(7):1703-14. doi: 10.1007/s00330-010-1734-6. PubMed PMID: 20179939.

51.   Vandecaveye V, Dirix P, De Keyzer F, Op de Beeck K, Vander Poorten V, Hauben E, Lambrecht M, Nuyts S, Hermans R. Diffusion-weighted magnetic resonance imaging early after chemoradiotherapy to monitor treatment response in head-and-neck squamous cell carcinoma. Int J Radiat Oncol Biol Phys. 2012;82(3):1098-107. doi: 10.1016/j.ijrobp.2011.02.044. PubMed PMID: 21514067.

52.   Ding Y, Hazle JD, Mohamed AS, Frank SJ, Hobbs BP, Colen RR, Gunn GB, Wang J, Kalpathy-Cramer J, Garden AS, Lai SY, Rosenthal DI, Fuller CD. Intravoxel incoherent motion imaging kinetics during chemoradiotherapy for human papillomavirus-associated squamous cell carcinoma of the oropharynx: preliminary results from a prospective pilot study. NMR in biomedicine. 2015;28(12):1645-54. doi: 10.1002/nbm.3412. PubMed PMID: 26451969; PMCID: 4715635.

53.   Lambrecht M, Van Herck H, De Keyzer F, Vandecaveye V, Slagmolen P, Suetens P, Hermans R, Nuyts S. Redefining the target early during treatment. Can we visualize regional differences within the target volume using sequential diffusion weighted MRI? Radiotherapy and oncology : journal of the European Society for Therapeutic Radiology and Oncology. 2014;110(2):329-34. doi: 10.1016/j.radonc.2013.09.023. PubMed PMID: 24231234.

54.   Hauser T, Essig M, Jensen A, Gerigk L, Laun FB, Munter M, Simon D, Stieltjes B. Characterization and therapy monitoring of head and neck carcinomas using diffusion-imaging-based intravoxel incoherent motion parameters-preliminary results. Neuroradiology. 2013;55(5):527-36. doi: 10.1007/s00234-013-1154-9. PubMed PMID: 23417120.

55.   Campbell SR, Mohamed AS, Heukelom J, Awan MJ, Garden AS, Gunn GB, Rosenthal DI, Fuller

CD. Primary Tumor Regression Index: The Prognostic Value of Volumetric Image Guided Radiation

Therapy for Head and Neck Cancer. Int J Radiat Oncol Biol Phys. 2016;96(2s):E363-e4. Epub

2016/09/28. doi: 10.1016/j.ijrobp.2016.06.1544. PubMed PMID: 27674487.

56.   Gillies RJ, Kinahan PE, Hricak H. Radiomics: Images Are More than Pictures, They Are Data.

Radiology. 2016;278(2):563-77. doi: 10.1148/radiol.2015151169. PubMed PMID: 26579733.

57.   Aerts HJ, Velazquez ER, Leijenaar RT, Parmar C, Grossmann P, Carvalho S, Bussink J,

Monshouwer R, Haibe-Kains B, Rietveld D, Hoebers F, Rietbergen MM, Leemans CR, Dekker A,

Quackenbush J, Gillies RJ, Lambin P. Decoding tumour phenotype by noninvasive imaging using a

quantitative radiomics approach. Nature communications. 2014;5:4006. Epub 2014/06/04. doi:

10.1038/ncomms5006. PubMed PMID: 24892406; PMCID: PMC4059926.

58.   Zhai TT, Langendijk JA, van Dijk LV, Halmos GB, Witjes MJH, Oosting SF, Noordzij W, Sijtsema

NM, Steenbakkers R. The prognostic value of CT-based image-biomarkers for head and neck cancer

patients treated with definitive (chemo-)radiation. Oral Oncol. 2019;95:178-86. Epub 2019/07/28. doi:

10.1016/j.oraloncology.2019.06.020. PubMed PMID: 31345388.

59.   Zhu Y, Li H, Guo W, Drukker K, Lan L, Giger ML, Ji Y. Deciphering genomic underpinnings of

quantitative MRI-based radiomic phenotypes of invasive breast carcinoma. Sci Rep. 2015;5:Article

Number: 17787.

60.   Guo W, Li H, Zhu Y, Lan L, Yang S, Drukker K, Giger ML, Ji Y. Prediction of clinical phenotypes in

invasive breast carcinomas from the integration of radiomics and genomics data. J Med Imaging.

2015;2(4):041007. doi: 10.1117/1.JMI.2.4.041007.

61.   Li H, Zhu Y, Burnside E, Huang E, Drukker K, Hoadley K, Fan C, Conzen S, Zuley M, Net J, Sutton

E, Whitman G, Morris E, Perou C, Ji Y, Giger M. Quantitative MRI radiomics in the prediction of

molecular classifications of breast cancer subtypes in the TCGA/TCIA dataset. NPJ Breast Cancer.

2016;2:Article number: 16012.

62.   Li H, Zhu Y, Burnside ES, Drukker K, Hoadley KA, Fan C, Conzen SD, Lan L, Zuley M, Whitman G,

Sutton EJ, Net JM, Ganott M, Brandt KR, Bonaccio E, Rao A, Jaffe C, Huang E, Freymann JB, Kirby J,

Morris E, Perou CM, Ji Y, Giger ML. MRI radiomics signatures for predicting the risk of breast cancer

recurrence as given by research versions of gene assays of MammaPrint, Oncotype DX, and PAM50.

Radiology. 2016:152110.

63.   Burnside ES, Drukker K, Li H, Bonaccio E, Zuley M, Ganott M, Net JM, Sutton EJ, Brandt KR,

Whitman G, Le-Petross CH, Conzen SD, Lan L, Ji Y, Zhu Y, Jaffe C, Huang E, Kirby J, Freymann JB, Morris

E, Giger ML. Using computer-extracted image phenotypes from tumors on breast magnetic resonance

imaging to predict breast cancer pathologic stage. Cancer. 2015;122(5):748-57. doi:

10.1002/cncr.29791.

64.   Gevaert O, Xu J, Hoang CD, Leung AN, Xu Y, Quon A, Rubin DL, Napel S, Plevritis SK. Non-small

cell lung cancer: identifying prognostic imaging biomarkers by leveraging public gene expression

microarray data--methods and preliminary results. Radiology. 2012;264(2):387-296. doi: 10.1148/radiol.12111607.

65.   Aerts HJWL, E.R.Velazquez, Leijenaar RTH, Parmar C, Grossmann P, Carvalho S, Bussink J, Monshouwer R, B.Haibe-Kains, Rietveld D, Hoebers F, Rietbergen MM, Leemans CR, Dekker A, Quackenbush J, Gillies RJ, Lambin P. Decoding tumour phenotype by noninvasive imaging using a quantitative radiomics approach. Nat Commun. 2014;5(4006). doi: 10.1038/ncomms5006.

66.   Iyer PC, Dadu R, Ferrarotto R, Busaidy NL, Habra MA, Zafereo M, Gross N, Hess KR, Gule-Monroe M, Williams MD, Cabanillas ME. Real-World Experience with Targeted Therapy for the Treatment of Anaplastic Thyroid Carcinoma. Thyroid. 2018;28(1):79-87. Epub 2017/11/23. doi: 10.1089/thy.2017.0285. PubMed PMID: 29161986; PMCID: PMC6425981.

67.   Subbiah V, Kreitman RJ, Wainberg ZA, Cho JY, Schellens JHM, Soria JC, Wen PY, Zielinski C, Cabanillas ME, Urbanowitz G, Mookerjee B, Wang D, Rangwala F, Keam B. Dabrafenib and Trametinib Treatment in Patients With Locally Advanced or Metastatic BRAF V600-Mutant Anaplastic Thyroid Cancer. J Clin Oncol. 2018;36(1):7-13. Epub 2017/10/27. doi: 10.1200/jco.2017.73.6785. PubMed PMID: 29072975; PMCID: PMC5791845.

68.   Schweppe RE. Thyroid Cancer Cell Lines: Critical Models to Study Thyroid Cancer Biology and New Therapeutic Targets. Frontiers in endocrinology. 2012;3. doi: 10.3389/fendo.2012.00081.

69.   Phatak SS, Stephan CC, Cavasotto CN. High-throughput and in silico screenings in drug discovery. Expert Opin Drug Discov. 2009;4(9):947-59. Epub 2009/09/01. doi: 10.1517/17460440903190961. PubMed PMID: 23480542.

70.   Henderson YC, Ahn S-H, Ryu J, Chen Y, Williams MD, El-Naggar AK, Gagea M, Schweppe RE, Haugen BR, Lai SY, Clayman GL. Development and Characterization of Six New Human Papillary Thyroid Carcinoma Cell Lines. The Journal of Clinical Endocrinology & Metabolism. 2015;100(2):E243-E52. doi: doi:10.1210/jc.2014-2624. PubMed PMID: 25427145.

71.   Landa I, Pozdeyev N, Korch C, Marlow LA, Smallridge RC, Copland JA, Henderson YC, Lai SY, Clayman GL, Onoda N, Tan AC, Garcia-Rendueles MER, Knauf JA, Haugen BR, Fagin JA, Schweppe RE. Comprehensive Genetic Characterization of Human Thyroid Cancer Cell Lines: A Validated Panel for Preclinical Studies. Clin Cancer Res. 2019. Epub 2019/02/10. doi: 10.1158/1078-0432.Ccr-18-2953. PubMed PMID: 30737244.

72.   Maniakas A.; Henderson YCH, H.; Peng, S.; Chen, Y.; Jiang, Y.; Ji, S.; Cardenas, M.; Chiu, Y.; Bell, D.; Wiliams, M. D.; Hofmann, M-C.; Scherer, S. E.; Wheeler, D. A.; Busaidy N. L.; Dadu, R.; Wang, J. R.; Cabanillas, M. E.; Zafereo, M.; Johnson, F. M.; Lai, S. Y. . Novel anaplastic thyroid cancer PDXs and cell lines: Expanding preclinical models of genetic diversity Submitted. 2021.

73.   Mutic S, Dempsey JF. The ViewRay system: magnetic resonance-guided and controlled radiotherapy. Seminars in radiation oncology. 2014;24(3):196-9. doi: 10.1016/j.semradonc.2014.02.008. PubMed PMID: 24931092.

74.   Raaymakers BW, de Boer JC, Knox C, Crijns SP, Smit K, Stam MK, van den Bosch MR, Kok JG, Lagendijk JJ. Integrated megavoltage portal imaging with a 1.5 T MRI linac. Phys Med Biol. 2011;56(19):N207-14. doi: 10.1088/0031-9155/56/19/N01. PubMed PMID: 21934191.

75.   Fallone BG, Murray B, Rathee S, Stanescu T, Steciw S, Vidakovic S, Blosser E, Tymofichuk D. First

MR images obtained during megavoltage photon irradiation from a prototype integrated linac-MR

system. Med Phys. 2009;36(6):2084-8. doi: 10.1118/1.3125662. PubMed PMID: 19610297.

76.   Matakos A, Balter J, Cao Y. Estimation of geometrically undistorted B(0) inhomogeneity maps.

Phys Med Biol. 2014;59(17):4945-59. doi: 10.1088/0031-9155/59/17/4945. PubMed PMID: 25109506;

PMCID: PMC4159702.

77.   Hong C, Lee DH, Han BS. Characteristics of geometric distortion correction with increasing field-

of-view in open-configuration MRI. Magn Reson Imaging. 2014;32(6):786-90. doi:

10.1016/j.mri.2014.02.007. PubMed PMID: 24698340.

78.   Aubry JF, Cheung J, Morin O, Beaulieu L, Hsu IC, Pouliot J. Investigation of geometric distortions

on magnetic resonance and cone beam computed tomography images used for planning and

verification of high-dose rate brachytherapy cervical cancer treatment. Brachytherapy. 2010;9(3):266-

73. doi: 10.1016/j.brachy.2009.09.004. PubMed PMID: 20149759.

79.   Webster GJ, Kilgallon JE, Ho KF, Rowbottom CG, Slevin NJ, Mackay RI. A novel imaging

technique for fusion of high-quality immobilised MR images of the head and neck with CT scans for

radiotherapy target delineation. Br J Radiol. 2009;82(978):497-503. doi: 10.1259/bjr/50709041.

PubMed PMID: 19221183.

80.   Weygand J, Fuller CD, Ibbott GS, Mohamed ASR, Ding Y, Yang J, Hwang K-P, Wang J. Spatial

Precision in Magnetic Resonance Imaging–Guided Radiation Therapy: The Role of Geometric Distortion.

International Journal of Radiation Oncology*Biology*Physics. 2016;95(4):1304-16. doi:

http://dx.doi.org/10.1016/j.ijrobp.2016.02.059.

81.   Stanescu T, Wachowicz K, Jaffray DA. Characterization of tissue magnetic susceptibility-induced

distortions for MRIgRT. Med Phys. 2012;39(12):7185-93. doi: 10.1118/1.4764481. PubMed PMID:

23231269.

82.   Wang H, Balter J, Cao Y. Patient-induced susceptibility effect on geometric distortion of clinical

brain MRI for radiation treatment planning on a 3T scanner. Phys Med Biol. 2013;58(3):465-77. doi:

10.1088/0031-9155/58/3/465. PubMed PMID: 23302471.

83.   Jager EA, Kasperts N, Caldas-Magalhaes J, Philippens ME, Pameijer FA, Terhaard CH,

Raaijmakers CP. GTV delineation in supraglottic laryngeal carcinoma: interobserver agreement of CT

versus CT-MR delineation. Radiat Oncol. 2015;10:26. doi: 10.1186/s13014-014-0321-4. PubMed PMID:

25612508; PMCID: PMC4327804.

84.   Ding Y, Mohamed ASR, Yang J, Colen RR, Frank SJ, Wang J, Wassal EY, Wang W, Kantor ME,

Balter PA, Rosenthal DI, Lai SY, Hazle JD, Fuller CD. Prospective observer and software-based

assessment of magnetic resonance imaging quality in head and neck cancer: Should standard

positioning and immobilization be required for radiation therapy applications? Practical Radiation

Oncology. 2015;5(4):e299-e308. doi: http://dx.doi.org/10.1016/j.prro.2014.11.003.

85.   Segedin B, Petric P. Uncertainties in target volume delineation in radiotherapy - are they

relevant and what can we do about them? Radiology and oncology. 2016;50(3):254-62. Epub

2016/09/30. doi: 10.1515/raon-2016-0023. PubMed PMID: 27679540; PMCID: Pmc5024655.

306

86.   Rasch CR, Steenbakkers RJ, Fitton I, Duppen JC, Nowak PJ, Pameijer FA, Eisbruch A, Kaanders JH, Paulsen F, van Herk M. Decreased 3D observer variation with matched CT-MRI, for target delineation in Nasopharynx cancer. Radiation oncology. 2010;5:21. Epub 2010/03/17. doi: 10.1186/1748-717x-5-21. PubMed PMID: 20230613; PMCID: Pmc2842278.

87.   Barth BK, Cornelius A, Nanz D, Eberli D, Donati OF. Diffusion-Weighted Imaging of the Prostate: Image Quality and Geometric Distortion of Readout-Segmented Versus Selective-Excitation Accelerated Acquisitions. Investigative radiology. 2015;50(11):785-91. Epub 2015/07/07. doi: 10.1097/rli.0000000000000184. PubMed PMID: 26146870.

88.   Verhappen MH, Pouwels PJ, Ljumanovic R, van der Putten L, Knol DL, De Bree R, Castelijns JA. Diffusion-weighted MR imaging in head and neck cancer: comparison between half-fourier acquired single-shot turbo spin-echo and EPI techniques. AJNR American journal of neuroradiology. 2012;33(7):1239-46. Epub 2012/02/11. doi: 10.3174/ajnr.A2949. PubMed PMID: 22322615.

89.   Wang D, Strugnell W, Cowin G, Doddrell DM, Slaughter R. Geometric distortion in clinical MRI systems Part I: evaluation using a 3D phantom. Magnetic resonance imaging. 2004;22(9):1211-21. Epub 2004/12/21. doi: 10.1016/j.mri.2004.08.012. PubMed PMID: 15607092.

90.   Port JD, Pomper MG. Quantification and minimization of magnetic susceptibility artifacts on GRE images. Journal of computer assisted tomography. 2000;24(6):958-64. Epub 2000/12/06. PubMed PMID: 11105718.

91.   Gillison ML, Chaturvedi AK, Anderson WF, Fakhry C. Epidemiology of Human Papillomavirus-Positive Head and Neck Squamous Cell Carcinoma. Journal of clinical oncology : official journal of the

American Society of Clinical Oncology. 2015;33(29):3235-42. Epub 2015/09/10. doi:

10.1200/jco.2015.61.6995. PubMed PMID: 26351338; PMCID: PMC4979086.

92.   Schwartz DL, Garden AS, Shah SJ, Chronowski G, Sejpal S, Rosenthal DI, Chen Y, Zhang Y, Zhang

L, Wong PF, Garcia JA, Kian Ang K, Dong L. Adaptive radiotherapy for head and neck cancer--dosimetric

results from a prospective clinical trial. Radiotherapy and oncology : journal of the European Society for

Therapeutic Radiology and Oncology. 2013;106(1):80-4. Epub 2013/02/02. doi:

10.1016/j.radonc.2012.10.010. PubMed PMID: 23369744.

93.   Schwartz DL, Garden AS, Thomas J, Chen Y, Zhang Y, Lewin J, Chambers MS, Dong L. Adaptive

radiotherapy for head-and-neck cancer: initial clinical outcomes from a prospective trial. International

journal of radiation oncology, biology, physics. 2012;83(3):986-93. doi: 10.1016/j.ijrobp.2011.08.017.

PubMed PMID: 22138459.

94.   Wippold FJ, 2nd. Head and neck imaging: the role of CT and MRI. Journal of magnetic resonance

imaging : JMRI. 2007;25(3):453-65. Epub 2007/02/07. doi: 10.1002/jmri.20838. PubMed PMID:

17279529.

95.   Cardenas CE, Mohamed ASR, Tao R, Wong AJR, Awan MJ, Kuruvila S, Aristophanous M, Gunn

GB, Phan J, Beadle BM, Frank SJ, Garden AS, Morrison WH, Fuller CD, Rosenthal DI. Prospective

Qualitative and Quantitative Analysis of Real-Time Peer Review Quality Assurance Rounds Incorporating

Direct Physical Examination for Head and Neck Cancer Radiation Therapy. International Journal of

Radiation Oncology*Biology*Physics. 2017;98(3):532-40. doi:

http://dx.doi.org/10.1016/j.ijrobp.2016.11.019.

96.   Wopken K, Bijl HP, van der Schaaf A, van der Laan HP, Chouvalova O, Steenbakkers RJHM, Doornaert P, Slotman BJ, Oosting SF, Christianen MEMC, van der Laan BFAM, Roodenburg JLN, René Leemans C, Verdonck-de Leeuw IM, Langendijk JA. Development of a multivariable normal tissue complication probability (NTCP) model for tube feeding dependence after curative radiotherapy/chemo-radiotherapy in head and neck cancer. Radiotherapy and Oncology. 2014;113(1):95-101. doi: https://doi.org/10.1016/j.radonc.2014.09.013.

97.   Christianen MEMC, Schilstra C, Beetz I, Muijs CT, Chouvalova O, Burlage FR, Doornaert P, Koken PW, Leemans CR, Rinkel RNPM, de Bruijn MJ, de Bock GH, Roodenburg JLN, van der Laan BFAM, Slotman BJ, Verdonck-de Leeuw IM, Bijl HP, Langendijk JA. Predictive modelling for swallowing dysfunction after primary (chemo)radiation: Results of a prospective observational study. Radiotherapy and Oncology. 2012;105(1):107-14. doi: https://doi.org/10.1016/j.radonc.2011.08.009.

98.   Boomsma MJ, Bijl HP, Christianen MEMC, Beetz I, Chouvalova O, Steenbakkers RJHM, van der Laan BFAM, Wolffenbuttel BHR, Oosting SF, Schilstra C, Langendijk JA. A Prospective Cohort Study on Radiation-induced Hypothyroidism: Development of an NTCP Model. International Journal of Radiation Oncology*Biology*Physics. 2012;84(3):e351-e6. doi: https://doi.org/10.1016/j.ijrobp.2012.05.020.

99.   Beetz I, Schilstra C, van der Schaaf A, van den Heuvel ER, Doornaert P, van Luijk P, Vissink A, van der Laan BFAM, Leemans CR, Bijl HP, Christianen MEMC, Steenbakkers RJHM, Langendijk JA. NTCP models for patient-rated xerostomia and sticky saliva after treatment with intensity modulated radiotherapy for head and neck cancer: The role of dosimetric and clinical factors. Radiotherapy and Oncology. 2012;105(1):101-6. doi: https://doi.org/10.1016/j.radonc.2012.03.004.

100.   Blanchard P, Wong AJ, Gunn GB, Garden AS, Mohamed ASR, Rosenthal DI, Crutison J, Wu R, Zhang X, Zhu XR, Mohan R, Amin MV, Fuller CD, Frank SJ. Toward a model-based patient selection strategy for proton therapy: External validation of photon-derived normal tissue complication probability models in a head and neck proton therapy cohort. Radiotherapy and Oncology. 2016;121(3):381-6. doi: https://doi.org/10.1016/j.radonc.2016.08.022.

101.   Ang KK, Sturgis EM. Human papillomavirus as a marker of the natural history and response to therapy of head and neck squamous cell carcinoma. Seminars in radiation oncology. 2012;22(2):128-42. Epub 2012/03/06. doi: 10.1016/j.semradonc.2011.12.004. PubMed PMID: 22385920.

102.   Jung AC, Briolat J, Millon R, de Reynies A, Rickman D, Thomas E, Abecassis J, Clavel C, Wasylyk B. Biological and clinical relevance of transcriptionally active human papillomavirus (HPV) infection in oropharynx squamous cell carcinoma. International journal of cancer. 2010;126(8):1882-94. Epub 2009/10/02. doi: 10.1002/ijc.24911. PubMed PMID: 19795456.

103.   Doescher J, Veit JA, Hoffmann TK. [The 8th edition of the AJCC Cancer Staging Manual : Updates in otorhinolaryngology, head and neck surgery]. Hno. 2017. Epub 2017/07/19. doi: 10.1007/s00106-017-0391-3. PubMed PMID: 28717958.

104.   Langendijk JA, Doornaert P, Verdonck-de Leeuw IM, Leemans CR, Aaronson NK, Slotman BJ. Impact of late treatment-related toxicity on quality of life among patients with head and neck cancer treated with radiotherapy. Journal of clinical oncology : official journal of the American Society of Clinical Oncology. 2008;26(22):3770-6. Epub 2008/08/02. doi: 10.1200/jco.2007.14.6647. PubMed PMID: 18669465.

105.   Kofler B, Laban S, Busch CJ, Lorincz B, Knecht R. New treatment strategies for HPV-positive head and neck cancer. European archives of oto-rhino-laryngology : official journal of the European Federation of Oto-Rhino-Laryngological Societies (EUFOS) : affiliated with the German Society for Oto-Rhino-Laryngology - Head and Neck Surgery. 2014;271(7):1861-7. Epub 2013/08/13. doi: 10.1007/s00405-013-2603-0. PubMed PMID: 23934317.

106.   Masterson L, Moualed D, Liu ZW, Howard JE, Dwivedi RC, Tysome JR, Benson R, Sterling JC, Sudhoff H, Jani P, Goon PK. De-escalation treatment protocols for human papillomavirus-associated oropharyngeal squamous cell carcinoma: a systematic review and meta-analysis of current clinical trials. European journal of cancer (Oxford, England : 1990). 2014;50(15):2636-48. Epub 2014/08/06. doi: 10.1016/j.ejca.2014.07.001. PubMed PMID: 25091798.

107.   Mirghani H, Amen F, Blanchard P, Moreau F, Guigay J, Hartl DM, Lacau St Guily J. Treatment de-escalation in HPV-positive oropharyngeal carcinoma: ongoing trials, critical issues and perspectives. International journal of cancer. 2015;136(7):1494-503. Epub 2014/03/14. doi: 10.1002/ijc.28847. PubMed PMID: 24622970.

108.   Marur S, Li S, Cmelak AJ, Gillison ML, Zhao WJ, Ferris RL, Westra WH, Gilbert J, Bauman JE, Wagner LI, Trevarthen DR, Balkrishna J, Murphy BA, Agrawal N, Colevas AD, Chung CH, Burtness B. E1308: Phase II Trial of Induction Chemotherapy Followed by Reduced-Dose Radiation and Weekly Cetuximab in Patients With HPV-Associated Resectable Squamous Cell Carcinoma of the Oropharynx-ECOG-ACRIN Cancer Research Group. Journal of clinical oncology : official journal of the American

Society of Clinical Oncology. 2017;35(5):490-7. Epub 2016/12/29. doi: 10.1200/jco.2016.68.3300. PubMed PMID: 28029303; PMCID: PMC5455313.

109.   Chen AM, Felix C, Wang PC, Hsu S, Basehart V, Garst J, Beron P, Wong D, Rosove MH, Rao S, Melanson H, Kim E, Palmer D, Qi L, Kelly K, Steinberg ML, Kupelian PA, Daly ME. Reduced-dose radiotherapy for human papillomavirus-associated squamous-cell carcinoma of the oropharynx: a single-arm, phase 2 study. The Lancet Oncology. 2017;18(6):803-11. Epub 2017/04/25. doi: 10.1016/s1470-2045(17)30246-2. PubMed PMID: 28434660.

110.   Rainey HR, E.;, Selkridge, I. Abstract (Standard of care vs reduced-dose chemoradiation after induction chemotherapy in HPV + oropharyngeal carcinoma patients). Journal of clinical oncology : official journal of the American Society of Clinical Oncology. 2017;35((1)): p. 6069.

111.   Chera BS, Amdur RJ, Tepper J, Qaqish B, Green R, Aumer SL, Hayes N, Weiss J, Grilley-Olson J, Zanation A, Hackman T, Funkhouser W, Sheets N, Weissler M, Mendenhall W. Phase 2 Trial of De-intensified Chemoradiation Therapy for Favorable-Risk Human Papillomavirus-Associated Oropharyngeal Squamous Cell Carcinoma. International journal of radiation oncology, biology, physics. 2015;93(5):976-85. Epub 2015/11/20. doi: 10.1016/j.ijrobp.2015.08.033. PubMed PMID: 26581135.

112.   Lee N, Schoder H, Beattie B, Lanning R, Riaz N, McBride S, Katabi N, Li D, Yarusi B, Chan S, Mitrani L, Zhang Z, Pfister DG, Sherman E, Baxi S, Boyle J, Morris LG, Ganly I, Wong R, Humm J. Strategy of Using Intratreatment Hypoxia Imaging to Selectively and Safely Guide Radiation Dose De-escalation Concurrent With Chemotherapy for Locoregionally Advanced Human Papillomavirus-Related Oropharyngeal Carcinoma. International journal of radiation oncology, biology, physics. 2016;96(1):9-

17. Epub 2016/08/12. doi: 10.1016/j.ijrobp.2016.04.027. PubMed PMID: 27511842; PMCID: PMC5035649.

113.   Blanchard P, Wong AJ, Gunn GB, Garden AS, Mohamed ASR, Rosenthal DI, Crutison J, Wu R, Zhang X, Zhu XR, Mohan R, Amin MV, Fuller CD, Frank SJ. Toward a model-based patient selection strategy for proton therapy: External validation of photon-derived normal tissue complication probability models in a head and neck proton therapy cohort. Radiother Oncol. 2016;121(3):381-6. Epub 2016/09/20. doi: 10.1016/j.radonc.2016.08.022. PubMed PMID: 27641784; PMCID: PMC5474306.

114.   Dowthwaite SA, Franklin JH, Palma DA, Fung K, Yoo J, Nichols AC. The role of transoral robotic surgery in the management of oropharyngeal cancer: a review of the literature. ISRN oncology. 2012;2012:945162. Epub 2012/05/19. doi: 10.5402/2012/945162. PubMed PMID: 22606380; PMCID: PMC3347745.

115.   Cartmill B, Cornwell P, Ward E, Davidson W, Nund R, Bettington C, Rahbari RM, Poulsen M, Porceddu S. Emerging understanding of dosimetric factors impacting on dysphagia and nutrition following radiotherapy for oropharyngeal cancer. Head & neck. 2013;35(8):1211-9. Epub 2012/06/26. doi: 10.1002/hed.23040. PubMed PMID: 22730150.

116.   Feng FY, Kim HM, Lyden TH, Haxer MJ, Feng M, Worden FP, Chepeha DB, Eisbruch A. Intensity-modulated radiotherapy of head and neck cancer aiming to reduce dysphagia: early dose-effect relationships for the swallowing structures. International journal of radiation oncology, biology, physics. 2007;68(5):1289-98. Epub 2007/06/15. doi: 10.1016/j.ijrobp.2007.02.049. PubMed PMID: 17560051.

117.	Caudell JJ, Schaner PE, Desmond RA, Meredith RF, Spencer SA, Bonner JA. Dosimetric factors associated with long-term dysphagia after definitive radiotherapy for squamous cell carcinoma of the head and neck. International journal of radiation oncology, biology, physics. 2010;76(2):403-9. Epub 2009/05/27. doi: 10.1016/j.ijrobp.2009.02.017. PubMed PMID: 19467801.

118.	Duprez F, Madani I, De Potter B, Boterberg T, De Neve W. Systematic review of dose--volume correlates for structures related to late swallowing disturbances after radiotherapy for head and neck cancer. Dysphagia. 2013;28(3):337-49. Epub 2013/02/23. doi: 10.1007/s00455-013-9452-2. PubMed PMID: 23429941.

119.	Barker JL, Jr., Garden AS, Ang KK, O'Daniel JC, Wang H, Court LE, Morrison WH, Rosenthal DI, Chao KS, Tucker SL, Mohan R, Dong L. Quantification of volumetric and geometric changes occurring during fractionated radiotherapy for head-and-neck cancer using an integrated CT/linear accelerator system. International journal of radiation oncology, biology, physics. 2004;59(4):960-70. Epub 2004/07/06. doi: 10.1016/j.ijrobp.2003.12.024. PubMed PMID: 15234029.

120.	Hansen EK, Bucci MK, Quivey JM, Weinberg V, Xia P. Repeat CT imaging and replanning during the course of IMRT for head-and-neck cancer. International journal of radiation oncology, biology, physics. 2006;64(2):355-62. Epub 2005/11/01. doi: 10.1016/j.ijrobp.2005.07.957. PubMed PMID: 16256277.

121.	Geets X, Tomsej M, Lee JA, Duprez T, Coche E, Cosnard G, Lonneux M, Gregoire V. Adaptive biological image-guided IMRT with anatomic and functional imaging in pharyngo-laryngeal tumors: impact on target volume delineation and dose distribution using helical tomotherapy. Radiotherapy and

314

oncology : journal of the European Society for Therapeutic Radiology and Oncology. 2007;85(1):105-15. Epub 2007/06/15. doi: 10.1016/j.radonc.2007.05.010. PubMed PMID: 17562346.

122.   Veiga C, McClelland J, Moinuddin S, Lourenco A, Ricketts K, Annkah J, Modat M, Ourselin S, D'Souza D, Royle G. Toward adaptive radiotherapy for head and neck patients: Feasibility study on using CT-to-CBCT deformable registration for "dose of the day" calculations. Med Phys. 2014;41(3):031703. Epub 2014/03/07. doi: 10.1118/1.4864240. PubMed PMID: 24593707.

123.   Bussink J, van Herpen CM, Kaanders JH, Oyen WJ. PET-CT for response assessment and treatment adaptation in head and neck cancer. The Lancet Oncology. 2010;11(7):661-9. Epub 2010/03/17. doi: 10.1016/s1470-2045(09)70353-5. PubMed PMID: 20226735.

124.   Dirix P, Vandecaveye V, De Keyzer F, Stroobants S, Hermans R, Nuyts S. Dose painting in radiotherapy for head and neck squamous cell carcinoma: value of repeated functional imaging with (18)F-FDG PET, (18)F-fluoromisonidazole PET, diffusion-weighted MRI, and dynamic contrast-enhanced MRI. Journal of nuclear medicine : official publication, Society of Nuclear Medicine. 2009;50(7):1020-7. Epub 2009/06/16. doi: 10.2967/jnumed.109.062638. PubMed PMID: 19525447.

125.   Subesinghe M, Scarsbrook AF, Sourbron S, Wilson DJ, McDermott G, Speight R, Roberts N, Carey B, Forrester R, Gopal SV, Sykes JR, Prestwich RJ. Alterations in anatomic and functional imaging parameters with repeated FDG PET-CT and MRI during radiotherapy for head and neck cancer: a pilot study. BMC cancer. 2015;15:137. Epub 2015/04/18. doi: 10.1186/s12885-015-1154-8. PubMed PMID: 25885109; PMCID: PMC4374581.

126.   Ang KK, Harris J, Wheeler R, Weber R, Rosenthal DI, Nguyen-Tan PF, Westra WH, Chung CH, Jordan RC, Lu C, Kim H, Axelrod R, Silverman CC, Redmond KP, Gillison ML. Human papillomavirus and survival of patients with oropharyngeal cancer. The New England journal of medicine. 2010;363(1):24-35. Epub 2010/06/10. doi: 10.1056/NEJMoa0912217. PubMed PMID: 20530316; PMCID: PMC2943767.

127.   Vandecaveye V, De Keyzer F, Nuyts S, Deraedt K, Dirix P, Hamaekers P, Vander Poorten V, Delaere P, Hermans R. Detection of head and neck squamous cell carcinoma with diffusion weighted MRI after (chemo)radiotherapy: correlation between radiologic and histopathologic findings. Int J Radiat Oncol Biol Phys. 2007;67(4):960-71. doi: 10.1016/j.ijrobp.2006.09.020. PubMed PMID: 17141979.

128.   Kim S, Loevner L, Quon H, Sherman E, Weinstein G, Kilger A, Poptani H. Diffusion-weighted magnetic resonance imaging for predicting and detecting early response to chemoradiation therapy of squamous cell carcinomas of the head and neck. Clin Cancer Res. 2009;15(3):986-94. doi: 10.1158/1078-0432.CCR-08-1287. PubMed PMID: 19188170; PMCID: PMC2673914.

129.   Volinsky CT, Raftery AE. Bayesian information criterion for censored survival models. Biometrics. 2000;56(1):256-62. Epub 2000/04/28. doi: 10.1111/j.0006-341x.2000.00256.x. PubMed PMID: 10783804.

130.   Raftery AE. Bayesian model selection in social research. Sociological methodology. 1995:111-63.

131.   Baliyan V, Das CJ, Sharma R, Gupta AK. Diffusion weighted imaging: Technique and applications. World J Radiol. 2016;8(9):785-98. doi: 10.4329/wjr.v8.i9.785. PubMed PMID: 27721941.

132.   Chung SR, Choi YJ, Suh CH, Lee JH, Baek JH. Diffusion-weighted Magnetic Resonance Imaging for Predicting Response to Chemoradiation Therapy for Head and Neck Squamous Cell Carcinoma: A Systematic Review. Korean journal of radiology. 2019;20(4):649-61. Epub 2019/03/20. doi: 10.3348/kjr.2018.0446. PubMed PMID: 30887747; PMCID: PMC6424826.

133.   King AD, Thoeny HC. Functional MRI for the prediction of treatment response in head and neck squamous cell carcinoma: potential and limitations. Cancer Imaging. 2016;16(1):23-. doi: 10.1186/s40644-016-0080-6. PubMed PMID: 27542718.

134.   King AD, Mo FK, Yu KH, Yeung DK, Zhou H, Bhatia KS, Tse GM, Vlantis AC, Wong JK, Ahuja AT. Squamous cell carcinoma of the head and neck: diffusion-weighted MR imaging for prediction and monitoring of treatment response. Eur Radiol. 2010;20(9):2213-20. Epub 2010/03/24. doi: 10.1007/s00330-010-1769-8. PubMed PMID: 20309553.

135.   Ng SH, Lin CY, Chan SC, Yen TC, Liao CT, Chang JT, Ko SF, Wang HM, Huang SF, Lin YC, Wang JJ. Dynamic contrast-enhanced MR imaging predicts local control in oropharyngeal or hypopharyngeal squamous cell carcinoma treated with chemoradiotherapy. PloS one. 2013;8(8):e72230. Epub 2013/08/21. doi: 10.1371/journal.pone.0072230. PubMed PMID: 23951300; PMCID: PMC3737151.

136.   Ohnishi K, Shioyama Y, Hatakenaka M, Nakamura K, Abe K, Yoshiura T, Ohga S, Nonoshita T, Yoshitake T, Nakashima T, Honda H. Prediction of local failures with a combination of pretreatment tumor volume and apparent diffusion coefficient in patients treated with definitive radiotherapy for hypopharyngeal or oropharyngeal squamous cell carcinoma. Journal of radiation research. 2011;52(4):522-30. Epub 2011/09/10. doi: 10.1269/jrr.10178. PubMed PMID: 21905311.

317

137.   Hatakenaka M, Nakamura K, Yabuuchi H, Shioyama Y, Matsuo Y, Ohnishi K, Sunami S, Kamitani

T, Setoguchi T, Yoshiura T, Nakashima T, Nishikawa K, Honda H. Pretreatment apparent diffusion

coefficient of the primary lesion correlates with local failure in head-and-neck cancer treated with

chemoradiotherapy or radiotherapy. Int J Radiat Oncol Biol Phys. 2011;81(2):339-45. Epub 2010/09/14.

doi: 10.1016/j.ijrobp.2010.05.051. PubMed PMID: 20832179.

138.   Ding Y, Fuller C, Mohamed A, Frank S, Rosenthal D, Colen R, Hazle J. Intravoxel Incoherent

Motion Magnetic Resonance Imaging of Oropharyngeal Cancer in Response to Chemoradiation

Therapy. International Journal of Radiation Oncology, Biology, Physics. 2014;90(1):S75.

139.   Teng MS, Futran ND. Osteoradionecrosis of the mandible. Current Opinion in Otolaryngology &

Head and Neck Surgery. 2005;13(4):217-21. doi: 10.1097/01.moo.0000170527.59017.ff. PubMed PMID:

00020840-200508000-00004.

140.   Jereczek-Fossa BA, Orecchia R. Radiotherapy-Induced Mandibular Bone Complications. Cancer

Treatment Reviews. 2002;28(1):65-74. doi: https://doi.org/10.1053/ctrv.2002.0254.

141.   Sciubba JJ, Goldenberg D. Oral complications of radiotherapy. The Lancet Oncology.

2006;7(2):175-83. doi: https://doi.org/10.1016/S1470-2045(06)70580-0.

142.   Siegel RL, Miller KD, Jemal A. Cancer statistics, 2019. CA: A Cancer Journal for Clinicians.

2019;69(1):7-34. doi: 10.3322/caac.21551.

143.   O'Sullivan B, Huang SH, Su J, Garden AS, Sturgis EM, Dahlstrom K, Lee N, Riaz N, Pei X, Koyfman

SA, Adelstein D, Burkey BB, Friborg J, Kristensen CA, Gothelf AB, Hoebers F, Kremer B, Speel E-J, Bowles

DW, Raben D, Karam SD, Yu E, Xu W. Development and validation of a staging system for HPV-related

oropharyngeal cancer by the International Collaboration on Oropharyngeal cancer Network for Staging

(ICON-S): a multicentre cohort study. Lancet Oncol. 2016;17(4):440-51. Epub 2016/02/27. doi:

10.1016/S1470-2045(15)00560-4. PubMed PMID: 26936027.

144.   Chaturvedi AK, Anderson WF, Lortet-Tieulent J, Curado MP, Ferlay J, Franceschi S, Rosenberg

PS, Bray F, Gillison ML. Worldwide trends in incidence rates for oral cavity and oropharyngeal cancers. J

Clin Oncol. 2013;31(36):4550-9. Epub 2013/11/18. doi: 10.1200/JCO.2013.50.3870. PubMed PMID:

24248688.

145.   Mohamed ASR, Hobbs BP, Hutcheson KA, Murri MS, Garg N, Song J, Brandon Gunn G,

Sandulache V, Beadle BM, Phan J, Morrison WH, Frank SJ, Blanchard P, Garden AS, El-Halawani H,

Kamal M, Chambers MS, Lewin JS, Ferrarotto R, Ronald Zhu X, Zhang X, Hofstede TM, Cardoso RC,

Gillenwater AM, Sturgis EM, Weber RS, Rosenthal DI, Fuller CD, Lai SY. Dose-volume correlates of

mandibular osteoradionecrosis in Oropharynx cancer patients receiving intensity-modulated

radiotherapy: Results from a case-matched comparison. Radiotherapy and Oncology. 2017;124(2):232-

9. doi: https://doi.org/10.1016/j.radonc.2017.06.026.

146.   Beadle BM, Liao KP, Chambers MS, Elting LS, Buchholz TA, Kian Ang K, Garden AS, Guadagnolo

BA. Evaluating the impact of patient, tumor, and treatment characteristics on the development of jaw

complications in patients treated for oral cancers: a SEER-Medicare analysis. Head & neck.

2013;35(11):1599-605. doi: 10.1002/hed.23205. PubMed PMID: 23150453.

147.   Costa DA, Costa TP, Netto EC, Joaquim N, Ventura I, Pratas AC, Winckler P, Silva IP, Pinho AC,

Sargento IG, Guerreiro FG, Moreira AR. New perspectives on the conservative management of

319

osteoradionecrosis of the mandible: A literature review. Head Neck. 2016;38(11):1708-16. Epub

2016/10/19. doi: 10.1002/hed.24495. PubMed PMID: 27240248.

148.   Lambade PN, Lambade D, Goel M. Osteoradionecrosis of the mandible: a review. Oral

Maxillofac Surg. 2013;17(4):243-9. Epub 2012/10/12. doi: 10.1007/s10006-012-0363-4. PubMed PMID:

23053252.

149.   Zaghi S, Miller M, Blackwell K, Palla B, Lai C, Nabili V. Analysis of surgical margins in cases of

mandibular osteoradionecrosis that progress despite extensive mandible resection and free tissue

transfer. Am J Otolaryngol. 2012;33(5):576-80. Epub 2012/04/24. doi: 10.1016/j.amjoto.2012.03.001.

PubMed PMID: 22521236.

150.   Wang CC, Cheng MH, Hao SP, Wu CC, Huang SS. Osteoradionecrosis with combined

mandibulotomy and marginal mandibulectomy. Laryngoscope. 2005;115(11):1963-7. Epub 2005/12/02.

doi: 10.1097/01.mlg.0000178374.29219.5e. PubMed PMID: 16319606.

151.   Hamilton JD, Lai SY, Ginsberg LE. Superimposed infection in mandibular osteoradionecrosis:

diagnosis and outcomes. J Comput Assist Tomogr. 2012;36(6):725-31. Epub 2012/11/30. doi:

10.1097/RCT.0b013e3182702f09. PubMed PMID: 23192211; PMCID: PMC3917313.

152.   Khojastepour L, Bronoosh P, Zeinalzade M. Mandibular bone changes induced by head and

neck radiotherapy. Indian J Dent Res. 2012;23(6):774-7. Epub 2013/05/08. doi: 10.4103/0970-

9290.111258. PubMed PMID: 23649062.

153.   Chan WP, Liu YJ, Huang GS, Lin MF, Huang S, Chang YC, Jiang CC. Relationship of idiopathic

osteonecrosis of the femoral head to perfusion changes in the proximal femur by dynamic contrast-

enhanced MRI. AJR Am J Roentgenol. 2011;196(3):637-43. Epub 2011/02/24. doi: 10.2214/AJR.10.4322.

PubMed PMID: 21343508.

154.   Dyke JP, Lazaro LE, Hettrich CM, Hentel KD, Helfet DL, Lorich DG. Regional analysis of femoral

head perfusion following displaced fractures of the femoral neck. J Magn Reson Imaging.

2015;41(2):550-4. Epub 2013/12/18. doi: 10.1002/jmri.24524. PubMed PMID: 24338938.

155.   Ma HT, Griffith JF, Zhao X, Lv H, Yeung DK, Leung PC. Relationship between marrow perfusion

and bone mineral density: a pharmacokinetic study of DCE-MRI. Conference proceedings : Annual

International Conference of the IEEE Engineering in Medicine and Biology Society IEEE Engineering in

Medicine and Biology Society Annual Conference. 2012;2012:377-9. Epub 2013/02/01. doi:

10.1109/embc.2012.6345947. PubMed PMID: 23365908.

156.   Ma HT, Lv H, Griffith JF, Yuan J, Leung PC. Bone marrow perfusion of proximal femur varied

with BMD--a longitudinal study by DCE-MRI. Conference proceedings : Annual International

Conference of the IEEE Engineering in Medicine and Biology Society IEEE Engineering in Medicine and

Biology Society Annual Conference. 2013;2013:2607-10. Epub 2013/10/11. doi:

10.1109/embc.2013.6610074. PubMed PMID: 24110261.

157.   Marx RE. Osteoradionecrosis: a new concept of its pathophysiology. J Oral Maxillofac Surg.

1983;41(5):283-8. doi: 10.1016/0278-2391(83)90294-x. PubMed PMID: 6572704.

158.   Joint H, Neck Radiotherapy MRIDC, Sandulache VC, Hobbs BP, Mohamed ASR, Frank SJ, Song J,

Ding Y, Ger R, Court LE, Kalpathy-Cramer J, Hazle JD, Wang J, Awan MJ, Rosenthal DI, Garden AS, Gunn

GB, Colen RR, Elshafeey N, Elbanan M, Hutcheson KA, Lewin JS, Chambers MS, Hofstede TM, Weber RS,

321

Lai SY, Fuller CD. Dynamic contrast-enhanced MRI detects acute radiotherapy-induced alterations in mandibular microvasculature: prospective assessment of imaging biomarkers of normal tissue injury. Scientific Reports. 2016;6:29864. doi: 10.1038/srep29864

https://www.nature.com/articles/srep29864#supplementary-information.

159.	Chan T, Marquina A, Mulet P. High-order total variation-based image restoration. Siam J Sci Comput. 2000;22(2):503-16. doi: Doi 10.1137/S1064827598344169. PubMed PMID: WOS:000089065200006.

160.	He R, Ding Y, Mohamed AS, Ng SP, Ger R, Elhalawani H, Elgohari B, Young K, Hutcheson K, Fuller C, Lai S. Simultaneously spatial and temporal higher-order total variations for noise suppression and motion reduction in DCE and IVIM: SPIE; 2020.

161.	Balvay D, Ponvianne Y, Claudon M, Cuenod CA, editors. Arterial input function: Relevance of eleven analytical models in DCE-MRI studies. 2008 5th IEEE International Symposium on Biomedical Imaging: From Nano to Macro; 2008 14-17 May 2008.

162.	Le Saux O, Italiano A, Spaeth D, Heudel P, Filleron T, Albiges L, Bachelot T, Goncalves A, Pierga JY, Barlesi F, Boige V, Lebbe C, Mortier L, Frenel JS, Tredan O, Jimenez M, Legrand F, Ferte C. A multicenter, prospective trial in progress exploring the association between low level of genomic alteration and exceptional and unexpected response to targeted therapies in patients with solid tumors. Cancer Research. 2018;78(13). doi: 10.1158/1538-7445.Am2018-Ct153. PubMed PMID: WOS:000468818900140.

163.   Murase K. Efficient method for calculating kinetic parameters using T1-weighted dynamic contrast-enhanced magnetic resonance imaging. Magnetic resonance in medicine. 2004;51(4):858-62. Epub 2004/04/06. doi: 10.1002/mrm.20022. PubMed PMID: 15065262.

164.   Jones KM, Pagel MD, Cardenas-Rodriguez J. Linearization improves the repeatability of quantitative dynamic contrast-enhanced MRI. Magnetic resonance imaging. 2018;47:16-24. Epub 2017/11/21. doi: 10.1016/j.mri.2017.11.002. PubMed PMID: 29155024; PMCID: PMC5828901.

165.   Sourbron SP, Buckley DL. Classic models for dynamic contrast-enhanced MRI. NMR in Biomedicine. 2013;26(8):1004-27. doi: 10.1002/nbm.2940.

166.   Store G, Smith HJ, Larheim TA. Dynamic MR imaging of mandibular osteoradionecrosis. Acta Radiol. 2000;41(1):31-7. Epub 2000/02/09. PubMed PMID: 10665867.

167.   García-Ferrer L, Bagán JV, Martínez-Sanjuan V, Hernandez-Bazan S, García R, Jiménez-Soriano Y, Hervas V. MRI of mandibular osteonecrosis secondary to bisphosphonates. AJR American journal of roentgenology. 2008;190(4):949-55. doi: 10.2214/AJR.07.3045. PubMed PMID: 18356441.

168.   Hermans R, Fossion E, Ioannides C, Van den Bogaert W, Ghekiere J, Baert AL. CT findings in osteoradionecrosis of the mandible. Skeletal Radiol. 1996;25(1):31-6. doi: 10.1007/s002560050028. PubMed PMID: 8717116.

169.   Cohen J. Statistical power analysis for the behavioral sciences. 2nd ed. Hillsdale, N.J.: L. Erlbaum Associates; 1988. xxi, 567 p. p.

170.   Bauerle T, Bartling S, Berger M, Schmitt-Graff A, Hilbig H, Kauczor HU, Delorme S, Kiessling F. Imaging anti-angiogenic treatment response with DCE-VCT, DCE-MRI and DWI in an animal model of

breast cancer bone metastasis. Eur J Radiol. 2010;73(2):280-7. Epub 2008/12/17. doi: 10.1016/j.ejrad.2008.10.020. PubMed PMID: 19070445.

171.   Dafni H, Kim SJ, Bankson JA, Sankaranarayanapillai M, Ronen SM. Macromolecular dynamic contrast-enhanced (DCE)-MRI detects reduced vascular permeability in a prostate cancer bone metastasis model following anti-platelet-derived growth factor receptor (PDGFR) therapy, indicating a drop in vascular endothelial growth factor receptor (VEGFR) activation. Magnetic resonance in medicine. 2008;60(4):822-33. Epub 2008/09/26. doi: 10.1002/mrm.21727. PubMed PMID: 18816866; PMCID: PMC4059608.

172.   Joint H, Neck Radiotherapy MRIDC. A Multi-Institutional Comparison of Dynamic Contrast-Enhanced Magnetic Resonance Imaging Parameter Calculations. Sci Rep. 2017;7(1):11185. Epub 2017/09/13. doi: 10.1038/s41598-017-11554-w. PubMed PMID: 28894197; PMCID: PMC5593829.

173.   Galbraith SM, Lodge MA, Taylor NJ, Rustin GJ, Bentzen S, Stirling JJ, Padhani AR. Reproducibility of dynamic contrast-enhanced MRI in human muscle and tumours: comparison of quantitative and semi-quantitative analysis. NMR Biomed. 2002;15(2):132-42. Epub 2002/03/01. doi: 10.1002/nbm.731. PubMed PMID: 11870909.

174.   Dawson LA, Anzai Y, Marsh L, Martel MK, Paulino A, Ship JA, Eisbruch A. Patterns of local-regional recurrence following parotid-sparing conformal and segmental intensity-modulated radiotherapy for head and neck cancer. Int J Radiat Oncol. 2000;46(5):1117-26. doi: Doi 10.1016/S0360-3016(99)00550-7. PubMed PMID: WOS:000085978700005.

175.   Chao KSC, Ozyigit G, Tran BN, Cengiz M, Dempsey JF, Low DA. Patterns of failure in patients receiving definitive and postoperative IMRT for head-and-neck cancer. Int J Radiat Oncol. 2003;55(2):312-21. doi: Pii S0360-3016(02)03940-8

Doi 10.1016/S0360-3016(02)03940-8. PubMed PMID: WOS:000181323400004.

176.   Yao M, Dornfeld KJ, Buatti JM, Skwarchuk M, Tan H, Nguyen T, Wacha J, Bayouth JE, Funk GF, Smith RB, Graham SM, Chang K, Hoffman HT. Intensity-modulated radiation treatment for head-and-neck squamous cell carcinoma--the University of Iowa experience. International journal of radiation oncology, biology, physics. 2005;63(2):410-21. doi: 10.1016/j.ijrobp.2005.02.025. PubMed PMID: 16168834.

177.   Daly ME, Lieskovsky Y, Pawlicki T, Yau J, Pinto H, Kaplan M, Fee WE, Koong A, Goffinet DR, Xing L, Le QT. Evaluation of patterns of failure and subjective salivary function in patients treated with intensity modulated radiotherapy for head and neck squamous cell carcinoma. Head Neck-J Sci Spec. 2007;29(3):211-20. doi: Doi 10.1002/Hed.20505. PubMed PMID: WOS:000244459100002.

178.   Sanguineti G, Gunn GB, Endres EJ, Chaljub G, Cheruvu P, Parker B. Patterns of locoregional failure after exclusive IMRT for oropharyngeal carcinoma. International journal of radiation oncology, biology, physics. 2008;72(3):737-46. doi: 10.1016/j.ijrobp.2008.01.027. PubMed PMID: 18486356.

179.   Crum WR, Hartkens T, Hill DL. Non-rigid image registration: theory and practice. The British journal of radiology. 2004;77 Spec No 2:S140-53. PubMed PMID: 15677356.

180.   Castadot P, Lee JA, Parraga A, Geets X, Macq B, Gregoire V. Comparison of 12 deformable registration strategies in adaptive radiation therapy for the treatment of head and neck tumors.

325

Radiotherapy and oncology : journal of the European Society for Therapeutic Radiology and Oncology. 2008;89(1):1-12. doi: 10.1016/j.radonc.2008.04.010. PubMed PMID: 18501456.

181.   Lee C, Langen KM, Lu W, Haimerl J, Schnarr E, Ruchala KJ, Olivera GH, Meeks SL, Kupelian PA, Shellenberger TD, Manon RR. Evaluation of geometric changes of parotid glands during head and neck cancer radiotherapy using daily MVCT and automatic deformable registration. Radiotherapy and oncology : journal of the European Society for Therapeutic Radiology and Oncology. 2008;89(1):81-8. doi: 10.1016/j.radonc.2008.07.006. PubMed PMID: 18707786.

182.   Huger S, Graff P, Harter V, Marchesi V, Royer P, Diaz JC, Aouadi S, Wolf D, Peiffert D, Noel A. Evaluation of the Block Matching deformable registration algorithm in the field of head-and-neck adaptive radiotherapy. Physica medica : PM : an international journal devoted to the applications of physics to medicine and biology : official journal of the Italian Association of Biomedical Physics. 2013. doi: 10.1016/j.ejmp.2013.09.001. PubMed PMID: 24090743.

183.   Mohamed AS, Ruangskul MN, Awan MJ, Baron CA, Kalpathy-Cramer J, Castillo R, Castillo E, Guerrero TM, Kocak-Uzel E, Yang J, Court LE, Kantor ME, Gunn GB, Colen RR, Frank SJ, Garden AS, Rosenthal DI, Fuller CD. Quality Assurance Assessment of Diagnostic and Radiation Therapy-Simulation CT Image Registration for Head and Neck Radiation Therapy: Anatomic Region of Interest-based Comparison of Rigid and Deformable Algorithms. Radiology. 2014:132871. doi: 10.1148/radiol.14132871. PubMed PMID: 25380454.

184.   Johnson B, Sales L, Winston A, Liao J, Laramore G, Parvathaneni U. Fabrication of customized tongue-displacing stents: considerations for use in patients receiving head and neck radiotherapy. J Am Dent Assoc. 2013;144(6):594-600. PubMed PMID: 23729456.

185.   Goel A, Tripathi A, Chand P, Singh SV, Pant MC, Nagar A. Use of Positioning Stents in Lingual Carcinoma Patients Subjected to Radiotherapy. Int J Prosthodont. 2010;23(5):450-2. PubMed PMID: WOS:000282057300013.

186.   Tao R, Fuller CD, Gunn GB, Beadle BM, Phan J, Frank SJ, Garden AS, Morrison WH, Ang KK, Rosenthal DI. Real-time Peer Review Quality Assurance Conferences Incorporating Physical Examination for Head-and-Neck Cancer Radiation Therapy Result in Clinically Meaningful Target Volume Alteration: Results of a Prospective Volumetric Analysis. International journal of radiation oncology, biology, physics. 2012;84(3):S151.

187.   Rosenthal DI, Asper JA, Barker JL, Garden AS, Chao KSC, Morrison WH, Weber RS, Ang KK. Importance of patient examination to clinical quality assurance in head and neck radiation oncology. Head Neck-J Sci Spec. 2006;28(11):967-73. doi: Doi 10.1002/Hed.20446. PubMed PMID: WOS:000241460300001.

188.   International Commission on Radiation Units and Measurements. ICRU Report 62. Prescribing, recording, and reporting photon beam therapy (Supplement to ICRU Report 50)ICRU, Bethesda, MD. Oxford University Press, Oxford, United Kingdom. 1999.

189.   International Commission on Radiation Units and Measurements. ICRU Report 50. Prescribing,

recording, and reporting photon beam therapy ICRU, Bethesda, MD. Oxford University Press, Oxford,

United Kingdom. 1993.

190.   International Commission on Radiation Units and Measurements. ICRU Report 83: prescribing,

recording and reporting photon-beam intensity-modulated radiation therapy (IMRT). Journal of the

ICRU. 2010;10:1-106.

191.   Wilke CT, Zaid M, Chung C, Fuller CD, Mohamed AS, Skinner H, Phan J, Gunn GB, Morrison WH,

Garden AS. Design and fabrication of a 3D–printed oral stent for head and neck radiotherapy from

routine diagnostic imaging. 3D printing in medicine. 2017;3(1):1-6.

192.   Huang DT, Johnson CR, Schmidt-Ullrich R, Grimes M. Postoperative radiotherapy in head and

neck carcinoma with extracapsular lymph node extension and/or positive resection margins: A

comparative study. International Journal of Radiation Oncology*Biology*Physics. 1992;23(4):737-42.

doi: http://dx.doi.org/10.1016/0360-3016(92)90646-Y.

193.   Ang KK, Trotti A, Brown BW, Garden AS, Foote RL, Morrison WH, Geara FB, Klotch DW,

Goepfert H, Peters LJ. Randomized trial addressing risk features and time factors of surgery plus

radiotherapy in advanced head-and-neck cancer. International Journal of Radiation

Oncology*Biology*Physics. 2001;51(3):571-8. doi: http://dx.doi.org/10.1016/S0360-3016(01)01690-X.

194.   Robertson AG, Soutar DS, Paul J, Webster M, Leonard AG, Moore KP, McManners J, Yosef HM,

Canney P, Errington RD, Hammersley N, Singh R, Vaughan D. Early closure of a randomized trial: Surgery

and postoperative radiotherapy versus radiotherapy in the management of intra-oral tumours. Clinical

Oncology. 1998;10(3):155-60. doi: http://dx.doi.org/10.1016/S0936-6555(98)80055-1.

195.   Boero IJ, Paravati AJ, Xu B, Cohen EEW, Mell LK, Le Q-T, Murphy JD. Importance of Radiation

Oncologist Experience Among Patients With Head-and-Neck Cancer Treated With Intensity-Modulated

Radiation Therapy. J Clin Oncol. 2016;34(7):684-90. doi: doi:10.1200/JCO.2015.63.9898. PubMed PMID:

26729432.

196.   Blanchard P, Baujat B, Holostenco V, Bourredjem A, Baey C, Bourhis J, Pignon JP, Grp M-CC.

Meta-analysis of chemotherapy in head and neck cancer (MACH-NC): A comprehensive analysis by

tumour site. Radiotherapy and Oncology. 2011;100(1):33-40. doi: 10.1016/j.radonc.2011.05.036.

PubMed PMID: WOS:000295243200006.

197.   Daly ME, Le QT, Kozak MM, Maxim PG, Murphy JD, Hsu A, Loo BW, Kaplan MJ, Fischbein NJ,

Chang DT. Intensity-Modulated Radiotherapy for Oral Cavity Squamous Cell Carcinoma: Patterns of

Failure and Predictors of Local Control. Int J Radiat Oncol. 2011;80(5):1412-22. doi:

10.1016/j.ijrobp.2010.04.031. PubMed PMID: WOS:000293207600020.

198.   Ooishi M, Motegi A, Kawashima M, Arahira S, Zenda S, Nakamura N, Ariji T, Tokumaru S,

Sakuraba M, Tahara M, Hayashi R, Akimoto T. Patterns of failure after postoperative intensity-

modulated radiotherapy for locally advanced and recurrent head and neck cancer. Japanese journal of

clinical oncology. 2016;46(10):919-27. doi: 10.1093/jjco/hyw095. PubMed PMID: 27511989.

199.   Yao M, Chang K, Funk GF, Lu H, Tan H, Wacha J, Dornfeld KJ, Buatti JM. The failure patterns of

oral cavity squamous cell carcinoma after intensity-modulated radiotherapy-the university of iowa

experience. International journal of radiation oncology, biology, physics. 2007;67(5):1332-41. Epub

2007/02/06. doi: 10.1016/j.ijrobp.2006.11.030. PubMed PMID: 17276613.

200.   Studer G, Zwahlen RA, Graetz KW, Davis BJ, Glanzmann C. IMRT in oral cavity cancer. Radiation

Oncology (London, England). 2007;2:16. doi: 10.1186/1748-717x-2-16. PubMed PMID: 17430599;

PMCID: Pmc1855346.

201.   Gomez DR, Zhung JE, Gomez J, Chan K, Wu AJ, Wolden SL, Pfister DG, Shaha A, Shah JP, Kraus

DH, Wong RJ, Lee NY. Intensity-Modulated Radiotherapy in Postoperative Treatment of Oral Cavity

Cancers. International Journal of Radiation Oncology*Biology*Physics. 2009;73(4):1096-103. doi:

http://dx.doi.org/10.1016/j.ijrobp.2008.05.024.

202.   Daly ME, Le Q-T, Kozak MM, Maxim PG, Murphy JD, Hsu A, Loo Jr BW, Kaplan MJ, Fischbein NJ,

Chang DT. Intensity-Modulated Radiotherapy for Oral Cavity Squamous Cell Carcinoma: Patterns of

Failure and Predictors of Local Control. International Journal of Radiation Oncology*Biology*Physics.

2011;80(5):1412-22. doi: http://dx.doi.org/10.1016/j.ijrobp.2010.04.031.

203.   Sher DJ, Thotakura V, Balboni TA, Norris Jr CM, Haddad RI, Posner MR, Lorch J, Goguen LA,

Annino DJ, Tishler RB. Treatment of Oral Cavity Squamous Cell Carcinoma With Adjuvant or Definitive

Intensity-Modulated Radiation Therapy. International Journal of Radiation Oncology*Biology*Physics.

2011;81(4):e215-e22. doi: http://dx.doi.org/10.1016/j.ijrobp.2011.02.023.

204.   Chan AK, Huang SH, Le LW, Yu E, Dawson LA, Kim JJ, John Cho BC, Bayley AJ, Ringash J,

Goldstein D, Chan K, Waldron J, O'Sullivan B, Cummings B, Hope AJ. Postoperative intensity-modulated

radiotherapy following surgery for oral cavity squamous cell carcinoma: Patterns of failure. Oral

Oncology. 2013;49(3):255-60. doi: http://dx.doi.org/10.1016/j.oraloncology.2012.09.006.

205.   Gunn GB, Blanchard P, Garden AS, Zhu XR, Fuller CD, Mohamed AS, Morrison WH, Phan J,

Beadle BM, Skinner HD, Sturgis EM, Kies MS, Hutcheson KA, Rosenthal DI, Mohan R, Gillin MT, Frank SJ.

Clinical Outcomes and Patterns of Disease Recurrence After Intensity Modulated Proton Therapy for

Oropharyngeal Squamous Carcinoma. International Journal of Radiation Oncology • Biology •

Physics.95(1):360-7. doi: 10.1016/j.ijrobp.2016.02.021.

206.   Mohamed AS, Awan M, Kocak E, Beadle BM, Kantor ME, Gunn GB, Garden AS, Rosenthal DI,

Fuller CD. Methods for Analysis and Reporting the Patterns of Locoregional Failure in the Era of IMRT

for Head and Neck Cancer: Deformable Image Registration–Based Quality Assurance Workflow.

International Journal of Radiation Oncology*Biology*Physics. 2014;90(1, Supplement):S569-S70. doi:

http://dx.doi.org/10.1016/j.ijrobp.2014.05.1719.

207.   Mohamed ASR, Rosenthal DI, Awan MJ, Garden AS, Kocak-Uzel E, Belal AM, El-Gowily AG, Phan

J, Beadle BM, Gunn GB, Fuller CD. Methodology for analysis and reporting patterns of failure in the Era

of IMRT: head and neck cancer applications. Radiation Oncology. 2016;11(1):1-10. doi: 10.1186/s13014-

016-0678-7.

208.   Quinlan-Davidson SR, Mohamed ASR, Myers JN, Gunn GB, Johnson FM, Skinner H, Beadle BM,

Gillenwater AM, Phan J, Frank SJ, William WN, Wong AJ, Lai SY, Fuller CD, Morrison WH, Rosenthal DI,

Garden AS. Outcomes of oral cavity cancer patients treated with surgery followed by postoperative

intensity modulated radiation therapy. Oral Oncology. 2017;72:90-7. doi:

http://dx.doi.org/10.1016/j.oraloncology.2017.07.002.

209.   Pignon JP, le Maitre A, Maillard E, Bourhis J, Group M-NC. Meta-analysis of chemotherapy in

head and neck cancer (MACH-NC): an update on 93 randomised trials and 17,346 patients.

Radiotherapy and oncology : journal of the European Society for Therapeutic Radiology and Oncology.

2009;92(1):4-14. doi: 10.1016/j.radonc.2009.04.014. PubMed PMID: 19446902.

210.   Chow TL, Chow TK, Chan TTF, Yu NF, Fung SC, Lam SH. Contralateral neck recurrence of

squamous cell carcinoma of oral cavity and oropharynx. Journal of Oral and Maxillofacial Surgery.

2004;62(10):1225-8. doi: http://dx.doi.org/10.1016/j.joms.2004.03.013.

211.   Kurita H, Koike T, Narikawa J-n, Sakai H, Nakatsuka A, Uehara S, Kobayashi H, Kurashina K.

Clinical predictors for contralateral neck lymph node metastasis from unilateral squamous cell

carcinoma in the oral cavity. Oral Oncology. 2004;40(9):898-903. doi:

http://dx.doi.org/10.1016/j.oraloncology.2004.04.004.

212.   Metcalfe E, Aspin L, Speight R, Ermis E, Ramasamy S, Cardale K, Dyker KE, Sen M, Prestwich RJ.

Postoperative (Chemo)Radiotherapy for Oral Cavity Squamous Cell Carcinomas: Outcomes and Patterns

of Failure. Clin Oncol (R Coll Radiol). 2017;29(1):51-9. Epub 2016/10/08. doi:

10.1016/j.clon.2016.09.008. PubMed PMID: 27712917.

213.   Chao KSC, Ozyigit G, Tran BN, Cengiz M, Dempsey JF, Low DA. Patterns of failure in patients

receiving definitive and postoperative IMRT for head-and-neck cancer. International Journal of

Radiation Oncology*Biology*Physics. 2003;55(2):312-21. doi: http://dx.doi.org/10.1016/S0360-3016(02)03940-8.

214.   Popovtzer A, Gluck I, Chepeha DB, Teknos TN, Moyer JS, Prince ME, Bradford CR, Eisbruch A. The Pattern of Failure After Reirradiation of Recurrent Squamous Cell Head and Neck Cancer: Implications for Defining the Targets. International Journal of Radiation Oncology*Biology*Physics. 2009;74(5):1342-7. doi: http://dx.doi.org/10.1016/j.ijrobp.2008.10.042.

215.   Dawson LA, Anzai Y, Marsh L, Martel MK, Paulino A, Ship JA, Eisbruch A. Patterns of local-regional recurrence following parotid-sparing conformal and segmental intensity-modulated radiotherapy for head and neck cancer. International Journal of Radiation Oncology*Biology*Physics. 2000;46(5):1117-26. doi: http://dx.doi.org/10.1016/S0360-3016(99)00550-7.

216.   Due AK, Vogelius IR, Aznar MC, Bentzen SM, Berthelsen AK, Korreman SS, Kristensen CA, Specht L. Methods for estimating the site of origin of locoregional recurrence in head and neck squamous cell carcinoma. Strahlentherapie und Onkologie. 2012;188(8):671-6. doi: 10.1007/s00066-012-0127-y.

217.   Raktoe SAS, Dehnad H, Raaijmakers CPJ, Braunius W, Terhaard CHJ. Origin of Tumor Recurrence After Intensity Modulated Radiation Therapy for Oropharyngeal Squamous Cell Carcinoma. International Journal of Radiation Oncology*Biology*Physics. 2013;85(1):136-41. doi: http://dx.doi.org/10.1016/j.ijrobp.2012.02.042.

218.   Rosenthal DI, Asper JA, Barker JL, Garden AS, Chao KSC, Morrison WH, Weber RS, Ang KK. Importance of patient examination to clinical quality assurance in head and neck radiation oncology. Head & Neck. 2006;28(11):967-73. doi: 10.1002/hed.20446.

219.   Dawson LA, Anzai Y, Marsh L, Martel MK, Paulino A, Ship JA, Eisbruch A. Patterns of local-regional recurrence following parotid-sparing conformal and segmental intensity-modulated radiotherapy for head and neck cancer. Int J Radiat Oncol Biol Phys. 2000;46(5):1117-26. PubMed PMID: 10725621.

220.   Berwouts D, Olteanu LAM, Duprez F, Vercauteren T, De Gersem W, De Neve W, Van de Wiele C, Madani I. Three-phase adaptive dose-painting-by-numbers for head-and-neck cancer: initial results of the phase I clinical trial. Radiotherapy and Oncology. 2013;107(3):310-6. doi: DOI 10.1016/j.radonc.2013.04.002. PubMed PMID: WOS:000323869100009.

221.   Chang JH, Wada M, Anderson NJ, Joon DL, Lee ST, Gong SJ, Gunawardana DH, Sachinidis J, O'Keefe G, Gan HK, Khoo V, Scott AM. Hypoxia-targeted radiotherapy dose painting for head and neck cancer using F-18-FMISO PET: A biological modeling study. Acta Oncologica. 2013;52(8):1723-9. doi: Doi 10.3109/0284186x.2012.759273. PubMed PMID: WOS:000325526300019.

222.   Duprez F, De Neve W, De Gersem W, Coghe M, Madani I. Adaptive Dose Painting by Numbers for Head-and-Neck Cancer. International Journal of Radiation Oncology Biology Physics. 2011;80(4):1045-55. doi: DOI 10.1016/j.ijrobp.2010.03.028. PubMed PMID: WOS:000292486200013.

223.   Grosu A, Piert M, Souvatzoglou M, Wiedenmann N, Machulla H, Pigorsch S, Roper B, Schwaiger M, Molls M. Hypoxia Imaging with 18F-FAZA-PET for dose painting using intensity modulated radiotherapy in patients with head and neck cancer. International Journal of Radiation Oncology Biology Physics. 2005;63(2):S132-S3. doi: DOI 10.1016/j.ijrobp.2005.07.225. PubMed PMID: WOS:000232083300222.

224.   Houweling AC, Wolf AL, Vogel WV, Hamming-Vrieze O, van Vliet-Vroegindeweij C, de Kamer JBV, van der Heide UA. FDG-PET and diffusion-weighted MRI in head-and-neck cancer patients: Implications for dose painting. Radiotherapy and Oncology. 2013;106(2):250-4. doi: DOI 10.1016/j.radonc.2013.01.003. PubMed PMID: WOS:000318583600018.

225.   Madani I, Duprez F, Boterberg T, Van de Wiele C, Bonte K, Deron P, De Gersem W, Coghe M, De Neve W. Maximum tolerated dose in a phase I trial on adaptive dose painting by numbers for head and neck cancer. Radiotherapy and Oncology. 2011;101(3):351-5. doi: DOI 10.1016/j.radonc.2011.06.020. PubMed PMID: WOS:000298894700002.

226.   Madani I, Duthoy W, Derie C, De Gersem W, Boterberg T, Saerens M, Jacobs F, Gregoire V, Lonneux M, Vakaet L, Vanderstraeten B, Bauters W, Bonte K, Thierens H, De Neve W. Positron emission tomography-guided, focal-dose escalation using intensity-modulated radiotherapy for head and neck cancer. International Journal of Radiation Oncology Biology Physics. 2007;68(1):126-35. doi: DOI 10.1016/j.ijrobp.2006.12.070. PubMed PMID: WOS:000246046000017.

227.   Thorwarth D, Eschmann SM, Paulsen F, Alber M. Hypoxia dose painting based on functional FMISO PET imaging for head-and-neck cancer patients: A feasibility study. International Journal of Radiation Oncology Biology Physics. 2006;66(3):S186-S. doi: DOI 10.1016/j.ijrobp.2006.07.361. PubMed PMID: WOS:000241221600311.

228.   Shi X, Meng X, Sun X, Xing L, Yu J. PET/CT imaging-guided dose painting in radiation therapy. Cancer Letters. 2014;355(2):169-75. doi: http://dx.doi.org/10.1016/j.canlet.2014.07.042.

229.   Heukelom J, Hamming O, Bartelink H, Hoebers F, Giralt J, Herlestam T, Verheij M, Brekel Mvd, Vogel W, Slevin N, Deutsch E, Sonke J-J, Lambin P, Rasch C. Adaptive and innovative Radiation Treatment FOR improving Cancer treatment outcomE (ARTFORCE); a randomized controlled phase II trial for individualized treatment of head and neck cancer. BMC Cancer. 2013;13(1):84. doi: 10.1186/1471-2407-13-84.

230.   Aerts HJ, van Baardwijk AA, Petit SF, Offermann C, Loon J, Houben R, Dingemans AM, Wanders R, Boersma L, Borger J, Bootsma G, Geraedts W, Pitz C, Simons J, Wouters BG, Oellers M, Lambin P, Bosmans G, Dekker AL, De Ruysscher D. Identification of residual metabolic-active areas within individual NSCLC tumours using a pre-radiotherapy (18)Fluorodeoxyglucose-PET-CT scan. Radiother Oncol. 2009;91(3):386-92. Epub 2009/03/31. doi: 10.1016/j.radonc.2009.03.006. PubMed PMID: 19329207; PMCID: Pmc4693609.

231.   Cardenas CE, Mohamed ASR, Tao R, Wong AJR, Awan MJ, Kuruvila S, Aristophanous M, Gunn GB, Phan J, Beadle BM, Frank SJ, Garden AS, Morrison WH, Fuller CD, Rosenthal DI. Prospective Qualitative and Quantitative Analysis of Real-time Peer Review Quality Assurance Rounds Incorporating Direct Physical Examination for Head and Neck Cancer Radiation Therapy. International Journal of Radiation Oncology*Biology*Physics. doi: http://dx.doi.org/10.1016/j.ijrobp.2016.11.019.

232.   Zeidan OA, Langen KM, Meeks SL, Manon RR, Wagner TH, Willoughby TR, Jenkins DW, Kupelian PA. Evaluation of image-guidance protocols in the treatment of head and neck cancers. International journal of radiation oncology, biology, physics. 2007;67(3):670-7. doi: 10.1016/j.ijrobp.2006.09.040. PubMed PMID: 17197123.

233.   Aristophanous M, Penney BC, Martel MK, Pelizzari CA. A Gaussian mixture model for definition of lung tumor volumes in positron emission tomography. Medical Physics. 2007;34(11):4223-35. doi: https://doi.org/10.1118/1.2791035.

234.   Caldas Magalhaes J, Raaijmakers CP, Aristophanous M, Lee JA, Kasperts N, Jager EA, Kooij N, Terhaard CH, Philippens ME. FDG-PET Semi automatic Segmentation Methods for GTV Delineation in Laryngeal and Hypopharyngeal Cancer. International journal of radiation oncology, biology, physics. 2014;90(1):S536. doi: 10.1016/j.ijrobp.2014.05.1631.

235.   Mohamed AS, Rosenthal DI, Awan MJ, Garden AS, Kocak-Uzel E, Belal AM, El-Gowily AG, Phan J, Beadle BM, Gunn GB. Methodology for analysis and reporting patterns of failure in the Era of IMRT: head and neck cancer applications. Radiation oncology. 2016;11(1):95.

236.   Mohamed AS, Ruangskul M-N, Awan MJ, Baron CA, Kalpathy-Cramer J, Castillo R, Castillo E, Guerrero TM, Kocak-Uzel E, Yang J. Quality assurance assessment of diagnostic and radiation therapy–simulation CT image registration for head and neck radiation therapy: anatomic region of interest–based comparison of rigid and deformable algorithms. Radiology. 2015;274(3):752-63.

237.   Bevington PR, Robinson DK. Data reduction and error analysis. McGraw‑Hill, New York. 2003.

238.   Das SK, Ten Haken RK. Functional and molecular image guidance in radiotherapy treatment planning optimization. Seminars in radiation oncology. 2011;21(2):111-8. Epub 2011/03/02. doi: 10.1016/j.semradonc.2010.10.002. PubMed PMID: 21356479; PMCID: PMC3062208.

239. Phelps ME. Positron emission tomography provides molecular imaging of biological processes. Proceedings of the National Academy of Sciences of the United States of America. 2000;97(16):9226-33. Epub 2000/08/02. doi: 10.1073/pnas.97.16.9226. PubMed PMID: 10922074; PMCID: PMC16850.

240. Dierckx RA, Van de Wiele C. FDG uptake, a surrogate of tumour hypoxia? European journal of nuclear medicine and molecular imaging. 2008;35(8):1544-9. Epub 2008/05/30. doi: 10.1007/s00259-008-0758-5. PubMed PMID: 18509637; PMCID: PMC2491423.

241. Castelli J, De Bari B, Depeursinge A, Simon A, Devillers A, Roman Jimenez G, Prior J, Ozsahin M, de Crevoisier R, Bourhis J. Overview of the predictive value of quantitative 18 FDG PET in head and neck cancer treated with chemoradiotherapy. Critical reviews in oncology/hematology. 2016;108:40-51. Epub 2016/12/10. doi: 10.1016/j.critrevonc.2016.10.009. PubMed PMID: 27931839.

242. Boellaard R. Standards for PET image acquisition and quantitative data analysis. Journal of nuclear medicine : official publication, Society of Nuclear Medicine. 2009;50 Suppl 1:11s-20s. Epub 2009/04/22. doi: 10.2967/jnumed.108.057182. PubMed PMID: 19380405.

243. Soto DE, Kessler ML, Piert M, Eisbruch A. Correlation between pretreatment FDG-PET biological target volume and anatomical location of failure after radiation therapy for head and neck cancers. Radiother Oncol. 2008;89(1):13-8. Epub 2008/06/17. doi: 10.1016/j.radonc.2008.05.021. PubMed PMID: 18555547; PMCID: PMC2684445.

244. Due AK, Vogelius IR, Aznar MC, Bentzen SM, Berthelsen AK, Korreman SS, Loft A, Kristensen CA, Specht L. Recurrences after intensity modulated radiotherapy for head and neck squamous cell carcinoma more likely to originate from regions with high baseline [18F]-FDG uptake. Radiother Oncol.

2014;111(3):360-5. Epub 2014/07/06. doi: 10.1016/j.radonc.2014.06.001. PubMed PMID: 24993331;

PMCID: PMC4469149.

245.   Schwartz J, Humm JL, Gonen M, Kalaigian H, Schoder H, Larson SM, Nehmeh SA. Repeatability

of SUV measurements in serial PET. Med Phys. 2011;38(5):2629-38. Epub 2011/07/23. doi:

10.1118/1.3578604. PubMed PMID: 21776800; PMCID: PMC7986573.

246.   Torre LA, Bray F, Siegel RL, Ferlay J, Lortet-Tieulent J, Jemal A. Global cancer statistics. CA

Cancer J Clin. 2015;65(2):87-108.

247.   Society AC. Cancer Facts & Figures 2016: Atlanta: American Cancer Society 2016.

248.   Li R, Agrawal N, Fakhry C. Anatomical Sites and Subsites of Head and Neck Cancer. HPV and

Head and Neck Cancers2015. p. 1-11.

249.   Fakhry C, Zhang Q, Nguyen-Tan PF. Human papillomavirus and overall survival after progression

of oropharyngeal squamous cell carcinoma. J Clin Oncol. 2014;32(30):3365-73.

250.   Jiang W, Chamberlain PD, Garden AS. Prognostic value of p16 expression in Epstein-Barr virus-

positive nasopharyngeal carcinomas. Head Neck. 2016;38(Suppl 1):E1459-66. doi: 10.1002/hed.24258.

251.   Maasland DHE, Brandt PAvd, Kremer B. Alcohol consumption, cigarette smoking and the risk of

subtypes of head-neck cancer: results from the Netherlands Cohort Study. BMC Cancer. 2014;14(187).

252.   Sturgis EM, Cinciripini PM. Trends in head and neck cancer incidence in relation to smoking

prevalence: an emerging epidemic of human papillomavirus-associated cancers? Cancer.

2007;110(7):1429-35.

339

253.	Nutting CM, Morden JP, Harrington KJ. Parotid-sparing intensity modulated versus conventional radiotherapy in head and neck cancer (PARSPORT): a phase 3 multicentre randomised controlled trial. Lancet Oncol. 2011;12(2):127-36.

254.	Dahiya K, Dhankhar R. Updated overview of current biomarkers in head and neck carcinoma. World J Methodol. 2016;6(1):77-86.

255.	Skinner HD, Sandulache VC, Ow TJ. TP53 disruptive mutations lead to head and neck cancer treatment failure through inhibition of radiation-induced senescence. Clin Cancer Res. 2012;18(1):290-300. doi: 10.1158/1078-0432.

256.	Jamshidi N, Diehn M, Bredel M, Kuo MD. Illuminating radiogenomic characteristics of glioblastoma multiforme through integration of MR imaging, messenger RNA expression, and DNA copy number variation. Radiology. 2014;270(1):212-22. doi: 10.1148/radiol.13130078.

257.	Karlo CA, Paolo PLD, Chaim J, Hakimi AA, Ostrovnaya I, Russo P, Hricak H, Motzer R, Hsieh JJ, Akin O. Radiogenomics of clear cell renal cell carcinoma: associations between CT imaging features and mutations. Radiology. 2014;270(2):464-71. doi: 10.1148/radiol.13130663.

258.	Yang YS, Guccione S, Bednarski MD. Comparing Genomic and Histologic Correlations to Radiographic Changes in Tumors: A Murine SCC VII Model Study. Acad Radiol. 2003;10(10):1165-75.

259.	Aerts HJWL, Velazquez ER, Leijenaar RTH. Decoding tumour phenotype by noninvasive imaging using a quantitative radiomics approach. Nat Commun. 2014;5(Article number: 4006). doi: 10.1038/ncomms5006.

260.   Pickering CR, Shah K, Ahmed S, Rao A, Frederick MJ, Zhang J, Unruh AK, Wang J, Ginsberg LE,

A.J. Kumar, Myers JN, Hamilton JD. CT imaging correlates of genomic expression for oral cavity

squamous cell carcinoma. AJNR Am J Neuroradiol. 2013;34(9):1818-22. doi: 10.3174/ajnr.A3635.

261.   Network CGA. Comprehensive genomic characterization of head and neck squamous cell

carcinomas. Nature. 2015;517(7536):576-82. doi: 10.1038/nature14129.

262.   Clark K, Vendt B, Smith K, Freymann J, Kirby J, Koppel P, Moore S, Phillips S, Maffitt D, Pringle

M, Tarbox L, Prior F. The Cancer Imaging Archive (TCIA): maintaining and operating a public information

repository. J Digit Imaging. 2013;26(6):1045-57. doi: 10.1007/s10278-013-9622-7.

263.   Zhang L, Fried DV, Fave XJ, Hunter LA, Yang J, Court LE. IBEX: an open infrastructure software

platform to facilitate collaborative work in radiomics. Med Phys. 2015;42(3):1341-53. doi:

10.1118/1.4908210.

264.   Zhu Y, Qiu P, Ji Y. TCGA-Assembler: open-source software for retrieving and processing TCGA

data. Nat Methods. 2014;11(6):599-600.

265.   Subramanian A, Tamayo P, Mootha VK, Mukherjee S, Ebert BL, Gillette MA, Paulovich A,

Pomeroy SL, TR TRG, Lander ES, Mesirov JP. Gene set enrichment analysis: a knowledge-based

approach for interpreting genome-wide expression profiles. Proc Natl Acad Sci USA.

2005;102(43):15545-50. doi: 10.1073/pnas.0506580102.

266.   Kanehisa M, Goto S, Sato Y, Furumichi M, Tanabe M. KEGG for integration and interpretation of

large-scale molecular data sets. Nucleic Acids Res. 2012;40(Database issue):D109-14. doi:

10.1093/nar/gkr988.

341

267.   Ho TK. The random subspace method for constructing decision forests. IEEE Trans Pattern Anal Mach Intell. 1998;20(8):832–44. doi: 10.1109/34.709601.

268.   Mehta CR, Patel NR. Algorithm 643. FEXACT: a Fortran subroutine for Fisher's exact test on unordered r*c contingency tables. ACM Trans Math Softw. 1986;12(2):154-61. doi: 10.1145/6497.214326.

269.   Clarkson DB, Fan Y, Joe H. A remark on algorithm 643: FEXACT: an algorithm for performing Fisher's exact test in r x c contingency tables. ACM Trans Math Softw. 1993;19:484–8. doi: 10.1145/168173.168412.

270.   Wong RS. Apoptosis in cancer: from pathogenesis to treatment. J Exp Clin Cancer Res. 2011. doi: 10.1186/1756-9966-30-87.

271.   Markwell SM, Weed SA. Tumor and stromal-based contributions to head and neck squamous cell carcinoma invasion. Cancers (Basel). 2015;7(1):382-406. doi: 10.3390/cancers7010382.

272.   Bian Y, Hall B, Sun ZJ, Molinolo A, Chen W, Gutkind JS, Waes CV, Kulkarni AB. Loss of TGF-β signaling and PTEN promotes head and neck squamous cell carcinoma through cellular senescence evasion and cancer-related inflammation. Oncogene. 2012;31(28):3322-32. doi: 10.1038/onc.2011.494.

273.   Xie N, Wang C, Zhuang Z, Hou J, Liu X, Wu Y, Liu H, Huang H. Decreased miR-320a promotes invasion and metastasis of tumor budding cells in tongue squamous cell carcinoma. Oncotarget. 2016;7(40):65744-57. doi: 10.18632/oncotarget.11612.

274.   Tu HF, Lin SC, Chang KW. MicroRNA aberrances in head and neck cancer: pathogenetic and clinical significance. Curr Opin Otolaryngol Head Neck Surg. 2013;21(2):104-11. doi: 10.1097/MOO.0b013e32835e1d6e.

275.   Iorio MV, Croce CM. MicroRNA dysregulation in cancer: diagnostics, monitoring and therapeutics. A comprehensive review. EMBO Mol Med. 2012;4(3):143-59. doi: 10.1002/emmm.201100209.

276.   Sethi N, Wright A, Wood H, Rabbitts P. MicroRNAs and head and neck cancer: reviewing the first decade of research. Eur J Cancer. 2014;50(15):2619-35. doi: 10.1016/j.ejca.2014.07.012.

277.   Ramdas L, Giri U, Ashorn CL, Coombes KR, El-Naggar A, Ang KK, Story MD. miRNA expression profiles in head and neck squamous cell carcinoma and adjacent normal tissue. Head Neck. 2009;31(5):642-54. doi: 10.1002/hed.21017.

278.   Yu BL, Peng XH, Zhao FP, Liu X, Lu J, Wang L, Li G, Chen HH, Li XP. MicroRNA-378 functions as an onco-miR in nasopharyngeal carcinoma by repressing TOB2 expression. Int J Oncol. 2014;44(4):1215-22. doi: 10.3892/ijo.2014.2283.

279.   Martin D, Abba MC, Molinolo AA, Vitale-Cross L, Wang Z, Zaida M, Delic NC, Samuels Y, Lyons JG, Gutkind JS. The head and neck cancer cell oncogenome: a platform for the development of precision molecular therapies. Oncotarget. 2014;5(19):8906-23.

280.   Sok JC, Lee JA, Dasari S, Joyce S, Contrucci SC, Egloff AM, Trevelline BK, Joshi R, Kumari N, Grandis JR, Thomas SM. Collagen type XI α1 facilitates head and neck squamous cell cancer growth and invasion. Br J Cancer. 2013;109(12):3049-56.

281.   Bogowicz M, Riesterer O, Ikenberg K, Stieb S, Moch H, Studer G, Guckenberger M, Tanadini-Lang S. Computed tomography radiomics predicts HPV status and local tumor control after definitive radiochemotherapy in head and neck squamous cell carcinoma. Int J Radiat Oncol Biol Phys. 2017;99(4):921-8.

282.   Zhu Y, Xu Y, Helseth DL, Gulukota K, Yang S, Pesce LL, Mitra R, Müller P, Sengupta S, Guo W, Silverstein JC, Foster I, Parsad N, White KP, Ji Y. Zodiac: A Comprehensive Depiction of Genetic Interactions in Cancer by Integrating TCGA Data. JNCI-J Natl Cancer Inst. 2015;107(8):djv129. doi: 10.1093/jnci/djv129.

283.   Boring CC, Squires TS, Tong T. Cancer statistics, 1992. CA Cancer J Clin. 1992;42(1):19-38. Epub 1992/01/01. doi: 10.3322/canjclin.42.1.19. PubMed PMID: 1728335.

284.   Siegel RL, Miller KD, Fuchs HE, Jemal A. Cancer Statistics, 2021. CA Cancer J Clin. 2021;71(1):7-33. doi: https://doi.org/10.3322/caac.21654.

285.   Mao Y, Xing M. Recent incidences and differential trends of thyroid cancer in the USA. Endocr Relat Cancer. 2016;23(4):313-22. Epub 2016/02/27. doi: 10.1530/erc-15-0445. PubMed PMID: 26917552; PMCID: PMC4891202.

286.   Lewinski A, Adamczewski Z. Papillary thyroid carcinoma: a cancer with an extremely diverse genetic background and prognosis. Pol Arch Intern Med. 2017;127(6):388-9. Epub 2017/07/07. doi: 10.20452/pamw.4058. PubMed PMID: 28680025.

287.   Bhatia A, Rao A, Ang KK, Garden AS, Morrison WH, Rosenthal DI, Evans DB, Clayman G,

Sherman SI, Schwartz DL. Anaplastic thyroid cancer: Clinical outcomes with conformal radiotherapy.

Head Neck. 2010;32(7):829-36. Epub 2009/11/04. doi: 10.1002/hed.21257. PubMed PMID: 19885924.

288.   Maniakas A, Dadu R, Busaidy NL, Wang JR, Ferrarotto R, Lu C, Williams MD, Gunn GB, Hofmann

M-C, Cote G, Sperling J, Gross ND, Sturgis EM, Goepfert RP, Lai SY, Cabanillas ME, Zafereo M. Evaluation

of Overall Survival in Patients With Anaplastic Thyroid Carcinoma, 2000-2019. JAMA Oncology.

2020;6(9):1397-404. doi: 10.1001/jamaoncol.2020.3362.

289.   Redig AJ, Janne PA. Basket trials and the evolution of clinical trial design in an era of genomic

medicine. J Clin Oncol. 2015;33(9):975-7. Epub 2015/02/11. doi: 10.1200/JCO.2014.59.8433. PubMed

PMID: 25667288.

290.   Sasanakietkul T, Murtha TD, Javid M, Korah R, Carling T. Epigenetic modifications in poorly

differentiated and anaplastic thyroid cancer. Mol Cell Endocrinol. 2018;469:23-37. Epub 2017/05/30.

doi: 10.1016/j.mce.2017.05.022. PubMed PMID: 28552796.

291.   Smith N, Nucera C. Personalized therapy in patients with anaplastic thyroid cancer: targeting

genetic and epigenetic alterations. J Clin Endocrinol Metab. 2015;100(1):35-42. Epub 2014/10/28. doi:

10.1210/jc.2014-2803. PubMed PMID: 25347569; PMCID: PMC4283016.

292.   Woodward EL, Biloglav A, Ravi N, Yang M, Ekblad L, Wennerberg J, Paulsson K. Genomic

complexity and targeted genes in anaplastic thyroid cancer cell lines. Endocr Relat Cancer.

2017;24(7):X2. Epub 2017/07/05. doi: 10.1530/ERC-16-0522e. PubMed PMID: 28673895.

293.   Kasaian K, Wiseman SM, Walker BA, Schein JE, Zhao Y, Hirst M, Moore RA, Mungall AJ, Marra MA, Jones SJ. The genomic and transcriptomic landscape of anaplastic thyroid cancer: implications for therapy. BMC Cancer. 2015;15:984. Epub 2015/12/19. doi: 10.1186/s12885-015-1955-9. PubMed PMID: 26680454; PMCID: PMC4683857.

294.   Kalu NN, Mazumdar T, Peng S, Tong P, Shen L, Wang J, Banerjee U, Myers JN, Pickering CR, Brunell D, Stephan CC, Johnson FM. Comprehensive pharmacogenomic profiling of human papillomavirus-positive and -negative squamous cell carcinoma identifies sensitivity to aurora kinase inhibition in KMT2D mutants. Cancer Lett. 2018;431:64-72. Epub 2018/05/29. doi: 10.1016/j.canlet.2018.05.029. PubMed PMID: 29807113.

295.   Coussens NP, Sittampalam GS, Guha R, Brimacombe K, Grossman A, Chung TDY, Weidner JR, Riss T, Trask OJ, Auld D, Dahlin JL, Devanaryan V, Foley TL, Mcgee J, Kahl SD, Kales SC, Arkin M, Baell J, Bejcek B, Gal-Edd N, Glicksman M, Haas JV, Iversen PW, Hoeppner M, Lathrop S, Sayers E, Liu HG, Trawick B, Mcvey J, Lemmon VP, Li ZY, McManus O, Minor L, Napper A, Wildey MJ, Pacifici R, Chin WW, Xia MH, Xu X, Lal-Nag M, Hall MD, Michael S, Inglese J, Simeonov A, Austin CP. Assay Guidance Manual: Quantitative Biology and Pharmacology in Preclinical Drug Discovery. Cts-Clinical and Translational Science. 2018;11(5):461-70. doi: 10.1111/cts.12570. PubMed PMID: WOS:000444225800003.

296.   Hafner M, Niepel M, Chung M, Sorger PK. Growth rate inhibition metrics correct for confounders in measuring sensitivity to cancer drugs. Nat Methods. 2016;13(6):521-7. Epub 2016/05/03. doi: 10.1038/nmeth.3853. PubMed PMID: 27135972; PMCID: PMC4887336.

297.   Ahn SH, Henderson Y, Kang Y, Chattopadhyay C, Holton P, Wang M, Briggs K, Clayman GL. An orthotopic model of papillary thyroid carcinoma in athymic nude mice. Arch Otolaryngol Head Neck Surg. 2008;134(2):190-7. Epub 2008/02/20. doi: 134/2/190 [pii]

10.1001/archoto.2007.36 [doi]. PubMed PMID: 18283163.

298.   Maniakas AH, Y. C.; Hei, H.; Peng, S.; Bell, D.; Wiliams, M. D.; Scherer, S. E.; Wheeler, D. A.; Clayman, G. L.; Zafereo, M.; Wang, J. R.; Cabanillas, M. E.; Johnson, F. M.; Lai, S. Y. Development and characterization of six novel anaplastic thyroid cancer patient-derived xenograft models. Submitted. 2020.

299.   Crisanti MC, Wallace AF, Kapoor V, Vandermeers F, Dowling ML, Pereira LP, Coleman K, Campling BG, Fridlender ZG, Kao GD, Albelda SM. The HDAC inhibitor panobinostat (LBH589) inhibits mesothelioma and lung cancer cells in vitro and in vivo with particular efficacy for small cell lung cancer. Molecular Cancer Therapeutics. 2009;8(8):2221-31. doi: 10.1158/1535-7163.Mct-09-0138.

300.   Williams MD, DeLellis RA, Erickson LA, Gupta R, Johnson SJ, Kameyama K, Natu S, Ng T, Perren A, Perrier ND, Seethala RR, Gill AJ. Pathology data set for reporting parathyroid carcinoma and atypical parathyroid neoplasm: recommendations from the International Collaboration on Cancer Reporting. Hum Pathol. 2021;110:73-82. Epub 2020/07/21. doi: 10.1016/j.humpath.2020.07.008. PubMed PMID: 32687943.

301.	Bradshaw-Pierce EL, Eckhardt SG, Gustafson DL. A Physiologically Based Pharmacokinetic Model of Docetaxel Disposition: from Mouse to Man. Clin Cancer Res. 2007;13(9):2768-76. doi: 10.1158/1078-0432.Ccr-06-2362.

302.	Jain S, Jirau-Serrano X, Zullo KM, Scotto L, Palermo CF, Sastra SA, Olive KP, Cremers S, Thomas T, Wei Y, Zhang Y, Bhagat G, Amengual JE, Deng C, Karan C, Realubit R, Bates SE, O'Connor OA. Preclinical Pharmacologic Evaluation of Pralatrexate and Romidepsin Confirms Potent Synergy of the Combination in a Murine Model of Human T-cell Lymphoma. Clin Cancer Res. 2015;21(9):2096-106. doi: 10.1158/1078-0432.Ccr-14-2249.

303.	Wang D, Iclozan C, Liu C, Xia C, Anasetti C, Yu XZ. LBH589 enhances T cell activation in vivo and accelerates graft-versus-host disease in mice. Biol Blood Marrow Transplant. 2012;18(8):1182-90.e1. Epub 2012/06/16. doi: 10.1016/j.bbmt.2012.06.002. PubMed PMID: 22698484; PMCID: PMC3417119.

304.	Flaherty KT, Puzanov I, Kim KB, Ribas A, McArthur GA, Sosman JA, O'Dwyer PJ, Lee RJ, Grippo JF, Nolop K, Chapman PB. Inhibition of mutated, activated BRAF in metastatic melanoma. N Engl J Med. 2010;363(9):809-19. Epub 2010/09/08. doi: 10.1056/NEJMoa1002011. PubMed PMID: 20818844; PMCID: PMC3724529.

305.	Luke JJ, Hodi FS. Vemurafenib and BRAF inhibition: a new class of treatment for metastatic melanoma. Clin Cancer Res. 2012;18(1):9-14. Epub 2011/11/16. doi: 10.1158/1078-0432.CCR-11-2197. PubMed PMID: 22083257.

306.	Shi H, Hugo W, Kong X, Hong A, Koya RC, Moriceau G, Chodon T, Guo R, Johnson DB, Dahlman KB, Kelley MC, Kefford RF, Chmielowski B, Glaspy JA, Sosman JA, van Baren N, Long GV, Ribas A, Lo RS.

348

Acquired resistance and clonal evolution in melanoma during BRAF inhibitor therapy. Cancer Discov.

2014;4(1):80-93. Epub 2013/11/23. doi: 10.1158/2159-8290.CD-13-0642. PubMed PMID: 24265155;

PMCID: PMC3936420.

307.   Flaherty KT, Infante JR, Daud A, Gonzalez R, Kefford RF, Sosman J, Hamid O, Schuchter L, Cebon

J, Ibrahim N, Kudchadkar R, Burris HA, 3rd, Falchook G, Algazi A, Lewis K, Long GV, Puzanov I, Lebowitz

P, Singh A, Little S, Sun P, Allred A, Ouellet D, Kim KB, Patel K, Weber J. Combined BRAF and MEK

inhibition in melanoma with BRAF V600 mutations. N Engl J Med. 2012;367(18):1694-703. Epub

2012/10/02. doi: 10.1056/NEJMoa1210093. PubMed PMID: 23020132; PMCID: PMC3549295.

308.   De Palma M, Hanahan D. The biology of personalized cancer medicine: facing individual

complexities underlying hallmark capabilities. Mol Oncol. 2012;6(2):111-27. Epub 2012/03/01. doi:

10.1016/j.molonc.2012.01.011. PubMed PMID: 22360993; PMCID: PMC5528366.

309.   Masui K, Gini B, Wykosky J, Zanca C, Mischel PS, Furnari FB, Cavenee WK. A tale of two

approaches: complementary mechanisms of cytotoxic and targeted therapy resistance may inform

next-generation cancer treatments. Carcinogenesis. 2013;34(4):725-38. Epub 2013/03/01. doi:

10.1093/carcin/bgt086. PubMed PMID: 23455378.

310.   Niu N, Wang L. In vitro human cell line models to predict clinical response to anticancer drugs.

Pharmacogenomics. 2015;16(3):273-85. Epub 2015/02/26. doi: 10.2217/pgs.14.170. PubMed PMID:

25712190; PMCID: PMC4358765.

311.   Leung AW, Dragowska WH, Ricaurte D, Kwok B, Mathew V, Roosendaal J, Ahluwalia A,

Warburton C, Laskin JJ, Stirling PC, Qadir MA, Bally MB. 3'-Phosphoadenosine 5'-phosphosulfate

synthase 1 (PAPSS1) knockdown sensitizes non-small cell lung cancer cells to DNA damaging agents. Oncotarget. 2015;6(19):17161-77. Epub 2015/07/30. doi: 10.18632/oncotarget.3635. PubMed PMID: 26220590; PMCID: PMC4627299.

312.   Hatano K, Kumar B, Zhang Y, Coulter JB, Hedayati M, Mears B, Ni X, Kudrolli TA, Chowdhury WH, Rodriguez R, DeWeese TL, Lupold SE. A functional screen identifies miRNAs that inhibit DNA repair and sensitize prostate cancer cells to ionizing radiation. Nucleic Acids Res. 2015;43(8):4075-86. Epub 2015/04/08. doi: 10.1093/nar/gkv273. PubMed PMID: 25845598; PMCID: PMC4417178.

313.   Benzina S, Pitaval A, Lemercier C, Lustremant C, Frouin V, Wu N, Papine A, Soussaline F, Romeo PH, Gidrol X. A kinome-targeted RNAi-based screen links FGF signaling to H2AX phosphorylation in response to radiation. Cell Mol Life Sci. 2015;72(18):3559-73. Epub 2015/04/22. doi: 10.1007/s00018-015-1901-7. PubMed PMID: 25894690; PMCID: PMC4548013.

314.   Higgins GS, Prevo R, Lee YF, Helleday T, Muschel RJ, Taylor S, Yoshimura M, Hickson ID, Bernhard EJ, McKenna WG. A small interfering RNA screen of genes involved in DNA repair identifies tumor-specific radiosensitization by POLQ knockdown. Cancer Res. 2010;70(7):2984-93. Epub 2010/03/18. doi: 10.1158/0008-5472.can-09-4040. PubMed PMID: 20233878; PMCID: PMC2848966.

315.   Nagel R, Stigter-van Walsum M, Buijze M, van den Berg J, van der Meulen IH, Hodzic J, Piersma SR, Pham TV, Jimenez CR, van Beusechem VW, Brakenhoff RH. Genome-wide siRNA Screen Identifies the Radiosensitizing Effect of Downregulation of MASTL and FOXM1 in NSCLC. Mol Cancer Ther. 2015;14(6):1434-44. Epub 2015/03/27. doi: 10.1158/1535-7163.mct-14-0846. PubMed PMID: 25808837.

316.   Tiwana GS, Prevo R, Buffa FM, Yu S, Ebner DV, Howarth A, Folkes LK, Budwal B, Chu KY, Durrant

L, Muschel RJ, McKenna WG, Higgins GS. Identification of vitamin B1 metabolism as a tumor-specific

radiosensitizing pathway using a high-throughput colony formation screen. Oncotarget.

2015;6(8):5978-89. Epub 2015/03/20. doi: 10.18632/oncotarget.3468. PubMed PMID: 25788274;

PMCID: PMC4467415.

317.   Brett-Morris A, Wright BM, Seo Y, Pasupuleti V, Zhang J, Lu J, Spina R, Bar EE, Gujrati M, Schur

R, Lu ZR, Welford SM. The polyamine catabolic enzyme SAT1 modulates tumorigenesis and radiation

response in GBM. Cancer Res. 2014;74(23):6925-34. Epub 2014/10/04. doi: 10.1158/0008-5472.can-14-

1249. PubMed PMID: 25277523; PMCID: PMC4423404.

318.   Zheng M, Morgan-Lappe SE, Yang J, Bockbrader KM, Pamarthy D, Thomas D, Fesik SW, Sun Y.

Growth Inhibition and Radiosensitization of Glioblastoma and Lung Cancer Cells by Small Interfering

RNA Silencing of Tumor Necrosis Factor Receptor–Associated Factor 2. Cancer Research.

2008;68(18):7570-8. doi: 10.1158/0008-5472.can-08-0632.

319.   Hodzic J, Dingjan I, Maas MJ, van der Meulen-Muileman IH, de Menezes RX, Heukelom S,

Verheij M, Gerritsen WR, Geldof AA, van Triest B, van Beusechem VW. A cell-based high-throughput

screening assay for radiation susceptibility using automated cell counting. Radiat Oncol. 2015;10:55.

Epub 2015/04/19. doi: 10.1186/s13014-015-0355-2. PubMed PMID: 25888875; PMCID: PMC4355372.

320.   Kafkafi N, Agassi J, Chesler EJ, Crabbe JC, Crusio WE, Eilam D, Gerlai R, Golani I, Gomez-Marin A,

Heller R, Iraqi F, Jaljuli I, Karp NA, Morgan H, Nicholson G, Pfaff DW, Richter SH, Stark PB, Stiedl O,

Stodden V, Tarantino LM, Tucci V, Valdar W, Williams RW, Würbel H, Benjamini Y. Reproducibility and

replicability of rodent phenotyping in preclinical studies. Neurosci Biobehav Rev. 2018;87:218-32. doi:

https://doi.org/10.1016/j.neubiorev.2018.01.003.

321.   Ghosh C, Kumar S, Kushchayeva Y, Gaskins K, Boufraqech M, Wei D, Gara SK, Zhang L, Zhang Y-

q, Shen M, Mukherjee S, Kebebew E. A Combinatorial Strategy for Targeting

BRAF^{V600E}-Mutant Cancers with BRAF^{V600E} Inhibitor (PLX4720)

and Tyrosine Kinase Inhibitor (Ponatinib). Clin Cancer Res. 2020;26(8):2022-36. doi: 10.1158/1078-

0432.Ccr-19-1606.

322.   Catalano MG, Pugliese M, Gargantini E, Grange C, Bussolati B, Asioli S, Bosco O, Poli R,

Compagnone A, Bandino A, Mainini F, Fortunati N, Boccuzzi G. Cytotoxic activity of the histone

deacetylase inhibitor panobinostat (LBH589) in anaplastic thyroid cancer in vitro and in vivo. Int J

Cancer. 2012;130(3):694-704. Epub 2011/03/15. doi: 10.1002/ijc.26057. PubMed PMID: 21400508.

323.   Tseng YT, Chang TC. Multimodality treatment of anaplastic thyroid cancer with nearly resolved

effect. J Formos Med Assoc. 2015;114(9):897-8. Epub 2014/04/24. doi: 10.1016/j.jfma.2014.03.006.

PubMed PMID: 24755268.

324.   Pudney D, Lau H, Ruether JD, Falck V. Clinical experience of the multimodality management of

anaplastic thyroid cancer and literature review. Thyroid. 2007;17(12):1243-50. Epub 2008/01/08. doi:

10.1089/thy.2007.0026. PubMed PMID: 18177257.

325.   Liu C, Zhu Y, Lou W, Nadiminty N, Chen X, Zhou Q, Shi XB, deVere White RW, Gao AC. Functional

p53 determines docetaxel sensitivity in prostate cancer cells. The Prostate. 2013;73(4):418-27. Epub

2012/09/19. doi: 10.1002/pros.22583. PubMed PMID: 22996738.

326.	San-Miguel JF, Hungria VT, Yoon SS, Beksac M, Dimopoulos MA, Elghandour A, Jedrzejczak WW, Günther A, Nakorn TN, Siritanaratkul N, Schlossman RL, Hou J, Moreau P, Lonial S, Lee JH, Einsele H, Sopala M, Bengoudifa BR, Binlich F, Richardson PG. Overall survival of patients with relapsed multiple myeloma treated with panobinostat or placebo plus bortezomib and dexamethasone (the PANORAMA 1 trial): a randomised, placebo-controlled, phase 3 trial. The Lancet Haematology. 2016;3(11):e506-e15. Epub 2016/10/19. doi: 10.1016/s2352-3026(16)30147-8. PubMed PMID: 27751707.

327.	Bahig H, Yuan Y, Mohamed ASR, Brock KK, Ng SP, Wang J, Ding Y, Hutcheson K, McCulloch M, Balter PA, Lai SY, Al-Mamgani A, Sonke J-J, van der Heide UA, Nutting C, Li XA, Robbins J, Awan M, Karam I, Newbold K, Harrington K, Oelfke U, Bhide S, Philippens MEP, Terhaard CHJ, McPartlin AJ, Blanchard P, Garden AS, Rosenthal DI, Gunn GB, Phan J, Cazoulat G, Aristophanous M, McSpadden KK, Garcia JA, van den Berg CAT, Raaijmakers CPJ, Kerkmeijer L, Doornaert P, Blinde S, Frank SJ, Fuller CD. Magnetic Resonance-based Response Assessment and Dose Adaptation in Human Papilloma Virus Positive Tumors of the Oropharynx treated with Radiotherapy (MR-ADAPTOR): An R-IDEAL stage 2a-2b/Bayesian phase II trial. Clinical and Translational Radiation Oncology. 2018;13:19-23. doi: https://doi.org/10.1016/j.ctro.2018.08.003.

328.	Kamal M, Mohamed ASR, Fuller CD, Sturgis EM, Johnson FM, Morrison WH, Gunn GB, Hutcheson KA, Phan J, Volpe S, Ng SP, Phan J, Cardenas C, Ferrarotto R, Frank SJ, Rosenthal DI, Garden AS. Patterns of Failure After Intensity Modulated Radiation Therapy in Head and Neck Squamous Cell Carcinoma of Unknown Primary: Implication of Elective Nodal and Mucosal Dose Coverage. Advances in Radiation Oncology. 2020;5(5):929-35. doi: https://doi.org/10.1016/j.adro.2020.04.025.

329. Nantavithya C, Gomez DR, Chang JY, Mohamed ASR, Fuller CD, Li H, Brooks ED, Gandhi SJ. An improved method for analyzing and reporting patterns of in-field recurrence after stereotactic ablative radiotherapy in early-stage non-small cell lung cancer. Radiotherapy and Oncology. 2020;145:209-14. doi: https://doi.org/10.1016/j.radonc.2020.01.002.

330. Waldram R, Taylor AE, Whittam S, Iyizoba-Ebozue Z, Murray L, Frood R, Cardale K, Dyker KE, Murray P, Ramasamy S, Sen M, Al-Qaisieh B, Prestwich RJD. Evaluation of Locoregional Recurrence Patterns Following Adjuvant (Chemo)Radiotherapy for Oral Cavity Carcinoma. Clinical Oncology. 2020;32(4):228-37. doi: https://doi.org/10.1016/j.clon.2019.10.002.

331. Definition of volumes. J ICRU. 2010;10:41-53. doi: 10.1093/jicru/ndq009.

332. Mohamed AS, Rosenthal DI, Awan MJ, Garden AS, Kocak-Uzel E, Belal AM, El-Gowily AG, Phan J, Beadle BM, Gunn GB, Fuller CD. Methodology for analysis and reporting patterns of failure in the Era of IMRT: head and neck cancer applications. Radiat Oncol. 2016;11(1):95. doi: 10.1186/s13014-016-0678-7.

333. Mi H, Petitjean C, Dubray B, Vera P, Ruan S. Robust feature selection to predict tumor treatment outcome. Artif Intell Med. 2015;64:195-204. doi: 10.1016/j.artmed.2015.07.002.

334. Hatt M, Tixier F, Pierce L, Kinahan PE, Rest CCL, Visvikis D. Characterization of PET/CT images using texture analysis: the past, the present… any future? Eur J Nucl Med Mol Imaging. 2017;44:151-65. doi: 10.1007/s00259-016-3427-0.

335. Soh LK, Tsatsoulis C. Texture analysis of SAR sea ice imagery using gray level co-occurrence matrices. IEEE Trans Geosci Remote Sens. 1999;37:780-95. doi: 10.1109/36.752194.

336.   Haralick RM, Shanmugam K, Dinstein I. Textural features for image classification. IEEE Trans Syst Man Cybern. 1973;6:610-21.

337.   Haralick RM, Shapiro LG. Computer and robot vision: Addison-Wesley Longman Publishing; 1992.

338.   Xiaoou T. Texture information in run-length matrices. IEEE Trans Image Process. 1998;7:1602-9. doi: 10.1109/83.725367.

339.   Amadasun M, King R. Textural features corresponding to textural properties. IEEE Trans Syst Man Cybern Syst. 1989;19:1264-74. doi: 10.1109/21.44046.

340.   Legland D, Kiêu K, Devaux MF. Computation of Minkowski measures on 2D and 3D binary images. Image Anal Stereol. 2011;26(2):83–92.

341.   Wang K, Singh D, Zeng Z, Coleman SJ, Huang Y, Savich GL, He X, Mieczkowski P, Grimm SA, Perou CM, MacLeod JN, Chiang DY, Prins JF, Liu J. MapSplice: Accurate mapping of RNA-seq reads for splice junction discovery. Nucleic Acids Res. 2010;38(18):e178. doi: 10.1093/nar/gkq622.

342.   Li B, Dewey CN. RSEM: accurate transcript quantification from RNA-Seq data with or without a reference genome. BMC Bioinformatics. 2011;12(323). doi: 10.1186/1471-2105-12-323.

343.   Olshen AB, Venkatraman ES, Lucito R, Wigler M. Circular binary segmentation for the analysis of array-based DNA copy number data. Biostatistics. 2004;5(4):557-72.

344.   Koboldt DC, Zhang Q, Larson DE, Shen D, McLellan MD, Lin L, Miller CA, Mardis ER, Ding L, Wilson RK. VarScan 2: somatic mutation and copy number alteration discovery in cancer by exome sequencing. Genome Res. 2012 22(3):568-76. doi: doi: 10.1101/gr.129684.111.

345.   Larson DE, Harris CC, Chen K, Koboldt DC, Abbott TE, Dooling DJ, Ley TJ, Mardis ER, Wilson RK, Ding L. SomaticSniper: identification of somatic point mutations in whole genome sequencing data. Bioinformatics. 2012;28(3):311-7.

346.   DePristo M, Banks E, Poplin R, Garimella K, Maguire J, Hartl C, Philippakis A, Angel Gd, Rivas MA, Hanna M, McKenna A, Fennell T, Kernytsky A, Sivachenko A, Cibulskis K, Gabriel S, Altshuler D, Daly M. A framework for variation discovery and genotyping using next-generation DNA sequencing data. Nature Genet. 2011;43:491-8.

347.   Network TCGA. Comprehensive molecular portraits of human breast tumours. Nature. 2012;490(7418):61-70. doi: 10.1038/nature11412.

348.   Väremo L, Nielsen J, Nookaew I. Enriching the gene set analysis of genome-wide data by incorporating directionality of gene expression and combining statistical hypotheses and methods. Nucleic Acids Res. 2013;41(8):4378-91. doi: 10.1093/nar/gkt111.

349.   Benjamini Y, Hochberg Y. Controlling the false discovery rate: a practical and powerful approach to multiple testing. J R Stat Soc Ser B-Stat Methodol. 1995;57(1):289-300. doi: 10.2307/2346101.

350.   Goonesekere NCW, Wang X, Ludwig L, Guda C. A meta analysis of pancreatic microarray datasets yields new targets as cancer genes and biomarkers. PLoS One. 2014;9(4). doi: 10.1371/journal.pone.0093046.

351.   Ho TK. Random decision forests. The 3rd Intl Conf on Doc Anal Rec; 14-16 August; Montreal, QC, Canada1995. p. 278-82.

Vita

Abdallah Sherif Radwan Mohamed was born in Alexandria, Egypt to Sherif Radwan Mohamed and Mona Abdallah Elkateb. In May 2005, Abdallah received his Bachelor degree of Medicine and Surgery (MBBch) from the Faculty of Medicine Alexandria University, Alexandria, Egypt. In May 2010, he received his Master's degree in clinical oncology and nuclear medicine, Faculty of Medicine Alexandria University, Alexandria, Egypt. In August 2017, he entered the Cancer Biology PhD program at the MD Anderson Cancer Center UTHealth Graduate School of Biomedical Sciences. He conducted his dissertation research under the guidance of Clifton D. Fuller, MD, PhD.

Permanent address:

3838 N. Braeswood Blvd.

TH20

Houston, TX 77025